UPC CTTC

Numerical Simulation of Newtonian/non-Newtonian Multiphase Flows: Deformation and Collision of Droplets

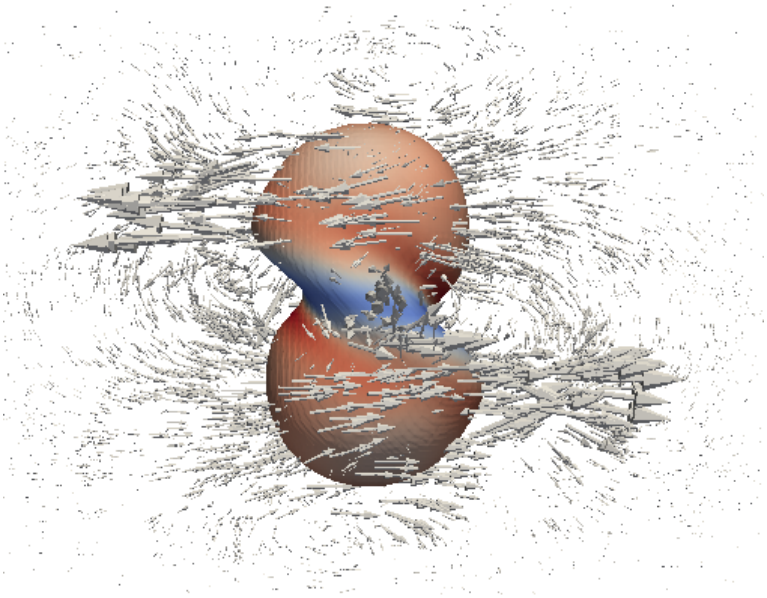

Centre Tecnològic de Transferència de Calor
Departament de Màquines i Motors Tèrmics
Universitat Politècnica de Catalunya

Ahmad Amani
Doctoral Thesis

Numerical Simulation of Newtonian/non-Newtonian Multiphase Flows: Deformation and Collision of Droplets

Ahmad Amani

TESI DOCTORAL

presentada al

Departament de Màquines i Motors Tèrmics
E.T.S.E.I.A.T.
Universitat Politècnica de Catalunya

per a l'obtenció del grau de
Doctor per la Universitat Politècnica de Catalunya

Terrassa, July 2018

Numerical Simulation of Newtonian/non-Newtonian Multiphase Flows: Deformation and Collision of Droplets

Ahmad Amani

Directors de la Tesi

Dr. Néstor Balcázar

Dr. F. Xavier Trias

Tutor de la Tesi

Dr. Assensi Oliva Llena

Tribunal Qualificador

Dr. Iztok Tiselj
University of Ljubljana

Dr. Jose Fernández Seara
University of Vigo

Dr. Joaquim Rigola Serrano
Polytechnic University of Catalonia

Acknowledgements

I would like to express my deep gratitude to Professor Assensi Oliva Llena, who provided me an opportunity to join their team, and gave me access to the laboratory and research facilities. Without his precious support it would not be possible to conduct this research.

I would like to thank Dr. Néstor Balcázar, for his insightful comments and encouragement, but also for the hard question which inspired me to widen my research from various perspectives.

I acknowledge the financial support of an FI research scholarship by the Agència de Gestió d'Ajuts Universitaris i de Recerca (AGAUR) of Generalitat de Catalunya (2016 FI-B 01059) and support of Dr. F. Xavier Trias with this regard.

Words cannot express how grateful I am to Dr. Fang Su for enlightening me with many glances of life and research.

Last but not the least, I would like to thank my family: my parents and my sisters for supporting me spiritually throughout writing this thesis and my life in general ...

Contents

List of Figures

List of Tables

Abstract

The complex nature of multiphase flows, particularly in the presence of non-Newtonian rheologies in the phases, limits the applicability of theoretical analysis of physical equations as well as setting up laboratory experiments. As a result, Computational Fluid Dynamics (CFD) techniques are essential tools to study these problems. In addition to the Newtonian multiphase flow problems, numerical simulation of complex multiphase fluid flows, e.g. synthetic polymer products have been subjected to numerous researches in the last few years, with applications in several industrial sections, e.g. in colouring, food and health products, casting, coating, drug delivery systems, etc. Despite the advances in numerical simulation techniques in this field in the past decade, the applicability of these approaches are limited by challenges appearing in specific applications, and particular consideration must be taken into account for each of these problems. The present thesis aims at three-dimensional numerical solution of Newtonian/non-Newtonian multiphase flow problems in the context of finite-volume discretization approach with applications in different natural and industrial processes.

In the context of previous researches in Multiphase flows done in Heat and Mass Transfer Technological Center (CTTC) research group, this thesis uses a conservative level-set interface tracking approach to deal with the moving interface of two immiscible fluids. The previous works on multiphase flow problems done at CTTC are mainly regarding introducing robust solvers capable of high-performance computing to study fundamental problems of bubbles, droplets. In this thesis, an attempt is made on using these techniques in solving two common industrial applications of multiphase flows, i.e. deformation of a droplet in shear and collision of droplets. The Navier-Stokes and level-set equations are solved using a finite-volume method on collocated grids.

This thesis is organized in five chapters. The first chapter aims at providing an introduction to the motivation behind this work. We also present some application of

the context of this thesis in industrial processes, followed by a small introductory on the CTTC research group, objectives and the outline of the thesis. The core of this thesis lays within chapters two, three and four.

In chapter 2, using a conservative level-set method, three-dimensional direct numerical simulation of binary droplets collision is performed. A novel lamella stabilization approach is introduced to numerically resolve the thin lamella film appeared during a broad range of collision regimes. This approach demonstrates to be numerically efficient and accurate compared with experimental data, with a significant save-up on computational costs in three-dimensional cases. The numerical tools introduced are validated and verified against different experimental results for a wide range of collision regimes where very good agreement is seen. Besides, for all the cases studied in this chapter, a detailed study of the energy budgets are provided.

In chapter 3, the physics of a single droplet subjected to shear flow is studied in details, with a primary focus on the effect of viscosity on walls critical confinement ratio. First, we highly validate the ability of the numerical tools on capturing the correct physics of droplet deformation where the extracted results are compared with available experimental, analytical and numerical data from the literature. This chapter continues by three-dimensional DNS study of subcritical (steady-state) and supercritical (breakup) deformations of the droplet for a wide range of walls confinement in different viscosity ratios. The results indicate the existence of two steady-state regions in a viscosity ratio-walls confinement ratio graph, which are separated by a breakup region. Overall, these achievements indicate a promising potential of the current approach for simulating droplet deformation and breakup, in applications of dispersion science and mixing processes.

In chapter 4, with the help of experience gained in the previous chapters, a finite-volume based conservative level-set method is used to numerically solve the non-Newtonian multiphase flow problems. One set of governing equations is written for the whole domain where different rheological properties may appear. Main challenging areas of numerical simulation of multiphase non-Newtonian fluids, including tracking of the interface, mass conservation of the phases, small timestep problems encountered by non-Newtonian fluids, numerical instabilities regarding the high Weissenberg

Number Problem (HWNP), instabilities encouraged by low solvent to polymer viscosity ratio in viscoelastic fluids and instabilities encountered by surface tensions are discussed and proper numerical treatments are provided in the proposed method. The numerical method is validated for different types of non-Newtonian fluids, e.g. shear-thinning, shear-thickening and viscoelastic fluids using structured and unstructured meshes, where the extracted results are compared against analytical, numerical and experimental data available in the literature.

List of Abbreviations

EL	**E**ulerian **L**agrangian
EE	**E**ulerian **E**ulerian
DNS	**D**irect **N**umerical **S**imulation
FD	**F**inite **D**ifference
FE	**F**inite **E**lement
FV	**F**inite **V**olume
VOF	**V**olume **O**f **F**luid
LS	**L**evel **S**et
CLS	**C**onservative **L**evel **S**et
CR	**C**onfinement **R**atio
SPC	**S**oft **P**ermanent **C**oalescence
HPC	**H**ard **P**ermanent **C**oalescence
CFRS	**C**oalescence **F**ollowed by **R**eflexive **S**eparation
CFSS	**C**oalescence **F**ollowed by **S**tretching **S**eparation
VF	**V**iscoelastic **F**luid
STF	**S**hear **T**hickening **F**luid
SThinningF	**S**hear **T**hinning **F**luid
GNF	**G**eneralized **N**ewtonian **F**luid
Wi	**Wi**ssenberg Number
HWNP	**H**igh **W**eissenberg **N**umber **P**roblem
BSD	**B**oth **S**ides **D**iffusion
PDPS	**P**ositive **D**efiniteness **P**reserving **S**cheme
LCR	**L**og **C**onformation **R**epresentation
SRCR	**S**quare **R**oot **C**onformation **R**epresentation
SVF	**S**tandard **V**iscoelastic **F**ormulation

List of Symbols

d	Diameter	m
ρ	Density	kg/m^3
μ	Dynamic Viscosity	$\mathrm{kg}/(\mathrm{ms})$
μ_0	Zero Shear Dynamic Viscosity	$\mathrm{kg}/(\mathrm{ms})$
μ_∞	Infinite Shear Dynamic Viscosity	$\mathrm{kg}/(\mathrm{ms})$
ν	Kinematic Viscosity	m^2/s
$\dot{\gamma}$	Shear Rate	s^{-1}
τ	Shear Stress	$\mathrm{kg}/(\mathrm{ms}^2)$
λ	Relaxation time	s
β	Retardation Ratio	-
$\mathbf{c}$	Conformation Tensor	-

To the memory of Reza...

Chapter 1

Introduction

1.1 Background and motivation

From fundamental physics, it is well known that the phase is defined as one of the states of matter. Therefore, the phase can be solid, liquid, or gas. Thus, In the simplest terms, multiphase flow is the simultaneous flow of more than one phase. however, in the context of this thesis, the term multiphase will be used to refer to the flows consisting of two immiscible Newtonian or non-Newtonian fluid phases separated by a differentiated interface.

Multiphase flows encompass phenomena in a broad category of different applications, in varying scales in nature along with scientific and industrial utilisation. For example, Droplets deformation and collision in a surrounding gas is of crucial importance in different applications from mixing process to reactor design engineering, microreactors, spray combustion (see figure 1.1), spray coating, drug delivery, etc [1–3]. Or in another example, multiphase flows exhibits in emulsification process with wast applications in food, chemical, and pharmaceutical industries. [4–6]. A significant category of multiphase flows is related to complex rheologies, where one or more phases exhibit non-Newtonian rheology. Interfacial complex fluid flows are of crucial importance in different applications, e.g. petrochemical, biochemical, food, and pharmaceuticals industries, to name just a few [7, 8]. The non-Newtonian rheology of one or more phases in a multiphase system has concrete importance in its operation. For instance, in multiphase reactors where many reactants may exhibit non-Newtonian behaviour, the exotic behaviours of non-Newtonian fluids like viscoelastic, offer a wider

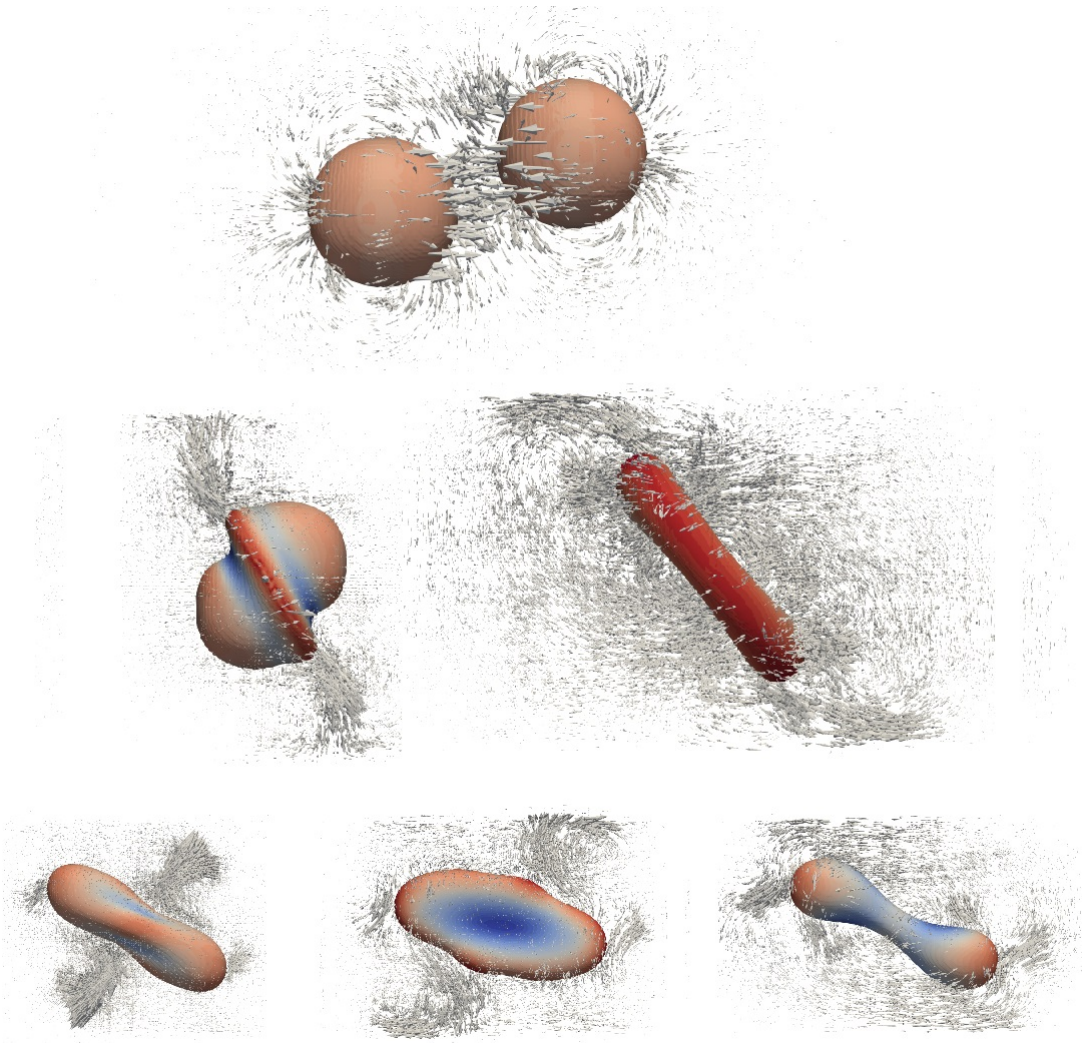

FIGURE 1.1: Application of the numerical solution of multiphase flows performed in the present thesis [1] in simulation of two tetradecane droplets collision in air matrix with applications in spray combustion.

variety of control and functionality with substantial effect in the performance of the system.

In general, there are three main approaches to study multiphase flow problems: (i) experimental analysis, using precise laboratory equipment (ii) theoretical analysis of the governing physical equations, and (iii) numerical solution using advanced computational techniques. The complex nature of multiphase flows, particularly in the presence of non-Newtonin rheologies in the phases, limits the applicability of theoretical analysis of mathematical equations as well as setting up laboratory experiments. On the other hand, the flexibility of numerical simulations on implementing different initial conditions, boundary conditions and fluid properties, as well as their capability to extract substantial information on the flow field, makes them extra appealing on studying multiphase flow problems.

The present work aims to shed some light on the numerical approaches in the simulation of multiphase Newtonian and non-Newtonian fluids. By progressively introducing numerical improvements, the proposed numerical method will be optimized, seeking to achieve robust numerical tool in solving multiphase flow problems with complex rheologies.

1.2 Computational methods in numerical solution of multiphase flows

Most of the methods in the mainstream of computational fluid dynamics employ some form of domain discretization. These methods aim to solve the underlying physical nature of the problem by first dividing the flow domain into a number of finite and non-overlapping sub-domains. Afterwards, it is required to convert the set of fundamental physical/mathematical equations into suitable algebraic forms. These equations are subsequently solved to yield the corresponding discrete values of the flow-field variables, including velocity, pressure, temperature and other transport variables of interest. Finite-difference (FD), finite-element (FE) and finite-volume (FV) methods are amongst the most main domain discretization approaches.

In the finite-difference method, the primary idea is in the utilization of Taylor series expansions at each point of the grid to form proper approximations of the partial

derivatives of the governing equations [9]. In the finite-element method, simple piecewise polynomial functions are employed on local elements to represent the variations of the unknown flow-field variables [10]. The finite-volume method, however, is one of the most common forms of discretizations in the numerical solution of fluid flows [11]. One of its most advantages is being consistent with the concept of the control volume approach. Similar to the finite-element, the finite-volume method can handle the arbitrary geometries with ease through the usage of structured, body-fitted and unstructured meshes. In this thesis, the finite-volume method is used to discritize the governing equations in the solution domain.

Regarding the numerical solution of multiphase flow problems, there are different approaches to handle the phases, including the Eulerian-Lagrangian (EL), Eulerian-Eulerian (EE), and Direct Numerical Simulation (DNS).

The EL approach is based on the effective coupling between a Eulerian field description for the solution of the continuous fluid phase and a Lagrangian scheme for determining the trajectories of the dispersed phase, particles, or bubbles as they move through the computational domain within this flow field [12, 13]. In the EE approach, the algebraic equations can be solved based on the full or partial, simultaneous or sequential, solution of the governing equations, where both phases are treated as interpenetrating continuous media, occupying the same space with different velocities and volume fractions for each phase [14, 15]. The DNS approach involves all fluid motions that are contained in the flow to understand the physics of the problem and its natural occurrence. In DNS, the equations are coupled with interface tracking (surface methods) or interface capturing (volume methods) schemes, in the framework of Lagrangian and Eulerian approaches, respectively [12, 13].

The main methods in the Lagrangian framework is front-tracking [16, 17] approach, where a stationary Eulerian grid is used for the fluid flow and the interface is tracked explicitly using a separate Lagrangian grid. This method precisely describes the multiphase flow, however, is complex to implement due to the need for re-meshing of the Lagrangian grid at each iteration. The main methods in the Eulerian framework could be categorized into three main types: (i) volume-of-fluid (VOF), (ii) level-set (LS), and (iii) hybrid, e.g. the LS/VOF. In all of these methods, multiphase flow is

solved using a single set of governing equations where the physical properties, for instance, density and viscosity vary smoothly across the moving interface. The VOF method conserves the mass of the phases properly, however, lacks the accuracy in calculations of normal and curvature of geometric interface properties. The reader can referred to [18] for a review on VOF method. On the other hand, level set approaches benefit from simplicity in calculations of geometric properties but lack in precise mass conservation [19]. The hybrid methods usually solve these problems; however, imply an increase in computational cost.

Due to the important advances in numerical techniques and computer hardware in the past decade, the field of DNS in solution of mutiphase fluid flows has experienced significant advances [20]. With the help of high-performance computing, the flow dynamics of multiphase flows can now be solved in great details leading to unprecedented insight.

In this thesis, an interface capturing Level-Set (LS) approach is used to perform DNS on multiphase flow problems where phases can be either Newtonian or non-Newtonian. This method is based on the tracking of a sharp interface which separates the two different fluids. Different phases can be unambiguously named dispersed or continuum, depending on the distribution of them.

1.3 CTTC research group

The Heat and Mass Transfer Technological Center (CTTC) of the Universitat Politécnica de Catalunya-Barcelona Tech (UPC), is a research group dedicated to accurate scientific analysis of engineering problems based on two main lines:

- Mathematical formulation, numerical resolution and experimental validation of fluid dynamics and heat and mass transfer phenomena, including natural and forced convection [21], turbulence modelling [22], combustion [23], multiphase flows [1, 24–43], solid-liquid phase change, radiation [44], porous media, numerical algorithms and solvers [45], high-performance computing [46], etc.

- The application of the acquired knowledge on thermal and fluid dynamic optimisation of thermal system and equipment.

The researchers in CTTC have been contributing in development of a CFD software platform called **TermoFluids** [47] that uses state-of-the-art numerical and physical models to perform accurate scientific analysis of engineering problems with emphasis on parallel computing and high efficiency in supercomputers.

Researchers at CTTC have access to a Beowulf cluster called *Joan Francesc Fernández (JFF)* with a total number of 2304 CPUs. JFF is benefiting from two types of cluster nodes:

- 128 cluster nodes where each of them has 2 AMD Opteron Quad Core processors with 8 Gigabytes of RAM memory, linked with an InfiniBand DDR 4X network interconnection between nodes with latencies of 2.6 microseconds and a 20Gbits/s bandwidth.

- 40 cluster nodes where each of them has 2 AMD Opteron with 16 Cores for each CPU linked with 64 Gigabytes of RAM memory and an InfiniBand QDR 4X network interconnection between nodes with latencies of 1.07 microseconds with a 40Gbits/s bandwidth.

Most of the parallel computations of the cases solved in this these are performed using this cluster.

The numerical algorithms for DNS of gas-liquid multiphase flows implemented in TermoFluids code have been introduced in Balcazar et al. [24] along with further works of non-isothermal two-phase flows in Balcázar et al. [29], coupled volume of fluid/level-set (VOF/LS) method in Balcázar et al. [25], multi-marker level-set method in Balcázar et al. [27], Adaptive mesh refinement (AMR) algorithms in Antepara et al. [32], single-phase free-surface flows in Schillaci et al. [36], and moving mesh techniques in Gutiérrez et al. [28]. The Navier-Stokes equations, energy equation, and interface capturing equations, are solved with a finite volume discretization of the physical domain on a collocated unstructured mesh. The current thesis is the first work in the content of conservative level-set method that performs DNS of deformation of droplets in shear flow and collision of droplets in substantial details, along with the extension of abilities of this approach in solving multiphase flows with complex rheologies.

1.4 Objective of the thesis

As discussed earlier, direct numerical simulation (DNS) of two-phase flows is a broad topic, with applications in a wide variety of environmental, geophysical and engineering processes. Due to these critical applications, in addition to the expansion of the computational power during the last decade, DNS of multiphase flows has drawn a lot of attention from the research community. However, this field is still far from maturity and sometimes unable to resolve many of its industrial applications, as there are many numerical difficulties dependednt on specific applications. For instance, regarding two main applications of DNS of multiphase flows considered in this thesis, deformation of droplets in shear flow and collision of droplets, there are many numerical challenges, e.g. small timesteps, sensitivity to numerical parameters, rupture of the entrapped gas film, and rupture of the lamella film, just to name a few. These challenges are in addition to the general difficulties in numerical simulation of multiphase flows, e.g. challenges related to the tracking of interfaces, mass conservation of the droplets, instabilities encountered by large density ratio and surface tensions. These problems are escalated in DNS of multiphase flows when at least one of the phases represents non-Newtonian behaviours. As a result, there is a severe need in a detailed understanding of the multiphase flow problems related to the specific applications in Newtonian and non-Newtonian fluids.

The main idea of this thesis is to provide a detailed study on the main challenges of three-dimensional multiphase flow problems related to the applications of shear deformation of a droplet and collision of the droplets. We will also analyze the problems when one of the phases represents non-Newtonian behaviour. In particular, we will mainly focus on the conservative level set (CLS) interface tracking approach. This approach has shown to be of the most promising technique to simulate multiphase flows among those tested at CTTC laboratory. Hence, we use this highly verified approach as the starting point of this thesis. The reader can refer to [24] for details on the applicability of this CLS approach.

Considering the actual state-of-the-art in multiphase flow modelling and numerical simulation methods, the main objectives of this thesis are:

- Investigate the main challenges in numerical simulation of multiphase flows appearing in the industrial applications with rheologies of Newtonian and non-Newtonian fluids. The main emphasis will be on the deformation of a droplet in shear flow and collision of the droplets.
- Develop a robust approach to solve non-Newtonian multiphase flow problems with different rheologies of shear-thinning, shear-thickening and viscoelastic.
- Provide the proper answers to the afformationed challenges, test and verify them.

The new solver for non-Newtonian multiphase flows should be implemented in the context of Termofluids code [47]. The resulting code must allow the high-performance computing of two-phase Newtonian/non-Newtonian flow problems with moving interface boundaries using millions of control volumes on parallel computers.

1.5 Thesis outline

As mentioned earlier, this thesis aims at analyzing two common industrial applications of multiphase flow problems, i.e. deformation and breakup of a droplet in shear flow and collision of the droplets. Besides a new approach based on the CLS method is presented to solve the challenging non-Newtonian multiphase flow problems. As a result, the next two chapters are allocated to the numerical simulation of collision of the droplets and deformation of a droplet in shear flow, respectively, followed by a chapter on details of the proposed approach for non-Newtonian multiphase flows.

In chapter 2, we use a set of state-of-the-art numerical tools, i.e. finite-volume conservative level-set interface capturing method, lamella stabilization approach, etc., to elaborately study the main collision regimes and provide a solution for the main challenges in this field. For instance calculation of gas film rupture time accurately solves the problem of retarded coalescence collisions while conserving the mass of the droplet, or introduced lamella stabilization approach eliminates the need of high-orders of magnitude grid refinements in capturing a stable lamella film which results in a huge reduction of computational cost while maintaining a good accuracy. Utmost efforts have been devoted to the accuracy of the results. For this reason, we highly validated and verified our numerical methods against experimental benchmarks available in the

literature. Many challenging cases have been solved, in which due to the complexity of some cases, this is the first time that their numerical solution is being presented. Supplementary videos of all the collision cases are provided to support and enhance the scientific content of this chapter and to further enrich the understanding of the whole phenomena of the collision cases in all collision regimes. In addition to the presented numerical tools, we provide energy analysis of the cases to offer a deeper insight into the crucial aspects of droplets collision including dissipation of the energy, kinetic energy recovery, etc.

In chapter 3 we perform numerical investigations on the physical nature of a droplet in shear flow. Similar to chapter 2, we validate and verify our numerical method against experimental data available in literature. Afterwards, we elaborately study the mutual effect of viscosity ratio and confinement of the walls on droplet deformation and break-up. Our results illustrate the existence of two steady-state regions separated by one break-up region for droplet under different confinements and viscosity ratios.

In chapter 4 we introduce a novel numerical methodology to accurately solve the interfacial flow problems where one or more phases represents non-Newtonian behaviour. We discuss the main challenges in this field in details and suggest the most prominent solution for each of them. Similar to the previous chapters, we validate and verify our numerical method against experimental, analytical and numerical data available in the literature. Our proposed approach has proven to be numerically stable for solutions with high Weissenberg number, and low solvent to polymer viscosity ratio.

In the last chapter 5, conclusion remarks and future works are presented. A list of publications resulting from this thesis and Supercomputing projects are provided in appendix A.

Chapter 2

Numerical study of binary droplets collision in the main collision regimes

Most of the contents of this chapter have been published as:

A. Amani, N. Balcázar, A. Naseri, A. Oliva. *A Study on Binary Collision of GNF Droplets Using a Conservative Level-Set Method.* In proceeding of 7th European Conference on Computational Fluid Dynamics (ECFD 7), June 2018, Glasgow.

A. Amani, N. Balcázar, E. Gutiérrez, A. Oliva. *Numerical study of binary droplets collision in the main collision regimes.* Chemical Engineering Journal, 1385-8947, 2019, https://doi.org/10.1016/j.cej.2019.03.188

Abstract. Direct numerical simulation of binary droplets collision in all collision regimes is done using a conservative level-set method. The Navier-Stokes quations and level-set equations are solved with a finite-volume method on a collocated grid. A novel lamella stabilization approach is introduced to numerically resolve the thin lamella film appeared during a broad range of collision regimes. This method proves to be direction-independent, numerically efficient and accurate compared with experimental data. When the droplets collide, the fluid between them is pushed outward, leaving a thin gas layer bounded by the surface of the droplets. This layer progressively gets thinner and depending on the collision regime, may rupture resulting in coalescence of the droplets or may linger resulting in bouncing-off the droplets. Embedded ghost-nodes layer makes it possible to mimic both bouncing and coalescence phenomena of the droplets collision. The numerical tools introduced are validated and verified against different experimental results for all the collision regimes. A very good agreement is observed between the results of this chapter and experimental data available in the literature. A detailed study of the energy budget for different shares of kinetic and dissipation energies inside of the droplet and matrix, in addition to the surface tension energy for studied cases, is provided. Supplementary quantitative values of viscous dissipation rate inside of the matrix and droplet, and also the radial expansion of the droplet are presented as well.

2.1 Introduction

The dynamics of binary droplets collision is of huge importance in different fields, from multiphase reactors [48], raindrop formation [49], ink-jet printing, spray combustion, emulsion stability, turbine blade cooling, spray coating [50, 51], to drug delivery, e.g. by encapsulating one liquid within another one used in the context of drugs in lungs [52]. Due to the complexity of the nature of droplets collision, this topic is one of the most challenging areas in the field of fluid dynamics. The outcome of the droplets collision can profoundly affect the overall performance of many systems. For example in fuel sprays near the injector in internal combustion engines or gelled hypergolic propellants in rocket engines, the outcome of the collisions, the size distribution, dissipated energy of the droplets and number of satellite droplets can affect the overall

combustion efficiency. Binary droplets collision as two droplets collide each other are the most common interaction in aerosol sprays where ternary and more complex collisions are rare. Droplets collision has been the topic of numerous investigations, including experimental, analytical and numerical studies.

Experimental research started with studying the interaction of falling water drops [53]. Brenn and Frohn [54] investigated the collision and coalescence of droplets of different liquids. Ashgriz and Poo [50] studied the binary collision of two water droplets of equal and unequal sizes. They concluded that the collision dynamics could be characterized based on the droplets size ratio, collision Weber number and the impact parameter (I) where the Weber number presents the ratio between inertial forces and surface tension and impact parameter characterizes the eccentricity of the droplets in the collision direction. Qian and Law [51] presented a detailed description of collision dynamics based on a series of time-resolved images of the collisions for different regimes of head-on and off-center. They provided a map based on Weber number and Impact parameter separating collision regimes in a We-I nomograph. They concluded the existence of five regimes as coalescence after minor deformation (I), bouncing (II), coalescence after substantial deformation (III), coalescence followed by separation for near head-on collision (IV), and coalescence followed by separation for off-center collision (V). Jiang, Umemura, and Law [55] investigated the collisional dynamics of equal-sized water and normal-alkane droplets. Willis and Orme [56] conducted experimental research on binary droplet collisions in a vacuum environment to study the dynamics of the collision in the absence of aerodynamic effects. Pan, Law, and Zhou [57] experimentally and numerically investigated the dynamics of head-on droplets collision. Utilizing the empirically supplied information in the numerical simulations, they further studied different parameters of the collision including gap gas width thickness and flow properties around the interface. Tang, Zhang, and Law [58] studied collision of unequal-sized droplets in different regimes. They provided a unified regime diagram concerning bouncing, coalescence, and separation for hydrocarbon and water droplets. On a more advanced work, Pan, Chou, and Tseng [59] used a technique developed for generating high-speed droplets to investigate binary droplets collision at Weber numbers up to 5100. Planchette et al. [60] experimentally examined the onset of fragmentation in head-on binary and ternary droplets collisions. With the help of

extracted data, they provided a general model for predicting the velocity threshold of fragmentation of collisions. Pan et al. [61] investigated the effect of surfactants on controlling the droplets bouncing and coalescence. Estrade et al. [62] studied the binary droplet collision of ethanol droplets. They also proposed a theoretical model to predict the droplet coalescence and bouncing outcome.

Analytical studies in this field are performed to a great extent to predict the outcome of a particular type of collision. Reitz and D. [63] presented a simplified model of a droplet-shattering collision. Gopinath [64] analyzed the head-on collision and subsequent rebound of two droplets for small Weber numbers. Bach, Koch, and Gopinath [65] presented a theory based on potential flow in the liquid, weak deformation of the gas-liquid interfaces, and non-continuum viscous flow in the lubrication gas film for minimal Weber numbers. Zhang and Law [66] suggested a unified theoretical description of head-on equal-sized droplets. They have made important advances in presenting a general formulation for a wide range of Weber numbers. In a more recent research, Li [67] predicted the coalescence-bouncing transition of head-on binary droplets collision using a macroscopic model. He has modified the Navier-Stokes equations to account for the inter-droplet gas film using the lubrication theory of Zhang and Law [66].

The flexibility of numerical simulations on implementing different initial conditions, boundary conditions and fluid properties, as well as their capability to extract substantial information on the flow field, makes them extra appealing on studying multiphase flow problems. Numerical simulations of droplets collision can provide significant details on the nature of the collision, e.g. energy analysis of the droplets, air gap thickness, velocity and vorticity fields which are difficult or impossible to capture experimentally or analytically. As a result, significant attention was given to numerical simulations of droplets collision.

The volume-of-fluid (VOF) method along with an adaptive mesh refinement methodology was employed by Nikolopoulos and Bergeles [68] to study the binary droplets collision for cases with Weber numbers up to 61.4. Good agreement was achieved between their simulations and the experimental results. In another work, Nikolopoulos, Theodorakakos, and Bergeles [69] studied the off-center binary droplets collision using an adaptive mesh refinement technique. However, a stable lamella film was not

captured for high Weber numbers. Chen et al. [70] studied the droplets collision dynamic using an improved VOF technique, an adaptive mesh refinement algorithm and mass transfer process. Although the VOF method conserves the mass property of the droplets, it suffers the accuracy for calculation of normal and curvature of the interfaces.

In the category of the level-set method, Pan and Suga [71] used a level-set/finite-volume method to simulate three-dimensional collisions for a wide range of Weber numbers. Uniform mesh with small grid sizes was used in their work ($D_0/60$-$D_0/80$ with D_0 as the initial diameter of the droplets). Good agreement was seen in their results compared with experimental-snapshots. Tanguy and Berlemont [72] applied a level-set/finite-difference approach on the collision of droplets for cases with Weber numbers up to 83. A disadvantage of the level-set method is that the discrete solution of transport equations is inclined to numerical error which results in loss or gain of mass in the droplets. Kwakkel, Breugem, and Boersma [73] developed a coupled level-set/volume-of-fluid (CLSVOF) method for droplet-laden flows to accommodate coalescence and breakup of the droplets. They have mentioned that the film drainage time calculated by the model of Zhang and Law [66] is not sufficiently accurate to capture the correct physics of the collision. Recently, Balcázar et al. [27] used a novel multiple-marker approach for simulating the bouncing of the droplets, in the framework of a conservative level-set method, which circumvents the mass conservation issue.

In the category of the front-tracking method, Nobari, Jan, and Tryggvason [74] conducted two-dimensional axisymmetric simulation of head-on collision process using a front-tracking/finite-difference method in low-density ratio flows. Later on, Pan, Law, and Zhou [57] used the three-dimensional version of this method to simulate cases with Weber numbers up to 13. Zhang and Zhanga [75] studied the kinetic energy recovery and the interface hysteresis of bouncing droplets. In the Front-tracking method, a fixed Eulerian grid is used for the fluid flow, and a separate Lagrangian grid is used to track the interface explicitly. Despite the accuracy of this method, it is complicated to implement (due to dynamic re-meshing of the Lagrangian interface mesh), and also difficulties arise when multiple interfaces interact with each other.

Moqaddam, Chikatamarla, and Karlin [76] used an entropic lattice Boltzmann

method to simulate high Weber number collision cases with lamella films. Premnath and Abraham [77] Used a multi-relaxation-time multiphase flow lattice Boltzmann model to solve head-on and off-center binary droplets collision. In another work Dupuy et al. [78] simulated high-pressure binary droplets collision. Baroudi, Kawaji, and Lee [79] examined the effect of initial conditions on the simulation of inertial coalescence of two droplets. Sun, Jia, and Wang [80] numerically investigated the head-on unequal-sized collision of droplets using a multiple-relaxation-time lattice Boltzmann model. Mazloomi, Chikatamarla, and Karlin [81] presented a novel thermodynamically consistent lattice Boltzmann model enable to control the dynamics at the liquid-vapor interface.

Despite all the advances in the numerical simulation of droplets collision, this area is still a challenging topic regarding the difficulties related to the tracking of interfaces, mass conservation of the droplets, numerical disintegration of the lamella film, instabilities encountered by large density ratio and surface tensions. In this chapter, we study the binary head-on and off-center collision of equal-sized droplets for all the collision regimes. We introduce a novel and computationally-efficient lamella stabilization approach to resolve the thin lamella film formed during a wide range of collision regimes. We perform the energy analysis of all the cases studied, and provide qualitative graphs to benchmark these cases for future validation purposes. Furthermore, to the best of the authors' knowledge, there are no previous studies of binary droplet collision using a conservative level-set (CLS) method. Therefore, as an additional novelty, this research is performed in the framework of a CLS method introduced in Balcazar et al. [24] for interface capturing on unstructured meshes. In the present CLS method, interface normals are computed using a least-squares method on a wide and symmetric nodes-stencil around the vertexes of the current cell. These normals are then used for an accurate computation of surface tension, without additional reconstruction of the distance function, as in geometrical volume-of-fluid/level-set methods [25] or fast-marching methods. Moreover, most computational operations are local, indeed this method has been efficiently implemented on parallel platforms [24, 30]. Furthermore, unstructured flux-limiter schemes introduced in [24] are used to advect the CLS function and momentum, avoiding numerical oscillations at discontinuities, and minimizing the numerical diffusion. Finally, the present finite-volume formulation is attractive due

to its simplicity and the satisfaction of the integral forms of the conservation laws over the entire domain.

The rest of the chapter is organized as follows: mathematical formulations are presented in section 2.2, numerical discretization of governing equations are described in section 2.3.1. Gas-film and lamella stabilization algorithms are explained in section 2.3.4 and 2.3.5, respectively. Results and discussions are reported in section 2.4 and at the end, conclusion remarks are provided in section 2.7.

2.2 Mathematical formulation

Navier-Stokes equations are used to describe the conservation of mass and momentum of two incompressible immiscible Newtonian fluids on a spacial domain Ω with boundary $\partial\Omega$ as following [24]:

$$\frac{\partial}{\partial t}(\rho\mathbf{v}) + \nabla\cdot(\rho\mathbf{v}\mathbf{v}) = \nabla\cdot\mathbf{S} + \rho\mathbf{g} + \sigma\kappa\mathbf{n}\delta_\Gamma \text{ in } \Omega \tag{2.1}$$

$$\mathbf{S} = -p\mathbf{I} + \mu(\nabla\mathbf{v} + (\nabla\mathbf{v})^T) \tag{2.2}$$

$$\nabla\cdot\mathbf{v} = 0 \text{ in } \Omega \tag{2.3}$$

where ρ and μ are density and dynamic viscosity of the fluids, $\mathbf{v}$ is the velocity field, $\mathbf{S}$ is the stress tensor, p pressure field, $\mathbf{g}$ gravitational acceleration and δ_Γ is the Dirac delta function concentrated at the interface (Γ). In this formulation, $\mathbf{n}$ is the normal unit vector outward to interface, κ is the interface curvature, and σ is the interface tension coefficient.

Taking into account that mass, density and viscosity are constant within each fluid, they can be defined as scalar-fields inside the whole domain as follows:

$$\rho = \rho_1 H + \rho_2(1-H) \tag{2.4}$$

$$\mu = \mu_1 H + \mu_2(1-H) \tag{2.5}$$

where H is the Heaviside step function taking the value one in dispersed phase and zero elsewhere. In this research, conservative level-set (CLS) method as introduced by Balcázar et al. [24] in the context of a finite-volume method and unstructured meshes

is used. Instead of the signed distance function, d(x,t), used to represent the interface in the classical level-set method, conservative LS method employs a regularized indicator function ϕ as below:

$$\phi(x,t) = \frac{1}{2}\left(tanh\left(\frac{d(x,t)}{2\varepsilon}\right)+1\right) \tag{2.6}$$

where ε is the parameter that sets the thickness of the interface. ϕ varies from 0 in one fluid to 1 in other fluid. With this formulation, interface is defined by $\Gamma = \{x|\phi(x,t) = 0.5\}$.

The level-set function is advected by velocity vector field, **v**, obtained from solution of Navier-Stokes equations. Taking into account the incompressibility constraint (equation 2.3), the interface transport equation can be transformed to the conservative form [24, 82] as:

$$\frac{\partial\phi}{\partial t} + \nabla\cdot\phi\mathbf{v} \quad = \quad 0 \tag{2.7}$$

Since sharp changes exist in level-set function at the interface, flux-limiter schemes are required to discretise the convective term to minimise numerical diffusion and avoid numerical instabilities at the interface. An additional re-initialization equation is used to keep the profile and thickness of the interface constant:

$$\frac{\partial\phi}{\partial\tau} + \nabla\cdot\phi\left(1-\phi\right)\mathbf{n}_{\tau=0} \quad = \quad \nabla\cdot\varepsilon\nabla\phi \tag{2.8}$$

This equation which is advanced in pseudo-time τ, consists of a compressive flux ($\phi(1-\phi)\mathbf{n}_{\tau=0}$) which keeps the level-set function compressed onto the interface along the normal vector **n**, and a diffusion term ($\nabla\cdot\varepsilon\nabla\phi$) which keeps the profile in prescribed characteristic thickness of ε. This parameter is defined based on the mesh resolution as [24, 82]:

$$\varepsilon \quad = \quad C_\varepsilon h^{1-\alpha} \tag{2.9}$$

where $h = (Vol_P)^{1/3}$ is the grid size, with Vol as the volume of the computational cell. Generally, the value of α can vary between [0,0.1], to overcome the possible numerical

instabilities, but in all of our simulations, α value was chosen equal to 0.0. The value of C_ε is equal to 0.5. Normal vector $\mathbf{n}$ and curvature κ of the interface, are obtained using [24]:

$$\mathbf{n} = \frac{\nabla\phi}{||\nabla\phi||} \tag{2.10}$$

$$\kappa(\phi) = -\nabla\cdot\mathbf{n} \tag{2.11}$$

The continuous surface force model (CSF) [83] is used for surface tension computation which converts the term $\sigma\kappa\mathbf{n}\delta_\Gamma$ in Eq. 2.1 to a volume force term of $\sigma\kappa(\phi)\nabla\phi$. Where $\nabla\phi$ is computed using least-square method based on vertex node stencils [24]. By applying this approach, the explicit tracking of the interface is not necessary.

2.3 Numerical method

2.3.1 Discretization of governing equations

Finite-volume (FV) approach is used to discretise the Navier-Stokes and level-set equations on a collocated grid meaning all the computed variables are stored at centroids of the cells [24]. A central difference (CD) scheme is used to discretise the compressive term of re-initialization equation (2.8) and diffusive fluxes at the faces. A distance-weighted linear interpolation is used to calculate the face values of physical properties and interface normals. The gradients are computed at the cell centroids by a least-squares method using a stencil that includes the cell-nodes around the vertexes of the current cell [24].

As in this chapter, we are analysing the energy budget of the collisions, the choice of flux-limiter in the discretization of convective terms of momentum and advection equations must be accordingly, to obtain the highest accuracy in total energy conservation of the system. Section 2.6 provides a detailed study on the effect of different flux-limiters on total energy conservation of a two-phase system and the spatial convergence rate of the chosen one. According to these results, unless otherwise is mentioned, a total-variation Diminishing (TVD) flux-limiter of Superbee is used in all the simulations of this chapter.

At discretized level, physical properties are regularized in the context of the CLS method. Therefore a linear average is used for density as $\rho = \rho_1\phi + \rho_2(1-\phi)$, and viscosity as $\mu = \mu_1\phi + \mu_2(1-\phi)$.

A classical fractional step projection method as described by Chorin [84] is used to solve the velocity-pressure coupling. The solution procedure is as follows:

1. Physical properties, interface geometric properties and velocity field are initialized.

2. Maximum allowable time step is calculated using the CFL conditions on the convective and diffusive terms of momentum equation and also by explicit treatment of surface tension as used by Balcazar et al. [24]:

$$\Delta t \equiv \alpha \times min\left(\frac{h}{\|V_P\|}, \frac{h^2\rho(\phi_P)}{\mu(\phi_P)}, h^{3/2}\left(\frac{\rho_1+\rho_2}{4\pi\sigma}\right)^{1/2}\right) \tag{2.12}$$

   where α is the CFL coefficient. In the simulations of this chapter, the value of α is equal to 0.1.

3. The advection equation (2.7) is integrated in time with a 3-step third order accurate TVD Runge-Kutta scheme [85].

4. The re-initialization equation (2.8) is integrated in pseudo time (τ) using a third order accurate TVD Runge-Kutta scheme. The time τ is used to lead the solution into a stationary state. Since an explicit scheme is used, the time step is restricted by the viscous term of equation 2.8 as $\Delta\tau = C_\tau min\left(h^2/\varepsilon_P\right)$ [24, 82]. One iteration is used to solve the discretized form of equation 2.8. The value of C_τ serving as a CFL-like coefficient for this equation is equal to 0.05.

5. Physical properties in the domain (density and viscosity) and geometrical properties at the interface (curvature and interface normal) are updated from the level-set field.

6. The velocity and pressure fields are calculated using a classical fractional-step method first introduced by Chorin [84]. The first step is to calculate the predicted

velocity **v**. A second-order Adam-Bashforth scheme is used on the temporal discretization of convective, diffusive and surface tension terms.

$$\frac{\rho \mathbf{v}^* - \rho^n \mathbf{v}^n}{\Delta t} = \frac{3}{2}(R_h^v)^n - \frac{1}{2}(R_h^v)^{n-1} \tag{2.13}$$

where $R_h^v = -\mathbf{C}_h(\rho \mathbf{v}) + \mathbf{D}_h(\mathbf{v}) + \sigma \kappa \nabla_h(\phi)$ with $\mathbf{C}_h(\rho \mathbf{v}) = \nabla_h \cdot (\rho \mathbf{v}\mathbf{v})$ as the convective operator, $\mathbf{D}_h(\mathbf{v}) = \nabla_h \cdot \left(\mu(\nabla_h \mathbf{v} + \nabla_h^T \mathbf{v})\right)$ as the diffusive operator and ∇_h as the gradient operator. In this equation, **n** represents the previous timestep and equation is integrated in conservative form.

A correction to the predicted velocity applies as:

$$\frac{\rho \mathbf{v}^{n+1} - \rho \mathbf{v}^*}{\Delta t} = -\nabla_h \mathbf{P}^{n+1} \tag{2.14}$$

By applying the incompressibility constraint ($\nabla \cdot \mathbf{v} = 0$), equation 2.14 changes to a Poisson equation as follows:

$$\nabla_h \cdot \left(\frac{1}{\rho}\nabla_h(\mathbf{P}^{n+1})\right) = \frac{1}{\Delta t}\nabla_h \cdot (\mathbf{v}^*) \tag{2.15}$$

The obtained linear system is solved using a preconditioned conjugated gradient method. At the end, the velocity $\mathbf{v}^{n+1}$ is corrected using:

$$\mathbf{v}^{n+1} = \mathbf{v}^* - \frac{\Delta t}{\rho}\nabla_h(\mathbf{P}^{n+1}) \tag{2.16}$$

7. To fulfill the incompressibility constraint (equation 2.3) and to avoid pressure-velocity decoupling on collocated meshes [86], a cell-face velocity is used to advect the momentum and CLS function, as introduced in [24, 87].

8. repeat steps 2 -7 to reach the desired time.

The reader is referred to [24, 87] for technical details on the finite-volume discretization of both the Navier-Stokes and conservative level-set equations on collocated

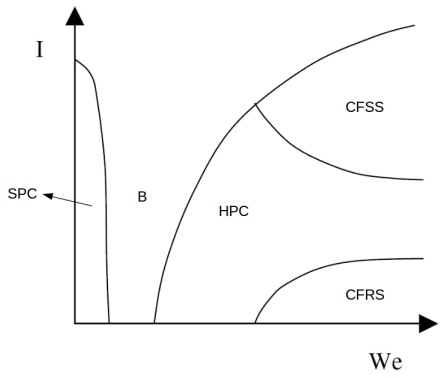

FIGURE 2.1: We-I diagram for collision outcome regimes [51]

unstructured grids. The numerical methods are implemented in an in-house parallel c++/MPI code called TermoFluids [47]. Validations and verifications of the numerical methods in the context of Conservative level-set method used in this work have been reported in [2, 24, 26, 28, 87–90].

2.3.2 Dimensionless collision parameters

Experimental studies are providing us with different correlations to understand the droplets collision. The main parameters are the surface tension coefficient σ, droplet viscosity μ_d, droplet density ρ_d, droplets relative velocity U_{rel}, and the impact parameter I. The following non-dimensional parameters are thus defined by most researchers to characterize the droplets collision:

$$We = \frac{\rho_d {U_{rel}}^2 D_0}{\sigma}, \quad Re = \frac{\rho_d U_{rel} D_0}{\mu_d}, \quad Oh = \frac{\mu_d}{\sqrt{\rho_d \sigma D_0}}, \quad I = \frac{b}{D_0} \tag{2.17}$$

where We is the Weber number presenting the ratio between inertial forces and surface tension, Re is the Reynolds number representing the ratio of the inertial and viscous forces, and Oh is the Ohnesorge number representing the ratio of viscous forces and the combined effect of inertial forces and surface tension. In this formulation D_0

is the value of droplet initial diameter and subscript **d** is the abbreviation of the word *droplet*. The impact parameter I characterizes the eccentricity of the collision with b as the inter-center distance of the droplets in direction normal to the collision.

Collision regimes of two equally sized Newtonian droplets are usually categorized in five main regimes as depicted in We-I diagram of figure 2.1:

1. SPC (soft permanent-coalescence): coalescence after minor deformation.
2. B: Bouncing of the droplets.
3. HPC (hard permanent-coalescence): Coalescence after substantial deformation, sub-categorized into:
   - Retarded permanent coalescence
   - Immediate permanent coalescence
4. CFRS (coalescence followed by reflexive separation): Coalescence followed by separation for near head-on collisions.
5. CFSS (coalescence followed by stretching separation): Coalescence followed by separation for off-center collisions.

In this study, we provide information regarding collision outcome and the physics of the phenomena in all these regimes.

2.3.3 Energy analysis of the system

For all the cases solved in this study, we have monitored the energy budget throughout the collision process. From energy conservation, we expect that the total energy (**TE**) of the system must be constant during the collision, and be equal to its initial value, i.e. the summation of the initial Kinetic energy ($\mathbf{KE}_{init}$) and the initial Surface tension energy ($\mathbf{STE}_{init}$). This value must be equal to the summation of kinetic, surface tension and total dissipated energies (**TDE**) in each given time t.

$$\mathbf{TE} = \mathbf{KE}_{init} + \mathbf{STE}_{init} = \mathbf{KE}(t) + \mathbf{STE}(t) + \mathbf{TDE}(t) \tag{2.18}$$

Kinetic energy [J] at a give time is calculated by summation of spacial integration of $\frac{1}{2}\rho V^2$ over all the cells with V as the second norm of the velocity vector in the cell P:

$$\mathbf{KE}(t) = \sum_{cells} \left(\int_p \frac{1}{2} \rho V^2 dv_p \right) \tag{2.19}$$

Surface tension energy [J] is calculated as $\sigma \mathbf{S}(t)$ where **S**(t) is the surface area of the interface. The value of **S**(t) is equal to:

$$\mathbf{S}(t) = \sum_{cells} \left(\int_p ||\nabla \phi|| dv_p \right) \tag{2.20}$$

TDE(t) [J] is calculated by temporal integration of viscous dissipation rate (**VDR**(t)) from the beginning of the simulation until time t:

$$\mathbf{TDE}(t) = \int_0^t \mathbf{VDR}(t) dt \tag{2.21}$$

VDR(t) [J/s] is obtained by summation of spatial integration of viscous dissipation function (**VDF**(t)) over all the cells:

$$\mathbf{VDR}(t) = \sum_{cells} \left(\int_p \mathbf{VDF}(t) dv_p \right) \tag{2.22}$$

In this formulation, the value of **VDF** [J/(s.m^3)] quantifies the local volumetric viscous dissipation rate in each cell and is calculated by:

$$\mathbf{VDF} = \mu \left(\nabla V + \nabla V^T \right) : \nabla V \tag{2.23}$$

The share of **KE** and **TDE** budgets could be divided into two subdomains of droplet and matrix using the introduced level-set function (ϕ), e.g.:

$$\mathbf{KE}_{drop} = \mathbf{KE} \times \phi \tag{2.24}$$

$$\mathbf{KE}_{matrix} = \mathbf{KE} \times (1 - \phi) \tag{2.25}$$

In order to investigate the accuracy of our results on calculations of energy budgets of the simulations, verification on these formulations on a three-dimensional droplet deformation test case are provided in section 2.5.

2.3.4 Gas-film stabilization approach

During the collision process, a thin gas film is formed between the droplets. The consistency of this gas film results in bouncing and rupture of it results in coalescence of the droplets. The thickness of this gas film is in the order of nanometers and CFD simulation of it is almost impossible. Different approaches have been tried by the researchers to tackle this problem. Mason, Stevens, and Harvie [91] presented a subgrid-scale model to account for the gas film drainage due to the computational difficulty of capturing all length scales involved with a single discretized mesh. Jiang and James [92] developed numerical models to incorporate the van-der-Waals forces in the Navier-Stokes equations with the assumption that the interface slope is small. They used two methods, one by introducing the van-der-Walls forces as a body force in the momentum equation and other by employing the van-der-Waals forces in terms of a disjoining pressure in the film depending on the film thickness. Li [67] employed a macroscopic model for head-on binary droplets collision solving five orders of magnitude length scale range of the problem.

According to the experimental results and analysis of Qian and Law [51], before coalescence, due to the existence of gas film between the droplets, the topology evolution of collision is similar to the bouncing of two droplets. The time when the thickness of inter-droplets gas film reaches a minimum value is noted as the critical time in topology evolution of the droplets collision. At this critical time, the droplets lack enough kinetic energy to squeeze the gas film further. The future of the collision depends on whether the gas film rupture will happen or not. Therefore, this critical time can also be assigned as the gas film rupture time.

In this study we have used ghost-nodes method to control the gas film rupture for cases of regimes *SPC*, *B* and *retarded HPC* . For these cases, instead of collision of two droplets, the collision of a droplet with a symmetry wall with ghost-nodes is studied. Figure 2.2 illustrates the concept of ghost-nodes layer in determining the

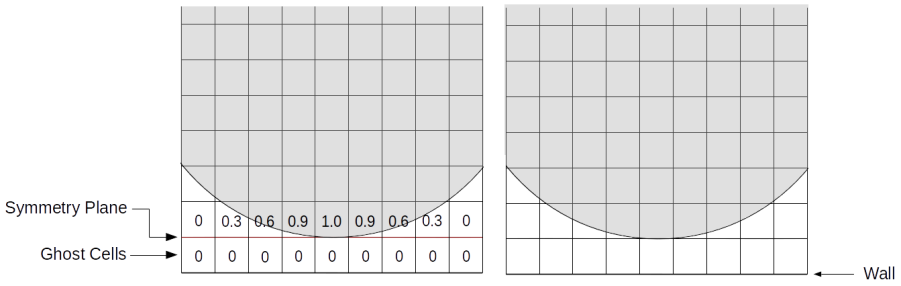

FIGURE 2.2: (left) Illustration of the implemented ghost-nodes and symmetry plane used to imitate the gas rupture persistence. (right) removal of ghost-nodes layer for the times after gas film rupture.

droplets collision outcome. Implementing the Dirichlet boundary condition for level-set function in these nodes imitates the persistence of gas film and thus bouncing of droplets. In the previous works in literature, the researchers were using the Neumann boundary condition in the ghost-nodes to imitate the rupture of the gas film, resulting in coalescence of the droplets. We believe this injects mass into the system and is not advised since it does not conserve the mass of the droplet. In this work, instead of using Neumann boundary condition on ghost-nodes layer to imitate the gas rupture, we merely remove the ghost-nodes layer, allowing the droplet to approach the wall with symmetry boundary condition applied to it.

Removing the ghost-nodes layer in a prescribed time enables us to model the retarded coalescence phenomena (SPC and retarded HPC regimes). Considering the above explanations, to simulate the retarded coalescence cases, one needs the time for rupture of the gas film. To do so, we first simulate a bouncing collision of a droplet with the ghost-nodes layer and monitor the thickness of the gas film during the collision process. The time where the gas film reaches its minimum value will be counted as the rupture time. We then restart the simulation and apply the calculated rupture time as the time when we remove the ghost-nodes layer from the simulation, e.g. change the collision regime from bouncing to coalescence. Thus, three steps are taken into account to simulate a head-on retarded coalescence of colliding droplets:

- Applying ghost-nodes layer boundary condition in the collision direction to monitor the thickness of the gas film during the collision process.

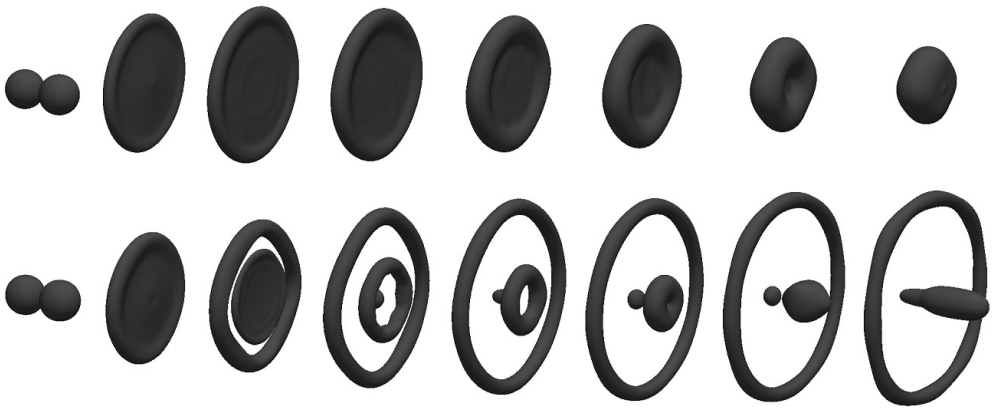

FIGURE 2.3: Droplets collision outcome for two cases of binary head-on collision with We=269 and Re=154. Stabilized lamella (first row) and standard simulation (second row). Both simulations performed in a domain with a fine grid size of h=D/50.

- Calculating the time related to minimum gas film thickness.
- Introducing this time as the time when the ghost-nodes layer is being removed from the simulation. (e.g. switching from bouncing regime into coalescence regime).

2.3.5 Lamella Stabilization Approach

In the collision of two droplets, there is a threshold of the governing parameters (Weber number and impact parameter I), in which for collisions with higher Weber number and smaller impact parameter, an extremely thin film called lamella is formed during the collision process. As reported in experimental studies [50, 51, 93], the rupture of the lamella film does not happen in droplets collision for Weber numbers as high as 2800 indicating that lamella rupture which happens in numerical simulations is a numerical artifact and needs to be prevented in order to capture the correct physics of the collision. The numerical rupture of lamella film results in deflection of the shape and physics of the collision complex [69]. Figure 2.3 illustrates exemplarily the shape of the collision outcome for two cases, one with lamella resolved and other with standard simulation.

The thickness of lamella film is of smallest scales of the simulations and numerical resolution of it implies enormous extra computational cost through the usage of

extremely fine meshes or adaptive-mesh-refinement (AMR) techniques. The thickness of the lamella film decreases as the Weber number increases, and in case of extremely high Weber numbers, e.g. in splashing collision of droplets, numerical resolution of this film by decreasing the mesh size or AMR techniques is almost impossible.

According to [94, 95], the primary cause of numerical lamella rupture is due to the interaction in the computation of surface tension forces of its both sides and also incorrect surface reconstruction caused by artificial interface interaction. Focke and Bothe [94] and Liu and Bothe [95] suggested that both of these problems could be prevented by identifying the lamella film and afterwards treating the cells of the opposite sides of the lamella as they called it *fully wetted*. They proceeded the solution by injecting mass into the lamella layer to keep its thickness more than one grid cell. In the algorithm of [94], it is necessary to calculate the angle between X direction and the lamella, immediately before its rupture, and then restart the simulation with the rotated domain so that lamella is perpendicular to the X direction. Proposed algorithm of [95] however can be used only for the head-on collision of the droplets where the collision solution could be replaced by the collision of one droplet with a ghost-nodes layer. In this section, we introduce a novel approach towards the stabilization of the lamella film which overcomes the aforementioned problems.

In the presented conservative level-set method, the interface profile is resolved in a smooth transition of ϕ at the interface. The width of the transition region depends on the diffusion coefficient ε defined in equation 2.9. Figure 2.4 presents the interface of an arbitrary collision of droplets in the matrix fluid, resolved by structured square grids along with the transition of the level-set function ϕ from 1 inside of the droplet to 0 in the matrix fluid for the direction $\mathbf{n}$ normal to the interface. Figure 2.5(a) presents the interface of the same collision as figure 2.4, advanced in time where the lamella film appears in the collision complex. Figure 2.5(b) illustrates the transition of the level-set function (ϕ) for the direction $\mathbf{n}$ normal to the interface from 0 in the matrix fluid, to 1 inside of the droplet and again to 0 in the matrix fluid. In this figure, $\boldsymbol{\ell}_2$ is the interface thickness in the lamella film and $\boldsymbol{\ell}_1$ is the length of the portion of lamella which contains only pure droplet material.

We define the physical center of the lamella film in $\mathbf{n}$ direction as cell $\mathbf{P}$ which

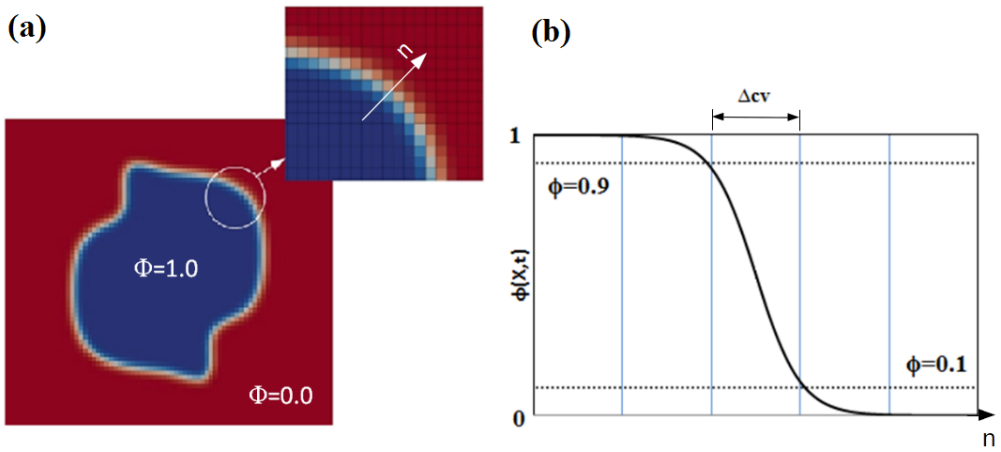

FIGURE 2.4: (a): Interface of an arbitrary collision of droplets in a matrix fluid along with (b): transition of the level-set function ϕ from 1 inside of the droplet to 0 in the matrix for the direction **n** normal to the interface.(Δ_{cv} is the grid size of the cell cv)

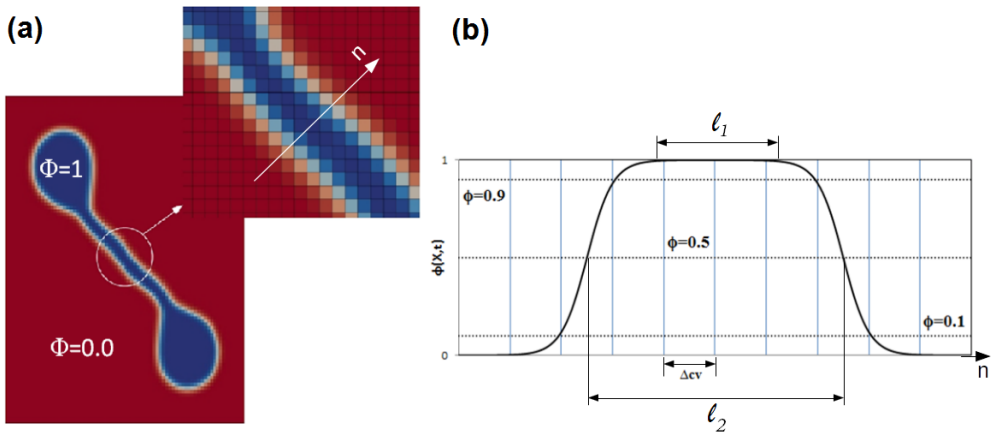

FIGURE 2.5: (a): The interface of the same collision as figure 2.4, advanced in time where the lamella film appears in the collision complex. (b): transition of the level-set function (ϕ) for the direction **n** normal to the lamella film from 0 in the matrix fluid, to 1 inside of the droplet and again to 0 in the matrix fluid. (ℓ_2 is the interface thickness in the lamella film and ℓ_1 is the length of the portion of lamella which contains only pure droplet material)

exhibits a behavior like figure 2.5(b). In a simulation, there might be many cells satisfying this condition. If $\ell_1 > \Delta_P$ (with Δ as the characteristic length of the cell in **n** direction), no special treatment of lamella is required. The numerical artifact of lamella starts when the value of this parameter decreases to $\ell_1 \leq \Delta_P$. In the moment in which $\ell_1 = \Delta_P$, supposing the neighboring cells of **P** in direction normal to the interface are F_1 and F_2, then the values of ϕ_{F_1} and ϕ_{F_2} will be smaller than $\phi_P = 1.0$. Keeping in mind the calculation of the $\nabla\phi$ described in section 2.3.1, at this moment, the value of $(\nabla\phi)_P$ will decrease dramatically, resulting in decreasing the value of $(\sigma\kappa(\phi)\nabla\phi)_P$ in momentum equation. Decreasing the value of surface tension at this point will accelerate the decay of its level-set function value which leads to the rupture of the lamella film. In order to prevent this, we propose to follow the lamella changes, considering the moment of $\ell_1 = \Delta_P$ as a milestone (herein after refereed to as *critical stage*), when the value of ϕ_P falls bellow 1.0, we add the value of $\zeta = (1.0 - \phi_P)$ to ϕ_P to keep its value at the critical stage of $\phi_P = 1.0$. The important question now is how to detect the points like **P** as the centers of the lamella film in **n** direction. We believe that if **P** point has the level-set characteristics as figure 2.5(b) in $\vec{\mathbf{n}}$ direction, it will also has similar behavior in at least one of the **X**, **Y** or **Z** directions. Thus, in order to simplify the solution procedure, we look for **P** points where they demonstrate the hunchback variation of ϕ not in $\vec{\mathbf{n}}$ direction but in at least one of the **X**, **Y** or **Z** directions, depending on which direction $\vec{\mathbf{n}}$ is more leaned towards. To do so, we propose the following steps for every point in the interface, within the solution algorithm:

1. Determine the direction of the checking (**X**, **Y** or **Z**): it is possible to use the value of $\vec{\mathbf{n}}$ vector at the cell location ($\vec{\mathbf{n}} = (n_x, n_y, n_z)$). The direction associated with the maximum absolute value of the components of $\vec{\mathbf{n}}$ will be the checking direction. E.g. if $|n_x| > |n_y| > |n_z|$, the checking direction will be **X**.

2. Find the neighboring points of the cell of interest in the calculated checking direction, (F_1 and F_2).

3. Check if the cell exhibits hunchback variation of ϕ at critical stage (e.g. if $\phi_P > \phi_{F_1}$ and $\phi_P > \phi_{F_2}$). If so, add the value of $\zeta = (1.0 - \phi_P)$ to ϕ_P.

The proposed lamella stabilization method is explained in algorithm 1. With special care, the whole solution procedure can be written without any **if** conditions, as

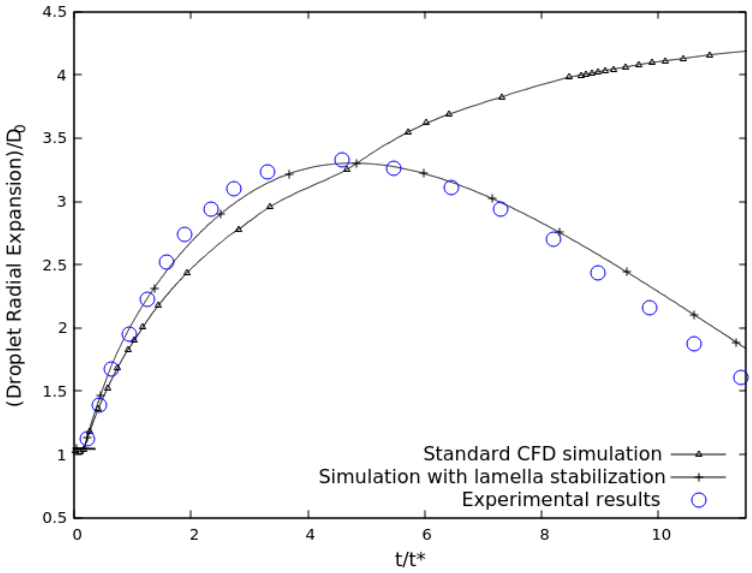

FIGURE 2.6: Radial expansion of the head-on collision complex of two droplets with We=269 and Re=154. Simulation results of standard CFD are compared with an equivalent case with lamella stabilized, and experimental results of [93]

we did, to impose the minimum possible computational cost. The algorithm to check and stabilize lamella can be started from the beginning of the simulations. Once the number of modified **P** cells from a non-zero value returns to zero, it means the lamella does not exist in the current state of the simulation anymore and the whole algorithm 1 could be stopped in order to save-up the computational cost.

Algorithm 1: The proposed general lamella stabilization algorithm

for *all the interface cells* **do**
  P = current cell;
  Checking direction = Corresponding direction of $\max(|n_x|,|n_y|,|n_z|)_{\mathbf{P}}$;
  F1, F2 = neighbors of **P** in checking direction;
  if $(\phi_p > \phi_{F1}$ *and* $\phi_p > \phi_{F2})$ **then**
    $\zeta = (1.0 - \phi_P)$;
    $\phi_P^{new} = \phi_P + \zeta$;
  end
end

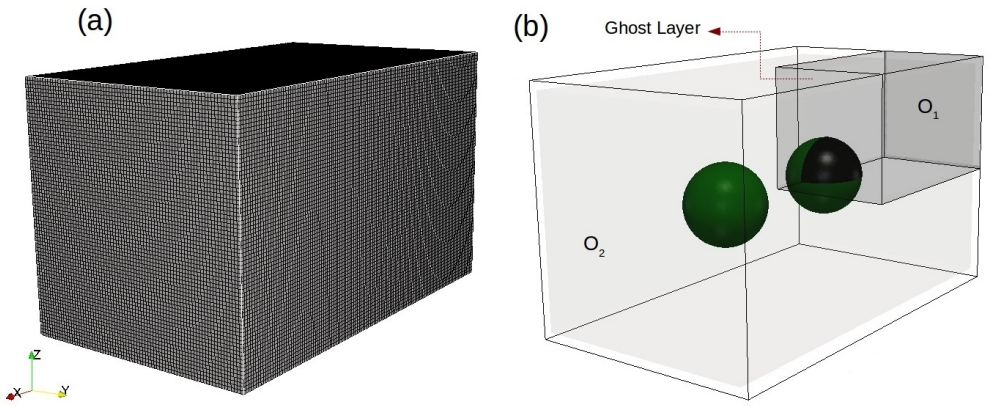

FIGURE 2.7: (a): Mesh configuration, structured cubic cells. (b): computational setup for the case that only collision of one-quarter of one droplet with ghost-nodes layer is being solved (gray domain, O_1, and black portion of the droplet) and the case that collision of two droplets is being solved (O_2).

This algorithm is an accurate, general-purpose, case-insensitive, and computationally efficient solution to lamella stabilization problem. Figure 2.6 provides the quantitative comparison of the droplet radial expansion for a head-on collision of two droplets with We=269 and Re=154 (the same collision case illustrated in figure 2.3). The results of experimental data of Willis and Orme [93] are compared with the numerical simulations done in this study, one with standard CFD simulation and other with proposed lamella stabilization approach in a domain with a grid size of h=D/50. It is plain to see that even for a fine grid size of h=D/50 used, the standard CFD simulation fails in capturing the correct topology of the collision. Simulation with the proposed lamella stabilization approach, however, yields in results with good agreement with experimental data.

2.4 Results and Discussions

Two initially separated droplets in a lighter environment collide in a domain with length L, width W and Height H in X, Y and Z directions, respectively. At the beginning of the simulation, the surrounding matrix gas is static while a uniform velocity is being imposed to the droplets giving them a relative velocity of U_{rel} in opposite directions. The characteristics of the simulations done in this study are presented in table 2.1. The

density and viscosity ratios for all the simulations are $\rho_d/\rho_m = 666$ and $\mu_d/\mu_m = 120$, respectively. In this notation, the subscript d stands for *droplet* and subscript m stands for *matrix*. These values of density and viscosity ratios are related to Tetradecane as droplet and Air as the matrix.

In this study, two different domains of O_1 and O_2 as presented in figure 2.7(b) are used. In the domain O_1, only one-eighth of the whole domain (O_2) is being solved. Instead of simulation of the collision of two droplets, the collision of one-fourth of only one droplet with the ghost-nodes layer, as explained in section 2.3.4, is being solved. Thus ghost-nodes layer boundary condition is applied on collision plane, symmetry boundary condition on the bottom and side walls (z_0 and y_0), and Neumann boundary condition on other walls. Simulations of cases SPC,B and HPC_1, are carried out in this domain. Using this domain saves-up in computational costs of the simulations but could only be used for the head-on collision of equal sized droplets. In the domain O_2, the collision of two droplets is being solved. All the other cases are solved in this domain with Neumann boundary condition applied on all of its walls. Computations have been performed using a Cartesian mesh of cubic grids with the edge size of h. This mesh was generated by a constant step extrusion of the two-dimensional y-z grid along the x-axis with the step size of h. Unless otherwise is mentioned, a grid size of h=$D_0/60$ is being used to discretize the domain O_1, and a grid size of h=$D_0/35$ is being used to discretize the domain O_2.

Figure 2.7(a) illustrates the mesh configuration and computational setup. For all the simulations of this study, time and lengths are non-dimensionalized using $t^* = D_0/U_{rel}$ and D_0, respectively. In the next subsections, the results regarding the cases tabulated in table 2.1 are presented and discussed in details. We select benchmark experimental results of Qian and Law [51] and Pan, Law, and Zhou [57] to validate our numerical results. These results have been used widely by the research community to validate different numerical tools. For all the cases solved in this chapter the videos of the collision process are provided in supplementary videos which could be found in [1]. In these videos time is being non-dimensionalized using the same characteristic time of $t^* = D_0/U_{rel}$ and the color contours represent the velocity magnitude on the droplets

TABLE 2.1: Characteristics of the simulations

Case	We	Re	I	$L/D_0 \times H/D_0 \times W/D_0$	$t_{rupture}/t^*$
SPC	2.3	46.83	0	$2.5\times1.5\times1.5$	0.7682
B	9.33	118.11	0	$2.5\times1.5\times1.5$	∞
HPC_1	13.63	143.6	0	$2.5\times1.5\times1.5$	0.8567
HPC_2	70.8	327	0.25	$5.0\times2.8\times2.8$	0.0
HPC_3	56.3	288.9	0.13	$5.0\times2.8\times2.8$	0.0
CFRS	61.4	296.5	0.06	$5.0\times2.8\times2.8$	0.0
$CFSS_1$	64.9	312.8	0.7	$6.8\times2.8\times2.8$	0.0
$CFSS_2$	48.1	270.1	0.39	$5.0\times2.8\times2.8$	0.0
$CFSS_3$	60.1	302.8	0.55	$5.0\times2.8\times2.8$	0.0
HWC	357	178	0.0	$5.0\times3.5\times3.5$	0.0

surface[1].

2.4.1 Retarded permanent coalescence

Cases SPC and HPC_1 are fitting in this category where the droplets do not coalescence immediately after their initial contact. For these cases, the rupture time of the gas film between the droplets plays a vital role in capturing the correct topological changes of the collision complex. This rupture time is calculated using the method explained in section 2.3.4. Figure 2.8 represents the non-dimensional inter-droplet gas film thickness as a function of time for two bouncing cases (simulations done with Dirichlet boundary condition for level-set function in the ghost-nodes layer) with characteristics as cases SPC and HPC_1. According to this figure, the bouncing simulations with characteristics of SPC and HPC_1 reach the minimum gas thickness at $t/t^* = 1.12$ and 1.25, respectively while $t/t^* = 0$ is the time when the inner-centre distance of the droplet with the ghost-nodes layer is $0.7D_0$. These values correspond to the $t_{rupture}/t^* = 0.7682$ and 0.8567, respectively, while $t_{rupture}/t^* = 0$ is the time when the droplet reaches the ghost-nodes layer. With the calculated values of gas film rupture time and the method explained in section 2.3.4, simulations of retarded coalescence of cases SPC and HPC_1 are performed. Figures 2.11 and 2.13 illustrate the topological changes of the collision complex for these cases, extracted in the same time instances

[1] 0 $U_{rel}/2$

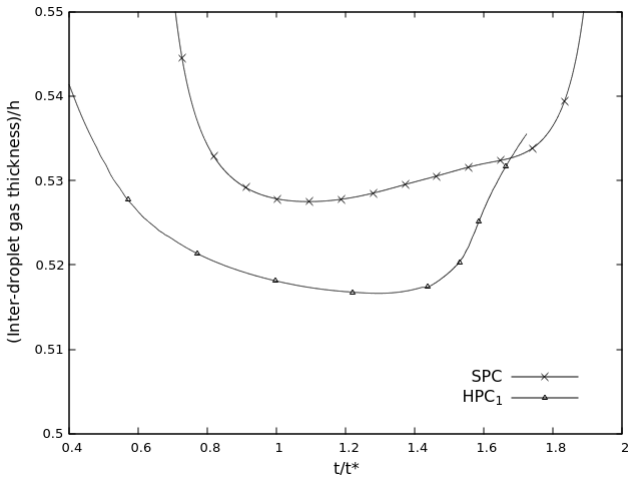

FIGURE 2.8: Non-dimensional inter-droplet gas thickness as a function of time for two bouncing cases with characteristics of cases *SPC* and HPC_1 of table 2.1

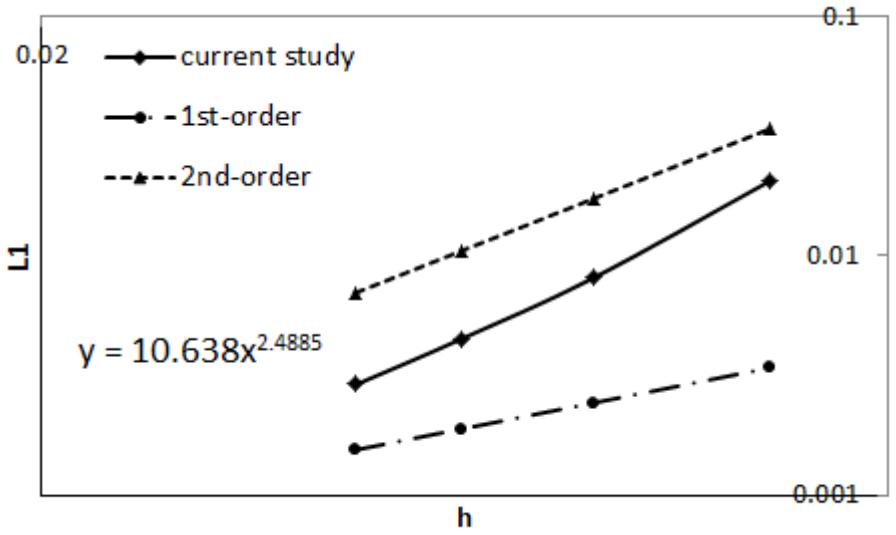

FIGURE 2.9: First norm of the error in calculation of energy budgets during the solution process of the case SPC inside of the domains with grid sizes of $h = D_0/25, D_0/35, D_0/45, D_0/55$ compared with the reference values of solution in a domain with grid size of $h = D_0/65$.

as experimental results of [57]. For the sake of clarity, the results extracted from domain O_1 are being reflected in X_0, Y_0 and Z_0 axes to form a whole droplet. A very good agreement is seen between the results of the current study, and the experimental results provided.

Figures 2.12 and 2.14 provide quantitative information regarding (left:) different normalized energy budgets including kinetic energy and total viscous dissipation energy inside of the droplet and matrix plus the droplet surface tension energy (hereinafter being referred as energy budget graph), and (right:) the normalized viscous dissipation rate of energy inside of the droplet and matrix (hereinafter being referred as VDR graph) and the normalized radial expansion of the droplet, Vs. non-dimensional time, for cases SPH and HPC_1, respectively. For both cases, surface tension energy is having a much higher share of the energy budget, than the kinetic energy of the droplet, especially for case SPH where the initial kinetic energy is almost negligible compared with the surface tension energy. For both cases, the surface tension energy increases as the droplet undergoes topological changes, until $t_{rupture}$ of the gas film, when a sudden dip in the surface tension energy is being witnessed. This sudden decrease is due to the elimination of the common surface between the droplets in the inter-droplet gas film.

Upon the coalescence of the droplets, there is a jump in the viscous dissipation rate of the droplets and matrix. Since the total dissipation energy is a time-integral of the viscous dissipation rate (see equation 2.21), this sudden increase in the viscous dissipation rate leads to a slightly delayed ramped increase in the dissipated energy for both cases. This increase compensates for the loss of surface tension energy, in the total energy of the system. Kinetic energy in the matrix for both cases is almost negligible.

A grid convergence analysis is provided on the energy budget calculations of the case *SPC*. Five meshes with different grid sizes of $h = D_0/25, D_0/35, D_0/45, D_0/55$ and $d/65$ are used to solve this case. The results of the solution with the finest grid ($h = D_0/65$) are selected as the reference data and the results of other simulations are compared with them. For each case, the errors related to the different energy budgets of kinetic, surface tension and viscous dissipation at each timestep are calculated. Accumulated value of these errors are calculated as the first norm of the error using $L_1 = \sum_i |e_i|$, where e_i is the difference between energy budgets of the simulation and

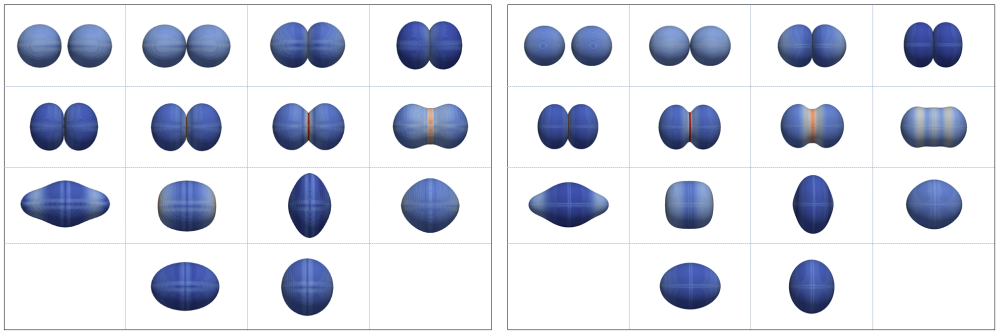

FIGURE 2.10: Topological changes of head-on binary droplets collision of case *SPH* with pressure contours on the droplet surface. Simulations done in a domain with the grid size of left: $h = D_0/25$, right: $h = D_0/65$.

its corresponding value in reference simulation at i-th iteration. Figure 2.9 presents the values of L_1 as a function of the grid size. As can be seen, the solution process illustrates an order of convergence of 2.48 in space. The topological changes of collision process of the solution in a domain with grid sizes of $h = D_0/25$ and $h = D_0/65$ are provided in 2.10.

2.4.2 Bouncing

Bouncing of the collided droplets corresponds to the case B of table 2.1. In this regime, the contact time is too short to allow full film drainage happens and as a result of the gas-film persistence in the inter-droplet region, the collision ends-up in bouncing. The droplet is initially placed at a distance of $0.7D_0$ with the ghost-nodes layer. The results of the simulation are illustrated in figure 2.15 compared with experimental results of [57] where good agreement is seen. For the sake of clarity, the results extracted from domain O_1 are being reflected in X_0, Y_0, and Z_0 axes to form a whole droplet. Moreover, in figure 2.16 (left), the energy budget graph, (right) the VDR and normalized radial expansion of the droplet are presented. Viscous dissipation energy is almost linear with time and is more prominent in droplet than in matrix. The kinetic energy of the matrix is almost negligible compared to other budgets of energy. Maximum viscous dissipation rate of the matrix happens around the contact time ($t/t^* \approx 0.45$) when the surface tension energy starts to increase, and kinetic energy of the droplet starts to decrease. The maximum surface tension energy, minimum kinetic energy and local

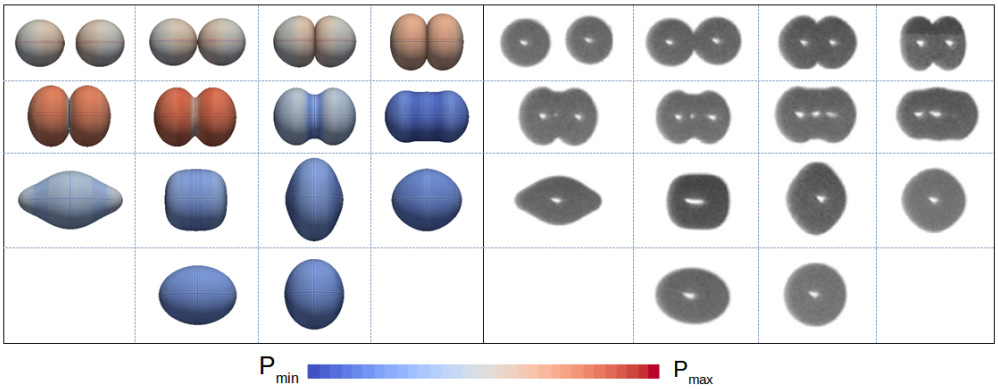

FIGURE 2.11: Topological changes of head-on binary droplets collision of case *SPH* in table 2.1. Right: experimental results of [57], Left: numerical simulation of current study with pressure contours on the droplet surface. These figures are extracted in the same time instances of experimental figures as t/t^*=[0.0, 0.34, 0.72, 1.08, 1.12, 1.16, 1.19, 1.27, 1.60, 1.92, 2.29, 2.82, 3.44, 3.88] with $t/t^* = 0.0$ as the time when the droplet distance to the ghost-nodes layer is $0.7D_0$. The video of the collision process of this case is provided in supplementary material of [1], videos SPC_a and SPC_b for side and oblique views, respectively.

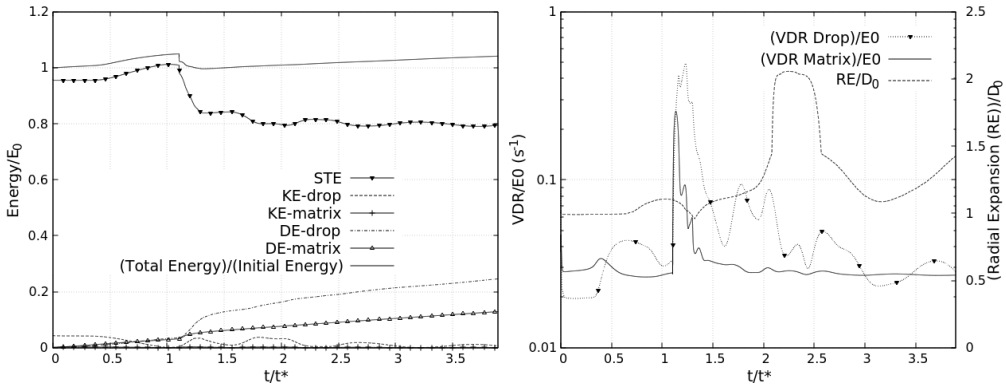

FIGURE 2.12: Left: Energy budget graph, Right: VDR and Normalized radial expansion of the droplet. All figure are related to case *SPC* of table 2.1 and corresponding figure of 2.11.

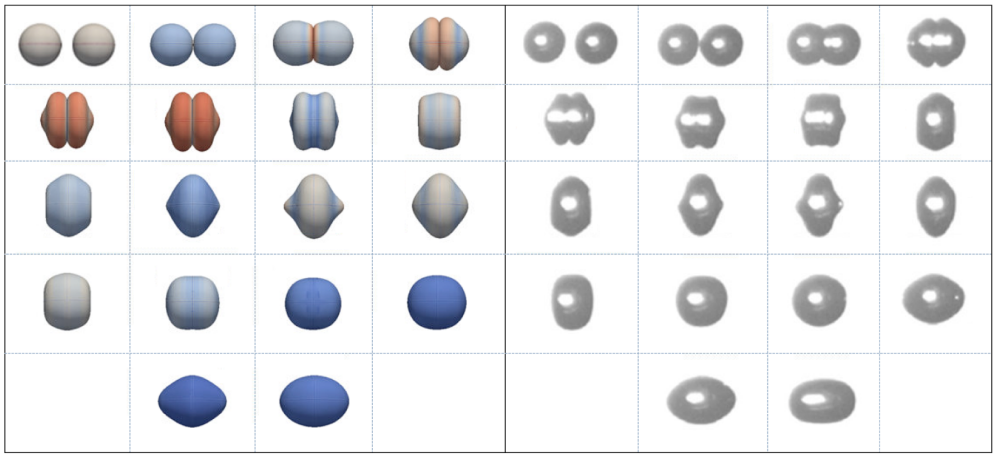

FIGURE 2.13: Topological changes of head-on binary droplet collision of case HPC_1 in table 2.1. Right: experimental results of [57], Left: numerical simulation of current study with pressure contours on the droplet surface. These figures are extracted in the same time instances of experimental figures as t/t^*=[0.17, 0.38, 0.62, 1.04, 1.27, 1.28, 1.39, 1.56, 1.74, 1.91, 2.01, 2.35, 2.68, 2.99, 3.13, 3.15, 3.63, 4.0] with $t/t^* = 0.0$ as the time when the droplet distance to the ghost-nodes layer is $0.7D_0$. The video of the collision process of this case is provided in supplementary material of [1], videos HPC_{1a} and HPC_{1b} for side and oblique views, respectively.

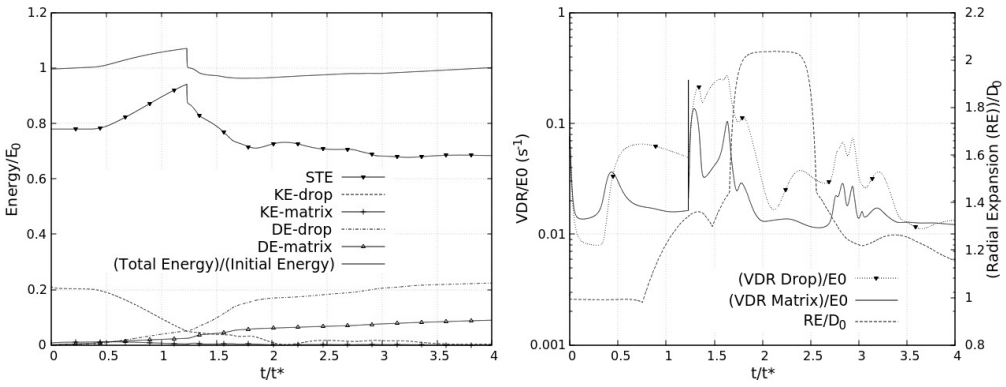

FIGURE 2.14: Left: Energy budget graph, Right: VDR and Normalized radial expansion of the droplet. All figure are related to case HPC_1 of table 2.1 and corresponding figure of 2.13.

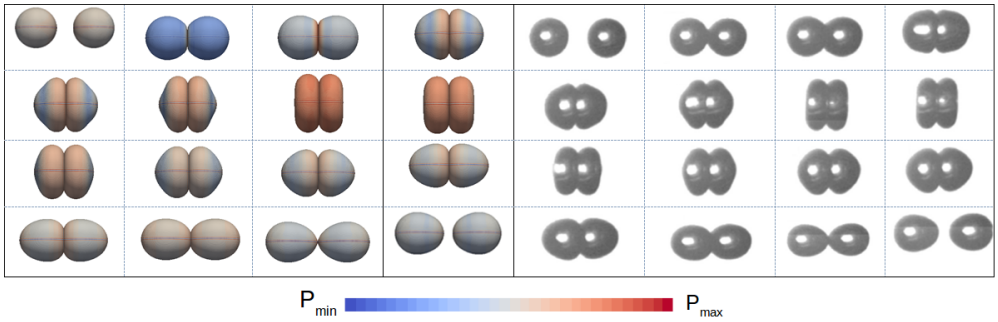

FIGURE 2.15: Topological changes of head-on binary droplet collision of case B in table 2.1. Right: experimental results of [57], Left: numerical simulation of current study with pressure contours on the droplet surface. These figures are extracted in the same time instances of experimental figures as t/t^*=[0.0, 0.5, 0.58, 0.88, 1.02, 1.17, 1.43, 1.61, 1.77, 1.90, 2.05, 2.20, 2.35, 2.64, 2.89, 3.22] with $t/t^=$0.0 as the time when the droplet distance to the ghost-nodes layer is $0.7D_0$ The video of the collision process of this case is provided in supplementary material of [1], videos B_a and B_b for side and oblique views, respectively.

minimum in viscous dissipation rate of the droplet, all happen in approximately the same time as the maximum radial expansion of the droplet. The initial budget of the kinetic energy of the droplet in bouncing regime (B), is higher than the SPH regime and is lower than the HPC_1 regime. However, the droplet kinetic energy recovery factor (KE_{final}/KE_0) for this case (regime B) is much higher than two previously studied cases (SPH and HPC_1) where the final value of kinetic energy of the droplet was almost zero. The total dissipated energy in this case is much lower than two previously studied cases of SPH and HPC_1.

2.4.3 Immediate permanent coalescence

Two off-center binary droplets collision cases of HPC_2 and HPC_3 of table 2.1 fit in the category of immediate permanent coalescence. In this regime of collision, the rupture of the gas film is very fast, resulting in immediate coalescence of the droplets. The droplets after collision retreat, and end-up in permanent coalescence. For both cases of HPC_2 and HPC_3, during the collision process, we witnessed the appearance of the lamella film. The perseverance of this film was being resolved numerically using the lamella stabilization algorithm described in section 2.3.5. The lamella film for cases

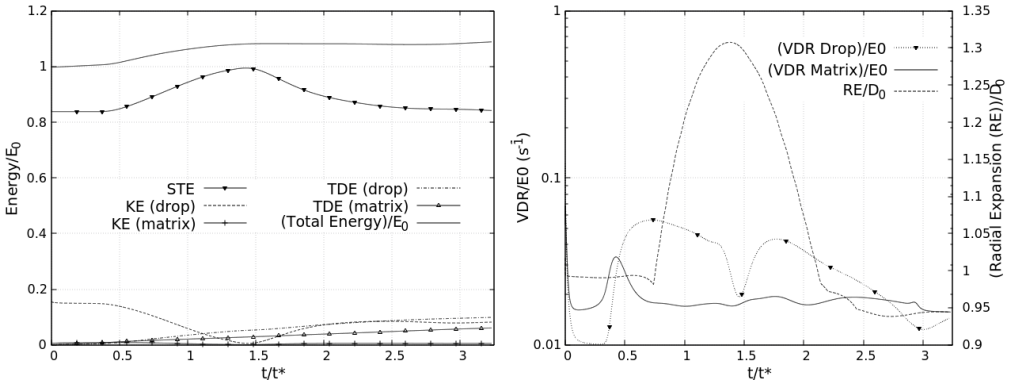

FIGURE 2.16: Left: Energy budget graph, Right: VDR and Normalized radial expansion of the droplet. All figure are related to case B of table 2.1 and corresponding figure of 2.15.

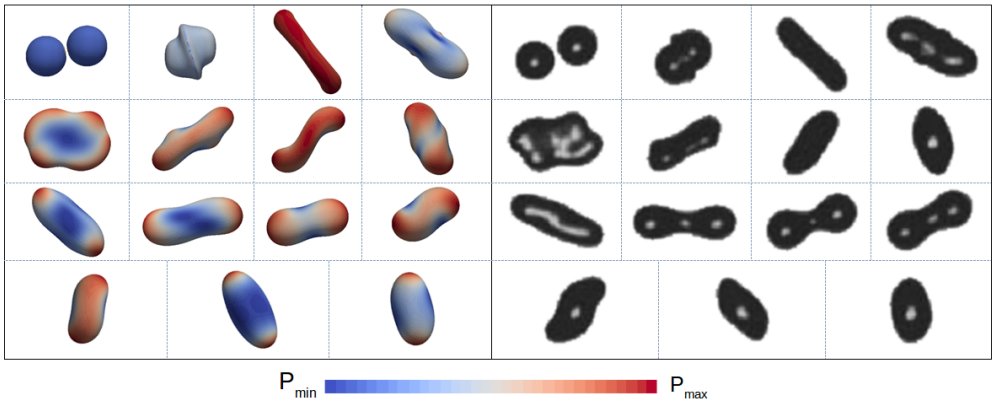

FIGURE 2.17: Topological changes of off-center binary droplets collision of case HPC_2 in table 2.1. Right: experimental results of [51], Left: numerical simulation of current study with pressure contours on the droplet surface. These figures are extracted in the same time instances of experimental figures as t/t^*=[0.0, 0.32, 1.81, 2.64, 3.44, 4.35, 5.08, 5.77, 7.0, 8.78, 10.12, 10.70, 11.79, 12.92, 16.91] with $t/t^* = 0.0$ as the time when the droplets centerline distance in collision direction is equal to D_0. The video of the collision process of this case is provided in supplementary material of [1], videos HPC_{2a} and HPC_{2b} for side and oblique views, respectively..

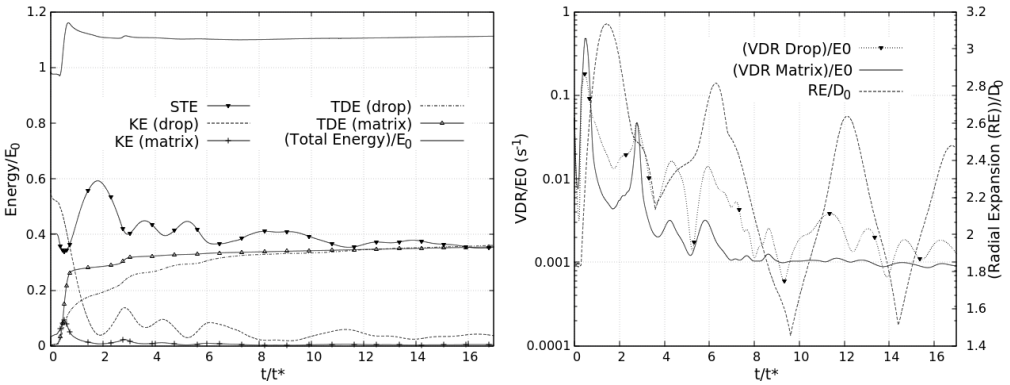

FIGURE 2.18: Left: Energy budget graph, Right: VDR and Normalized radial expansion of the droplet. All of these figures are related to case HPC_2 of table 2.1 and corresponding figure of 2.17.

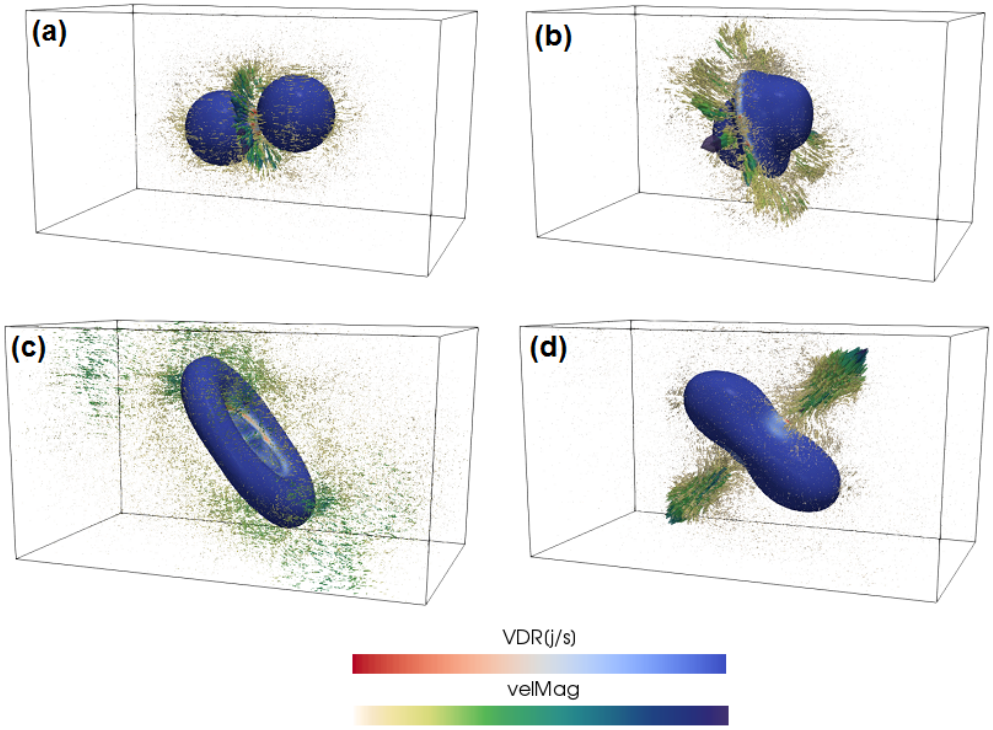

FIGURE 2.19: 3D representation of topological changes in startup collision of the case HPC_2 of table 2.1 and corresponding figure of 2.17 at times t/t^*=[0.0, 0.32, 1.81, 2.64] for (a), (b), (c) and (d), respectively. The color contours on the droplet surface represent the **VDR** and the surrounding vector illustrates the velocity vectors with contours as their magnitude in the matrix.

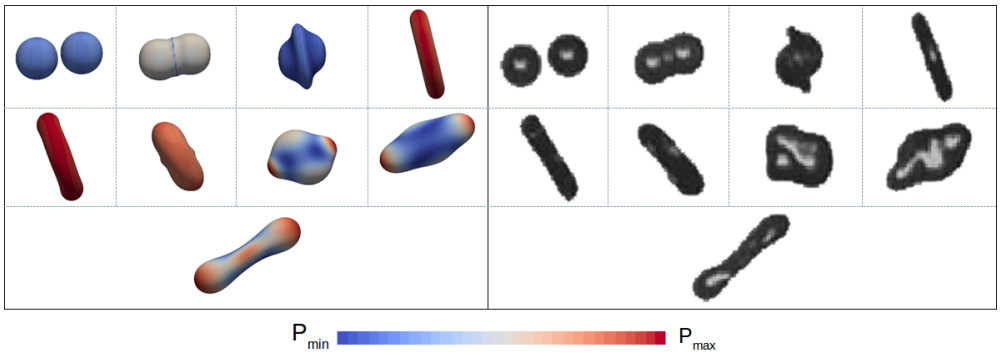

FIGURE 2.20: Topological changes of off-center binary droplet collision of case HPC_3 in table 2.1. Right: experimental results of [51], Left: numerical simulation of current study with pressure contours on the droplet surface. These figures are extracted in the same time instances of experimental figures as t/t^*=[0.0, 0.16, 0.46, 1.10, 1.70, 2.31, 2.77, 3.34, 4.31] with $t/t^* = 0.0$ as the time when the droplets centerline distance in collision direction is equal to D_0. The video of the collision process of this case is provided in supplementary material of [1], videos HPC_{3a} and HPC_{3b} for side and oblique views, respectively.

HPC_2 and HPC_3 appears in time periods of $t/t^* \approx [0.32 : 2.64]$ and $t/t^* \approx [0.46 : 1.70]$, respectively. Figures 2.17 and 2.20 represent the topological changes in the collision process, compared with the experimental results of [51] for the same time instances where a very good agreement is seen.

Figure 2.18 illustrates the energy budget graph, VDR graph and normalized radial expansion of the droplets, for case HPC_2. These information for case HPC_3 are presented in figure 2.22.

For the case of HPC_2 represented in figure 2.17, since the collision is off-center with a relatively high Impact parameter of 0.25, after coalescence, the resultant droplet has bulbous which stretch in the pre-coalescence moving direction of each droplet. Their kinetic energy is not high enough to induce breakup of the droplet into daughter (bulbous) droplets. The droplet continues on stretching until the kinetic energy reaches a local minimum value at a time around $t/t^* = 2$. At this time, the surface tension of the resultant droplet reaches a local maximum which retreats the droplet, resulting in pulling the bulbous back in reverse direction. Now the bulbous are moving in the reverse direction of the collision until again the kinetic energy of the droplet reaches a local minimum state and local maximum surface tension at this point retreats the

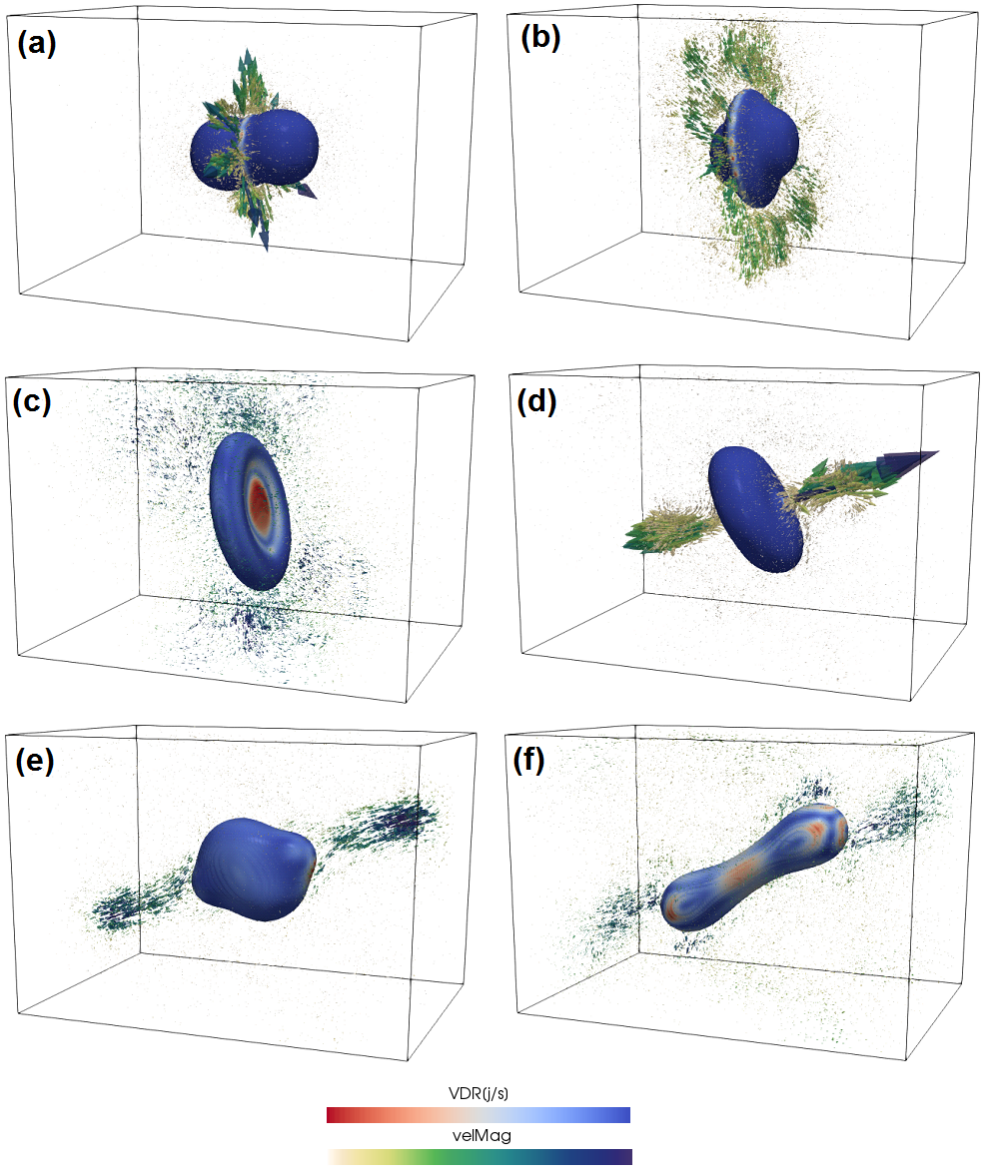

FIGURE 2.21: 3D representation of topological changes in startup collision of HPC_3 of table 2.1 and corresponding figure of 2.20 at times t/t^*=[0.16, 0.46, 1.10, 2.31, 2.77, 4.31] for (a) to (f), respectively. The color contours on the droplet surface represent the **VDR** and the surrounding vector illustrates the velocity vectors with contours as their magnitude in the matrix.

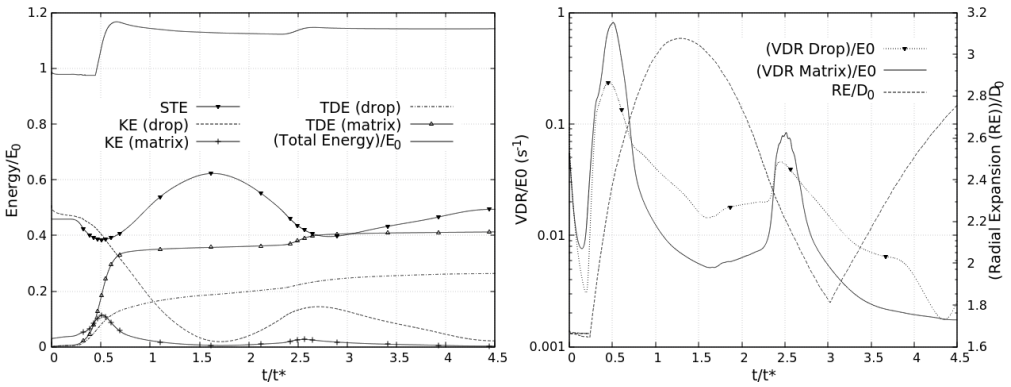

FIGURE 2.22: Left: Energy budget graph, Right: VDR and Normalized radial expansion of the droplet. All these figures are related to the case HPC_3 of table 2.1 and corresponding figure 2.20.

droplet. This process continues until viscosity dissipates the energy and the resultant droplet attains a uniform spherical shape. This process induces oscillations in the deformation of the droplet and can be seen in the kinetic energy of the droplet, surface tension energy, and radial expansion of the droplet. With the lower impact parameter of the case HPC_3 (I=0.13), we will not witness the moving of the bulbous at the tips of the resultant droplet as we observed in case HPC_2. The resultant droplet does not stretch in the collision direction as much as case HPC_2, and thus the oscillations in the droplet's kinetic energy, surface tension energy, viscous dissipation rates and radial expansion of the droplet are with more prominent frequency compared with case HPC_2.

Since the type of the coalescence in these cases is immediate, the surface that is being diminished at the moment of the coalescence and as a result, the eliminated surface tension energy (the dip in the STE graph) is lower compared with the retarded coalescence cases. Around the time of the coalescence, however, there is a sudden increase in the energy dissipated in the matrix, as can be seen in figure 2.18 and figure 2.22 for cases HPC_2 and HPC_3, respectively. We believe that part of this sudden change is not physical and is a numerical artifact related to the high escape velocity of the gas in this region. Around the time of the coalescence, the gas trapped between the droplets needs to be evacuated in a short time, resulting in a very high velocity of the gas in matrix fluid. Figures 2.19 and 2.21 illustrates the topological changes in

startup collision of cases HPC_2 and HPC_3, respectively. According to figure 2.18, there are two jumps in the viscous dissipation energy in the matrix, one for a time around the coalescence and other for $t/t^* \approx 3$. In the figure 2.19, we can see that for the time around coalescence (a and b), and also $t/t^* = 2.64$ the escape velocity of the gas is very high. For the case of HPC_3, the jumps in viscous dissipation energy in the matrix are in times around coalescence and $t/t^* \approx 2.5$. For this case by looking at the figure 2.21, we notice that the escape velocity of the gas film for times around coalescence (a and b) and also $t/t^* = 2.31$ (d) is much higher than the other times. This high sudden escape velocity of the gas introduces a very high velocity gradient in the matrix which escalates the value of the viscous dissipation energy in this zone. Accurate calculation of the velocity gradient in the matrix in this region is crucial for correct calculations of viscous dissipation energy. We believe the initial jump in the total energy of the system in these figures, is due to this problem. As could be seen in figure 2.18 and figure 2.22, there are sudden increases in the value of the viscous dissipation energy of the droplet in the same time as the matrix (around the time of coalescence) but comparably lower. We believe this jump is due to the mentioned high escape velocity of the matrix, since high escape velocity of the gas in matrix increases the velocity of nearby cells, including the droplet cells. This externally-imposed velocity gradient in the droplet results in an increase in the dissipated energy in the droplet.

This jump could be seen in the VDR graph of these cases, around the coalescence time as well. At the time of coalescence, the value of VDR for both cases in the matrix is higher than the droplet. Keeping in mind the VDF in equation (eq. 2.23), since the viscosity of the matrix is around 120 times lower than the droplet, this higher energy dissipation rate in matrix compared to the droplet, denotes much higher velocity gradients in the matrix, compared to the droplet. These values of VDR for both matrix and droplet decrease approximately 1000 times as time passes. Another point worth mentioning is that the local minimum of viscous dissipation rate happens at the time of the local maximum of surface tension and local minimum of kinetic energies.

2.4.4 Coalescence followed by reflexive separation

With further increase in the Weber number, the system of droplets will experience an immediate temporary coalescence followed by a reflexive separation, as case CFRS in

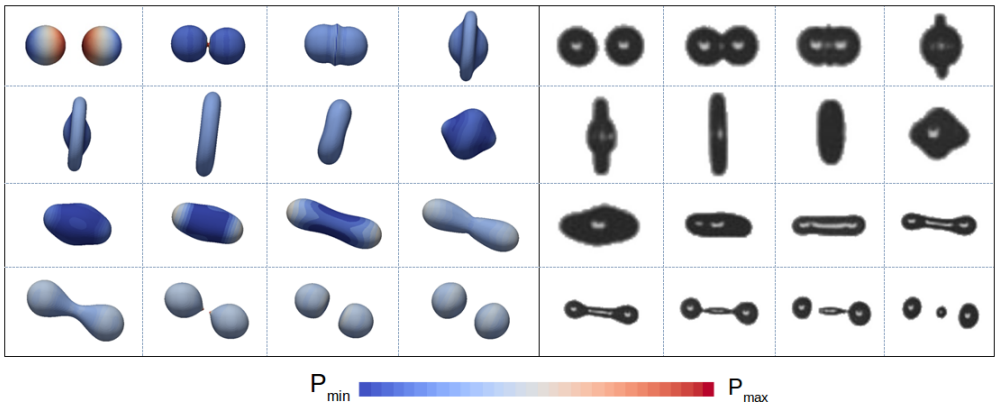

FIGURE 2.23: Topological changes of off-center binary droplet collision of case *CFRS* in table 2.1. Right: experimental results of [51], Left: numerical simulation of current study with pressure contours on the droplet surface. These figures are extracted in the same time instances of experimental figures as t/t^*=[-, 0.0, 0.29, 0.93, 1.16, 3.84, 4.54, 5.35, 7.16, 9.31, 10.47, 11.75, 12.22, 13.21, 15.95, 16.76] with $t/t^* = 0.0$ as the initial contact time of the droplets. The video of the collision process of this case is provided in supplementary material of [1], video CFRS.

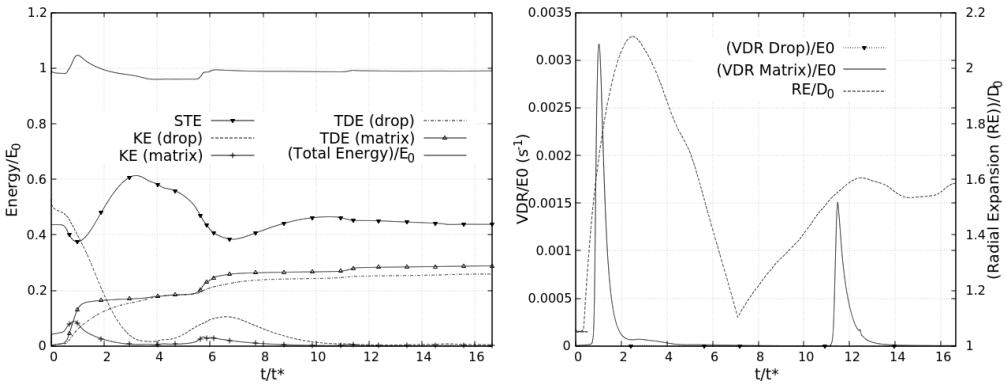

FIGURE 2.24: Left: Energy budget graph, Right: VDR and Normalized radial expansion of the droplet. These figures are related to the case *CFRS* of table 2.1 and corresponding figure 2.23.

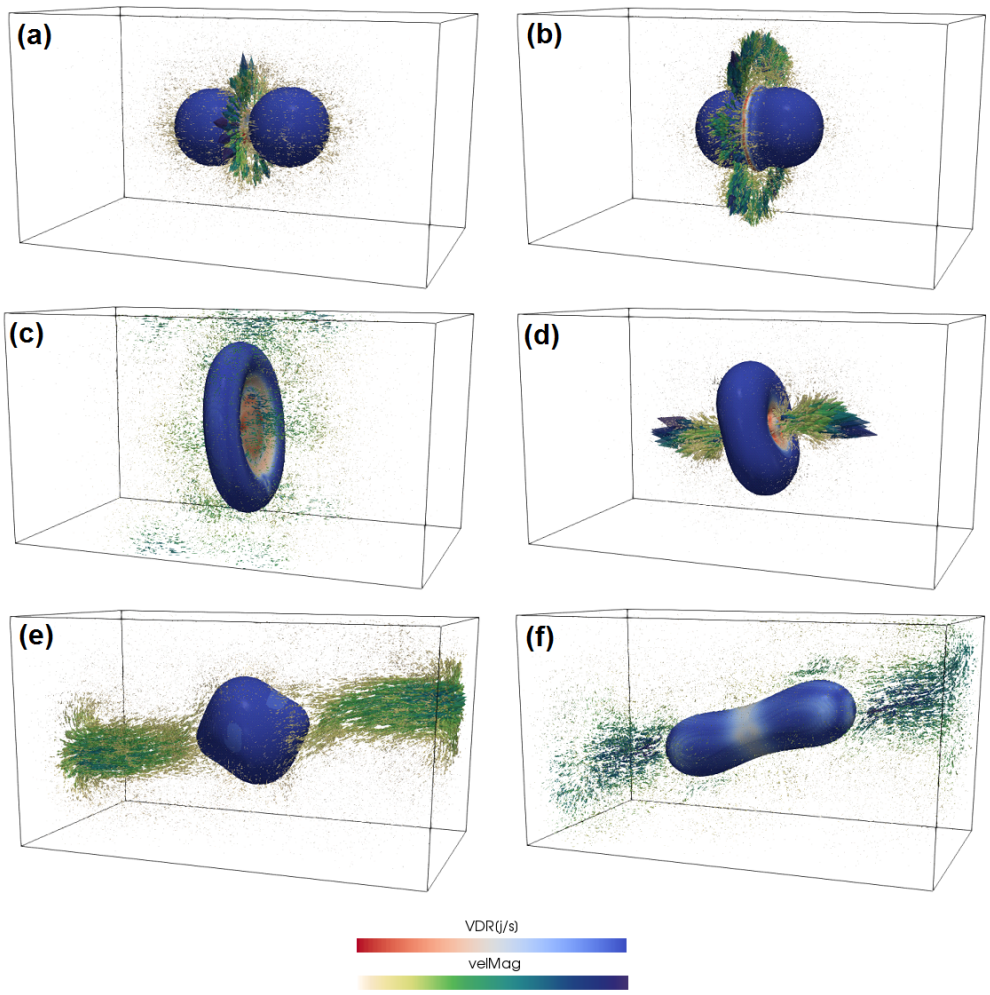

FIGURE 2.25: 3D representation of topological changes in start-up collision of case *CFRS* of table 2.1 and corresponding figure of 2.23 at times t/t^*=[0.0, 0.29, 3.84, 4.54, 5.35, 10.47] for (a) to (f), respectively. The color contours on the droplet surface represents the **VDR** and the surrounding vector illustrates the velocity vectors with contours as their magnitude in the matrix.

table 2.1. The separation of the droplets might be accompanied with satellite and sub-satellite droplets. Figure 2.23 depicts the collision outcome of the case CFRS solved in this study compared with experimental results of [51] for the same time instances. The droplets coalescence immediately after their initial contact. Thin lamella film forms for time period of $t/t^* \approx [1.16 : 4.54]$. The formation and evolution of the neck in the resultant droplet leads to the reflexive separation breakup in $t/t^* \approx 11.75$. Figure 2.24 represents the energy budget analysis along with the radial expansion of the collision process. Similar to the analysis of the cases in section 2.4.3, around the time of the coalescence, there is an immediate increase in VDR in matrix encountered by high gas escape velocity, and as a result an increase in the viscous dissipation energy in the matrix. The second jump in viscous dissipation rate in matrix happens at $t/t^* \approx 6$ which is the time when the resultant droplet is being retreated, and consequently, high gas escape velocity appears in areas close to the droplet tip. These jumps in the viscous dissipation rate results in a slightly delayed jump in the dissipated energy in the matrix (figure 2.24 left). The value of the viscous dissipation rate in the droplet is almost negligible. These very high gas escape velocities in the matrix could be seen qualitatively in figure 2.25, where (a) and (b) are related to the coalescence of the droplets and (d) and (e) are related to retreatment of the resultant droplet. Upon the higher dissipated energy in the matrix, there are jumps in the kinetic energy of the matrix, one for the times around coalescence and other for the times around the retreat of the resultant droplet ($t/t^* \approx 6$). The local extrema in radial expansion of the droplet and surface tension energy happen at the same time.

2.4.5 Coalescence followed by stretching separation

Figures 2.26, 2.28 and 2.30 illustrates the collision process of binary off-center droplets in *coalescence followed by stretching separation* regime for simulations done in this chapter along with the corresponding experimental results of [51] for cases $CFSS_1$, $CFSS_2$ and $CFSS_3$ of table 2.1. The lamella film forms in the cases of $CFSS_2$ and $CFSS_3$. According to our simulations, although in the case of $CFSS_3$, the lamella appears only for a short period during the collision process, its resolving is vital in correct capturing of the physics of the problem. High pressure in the neck right before the

breakup and formation of daughter droplets are common in all the cases. Figures extracted in this section for topological changes of the collision process in all the regimes are in good agreement with the experimental provided reference results.

According to the experimental analysis of [51], which is being abstracted in figure 2.1, the collisions in this regime have impact parameter (I) higher than a threshold, and lower than a maximum value. Collisions with impact parameters (I) lower than this threshold results in *hard permanent coalescence* or *coalescence followed by reflexive separation* regimes, and I values higher than the maximum, results in passing-by of the droplets with minor changes. E.g. the case $CFSS_2$ with I=0.39, is close to the regime *hard permanent coalescence* and our simulations with I value 10% smaller for this case ended-up in permanent coalescence. For this case ($CFSS_2$), the stretching of the droplet in the collision direction before breakup is smaller than the other two cases provided ($CFSS_1$ and $CFSS_3$), which is due to the smaller impact parameter of this case compared with other two cases.

Energy budgets graph along with normalized VDR and also normalized radial expansion of the droplet for case $CFSS_1$, $CFSS_2$ and $CFSS_3$ are presented in figures 2.27, 2.29 and 2.31, respectively. As discussed before, we observe a local maximum in the VDR graphs, around the coalescence times, resulting in a slightly delayed increase in dissipation energy in matrix and droplet around that time. For the case, $CFSS_1$, the kinetic energy of the droplet is not being drained totally, and it has a share of around 17% of the total energy at the end of the solution. For the case $CFSS_2$, we witness complementary oscillations in the energy budgets of surface tension energy and kinetic energy of the droplet similar to the case HPC_2 (figure 2.18). These oscillations happen due to the special collision characteristics. The kinetic energy stretches the resultant droplet in collision direction; thus the surplus surface tension energy retreats the resultant droplet and tries to contract it into a spherical and more stable shape which prompts overshoot in the value of the kinetic energy of the droplet. This process continues until the viscosity dissipates energy out of the system. These oscillations could be seen in the VDR of droplet and matrix as well as the radial expansion of the droplet.

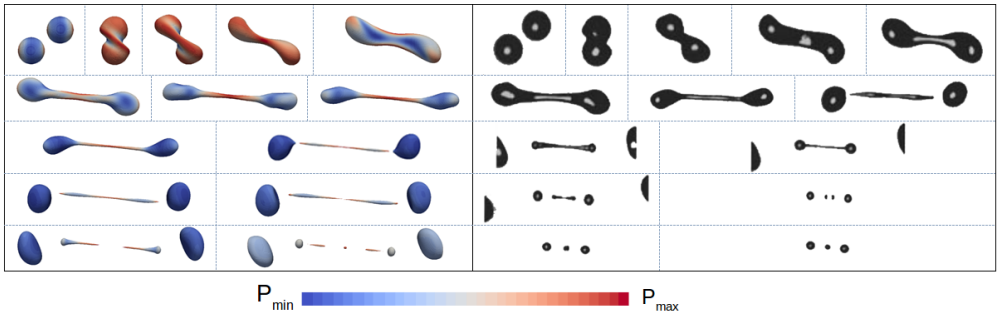

FIGURE 2.26: Topological changes of off-center binary droplets collision of the case $CFSS_1$ in table 2.1. Right: experimental results of [51], Left: numerical simulation of current study with pressure contours on the droplet surface. These figures are extracted in the same time instances of experimental figures as t/t^*=[0.0, 1.05, 1.75, 2.80, 3.85, 5.25, 6.30, 7.0, 7.70, 8.75, 9.10, 9.46, 10.16, 10.86] with $t/t^* = 0.0$ as the time when the droplets centerline distance in collision direction is equal to D_0. The video of the collision process of this case is provided in supplementary material of [1], videos $CFSS_{1a}$ and $CFSS_{1b}$ for side and oblique views, respectively.

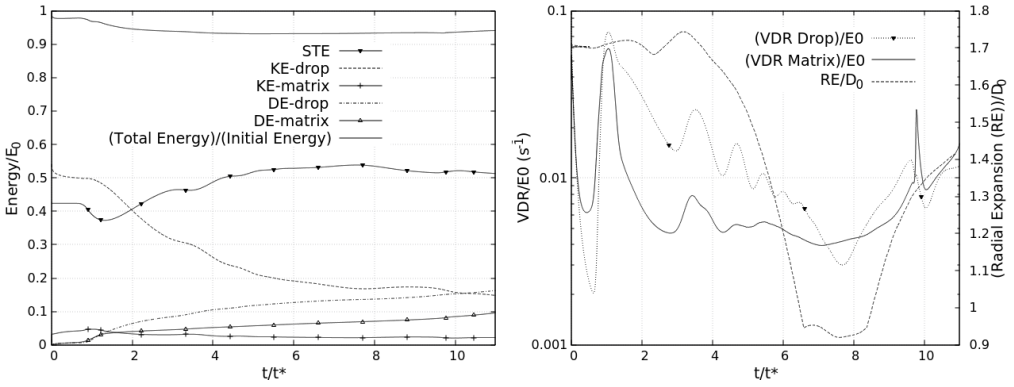

FIGURE 2.27: Left: Energy budget graph, Right: VDR and Normalized radial expansion of the droplet. These figures are related to the case $CFSS_1$ of table 2.1 and corresponding figure 2.26.

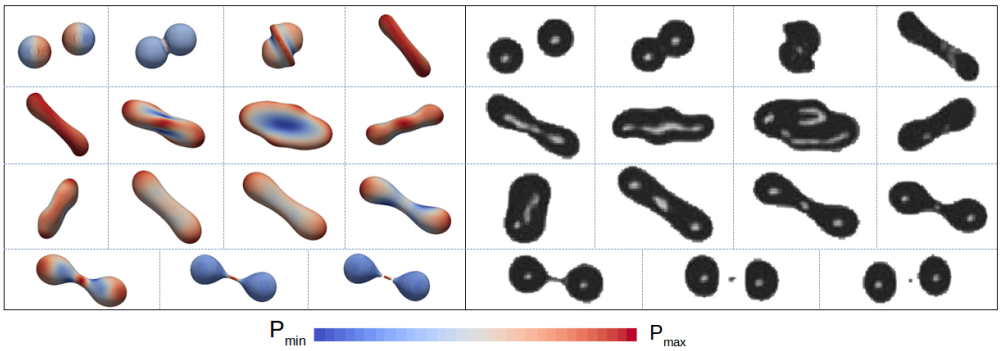

FIGURE 2.28: Topological changes of off-center binary droplet collision of case $CFSS_2$ in table 2.1. Right: experimental results of [51], Left: numerical simulation of current study with pressure contours on the droplet surface. These figures are extracted in the same time instances of experimental figures as t/t^*=[0.0, 0.23, 0.53, 1.73, 2.06, 2.60, 3.17, 4.21, 4.81, 6.61, 7.20, 7.95, 8.52, 8.91, 9.54] with $t/t^* = 0.0$ as the time when the droplets centerline distance in collision direction is equal to $1.32D_0$. The video of the collision process of this case is provided in supplementary material of [1], videos $CFSS_{2a}$ and $CFSS_{2b}$ for side and oblique views, respectively.

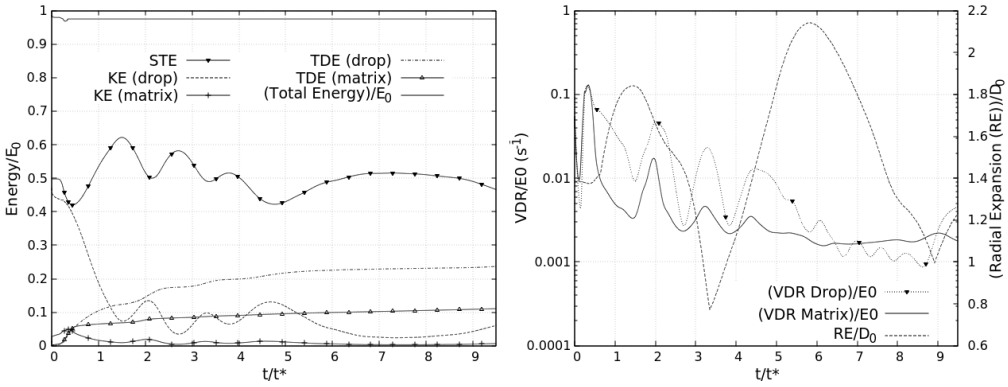

FIGURE 2.29: Left: Energy budget graph, Right: VDR and Normalized radial expansion of the droplet. These figures are related to the case $CFSS_2$ of table 2.1 and corresponding figure 2.28.

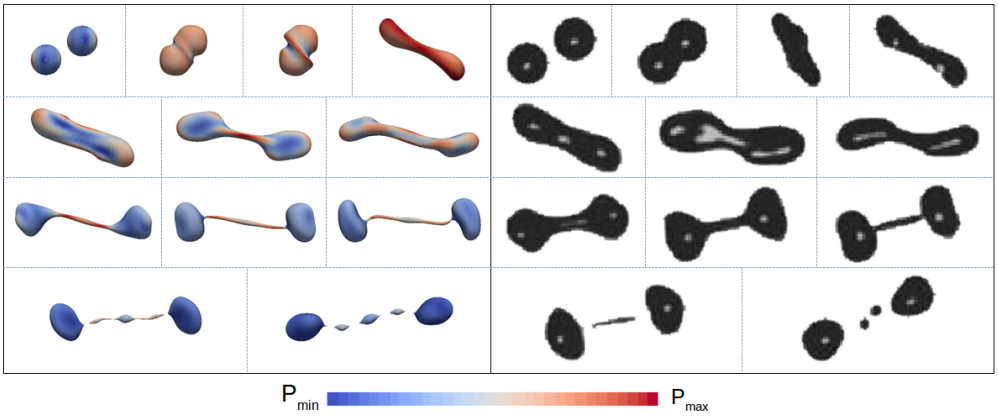

FIGURE 2.30: Topological changes of off-center binary droplet collision of case $CFSS_3$ in table 2.1. Right: experimental results of [51], Left: numerical simulation of current study with pressure contours on the droplet surface. These figures are extracted in the same time instances of experimental figures as t/t^*=[0.0, 0.29, 0.43, 1.65, 2.05, 2.85, 3.21, 4.34, 4.77, 5.14, 5.63, 6.36, 8.12] with $t/t^* = 0.0$ as the time when the droplets centerline distance in collision direction is equal to D_0. The video of the collision process of this case is provided in supplementary material of [1], videos $CFSS_{3a}$ and $CFSS_{3b}$ for side and oblique views, respectively.

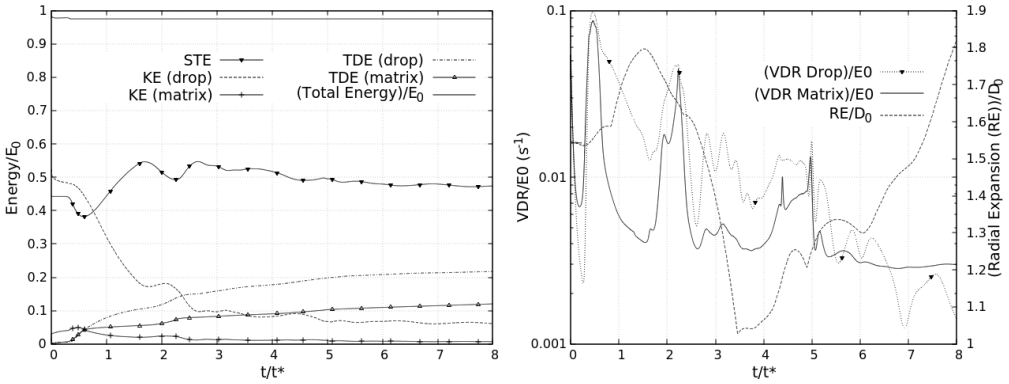

FIGURE 2.31: Left: Energy budget graph, Right: VDR and Normalized radial expansion of the droplet. These figures are related to the case $CFSS_3$ of table 2.1 and corresponding figure 2.30.

2.4.6 High Weber number collision (HWC)

In this section, the results related to the solution of a head-on binary droplet collision with a high Weber number of 357 are presented. Figure 2.32 illustrates the evolution of the droplets collision. Starting from the very beginning of the collision, the lamella film forms and lingers until times around $t/t^* \approx 10$. Figure 2.34 (right) represents the non-dimensional radial expansion of the resultant droplet, compared with the experimental data of [93]. Good agreement is seen between our results and the experimental data for this critical case.

Figures 2.34 (left) and (right) illustrates the energy budgets and VDR graphs, respectively. Contrary to the other cases presented so far, in this case, the initial share of the kinetic energy of the droplets is much higher than the initial surface tension energy. Shortly after the collision, the kinetic energy of the droplet starts to fade, and surface tension energy grows. As have been seen in previous cases, the viscous dissipation rate is maximum around the coalescence time. The jump in the viscous dissipation energy in the matrix and droplet happens around the coalescence time as well. As it was concluded earlier, this is due to the high escape gas velocity in the matrix around the coalescence time. Figure 2.33 illustrates a three-dimensional representation of the topological changes in startup behavior of the collision complex of this case with color contours on the droplet surface as a representation of the **VDR** and the surrounding vector as the velocity vectors in the matrix.

2.5 Validation of energy analysis formulations

An inviscid droplet is initially placed at the center of a cubic domain with the side length of $L = 2D_0$. The domain is filled with an inviscid matrix with a density ratio of $\rho_d/\rho_m = 100$. Three sets of simulations are performed to gradually investigate the accuracy of numerical formulations in capturing different terms of energy budgets. In all the cases, the simulation runs until $t/t^* = 1.0$ in a domain with the grid size of $h = L/100$.

1. In the first step, the droplet and matrix are both static. Free-slip boundary condition is applied on all the domain walls. In this case the total energy of the

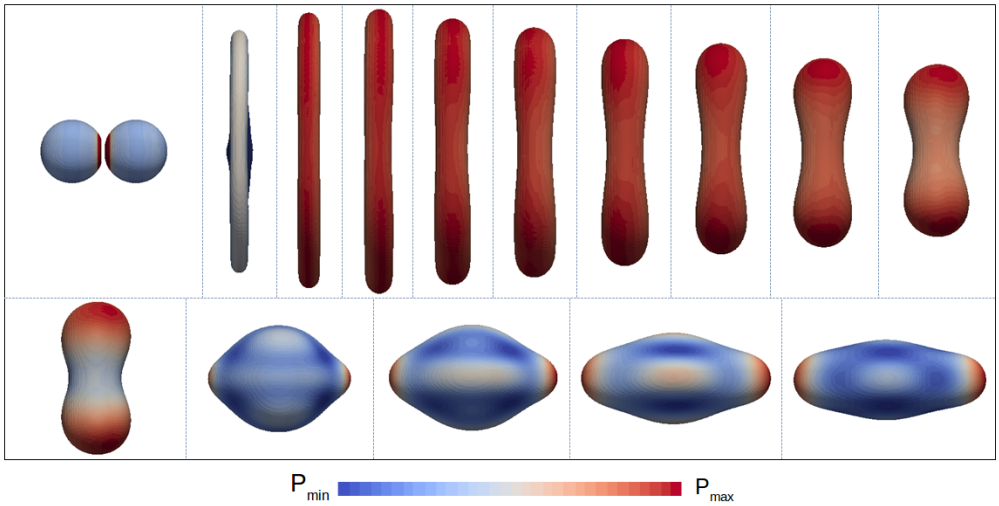

FIGURE 2.32: Snapshots of topological changes of numerical simulation of current study with pressure contours on the droplet surface for head-on binary droplet collision of case *HWC* in table 2.1. These figures are extracted in times of t/t^*=[0.0, 2.83, 4.25, 6.02, 7.80, 8.85, 9.92, 10.63, 11.70, 12.62, 13.55, 16.52, 17.6, 18.53, 20.0] with $t/t^* = 0.0$ as the time when the droplets initial contact happens. The video of the collision process of this case is provided in supplementary material of [1], videos HWC_a and WHC_b for side and oblique views, respectively..

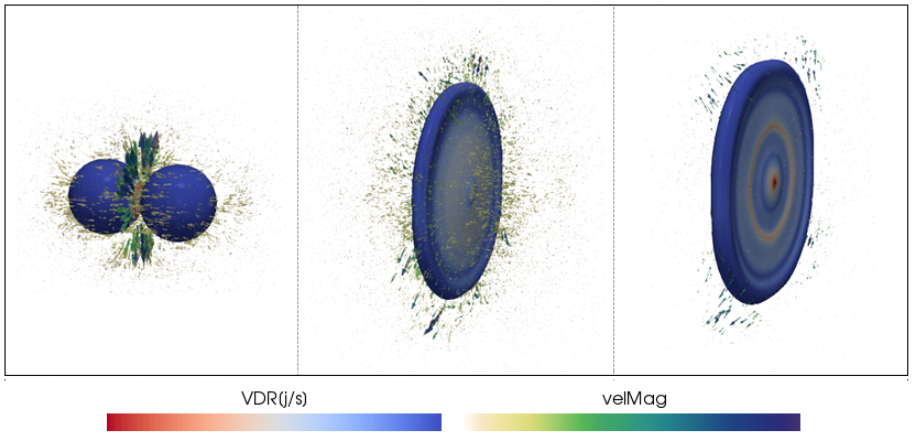

FIGURE 2.33: 3D representation of topological changes in start-up collision of case *HWC* of table 2.1 and corresponding figure 2.32 at times $t/t^* = [0.0, 2.83, 4.25]$ for figures from left to right, respectively. The color contours on the droplets surface represents the **VDR** and the surrounding vector illustrates the velocity vectors with contours as their magnitude in the matrix.

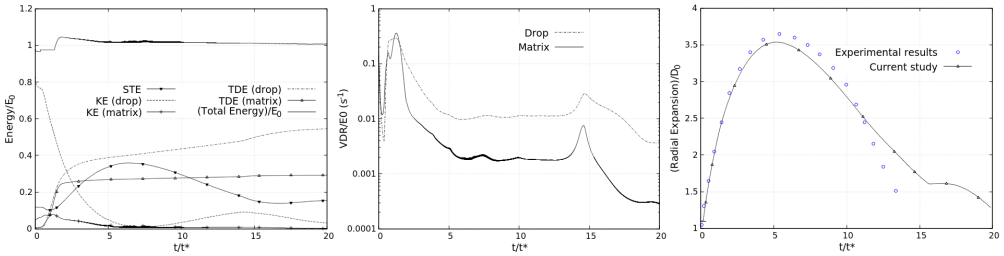

FIGURE 2.34: Left: Energy budget graph, Middle: VDR graph, Right: Normalized radial expansion of the resultant droplet compared with the experimental results of [93]. These figures are related to case *HWC* of table 2.1 and corresponding figure 2.32.

system is only limited to the surface tension energy (**STE**). As mentioned in the section 2.3.3, in the physical formulation, $\mathbf{STE} = \sigma S$. So any value calculated using the numerical formulation of equation 2.20 as $\sigma \sum_{cells} \left(\int_p ||\nabla \phi|| dv_p \right)$ must be equal to this value. In each iteration, the value of **STE** calculated using numerical formulation is compared with the physical formula and the error for that iteration is being calculated (e_i). The total relative error is estimated as $\xi = \sum_i |e_i| / (\sigma S_0) \times 100$, The value of this error in the simulation of this step was 0.02%, indicating good accuracy of numerical formulation of equation 2.20 in resolving the surface tension energy.

2. With the confidence on the accuracy of the calculation of surface tension energy, in the second simulation the droplet is being moved with an initial velocity of U corresponding to Weber number of 10 in X direction where periodic boundary condition is applied. Free-slip boundary condition is applied in the other directions. Initial energy of the system (E_0) is limited to the kinetic energy ($\mathbf{KE} = \frac{1}{2} m U^2$ where m is the mass of the droplet) and surface tension energy ($\mathbf{STE} = \sigma S$). In the absence of viscous dissipation, this value must be constant throughout the simulation. The error of numerical calculation of total energy compared with the physical formulations in each iteration is calculated (e_i). The total relative error is estimated as $\xi = \sum_i |e_i| / E_0 \times 100$. The value of this error for this test case was 0.09%.

3. With the confidence on the accuracy of the calculation of surface tension and

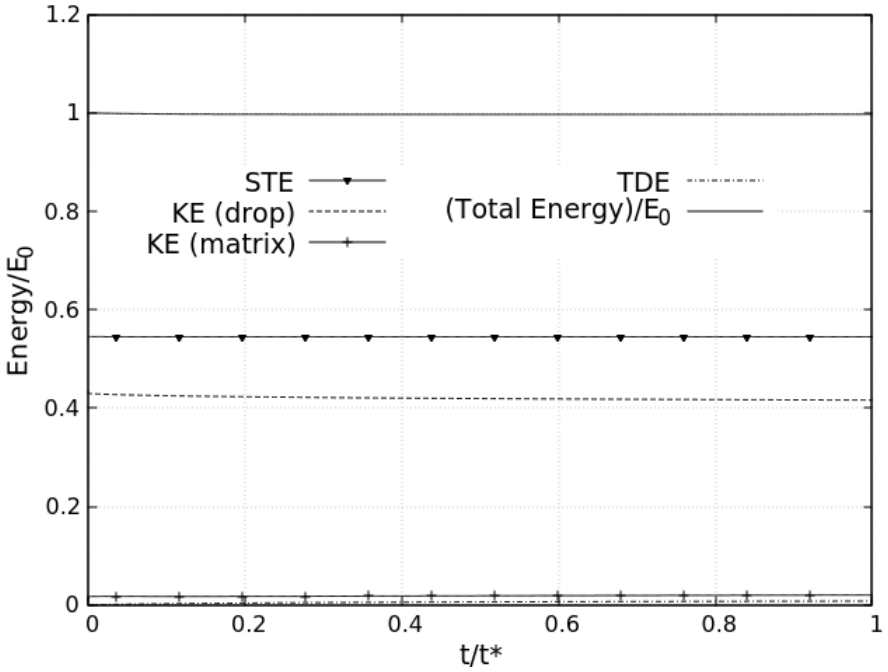

FIGURE 2.35: Normalized energy budget of STE, KE, and TDE for the last test case performed in 2.5

.

kinetic energies, the same simulation as previous one is repeated but for viscous droplet in a viscous matrix with droplet to matrix viscosity ratio of 100. This test case includes all the physical terms of the energy budget, including kinetic, surface tension, and viscous dissipation energies. The corresponding Reynolds number of the problem is equal to 200. The summation of kinetic, surface tension and viscous dissipation energies in each iteration must be equal to the initial energy of the system ($\frac{1}{2}mU^2 + \sigma S$). In each iteration, the error in calculation of total energy of the system compared with the initial energy is calculated (e_i). The total relative error is estimated as $\xi = \sum_i |e_i| / E_0 \times 100$. The value of this error at the end of the simulation was equal to 0.14% which verifies the accuracy of the numerical formulation in calculation of viscous dissipation energy.

The three sets of simulation performed in this section confirms the accuracy of our numerical implementation on energy analysis of the system. The evolution of different energy budgets in the last solution is depicted in figure 2.35.

2.6 Conservation of total energy and the role of flux-limiters

Finite volume flux-limiter schemes as introduced in Balcázar et al. [24, 29] are used in discretization of convective terms of momentum and advection equations, in order to avoid the spurious oscillations that would otherwise occur with high order spatial discretization schemes due to discontinuities imposed by level-set function across the interface. The formulations used in this research are the so-called Minmod, Sweby, Smart, Superbee, and Van-Leer limiters [96, 97]. In this formulation, the value of variable Ψ at the cell face (Ψ_f) is written as the sum of a diffusive first-order upwind part and an anti-diffusive term as [24, 29]:

$$\Psi_f = \Psi_C + \frac{1}{2} L(\theta_f)\left(\Psi_D - \Psi_C\right) \tag{2.26}$$

The anti-diffusive part is multiplied by the flux limiter $L(\theta_f)$ with θ_f defined as the upwind ratio of the consecutive gradients of Ψ.

$$L(\theta) = \begin{cases} max\left[0, min\left(1,\theta\right)\right], & Minmod \\ max\left[0, min\left(\beta\theta,1\right), min\left(\theta,\beta\right)\right], & Sweby \\ max\left[0, min\left(2\theta,\left(0.25+0.75\theta\right),4\right)\right], & Smart \\ max\left[0, min\left(2\theta,1\right), min\left(2,\theta\right)\right], & Superbee \\ \left(\theta+|\theta|\right)/\left(1+|\theta|\right), & Van-Leer \\ 0.0, & Upwind \end{cases} \tag{2.27}$$

In this study, we fixed the parameter β in Sweby flux-limiter to 1. In order to study the effect of different flux-limiters on conservation of total energy in the system, and choose the most consistent one, we perform numerical simulation of a droplet oscillation test case as initially solved by Mashayek and Ashgriz [98]. The test case includes the damping oscillation of a droplet released from its static condition at third mode, meaning the surface of the drop is initially perturbed from its spherical shape according to following spherical harmonics in the (r-z) coordinate system as:

$$h_{t=0}(\theta) = R_3\left(1 + 0.25\left(5cos^3\theta - 3cos\theta\right)\right) \tag{2.28}$$

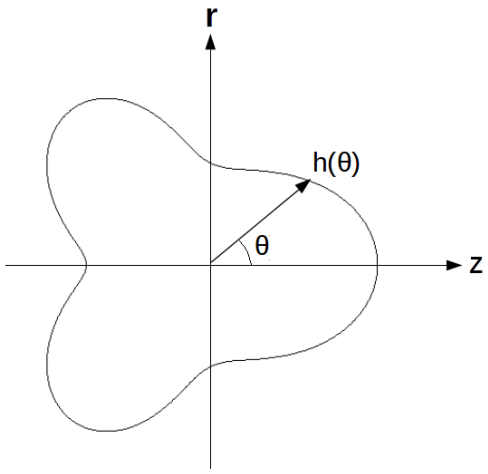

FIGURE 2.36: Schematic of the 2D droplet oscillation problem.

in this formulation, the amplitude of the initial perturbation is equal to 0.5, R_3 is used to maintain the volume of the droplet constant during the initial perturbation and is equal to 0.966. Simulations are done in Reynolds number of 100, with $Re = \sqrt{\sigma r_0 \rho_l}/\mu_l$. Figure 2.36 illustrates the coordinate system along with the initial shape of the perturbed droplet. Two-dimensional simulation domain has length and height of $6r_0$, with r_0 as the initial radius of the droplet. A density ratio and of $\rho_d/\rho_m = 1000$ and viscosity ratio of $\mu_d/\mu_m = 400$ are applied. Time is being non-dimensionalized using $t^* = \sqrt{\rho_d r_0^3/\sigma}$. Simulations are done until $t/t^* = 13.7$ with a constant timestep of $dt/t^* = 3.87 \times 10^{-4}$ for all the cases. A grid size of $h = 2r_0/35$ is used for all the cases unless otherwise is mentioned. Simulations are done with different flux-limiters. For each case, the error in total energy conservation at the end of the simulation is calculated as $\Delta E = |E_{final} - E_{init}|/E_{init}$ where E_{final} and E_{init} are final and initial values of total energy of the system. Table 2.2 represent this criteria for different flux-limiters tested in this section. According to this table, it is plain to see that the Superbee flux-limiter has lower error in conservation of the energy of the system and thus is more suitable in energy analysis study of this chapter. For the case where Upwind scheme is being applied on convective terms in the whole domain, the value of ΔE is 0.17 which is comparably higher than equivalent value of any other flux-limiter.

Figure 2.37 represents the results extracted in this study solved with Superbee flux

TABLE 2.2: Total energy conservation error of the droplet oscillation case of 2.6 for solutions with different flux-limiters.

Flux-limiter	Minmod	Sweby	Smart	Superbee	Van Leer
ΔE	0.0612	0.0202	-0.0310	0.0153	0.0376

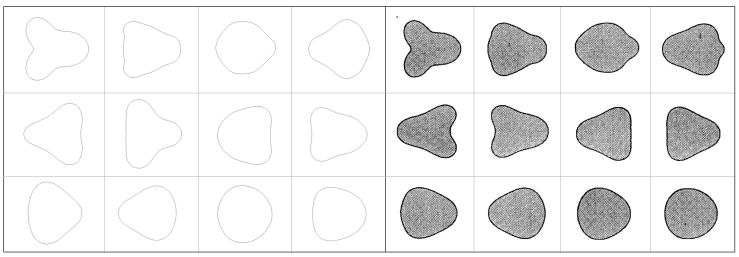

FIGURE 2.37: Time evolution of the oscillations in droplet deformation for droplet with initial perturbation as described in 2.6. Left: result extracted in current study with Superbee flux limiter. Right: reference data of [98]. The snapshots are extracted in the same time instant as $t/t^* = [0.0, 0.2, 0.35, 0.48, 0.63, 1.42, 1.94, 2.74, 4.10, 5.90, 8.90, 10.10]$.

limiter, compared with the reference data extracted in the same time instances. 2.38 illustrates the normalized energy budget of STE, KE, and TDE for droplet and matrix for the solution with Superbee flux-limiter. In this figure, the oscillations in kinetic energy of droplet, surface tension energy, and DE in matrix could be seen. Good conservation of total energy of the system is seen in this figure as well.

In order to analyze the spacial accuracy convergence of the total energy conservation, simulations of this case with Superbee flux-limiter with different grid sizes of $h = 2r_0/25, 2r_0/35$ and $2r_0/45$ are performed. A constant timestep is used for all the simulations. In each case, the ΔE error as mentioned earlier is calculated. In the imaginary perfect solution, the value of ΔE must be equal to zero. According to the results extracted, for the performed droplet oscillation case of this section, the error in total energy conservation of the system has a convergence rate of 1.74 in space.

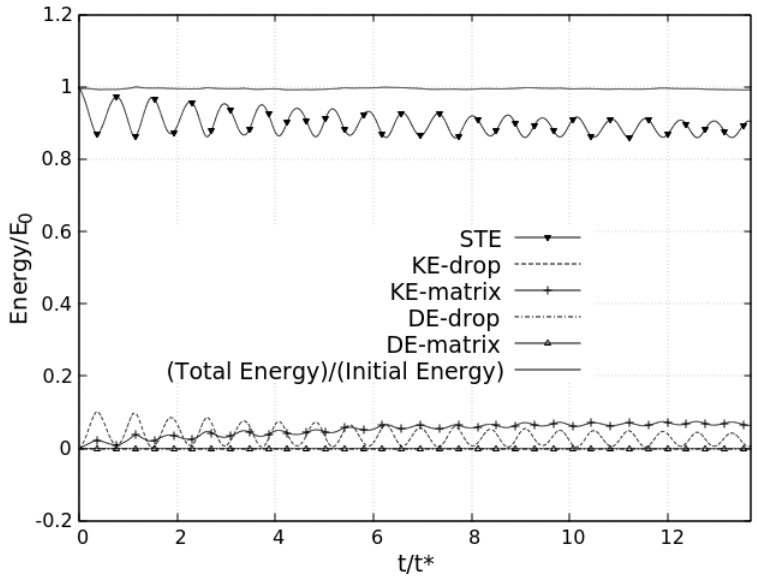

FIGURE 2.38: Normalized energy budget of STE, KE, and TDE for droplet and matrix fluids.

2.7 Conclusions

Direct numerical simulation of head-on and off-center binary droplets collision in all the regimes is performed using a conservative level-set method. The snapshots of evolution of the collision process are extracted and compared with available experimental data in the literature. Very good agreement is seen between the results of current study, and available experimental data. A novel lamella stabilization approach has been introduced which numerically resolves the lamella film, independent of its formation direction. A new ghost-nodes layer approach is proposed to prevent adding mass into the droplet. This ghost-nodes layer was used to extract the gas-film rupture time for the cases of retarded coalescence. A very profound energy analysis is provided for each case covering the main collision regimes which provides more insight into the collision process. According to the extracted results, the time and number of peaks and fluctuations of the surface tension energy are in qualitative agreement with the radial expansion of the droplets. The budget of matrix kinetic energy in all the cases is very small compared to kinetic energy of droplet, surface tension energy and viscous dissipation energy. The main gain in the kinetic energy of the matrix comes from the

escape of the gas film in the matrix when the droplets approach each other around the time of the coalescence and also when the resultant droplet expands after a major retreatment. The share of viscous dissipation energy of the matrix in the cases of coalescence followed by stretching separation is lower than the viscous dissipation energy of the droplet. This norm is reverse for all the other cases. Retreat in the collision process happens when the resultant droplet reaches the local minimum kinetic energy and surface tension reaches a local maximum value. At this time, the surplus surface tension energy mobilizes the resultant droplet causing an increase in the kinetic energy. Droplet kinetic energy recovery factor (KE_{final}/KE_0) is maximum for the bouncing regime (B). The total dissipated energy in this case is also minimum among all other regimes.

Acknowledgments

This work has been financially supported by the *Ministerio de Economía y Competitividad, Secretaría de Estado de Investigación, Desarrollo e Innovación*, Spain (ENE2015-70672-P). I acknowledge the financial support of an FI research scholarship by the *Agència de Gestió d'Ajuts Universitaris i de Recerca (AGAUR) of Generalitat de Catalunya* (2016 FI_B 01059). I thankfully acknowledge the computer resources at Altamira and the technical support provided by Instituto de Física de Cantabria - Universidad de Cantabria (RES-FI-2018-3-0045).

Chapter 3

Numerical study of droplet deformation in shear flow using a conservative level-set method

Most of the contents of this chapter have been published as:

A. Amani, N. Balcázar, J. Castro, A. Oliva. *Numerical study of droplet deformation in shear flow using a conservative level-set method.* Chemical Engineering Science, 207 (2019), 153-171 https://doi.org/10.1016/j.ces.2019.06.014

Abstract. This chapter is concerned with a numerical study on the behavior of a single Newtonian droplet suspended in another Newtonian fluid, all subjected to a simple shear flow. Conservative finite-volume approximation on a collocated three-dimensional grid along with a conservative Level-set method are used to solve the governing equations. Four parameters of capillary number (Ca), Viscosity ratio (λ), Reynolds number (Re) and walls confinement ratio are used to physically define the problem. The main focus of the current study is to investigate the effect of viscosity on critical walls confinment ratio. To do so, first, we validate the ability of proposed method on capturing the physics of droplet deformation including: steady-state subcritical deformation of non-confined droplet, breakup of supercritical conditioned droplet, steady-state deformation of moderate confined droplet, subcritical oscillation of highly-confined droplet, and the effect of viscosity ratio on deformation of the droplet. The extracted results are compared with available experimental, analytical and numerical data from the literature. Afterward, for a constant capillary number of 0.3 and a low Reynolds number of 1.0, subcritical (steady-state) and supercritical (breakup) deformations of the droplet for a wide range of walls confinement in different viscosity ratios are studied. The results indicate the existence of two steady-state regions in a viscosity ratio-walls confinement ratio graph which are separated by a break-up region.

3.1 Introduction

Droplets of one liquid dispersed in an immiscible liquid start to deform when subjected to shear flow. If the conditions are met, the droplet may even breakup into daughter droplets. The study of a droplet in shear flow is important from the aspect of dispersion science and mixing process. For example, it is possible to create a specific blend morphology by shearing emulsions between two parallel plates with a small separation [99] which has applications in Lab-on-a-Chip devices [100]. This area is not only limited to laminar flows. According to Komrakova et al. [101], even though the flow regime in stirred tank reactors is fully turbulent, the effect of the existing eddies on droplets could be modeled by a laminar shear flow. Study of shear deformation of droplets can provide crucial understanding in morphology development of the blends,

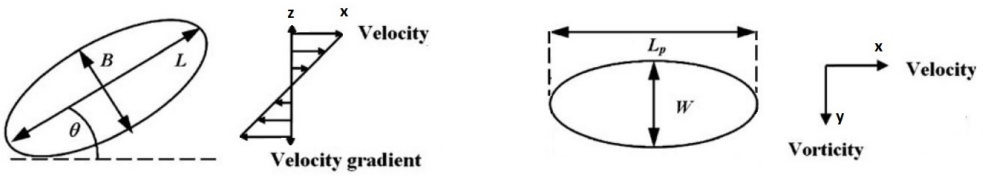

FIGURE 3.1: Schematic presentation of a deformed droplet along with related geometrical measurements in left: velocity-velocity gradient plane and right: velocity-vorticity plane

immiscible fluid displacement in enhanced oil recovery, refinement of liquids, carbon-dioxide sequestration, remediation of nonaqueous-phase liquids and emulsification.

Emulsification has wast applications in food, chemical, and pharmaceutical industries. Emulsification process takes place by applying shear stress against the surface tension, to elongate and then rupture a larger droplet into smaller ones. Emulsions can be made in many ways, however, shear mixing is one of the main methods. Thus studies of shear deformation of droplets can be beneficial to better understand the properties of emulsions and to provides a deeper insight into the rheological properties of the mixture. For instance, the critical conditions at which a droplet breaks-up is useful to quantify emulsion stability [5, 6].

Another important application of deformation and breakup of confined sheared droplets is on Droplet-based microfluidic technology which has recently been exploited to perform microfluidic functions. Its applications range from fast analytical systems and synthesis of advanced materials [102] to protein crystallization [103] and biological assays for living cells [104–106] . Precise control of droplet volumes and reliable manipulation of individual confined droplets have crucial effects on the performance of these systems and are still a challenge [107]. Another important aspect of this area of study is in reacting dispersions, where an understanding of the dynamics of the droplet is needed in order to gain a better perception on the mechanisms of molecular transport, rates of chemical reaction and polymerization of the dispersion [108].

Since the experimental researches of Taylor [109, 110], droplet deformation and breakup in shear flow evoked great interests. More details on these studies could be found in reviews done by Rallison [111], Stone [112], and Cristini and Renardy [113].

In the case where the droplet evolves to a steady shape, different parameters have

been used by researchers to measure the deformation attained by the droplet. The first one is the Taylor deformation parameter defined as $D = (L-B)/(L+B)$, where L and B are length and breadth of the drop, as shown in figure 3.1. Another parameter is the angle θ of orientation of the droplet with respect to the axis of shear strain. In addition to these parameters, Lp and W, as projected length and width of the droplet are used in literature and depicted in figure 3.1. In another experimental research, Marks [114] studied a single droplet undergoing end pinching in a strong shear flow in a process named "elongative end pinching". This process is in opposition to "retractive end pinching" process studied by Bentley and Leal [115]. Vananroye, Van Puyvelde, and Moldenaers [116] reported that confinement has a substantial effect on the critical capillary number. More studies in highly confined systems were done by Sibillo et al. [117], where they found oscillatory behavior in droplet deformation in high but subcritical capillary numbers. They also found complex breakup modes for supercritical capillary numbers. In the context of this chapter, subcritical, refers to conditions where the deformation of the droplet reaches steady-state without any breakup and supercritical refers to conditions where the deformation of the droplet leads to breakup.

Analytical studies in this field are limited. Shapira and Haber [118, 119] investigated the effect of two parallel walls on the motion of a nearly spherical droplet and the drag force acting on it. Roths et al. [120] reported that in two-dimensional cases with small capillary numbers, Taylor deformation parameter is a linear function of capillary number. Sman and Graaf [121] used a slope equal to $f(\lambda_\mu) = 1.4$ for this linear function where λ_μ is the viscosity ratio of droplet to matrix. In three-dimension however, Stone [112] used $f(\lambda_\mu) = (16+19\lambda_\mu/(16+16\lambda_\mu))$. Richardson [122] reported a trigonometric function between deformation (D) and orientation (θ) of the droplet as $D \sim \cos(2\theta)$. Toose, Geurts, and Kuerten [123] found out that time evolution of droplet deformation in two-dimension elongational flow follows the Oldroyd approximation and reported D=f(λ_μ)Ca exp(-$\gamma t/\tau$) where $\tau = Ca(1+\lambda_\mu)$, γ is the rate of strain tensor and Ca as the capillary number is a measure of the ratio between the viscous and interfacial tension stresses. In a more recent work, Minale [124] presented a phenomenological model for the effect of wall on deformation of an ellipsoidal droplet.

Besides the experimental and analytical studies, there are plenty of numerical researches in this field using mainly three methods of boundary integral, lattice Boltzmann (LB) and volume-of-fluid (VOF). Kennedy, Pozrikidis, and Skalak [108] and Kwak and Pozrikidis [125] and Janssen and Anderson [126] studied the droplet deformations using boundary integral method. Since in simulations of merging and folding interfaces in the boundary integral method, the interface point should be reconstructed, significant logical programming techniques are required which increases the computational costs. The mathematical implication of this method is described in Pozrikidis [127].

Using lattice Boltzmann model (LBM), Sman and Graaf [121] investigated the numerical criteria for correct analysis of emulsions and used them to study the droplet deformation and breakup in two-dimensional cases. Xi and Duncan [128] applied the LBM in conjugation with the interface force model presented by Shan and Chen [129] to simulate three-dimensional droplet deformation in simple shear flow. Komrakova et al. [101] used free energy LBM to perform three-dimensional simulations of liquid droplet deformation in simple shear flow for a wide range of flow conditions.

Volume-of-fluid (VOF) and coupled VOF/Level-set methods were used by many researchers [25, 113, 130–133] to investigate the droplet deformation and breakup in shear flow. Li, Renardy, and Renardy [130] presented results for different values of capillary numbers and reported that for supercritical cases, by increasing the capillary number, the number of daughter droplets increases. Renardy and Cristini [131] studied the effect of inertia on droplet breakup. They reported that inertia rotates the droplet toward the vertical direction, in a mechanism similar to aerodynamic lift, afterward the droplet experiences higher shear, which pulls the droplet apart horizontally. Renardy, Cristini, and Li [132] fixed the flow's strength and focused on trends for the droplet fragment distribution when the size of the droplet increases. Khismatullin, Renardy, and Cristini [133] found that for viscosity ratios greater than the critical value, inertia can be used as a mechanism of breakup. Cristini and Renardy [113] worked on the effect of inertia and scaling fragments after droplet breaks.

The studies on shear deformation of the droplets is not limited to Newtonian fluids. Verhulst et al. [134] studied the influence of matrix and droplet viscoelasticity

on the steady-state shear deformation of a droplet. Mukherjee and Sarkar [135] numerically investigated the effects of viscosity ratio on an Oldroyd-B droplet deforming in a Newtonian fluid under steady shear. They reported that the viscoelastic normal stresses reduce droplet deformation and increase critical capillary number. Hsu and Leal [136] studied the steady and transient deformations of a purely elastic droplet in a Newtonian fluid undergoing a planar extensional flow. They reported the absence of overshoot of the droplet deformation upon startup, and a relative insensitivity to the Deborah number. Ioannou et al. [137] investigated the droplet deformation and breakup under simple shear flow when droplet and/or matrix represents non-Newtonian shear-thinning or shear-thickening behaviors. They stated that the shear-thinning droplets behave similarly to highly-viscous Newtonian droplets.

In this chapter, we focus on three-dimensional simulations of droplet deformation and breakup in simple shear flow in the context of conservative level-set (CLS) method [1, 24, 138] with a finite-volume approach.

The first objective is to study the accuracy of our results on capturing the droplet's deformation and breakup in shear flow. The effect of domain size, mesh size and numerical parameters on the accuracy of the results are studied. Validation is done by analyzing the effect of different parameters including walls confinement, capillary number and viscosity ratio on the deformation and breakup of the droplet. The extracted results are compared with the available numerical, analytical and experimental data.

In the next step, the effect of walls confinement ratio on critical viscosity ratio for a constant capillary number of 0.3 and a low Reynolds number of 1.0 is studied. According to Vananroye, Van Puyvelde, and Moldenaers [139], for viscosity ratios smaller than 1, confinement suppresses breakup while for viscosity ratios bigger than 1, breakup is enhanced. Janssen et al. [140] further studied the deformation of a single droplet as a function of viscosity ratio and confinement ratio both experimentally and numerically using the boundary integral method. They discussed the critical capillary number for a wide range of viscosity ratios in different confinements and suggested that there is a generalized behavior on droplet breakup mechanism in confinement. They presented a graph of five regions for the critical capillary number in different confinements. Despite these studies, to the best of our knowledge, effect of viscosity

ratio on walls critical confinement ratio is yet to be discovered. In the last section of this chapter, we elaborately study this phenomenon for a given capillary number of 0.3 and a low Reynolds number of 1.0. Our results illustrate two steady-state and one breakup regions for droplet under different confinements and viscosity ratios.

The outline of this chapter is as follow: Mathematical formulations are presented in section 3.2. Employed numerical methods are explained in section 3.3. Section 3.6 involves the obtained results. Firstly we verify the accuracy of the method against different numerical, analytical and experimental data. In section 3.6.5, we study the effect of viscosity ratio on walls critical confinement ratio. Finally, concluding remarks are presented in section 3.7.

3.2 Mathematical formulation

Navier-Stokes equations are used to describe the conservation of mass and momentum of two incompressible immiscible newtonian fluids on a spacial domain Ω with boundary $\partial\Omega$ as following [1, 24]:

$$\frac{\partial}{\partial t}(\rho\mathbf{v})+\nabla.(\rho\mathbf{v}\mathbf{v}) = -\nabla p+\nabla.\mu\left(\nabla\mathbf{v}+(\nabla\mathbf{v})^T\right)+\rho\mathbf{g}+\sigma\kappa\mathbf{n}\delta_\Gamma \text{ in } \Omega \quad (3.1)$$

$$\nabla.\mathbf{v} = 0 \text{ in } \Omega \quad (3.2)$$

where ρ and μ are density and dynamic viscosity of the fluids, $\mathbf{v}$ is the velocity field, p pressure field, $\mathbf{g}$ gravitational acceleration and δ_Γ is the Dirac delta function concentrated at the interface (Γ). In this formulation, $\mathbf{n}$ is the unit normal vector outward to interface, κ is the interface curvature and σ is the interface tension coefficient.

Since the mass, density, and viscosity are constant within each fluid, they can be defined as scalar-fields inside the whole domain as follows:

$$\rho = \rho_1 H+\rho_2(1-H) \quad (3.3)$$

$$\mu = \mu_1 H+\mu_2(1-H) \quad (3.4)$$

where H is the Heaviside step function which takes the value one in dispersed phase and zero elsewhere.

In this research, conservative level-set (CLS) method [82], as introduced by Balcazar et al. [24] in the context of a finite-volume method for unstructured grid is used. Instead of the signed distance function, d(x,t), used to represent the interface in the classical level-set method, conservative LS method employs a regularized indicator function ϕ as below:

$$\phi(x,t) = \frac{1}{2}\left(tanh\left(\frac{d(x,t)}{2\varepsilon}\right)+1\right) \tag{3.5}$$

where ε is the parameter that sets the thickness of the interface. ϕ varies from 0 in one fluid to 1 in other fluid. With this formulation, interface is defined by $\Gamma = \{x|\phi(x,t) = 0.5\}$.

The level-set function is advected by velocity vector field, **v**, provided from solution of Navier-Stokes equations. Since the velocity field is solenoidal ($\nabla.\mathbf{v} = 0$), the interface transport equation can be written in conservative form [24, 82]:

$$\frac{\partial\phi}{\partial t} + \nabla.\phi\mathbf{v} = 0 \tag{3.6}$$

Since sharp changes exist in level set function at the interface, Superbee flux limiter scheme is used in discretization of the convective term in order to minimize numerical diffusion and to avoid numerical instabilities at the interface. To keep the profile and thickness of the interface constant, an additional re-initialization equation [27] is used:

$$\frac{\partial\phi}{\partial\tau} + \nabla.\phi\left(1-\phi\right)\mathbf{n}_{\tau=0} = \nabla.\varepsilon\nabla\phi \tag{3.7}$$

which is advanced in pseudo-time τ. This equation consists of a compressive flux: $\phi(1-\phi)\mathbf{n}_{\tau=0}$ and a diffusion term: $\nabla.\varepsilon\nabla\phi$. The first one keeps the level-set function compressed onto the interface along the normal vector **n**, and the second one keeps the profile in prescribed characteristic thickness of ε. This parameter is defined based on the mesh resolution as [24]:

$$\varepsilon_p = C_\varepsilon h^{1-\alpha} \tag{3.8}$$

where $h = (V_P)^{1/3}$ is the grid size based on volume V_P of cell P. In all the simulations

of this chapter, C_ε is constant and equal to 0.5. Parameter α, however, varies in order to change the thickness of the interface and can take values between [0,0.1], to overcome the possible numerical instabilities. Normal vector $\mathbf{n}$ on the interface and curvature κ of the interface, are obtained using [24]:

$$\mathbf{n} = \frac{\nabla\phi}{||\nabla\phi||} \tag{3.9}$$

$$\kappa(\phi) = -\nabla.\mathbf{n} \tag{3.10}$$

The continuous surface force model (CSF) [83] is used for surface tension computation which converts the term $\sigma\kappa\mathbf{n}\delta_\Gamma$ in Eq. 3.1 to a volume force term as follows [24]:

$$\sigma\kappa\mathbf{n}\delta_\Gamma = \sigma\kappa(\phi)\nabla\phi \tag{3.11}$$

where $\nabla\phi$ is computed using least-square method based on vertex node stencils [24]. By applying this approach, the explicit tracking of the interface is not necessary.

3.3 Numerical method

Finite-volume (FV) approach is used to discretize the Navier-Stokes and level-set equations on a collocated grid, so all the computed variables are stored at centroids of the cells [24]. A central difference (CD) scheme is used to discretize the compressive term of re-initialization equation (3.7) and diffusive fluxes at the faces. A distance-weighted linear interpolation is used to calculate the face values of physical properties and interface normals. The gradients are computed at the cell centroids using the least-squares method. For creeping flow regime, a central difference scheme and for non-creeping flow regimes a total-variation Diminishing (TVD) SUPERBEE flux limiter is used to discretize the convective term as implemented in Balcazar et al. [24], in order to improve the numerical stability of the solver. At discretized level, physical properties are regularized in the context of the CLS method. Therefore a linear average is used for density as $\rho = \rho_1\phi + \rho_2(1-\phi)$, and a harmonic average is used for viscosity as $\mu = \left(\frac{\phi}{\mu_1} + \frac{1-\phi}{\mu_2}\right)^{-1}$ [141–143]. Harmonic average of viscosity improves the accuracy

convergence of the results, compared with the linear average. As a comparison, velocity profile of a two-dimensional two-phase oscillating droplet is presented in section 3.4 where results of harmonic averages of viscosity are compared with results of linear average of viscosity for this problem.

A classical fractional step projection method as described by Chorin [84] is used to solve the velocity-pressure coupling. The solution procedure is as follows:

1. Physical properties, interface geometric properties and velocity field are initialized.

2. Allowable time step is calculated. The value of Δt is limited by CFL conditions on convective term and also by explicit treatment of surface tension as used by [1, 24]:

$$\Delta t_{conv} \equiv \alpha \times min(\frac{h}{\|V_P\|}) \tag{3.12}$$

$$\Delta t_{cap} \equiv \alpha \times min(h^{3/2}(\frac{\rho_1+\rho_2}{4\pi\sigma})^{1/2}) \tag{3.13}$$

   where α is CFL coefficient. The final global value of time step is the minimum of Δt_{conv} and Δt_{cap}. To decrease the computational costs, the maximum value of α which leads to a stable simulation is used. Unless otherwise mentions, this value is 0.1.

3. The advection equation (3.6) is integrated in time with a 3-step third order accurate TVD Runge-Kutta scheme [85].

4. The re-initialization equation (3.7) is integrated in pseudo time (τ) using a third order accurate TVD Runge-Kutta scheme. The time τ is used to lead the solution into a stationary state. Since an explicit scheme is used, the time step is restricted by the viscous term of equation 3.7 as follows [24, 82]:

$$\Delta\tau = C_\tau min\left(\frac{h^2}{\varepsilon_P}\right) \tag{3.14}$$

One iteration is used to solve the discretized form of equation 3.7. The value of C_τ in this formula serving as a CFL-like coefficient for this equation, can take values between [0.01,0.05].

5. Physical properties in the domain (density and viscosity) and geometrical properties at the interface (curvature and interface normal) are updated from the level set field.

6. The velocity and pressure fields are calculated using a fractional-step method. The first step is to calculate the predicted velocity $\mathbf{v}$. In the creeping flow regime, where the Reynolds number of the flow is close to zero, the diffusion term in momentum equation tends to control and decreases the time step. This implies a huge computational cost on simulations. To avoid this issue, diffusion term could be treated implicitly. So a second-order implicit Crank-Nicolson scheme is used to discretize the diffusion term of equation 3.1 while a second-order Adams-Bashforth scheme is used on convective, gravity and surface tension terms.

$$\frac{\rho\mathbf{v}^* - \rho^n\mathbf{v}^n}{\Delta t} = \frac{3}{2}(R_h^v)^n - \frac{1}{2}(R_h^v)^{n-1} + \frac{1}{2}\left(\mathbf{D}_h(\mathbf{v}^*) + \mathbf{D}_h(\mathbf{v}^n)\right) - \nabla_h p^n \quad (3.15)$$

where $R_h^v = -\mathbf{C}_h(\rho\mathbf{v}) + \rho\mathbf{g} + \sigma\kappa\nabla_h(\phi)$ with $\mathbf{C}_h(\rho\mathbf{v}) = \nabla_h.(\rho\mathbf{v}\mathbf{v})$ as the convective operator. In this equation, $\mathbf{D}_h(\mathbf{v}) = \nabla_h.\mu(\nabla_h\mathbf{v} + \nabla_h^T\mathbf{v})$ as the diffusion operator where ∇_h represent the gradient operator.
A term of pressure gradient of previous time step is added to the discretized form of equation 3.1. According to Armfield and Street [144], this will increase the accuracy of the momentum equation to a second order in time, and combined with proper boundary condition of Kim and Moin [145] even to a third order in time. In our case, the momentum equation has a second-order accuracy in time. In section 3.5, the convergence of implemented method for the accuracy of momentum equation in time is analyzed.
Next, a correction to the predicted velocity applies as:

$$\frac{\rho\mathbf{v}^{n+1} - \rho\mathbf{v}^*}{\Delta t} = -\nabla_h\pi^{n+1} \quad (3.16)$$

where π is the pressure correction term. By applying the incompressibility constraint ($\nabla.\mathbf{v} = 0$), equation 3.16 changes to a Poisson equation as follows:

$$\nabla_h.\left(\frac{1}{\rho}\nabla_h(\pi^{n+1})\right) = \frac{1}{\Delta t}\nabla_h.(\mathbf{v}^*) \tag{3.17}$$

The obtained linear system is solved using a preconditioned conjugated gradient method. At the end, the velocity $\mathbf{v}^{n+1}$ is corrected using:

$$\mathbf{v}^{n+1} = \mathbf{v}^* - \frac{\Delta t}{\rho}\nabla_h(\pi^{n+1}) \tag{3.18}$$

and the pressure is updated using:

$$\mathbf{p}^{n+1} = \mathbf{p}^n + \pi^{n+1} \tag{3.19}$$

7. In order to fulfill the incompressible constraint, Eq. 3.2, and to avoid pressure-velocity decoupling on collocated meshes [86, 146], a cell-face velocity is used to advect the momentum and CLS function, as introduced in [24].

8. repeat steps 2 -7 to reach the desired time.

The reader is referred to [24, 29] for technical details on the finite-volume discretization of both the Navier-Stokes and conservative level-set equations on collocated unstructured grids. The numerical methods are implemented in an in-house parallel c++/MPI code called TermoFluids [47]. Validations and verifications of the numerical methods in the context of Conservative level-set method used in this work have been reported in [1, 2, 24, 25, 27–29, 138].

3.4 Harmonic Vs. Linear Average of Viscosity

In order to compare the accuracy of harmonic versus linear average of viscosity, a two-dimensional test case of oscillation of a droplet in an adjacent matrix is studied. The domain is a square with the side length of 8r where r is the radius of the droplet. The

TABLE 3.1: Flow parameters of the 2D droplet oscillation test case

ρ_d/ρ_m	μ_d/μ_m	We	Re
666.08	119.08	5.0	6.25

TABLE 3.2: First-norm of the error in radial expansion of the 2D droplet oscillation test case

h	$L_{1,Harmonic}$	$L_{1,Linear}$
2r/30	0.244	0.285
2r/25	0.45	0.48
2r/20	0.85	0.75

droplet is placed at the center of the domain, (x_0, y_0). At time t=0, an initial velocity as following is applied to the droplet, causing an oscillation in its deformation:

$$U = u_0 \frac{x - x_0}{2r} \tag{3.20}$$

$$V = -u_0 \frac{y - y_0}{2r} \tag{3.21}$$

where U and V are velocities in x and y directions, respectively. Four different grid sizes used to solve this problem are h=r/10, 2r/25, r/15 and r/20, where the results of the finest grid are used as the reference to extract the order of accuracy convergence in space. Two different interpolation methods of linear and harmonic are applied in calculations of viscosity. Time is non-dimensionalized with $t^* = r/u_0$. A constant non-dimensional time-step of $dt' = dt/t^* = 7 \times 10^{-4}$ is used in all the simulations. The physical properties of the droplet and matrix are presented in table 3.1 where Weber and Reynolds numbers are defined as follows:

$$We = \frac{\rho_d u_0^2 r}{\sigma} \tag{3.22}$$

$$Re = \frac{\rho_d u_0 r}{\mu_D} \tag{3.23}$$

Simulations are performed until t*=10. The radial expansion of the droplet in y-direction as a function of time for these cases are presented in figure 3.2.

The U component of velocity in the centerline x-direction at $t' = 10$ is extracted as comparison criteria. The results of cases with h=r/20 for linear and harmonic cases

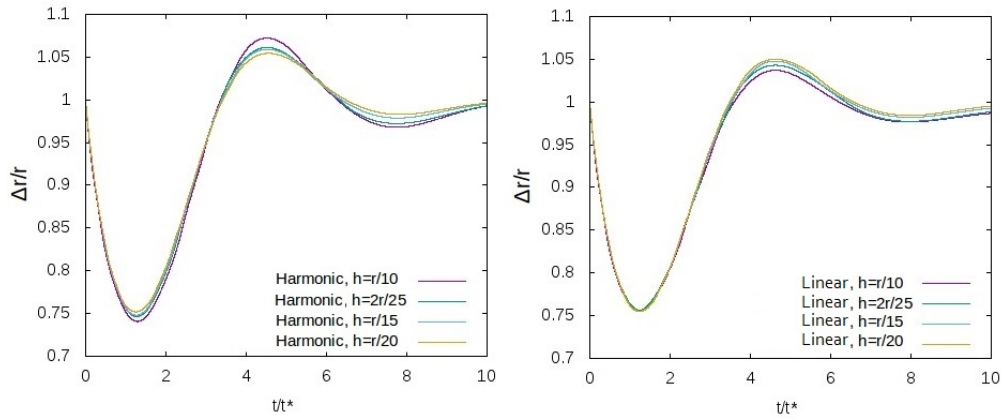

FIGURE 3.2: Time variation of non-dimensionalized radial expansion of the droplet in y-direction for cases with linear and harmonic interpolation of the viscosity in domain with different grid sizes.

are used as the reference of linear and harmonic cases, respectively. The first-norm of error for each case is extracted and used to calculate the convergence of the solution as $L_1 = \sum_i |e_i|$, where e_i is the point-wise error of each cell compared with its reference. These values are presented in table 3.2. According to the extracted results, the linear interpolation of viscosity has the convergence rate of 2.03 in space, while the same value for results of harmonic interpolation is 2.61.

3.5 Momentum Convergence Analysis

In order to evaluate the accuracy convergence of momentum equation in time, a 2D channel flow problem with the length of S_x and height of $S_y = H$ in x and y directions, is solved. The initial configuration of the domain is illustrated in figure 3.3. A periodic boundary condition is applied in X direction and no-slip boundary condition in Y. Numerical parameters to fully define this problem are presented in table 3.3. For this problem, analytical exact solution would be as follows:

$$V_x(y) = \frac{\partial P}{\partial x}\frac{h^2}{2\mu_i}\Big[\frac{2\mu_i}{\mu_1+\mu_2} + \frac{\mu_1-\mu_2}{\mu_1+\mu_2}(\frac{y}{h}) - (\frac{y}{h})^2\Big] \tag{3.24}$$

TABLE 3.3: Flow parameters of the 2D channel test case

ρ_1/ρ_2	μ_1/μ_2	σ	$\partial P/\partial x$
1.0	10	20	0.2

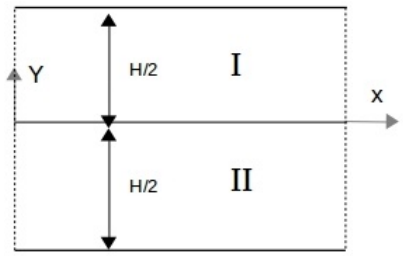

FIGURE 3.3: Schematic of the 2D channel flow problem.

where $i \in \{I, II\}$ determines the region of the fluid. Numerical simulations are done for enough long time to reach steady-state (t=30.0 s). Three different time steps of $dt = 2\times10^{-5}, 4\times10^{-5}$ and 8×10^{-5} for solutions in a domain with grid size of h=H/40 are used. Figure 3.4 represent the variation of x-direction velocity profile in y direction ($V_x(y)$) for cases with different time steps, along with the analytical exact solution.

In each case, x-direction velocity profile at t=30.0 is extracted to compare the results. The Analytical solution is used as the reference. The infinity-norm of error for each case is extracted and used to calculate the convergence of the solution as $L_\infty = max(|e_i|)$, where e_i is the point-wise error of each cell compared with its reference. Figure 3.5 illustrates the L_∞ of the error for different time steps. As can be seen, the convergence of error for this test case is almost 2.

3.6 Numerical experiments and discussion

A circular droplet with radius r is placed at the center of a domain with span S_x, S_y and S_z in x,y and z directions, respectively. Figure 3.6 illustrates the initial computational setup. The opposite x-direction velocities of $+U$ and $-U$ are imposed at the top and bottom walls inducing a shear rate of $\dot{\gamma} = 2U/S_z$ in the domain. A periodic boundary condition is applied in the flow direction (x) and Neumann boundary condition in y direction. Computations have been performed using a Cartesian mesh of cubic grids

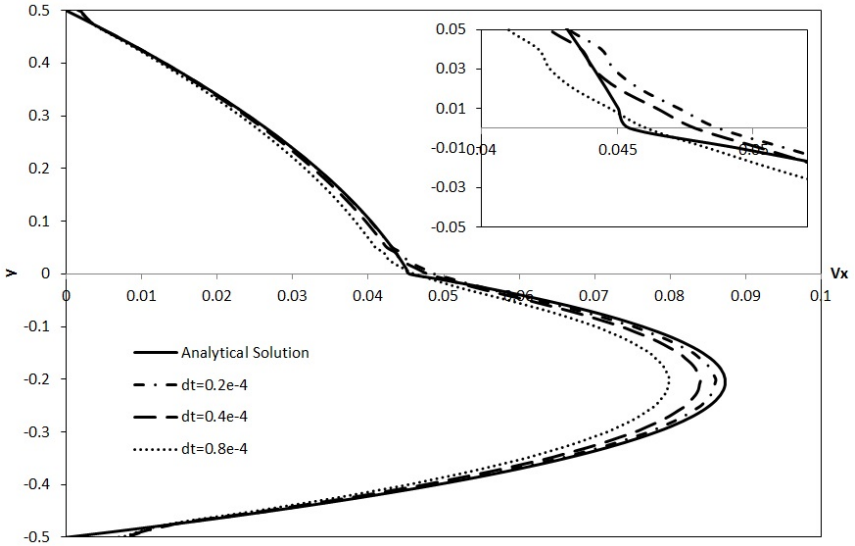

FIGURE 3.4: Variation of V_x velocity profile in y direction for cases with different time steps, along with the exact solution.

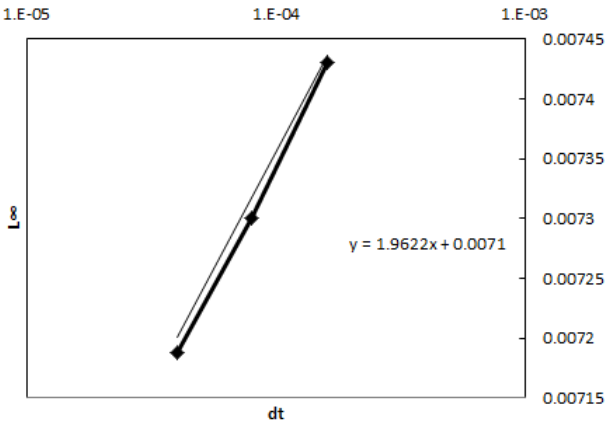

FIGURE 3.5: L_∞ of the error in $V_X(y)$ compared with the analytical solution, Vs. time step of the simulations.

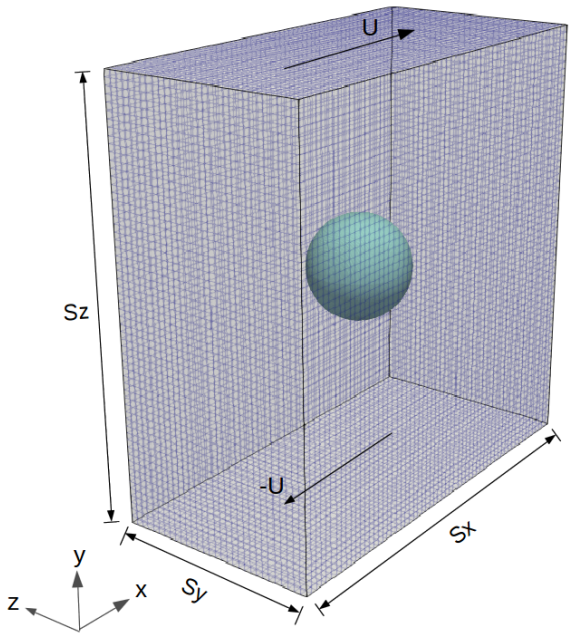

FIGURE 3.6: Computational setup in the cubic structured mesh

with the edge size of h. This mesh was generated by a constant step extrusion of the two-dimensional y-z grid along the x-axis with the step size of h. At the beginning of the simulation, a linear velocity field is applied inside of the domain varying from $-U$ at the bottom wall to $+U$ at the top wall. Simulations with different mesh resolutions are done to study the effect of the computational grid size.

The system can be physically defined by four parameters of Reynolds number (Re), capillary number (Ca), viscosity ratio ($\lambda = \mu_d / \mu_c$) and walls confinement ratio ($2r/S_z$) while c stands for *continuum* and d stands for *droplet*. For an arbitrary value of shear rate ($\dot{\gamma}$), the velocity at the top and bottom walls are calculated as $U = \dot{\gamma} S_z / 2$. Then viscosity is calculated using the Reynolds number as below:

$$Re = \frac{\rho_c \dot{\gamma} r^2}{\mu_c} \tag{3.25}$$

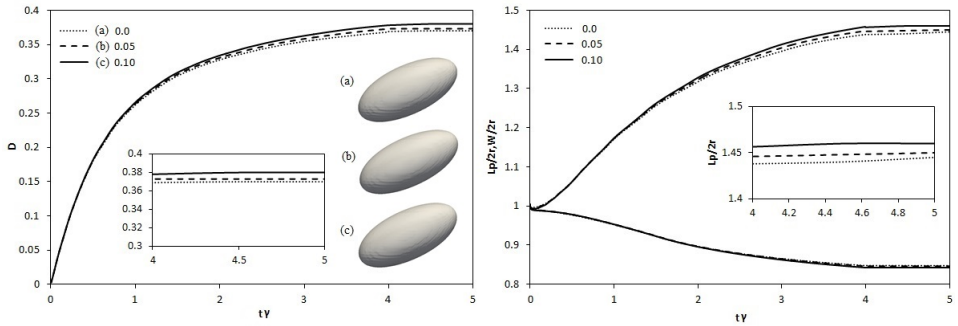

FIGURE 3.7: Left: Taylor deformation parameter (D), right: $L_p/2r$ and $W/2r$ parameters vs. $t\dot{\gamma}$ for subcritical cases with Re=0.1, Ca=0.3 and λ=1 all in a domain with $(S_x, S_y, S_z) = (8r, 4r, 8r)$ and grid size of $h = 2r/25$. All the cases have $C_\tau = 0.025$. Three different values of α = 0.0, 0.05 and 0.10 are tested.

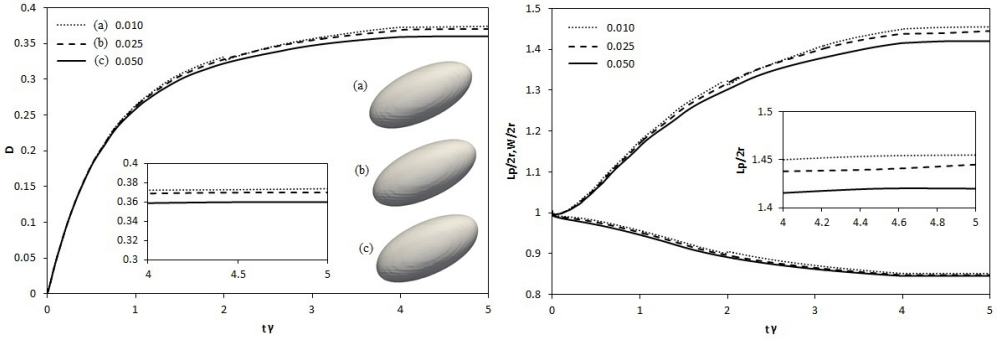

FIGURE 3.8: Left: Taylor deformation parameter (D), right: $L_p/2r$ and W/2r parameters vs. $t\dot{\gamma}$ for subcritical cases with Re=0.1, Ca=0.3 and λ=1 all in a domain with $(S_x, S_y, S_z) = (8r, 4r, 8r)$ and grid size of $h = 2r/25$. All the cases have $\alpha = 0.0$. Three different values of C_τ = 0.01, 0.025 and 0.050 are tested.

The capillary number is a dimensionless parameter defining the relative effect of the shear stress versus surface tension across the interface, given by:

$$Ca = \frac{\dot{\gamma}\mu_c r}{\sigma} \tag{3.26}$$

For a given value of Ca and Re numbers, and the calculated value of μ_c, the related value of σ is determined.

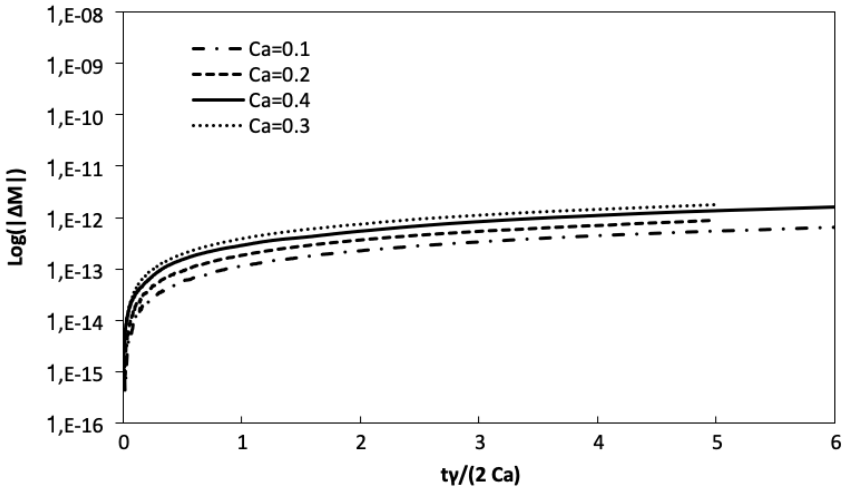

FIGURE 3.9: The evolution in the mass conservation error of the droplet for cases all with Re=0.1 and λ=1 in a domain with the grid size of $h = 2r/25$. The results of the simulation with four different capillary numbers of 0.1, 0.2, 0.3 and 0.4 are presented. ΔM for the droplet is $(M_t - M_0)/M_0$, where M_0 is droplet's initial mass and M_t is the mass at time t.

3.6.1 The effect of numerical parameters

The effect of variable CLS parameters of C_τ and α on final results is studied through a set of numerical simulations. These two parameters are introduced in equations 3.14 and 3.8, respectively. The results including time varying D, $L_p/2r$ and $W/2r$ parameters and steady-state shape of the droplet are presented in figures 3.7 and 3.8, for cases with Re=0.1, Ca=0.3, λ=1 in a domain with $(S_x, S_y, S_z) = (8r, 4r, 8r)$ with the grid size of $h = 2r/25$. In the cases of figure 3.7, for a constant value of C_τ=0.025, three different values of α=0.0, 0.05 and 0.10 are tested. In the cases of figure 3.8, for a constant value of α=0.0, three different values of C_τ=0.01, 0.025 and 0.050 are tested. The selected values include the boundaries of the proposed range for these parameters. According to these results, the variation of C_τ and α, has negligible influence on deformation of the droplet. For the rest of the simulations in this chapter, values of C_τ and α are 0.015 and 0.0, respectively.

In each iteration, droplet's mass conservation error is calculated using $\Delta M = (M_t - M_0)/M_0$, where M_0 is droplet's initial mass and M_t is droplet's mass at time t. In all the simulations of this research, droplet's mass conservation error is in the order of

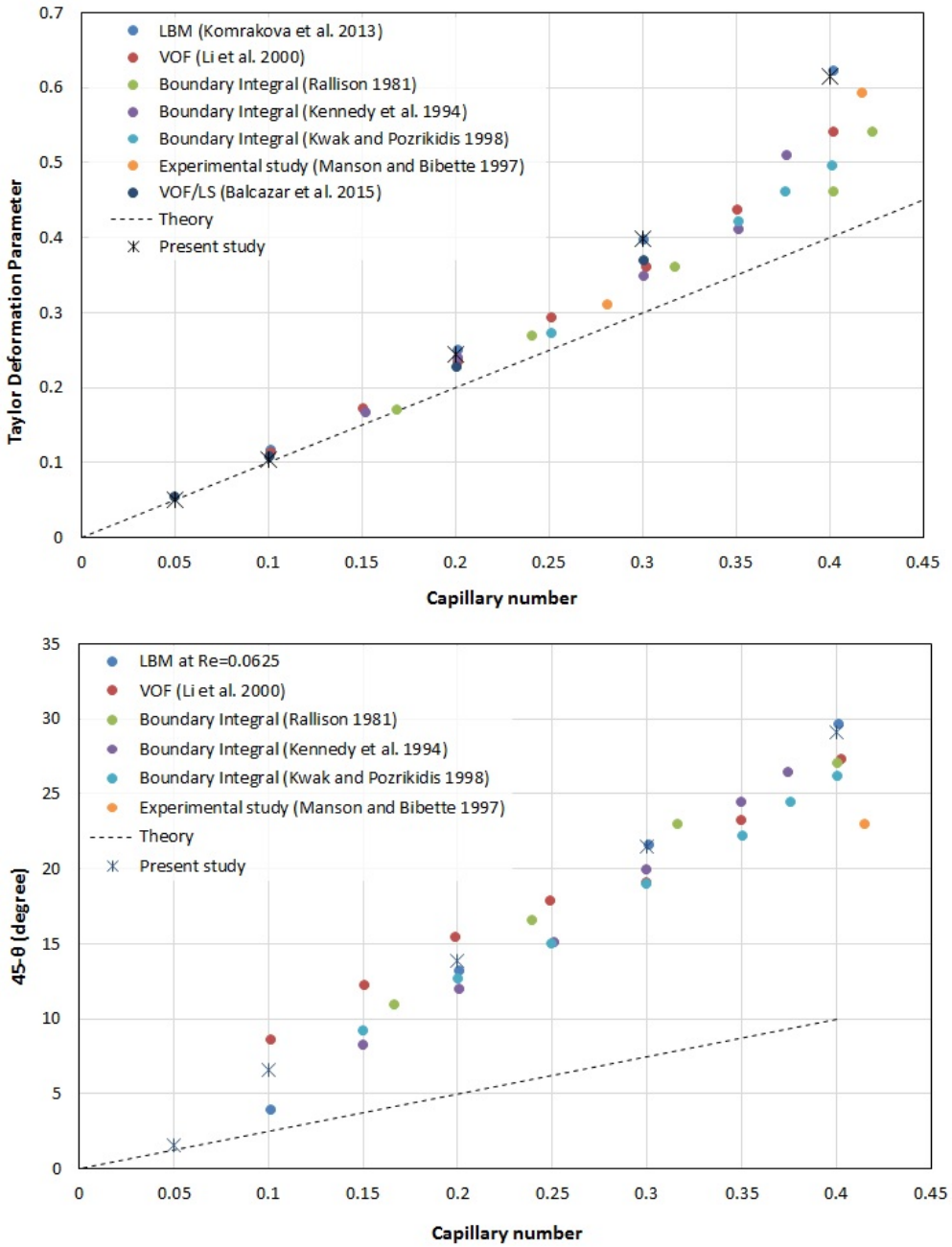

FIGURE 3.10: Taylor deformation parameter (D) and inclination of the droplet (45-θ) at steady-states for different capillary numbers, in Stokes flow conditions (Re=0.0625) with $\lambda = 1$. Dash line represents the asymptotic results by Cox [147] for small deformation.

TABLE 3.4: The effect of domain's length (S_x) on steady-state values of Taylor deformation parameter (D) and orientation angle (θ) for cases with $Re = 0.1, Ca = 0.3$ and $\lambda = 1$. The S_z and S_y of the domains are 8r and 4r, respectively.

S_x	$6r$	$8r$	$10r$
D	0.3823	0.3985	0.4039
θ	25.15	24.50	24.34

$O(10^{-12})$. Figure 3.9 presents the time variation of mass conservation error of the droplet for cases with Re=0.1 and λ=1, and four capillary numbers of 0.1, 0.2, 0.3 and 0.4, all in a domain with the grid size of $h = 2r/25$. Evidently, the mass conservation error of droplet in all the cases has converged to the order of $O(10^{-12})$.

In order to study the effect of domain's length on the results, simulations with $(Re, Ca, \lambda) = (0.1, 0.3, 1)$ in three domains with $(S_x, S_y, S_z) = (6r, 4r, 8r)$, $(8r, 4r, 8r)$ and $(10r, 4r, 8r)$ with grid size of $h = 2r/25$ are performed. The value of D and θ parameters for these cases are tabulated in table 3.4. It is plain to see that domains with lower lengths encounter with a lower value of D and higher inclination angle. Since periodic boundary condition is applied in the flow direction, it is important to make sure that the fluctuations in the velocity profile downwind of the domain will dissipate before passing through the periodic boundary and re-entering the domain. The ideal velocity profile at this location should linearly vary from -U at the bottom wall to +U at the top wall. According to measurements and extracted profiles, domain with $S_x = 6r$ has nonuniform velocity profile at the location of the periodic boundary. This issue affects the deformation of the droplet, while domain with $S_x = 10r$ has a much more uniform velocity distribution at this location. The standard deviation of D for cases with $S_x = 6r$ and $S_x = 8r$ is 1.1% while this value for cases with $S_x = 8r$ and $S_x = 10r$ is 0.3%. In order to reduce the computational cost, unless otherwise is mentioned, the length of the domains of simulations is $S_x = 8r$. According to our studies and Komrakova et al. [101], $S_y = 4r$ is wide enough to minimize the effect of the side walls on simulations and save-up in computational costs. Hence, unless otherwise is mentioned, domains with $S_y = 4r$ are used in the simulations.

Concerning with the effect of grid size on results, simulations with Re=0.1, λ=1 and two different capillary numbers of 0.1 and 0.4, as the boundaries of the subcritical

TABLE 3.5: The effect of grid size on Taylor deformation parameter (D) at steady-state for cases with Re=0.1, $\lambda = 1$ and two different capillary numbers of 0.1, 0.4.

mesh	h	Ca=0.1		Ca=0.4	
		D	ε_D	D	ε_D
M1	2r/25	0.1139	1.24%	0.6313	4.7%
M2	2r/30	0.1135	0.8%	0.6144	1.9%
M3	2r/35	0.1125	-	0.6030	-

regime of creeping flow, are done. Table 3.5 summarizes the Taylor deformation parameter for these cases solved in three different meshes of M1, M2, and M3. The mesh M3 (as it is formed with the finest grid) is used as the reference case, and the relative error of cases with meshes M1 and M2 with regards to the case with this mesh are calculated. According to these data, the error in Taylor deformation parameter of mesh M2 in the worse case is less than 2%. In favor of computational cost, unless otherwise is specified, simulations are done in domains with grid size of mesh M2.

3.6.2 The effect of capillary number

In order to study the accuracy of our results on capturing the effect of capillary number on deformation of the droplet in creeping flow condition, simulations with different capillary numbers of 0.05, 0.1, 0.2, 0.3 and 0.4 in flow with Re=0.0625 and $\lambda = 1$ are done. For the case with Ca=0.4, a domain length of $S_x = 12r$ is used to ensure acceptable uniform velocity profile at the location of the periodic boundary. Taylor deformation parameter (D) and inclination of the droplet (45-θ) are extracted and presented in figure 3.10. These data are compared with results available in the literature, done by different methods i.e. numerical methods including Lattice Boltzmann, VOF and boundary integral in addition to experimental and analytical methods. According to these results, by increasing the capillary number, both Taylor deformation parameter (D) and inclination of the droplet (45-θ) increases, meaning the droplet elongates more in the flow direction. For small values of capillary number, the results agree well with the theoretical studies of Cox [147]. However, by increasing the capillary number, asymptotic results of Cox [147] under-predicts the deformation parameters compared

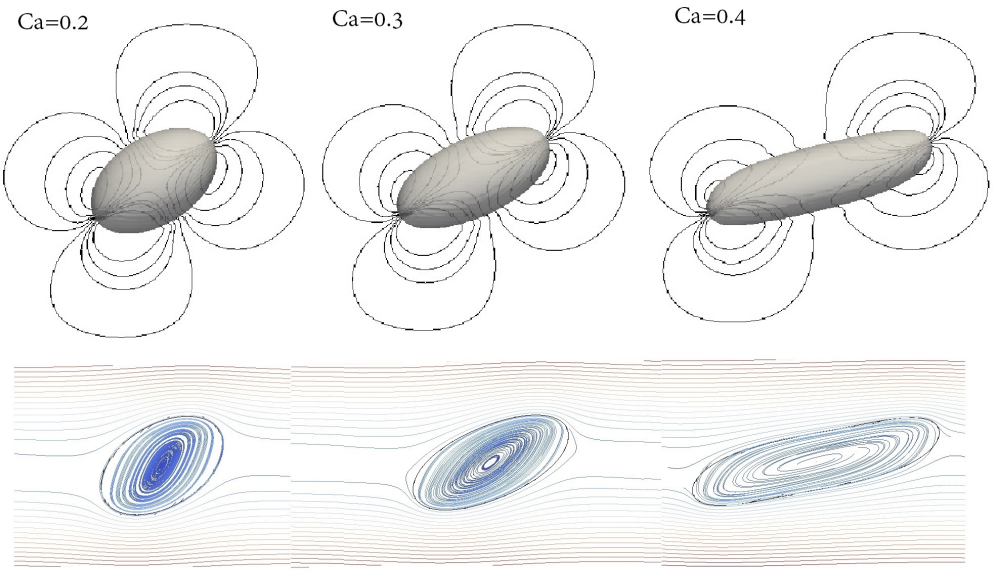

FIGURE 3.11: Top: droplet shape along with vorticity contours ($e_y.\nabla \times \mathbf{v}$) in x-z plane at $y = S_z/2$. bottom: cross section of droplet shape along with streamlines in the same plane. All the images are in steady-state of the solution with Re=0.0625, λ=1 and h=2r/25, for different capillary numbers of 0.2, 0.3 and 0.4.

with experimental and numerical data. This difference expands as capillary number increases. It is clear to see that the results extracted in this study agree well with the reference data.

For aforementioned cases, with capillary numbers of 0.2, 0.3 and 0.4, the steady-state droplet shape along with velocity streamlines and vorticity contours in x-z plane at $y = S_y/2$ ($e_y.\nabla \times \mathbf{v}$) are illustrated in figure 3.11. This figure also verifies that by increasing the capillary number, the droplet elongates more towards the flow direction. In the case of Ca=0.4, the tips of the droplet tilt towards the walls. This causes droplet not to be elliptical anymore and start to get a dumbbell shape. Figure 3.12 represents the evolution of droplet deformation of the mentioned cases with Ca=0.1, 0.2, 0.3 and 0.4. It is noticeable that by increasing the capillary number, the time required to reach the steady-state of the solution escalates. We believe the reason is due to lower surface tension for higher capillary numbers and hence, lower resistance of the droplet towards topological changes. This lower resistance leads to major changes in the deformation of the droplet, before reaching steady-state which requires more time. In this figure,

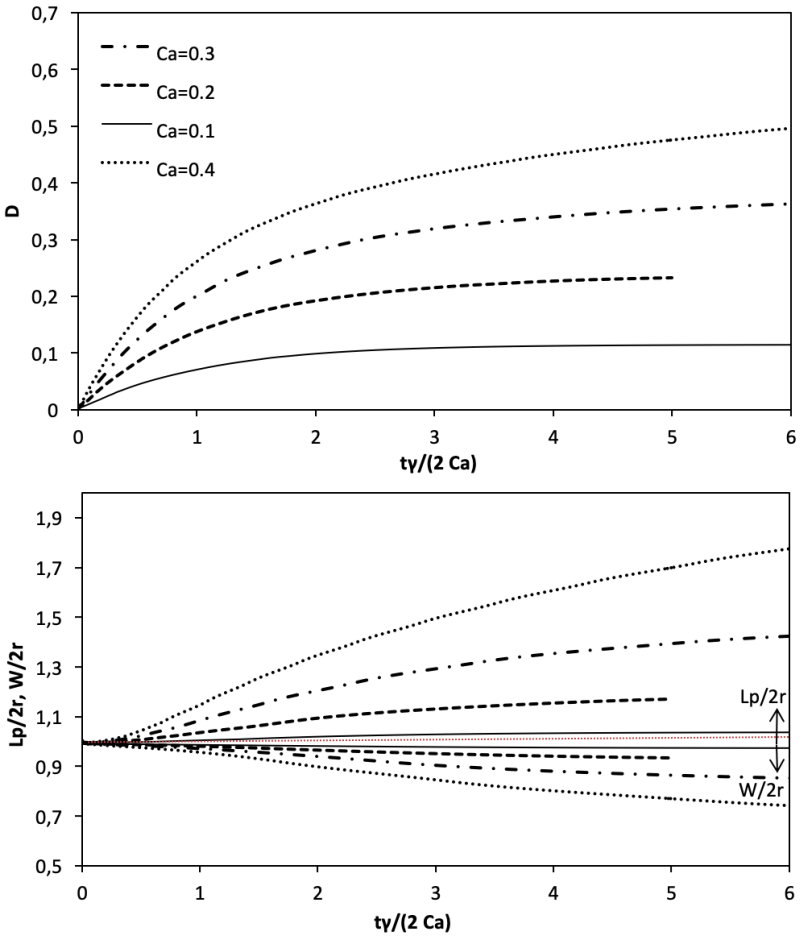

FIGURE 3.12: Startup variation of top: D and bottom: $L_p/2r$ and $W/2r$ parameters Vs. $t\dot{\gamma}/(2Ca)$ for subcritical cases with Re=0.0625 and λ=1. Cases with four different capillary numbers of 0.1, 0.2, 0.3 and 0.4 are tested.

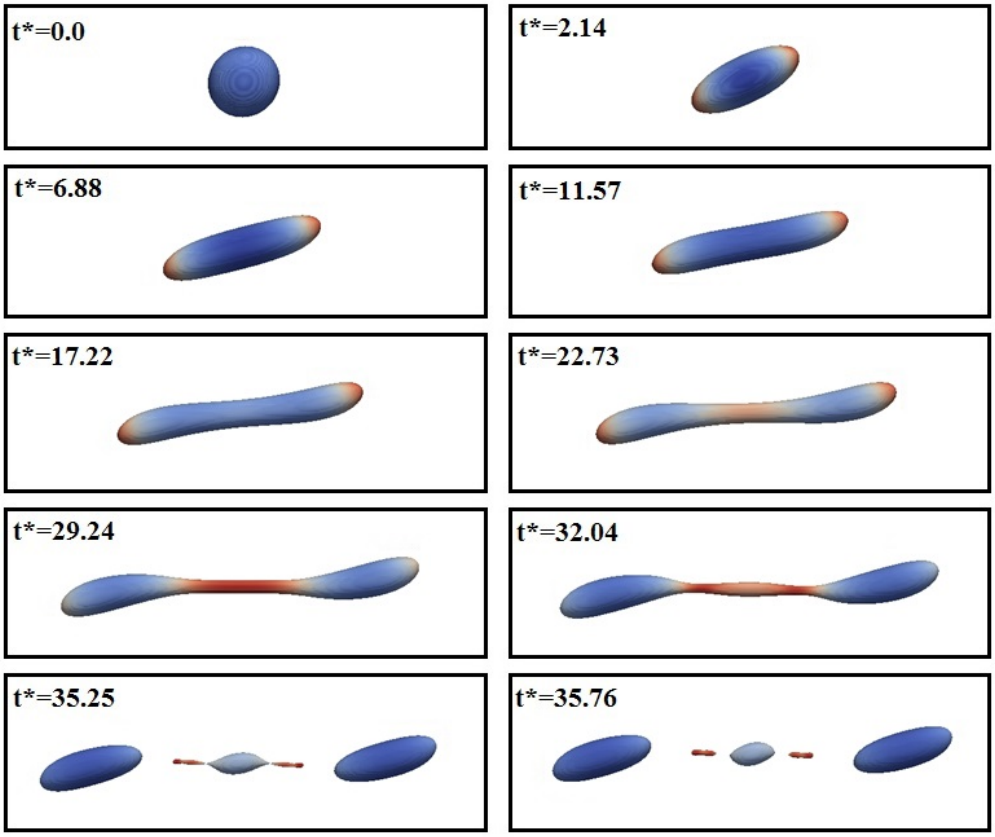

FIGURE 3.13: Evolution of droplet shape at Re=0.1, Ca=0.42 and λ=1, along with the pressure contours on the droplet surface, ($t^* = t\dot{\gamma}$)

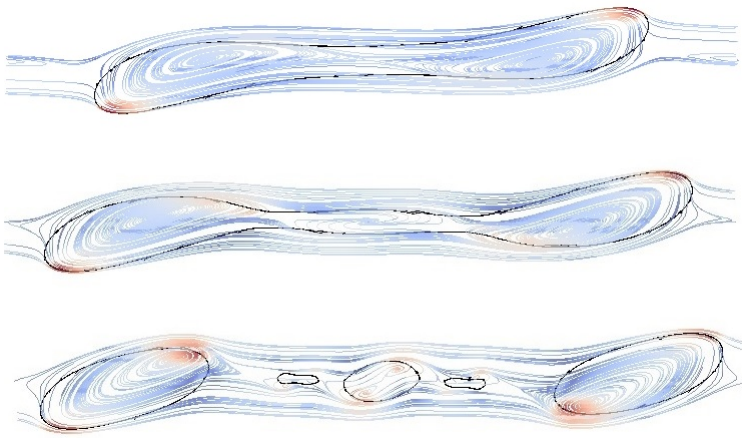

FIGURE 3.14: Evolution of the droplet shape and the flow pattern inside of the droplet, along with the vorticity magnitude contours all at $y = S_y/2$, for the case with Re=0.1, Ca=0.42 and λ=1. Snapshots are taken in times $t\dot{\gamma} = 25.20, 32.04$ and 35.76 (from top to bottom).

our simulation for Ca=0.4 has reached the steady-state after $t\dot{\gamma}$=20, but in order to avoid having a skewed graph, only the startup results until time $t\dot{\gamma}$=5 are shown.

According to the previous experimental, numerical and theoretical studies, in creeping flow conditions, when $\lambda < 4$, there is a critical capillary number (Ca_c) above which the droplet won't reach steady-state and continues to deform until breaks-up. The value of Ca_c is lowest for λ values roughly around 0.6 [148]. According to Rallison [111], this value is slightly less than Ca_c for $\lambda = 1$ which is around 0.41. As reported by Li, Renardy, and Renardy [130], in case of Ca=0.42, the droplet breaks into two daughter droplets, one satellite, and two sub-satellite droplets. In order to study the ability of the method on capturing the break-up, simulation with Ca=0.42, Re=0.1 and $\lambda = 1$ in a domain with $(S_x, S_y, S_z) = (12r, 4r, 8r)$ is carried out. This case is simulated long enough until the breakup of the droplet arose. The variation of droplet's shape in time is presented in figure 3.13. As expected, the droplet breaks-up into two daughters, one satellite in the middle and two sub-satellite droplets. The deformation starts by stretching of the droplet in flow direction forced by viscous shear stress of the flow. In this state, the droplet holds its elliptical shape (t*=0,2.14 and 6.88). Continuing on being imposed to the shear flow, the droplet then loses its elliptical shape, tips are tilted towards the walls and a waist starts to form in its center. The droplet stretches more

and gets longer in the flow direction while forming necks around its two tips. The stretching process continues until the waist gets thinner and necks cause an end pinching breakup into two daughter and one satellite droplets. Eventually, two sub-satellites depart from the satellite droplet. In this figure, the color contours imply the pressure on the surface of the droplet. In order to gain a better understanding of the breakup process, the final stages of the breakup of this case are illustrated in figure 3.14. This figure presents the cross-sectional profile of the surface of the droplet ($\phi = 0.5$) at three different times of $t\dot{\gamma}$=25.20, 32.04 and 35.76 along with the velocity streamlines and vorticity magnitude contours. According to this figure, at time $t\dot{\gamma}$=25.20, there are two visible vortices inside of the droplet elongated in the flow direction, each in one of the bulbous. As time passes to $t\dot{\gamma}$=32.04 and droplet evolves, a third vortex is formed inside of the waist of the droplet which is separated from the other two vortices by the necks. Towards the end, where the waist breaks into a satellite and two sub-satellite droplets, the vortex inside of it also divides into three vortices, one inside of each piece. The final shape at time $t\dot{\gamma}$=35.76 shows the existence of these five vortices inside of the daughter, satellite, and sub-satellite droplets.

3.6.3 The effect of Walls Confinement

In favor of studying the ability of the proposed method on capturing the effect of walls confinement on droplet deformation in subcritical regions, simulations with (Re, Ca, λ)=(0.1,0.3,1) and (0.1,0.1,1) are done in domains with different confinement ratios (2r/S_z). As reported by Renardy and Cristini [131], for the given Reynolds number of 0.1 and λ value of 1, capillary numbers of 0.1 and 0.3 are below the critical value (Ca_{cr}) which means the droplet must reach to a steady-state. Shapira and Haber [119] extracted the analytical expressions based on Lorentz's reflection method for droplet deformation in confined shear flow in small to moderate deformation regimes. They presented a first-order correction for the wall effect and claimed that the droplet shape was not altered compared to the unbounded shear flow but only the magnitude of deformation was increased.

The results of simulations of current study compared with the experimental data of Sibillo et al. [117] and analytical studies of Shapira and Haber [119] are presented in

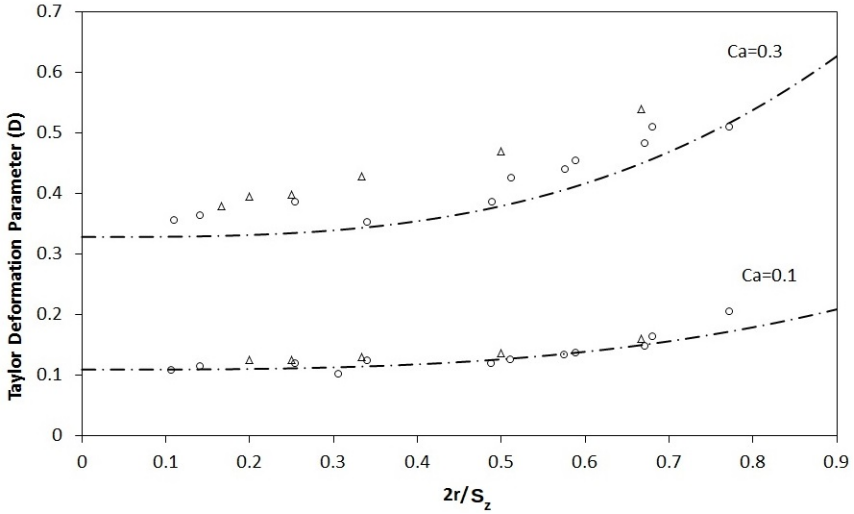

FIGURE 3.15: Taylor deformation parameter (D) for cases with Ca=0.1 and 0.3 with $\lambda = 1$ in different walls confinement ratios. Experimental data of Sibillo et al. [117] (○) and analytical data of Shapira and Haber [119] (dash dot lines) for Stokes flow regime, in comparison with results of current study for Re=0.1 (△)

figure 3.15. As can be seen in this figure, for both capillary numbers, Taylor deformation parameter (D) increases with increasing the walls confinement ratio ($2r/S_z$). In smaller capillary number (Ca=0.1) there is good agreement between analytical predictions of Shapira and Haber [119] and both experimental data of Sibillo et al. [117] and the results of current study. For cases with Ca=0.3, however, analytical predictions of Shapira and Haber [119] fails to predict the Taylor deformation parameter compared with experimental data of Sibillo et al. [117] and results of the present study. For all the cases, by decreasing the walls confinement ratio, the value of Taylor deformation parameter converges to a constant value.

In the next step, we study the startup behavior of a highly confined droplet with $2r/S_z = 0.83$, Ca=0.6, λ=0.32 and Re=0.0625 in a domain with $S_x = 16r$. As stated in Vananroye, Van Puyvelde, and Moldenaers [139], the critical capillary number for a case with λ=0.32, $2r/S_z$=0.83 and creeping flow condition is approximately equal to $(Ca_{cr} = 0.7)$. Thus for our intended case, we do not expect the breakup of the droplet.

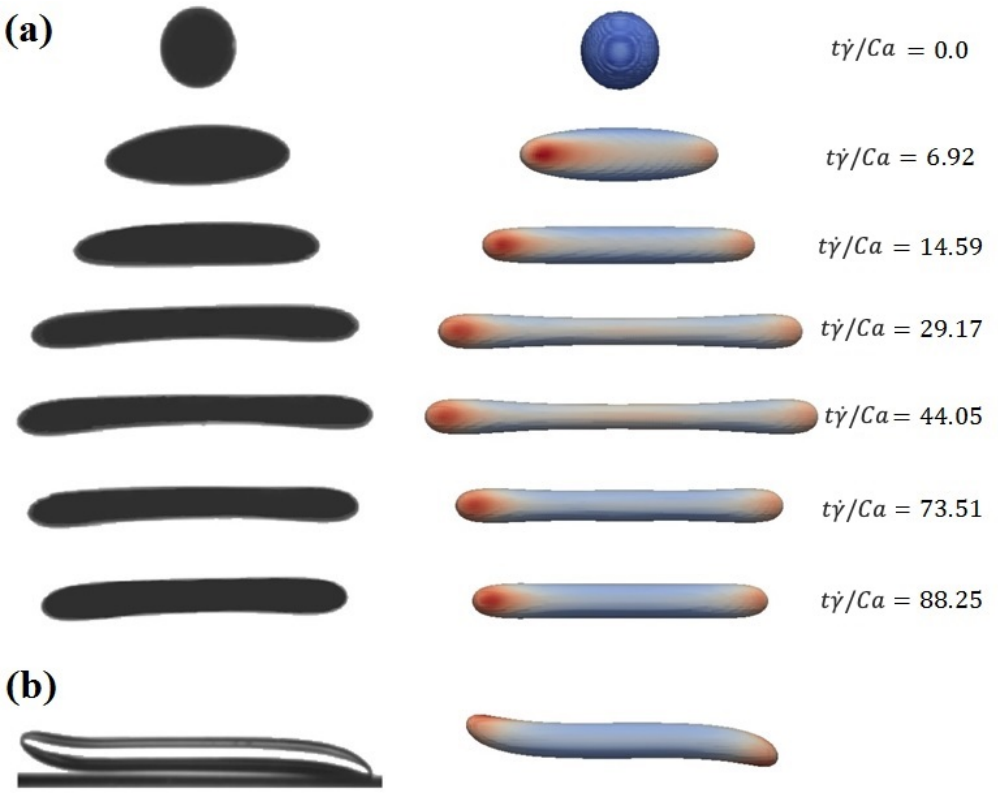

FIGURE 3.16: Time evolution of a highly confined droplet in creeping flow condition with $2r/S_z = 0.83$, $\lambda = 0.32$, and Ca=0.6, along with the pressure contours on the droplet's surface (right column) compared with experimental results of Vananroye et al. [149] (left column). (a): images taken in velocity-vorticity plane, (b): images taken in velocity-velocity gradient plane at $t\dot{\gamma}/Ca$=88.25

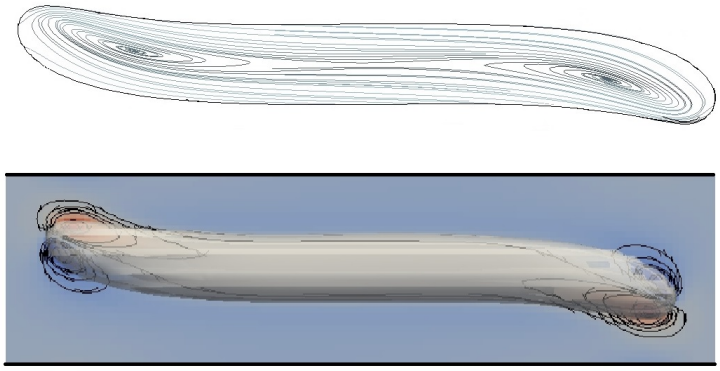

FIGURE 3.17: Top: Streamline contours inside of the droplet in x-z plane at $y = S_y/2$, Bottom: droplet shape along with the walls and vorticity contours ($e_y.\nabla \times \mathbf{v}$) in x-z plane at $y = S_y/2$. Both shapes illustrates a droplet in creeping flow conditions, with capillary number of 0.6, $\lambda = 0.32$, Reynolds number of 0.0625 and walls confinement ratio of $2r/S_z = 0.83$ at $t\dot{\gamma}/Ca$=88.25

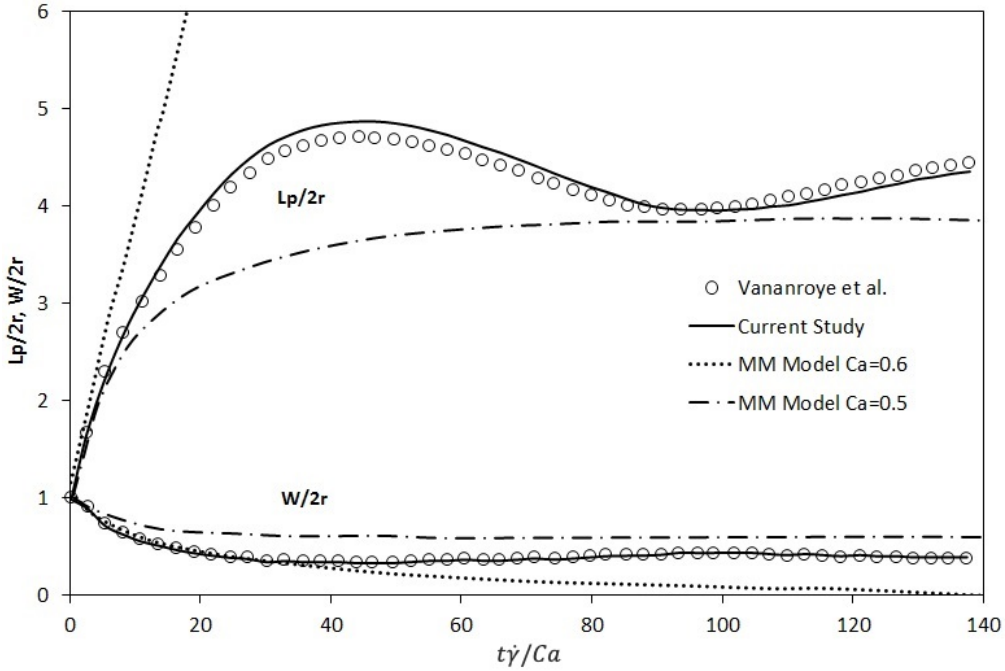

FIGURE 3.18: Startup behavior of a highly confined droplet with Re=0.0625, $2r/S_z = 0.83$, $\lambda = 0.32$, and Ca=0.6. compared with experimental results of Vananroye et al. [149] for creeping flow condition and confined MM model of Minale [124] for Ca=0.5, 0.6

Figure 3.16 illustrates the time evolution of the droplet in comparison with the same time instants of the experimental work of Vananroye et al. [149].

According to the figure 3.16(a), shortly after starting the simulation, the droplet starts to stretch in the flow direction. The stretching continues until the droplet reaches its maximum elongation at some time around $t\dot{\gamma}/Ca$=44, but instead of breaking up, the droplet retracts. According to figure 3.16(b), the central part of the droplet takes a cylindrical shape, oriented in the flow direction and the tips are tilted towards the walls giving the droplet a sigmoid shape. Figure 3.17 provides information about the streamline contours inside of the droplet and vorticity contours in $y = S_y/2$ plane. According to this figure, two vortices exist inside of the droplet which are stretched from the center of the droplet toward the tips.

Time variation of $W/2r$ and L_p/2r parameters, along with experimental data of Vananroye et al. [149] and analytical predictions of MM model Minale [124] are presented in figure 3.18. According to this figure, for the time around $t\dot{\gamma}/Ca \approx$44, the value of L_p/2r is maximum which is in agreement with information provided in figure 3.18. Also for the time around $t\dot{\gamma}/Ca \approx$95, the droplet starts to expand after reaching a local minimum length. It seems that these oscillations in the deformation of the droplet will last for a long time and reaching steady-state will take time much longer than the scale studied in this chapter ($t\dot{\gamma}/Ca =$140). It is worth mentioning that in this case a good agreement is seen between the experimental data and the results of current study. MM model of Minale [124] however fails to provide accurate information. In this model for Ca=0.6, the droplet continuously deforms until it breaks-up. For smaller capillary of 0.5, this model predicts a steady-state after $t\dot{\gamma}/Ca \approx$80 and does not predict any oscillations in the droplet deformation.

3.6.4 The effect of viscosity ratio

In order to study the accuracy of the method on a wider range of viscosity ratios, three simulations with viscosity ratios of λ=0.28, 1.2 and 1.9 all with Ca=0.2 and Re=0.1 are performed. The selected domain has walls confinement ratio of $2r/S_z = 0.73$. Figure 3.19 presents the startup transition of non-dimensionalized L and B parameters along with the experimental results of Vananroye et al. [149] and predictions of confined MM model of Minale [124]. It is clear to see that the startup transition of the droplets

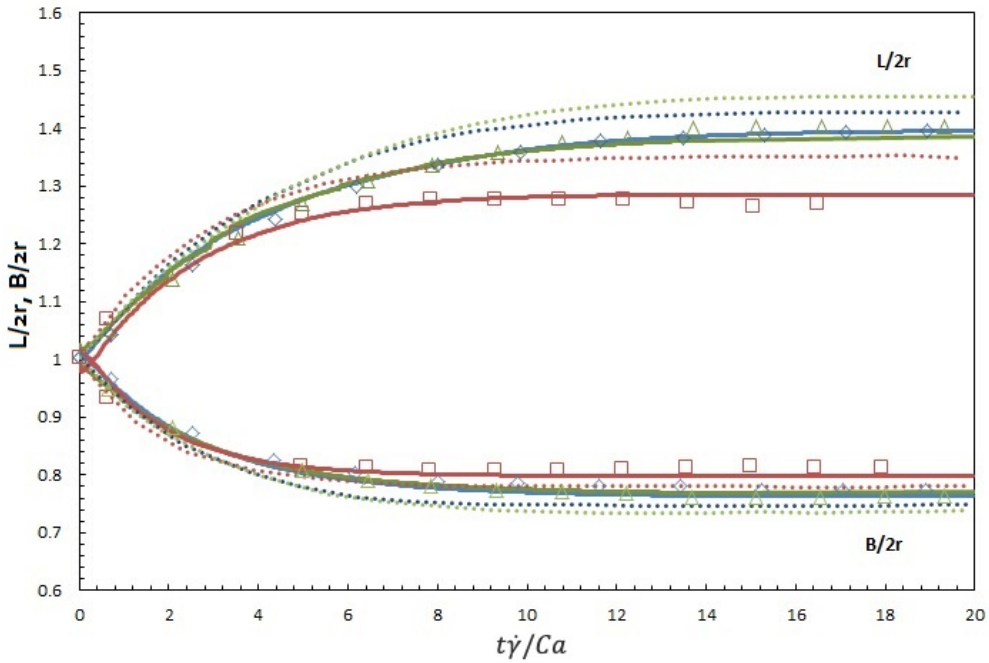

FIGURE 3.19: Effect of viscosity ratio on transition of droplet deformation for Ca=0.2 in a domain with confinement ratio of $2r/S_z = 0.73$. Comparison between extracted data from experimental results of Vananroye et al. [149] (symbols) and prediction of confined MM model of Minale [124] (dash lines) for creeping flow condition, along with the extracted results of current study (bold lines) for Re=0.1. Information in color red stand for $\lambda = 0.28$, color blue for $\lambda = 1.2$ and color green for $\lambda = 1.9$. The absolute time (t) is non-dimensionalized with characteristic emulsion time (τ).

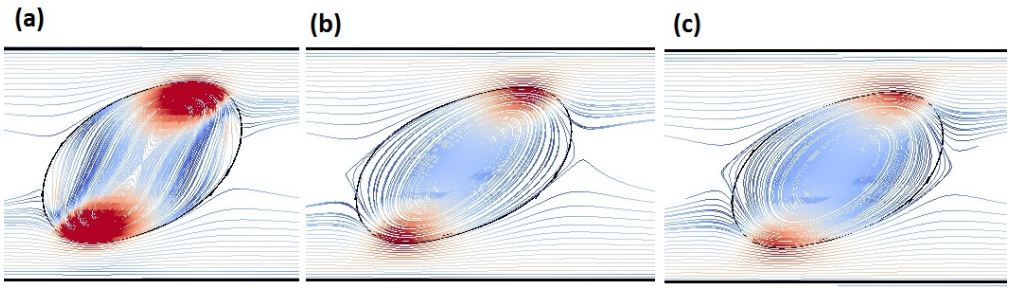

FIGURE 3.20: Cross sectional steady-state scheme of droplet in $y = S_y/2$, along with stream lines of the flow in different viscosity ratios of 0.28 (a), 1.2 (b) and 1.9 (c), for flow with Re=0.1 and Ca=0.2. All the simulations are done in a domain with $2r/S_z = 0.73$. The color contours presents the vorticity magnitude in aforementioned plane.

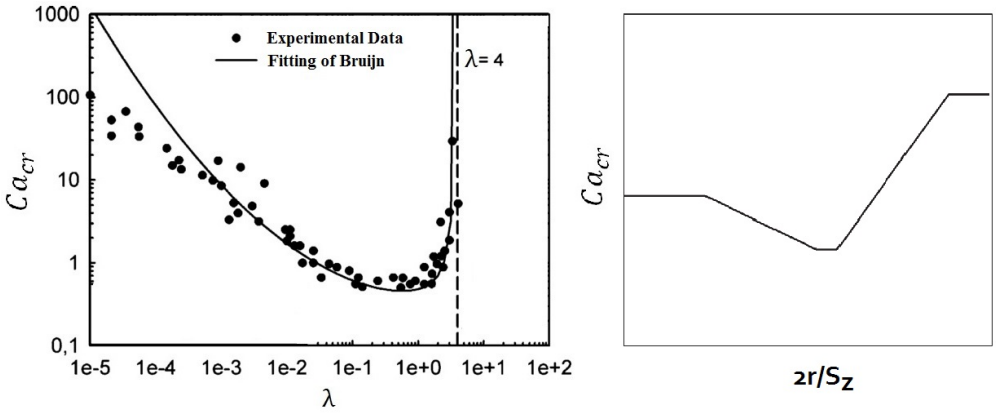

FIGURE 3.21: Left: Effect of viscosity ratio on droplet breakup in simple shear flow. Experimental data are extracted from Gace [148], Right: Schematic representation of the effect of walls confinment ratio on critical capillary number as presented in Janssen et al. [140]

in all three cases are similar, although approximately after $t\dot{\gamma}/Ca \approx 3$ the differences start. Good agreement is seen between experimental data and results extracted in this study. The MM model results also match the startup transition process predicted by experimental and numerical results. However, it over-predicts the deformation of the droplet for the rest of the simulations.

Figure 3.20 illustrates the cross-section of the droplet shape in x-z at $y = S_y/2$ plane at time $t\dot{\gamma}/Ca = 20$, along with the velocity streamlines and vorticity magnitude contours. According to this figure, for the case of $\lambda = 0.28$, there are two vortices inside of the droplet, but by increasing the viscosity ratio to 1.2 and 1.9, it decreases to one vortex. Also, the vorticity magnitude decreases by increasing the viscosity ratio. Since $\lambda = \mu_d/\mu_c$, smaller viscosity ratio means for a constant matrix viscosity, the droplet has lower viscosity, and hence lower resistance towards the gradual deformation. That justifies the bigger deformation in the flow pattern, two vortices and higher vorticity magnitude inside of the droplet with $\lambda = 0.28$.

3.6.5 The effect of viscosity ratio on walls critical confinement ratio

In previous sections, we validated the ability of our method on capturing the physics of problems with different walls confinements (section 3.6.3) and viscosity ratios (section

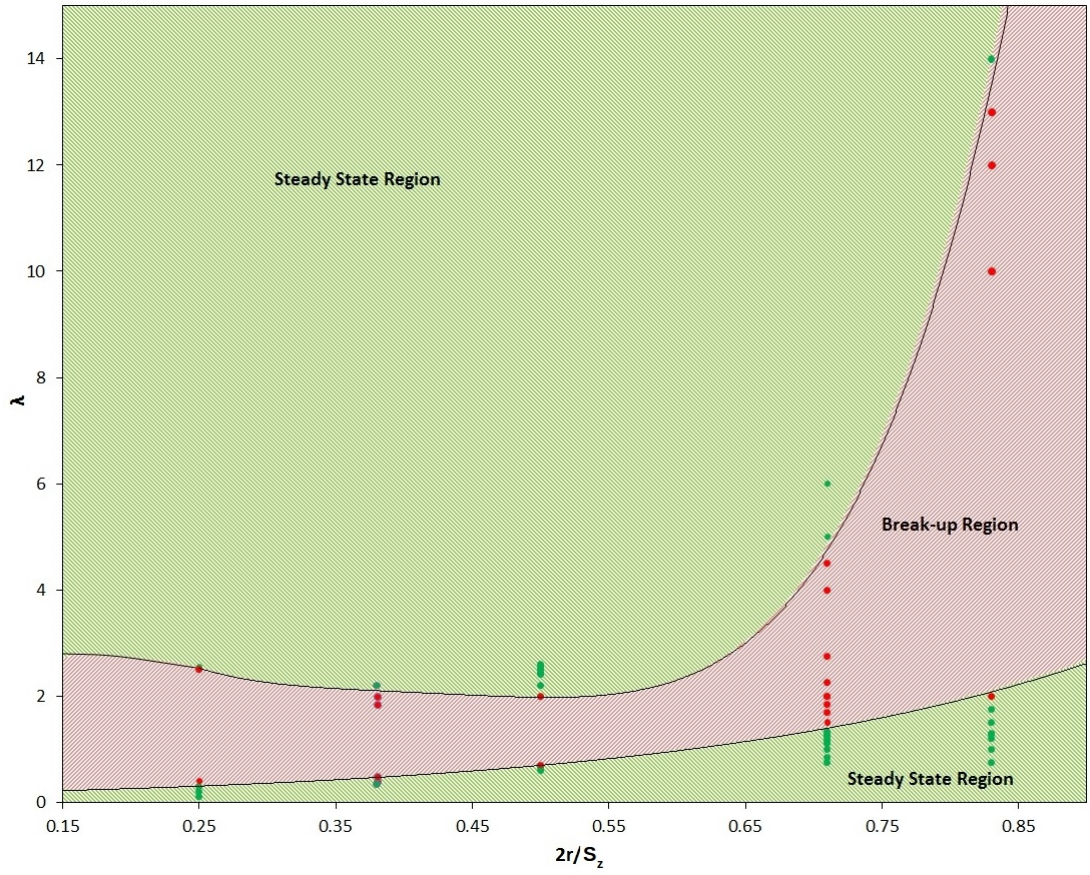

FIGURE 3.22: The effect of viscosity ratio on walls critical confinement ratio in steady-state deformation and breakup of the droplet, for given values of Ca=0.3 and Re=1.0 (The trend lines are added for the sake of clarity).

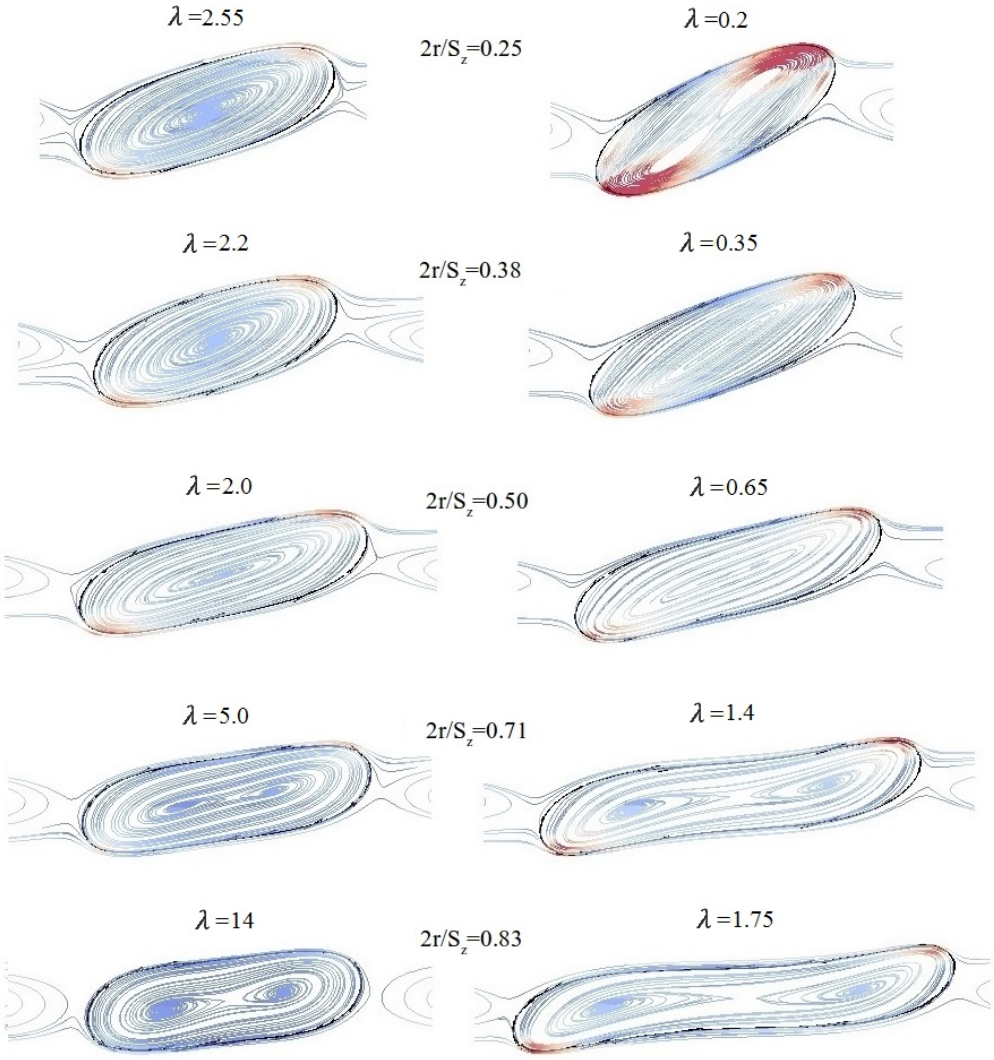

FIGURE 3.23: The steady-state droplet shape along with the streamlines of the flow inside of the droplet in $y = S_y/2$, for subcritical cases in higher steady-state region (left column), and subcritical cases in lower steady-state region (right column) in different confinement ratios. The color contours present the vorticity magnitude in the aforementioned plane.

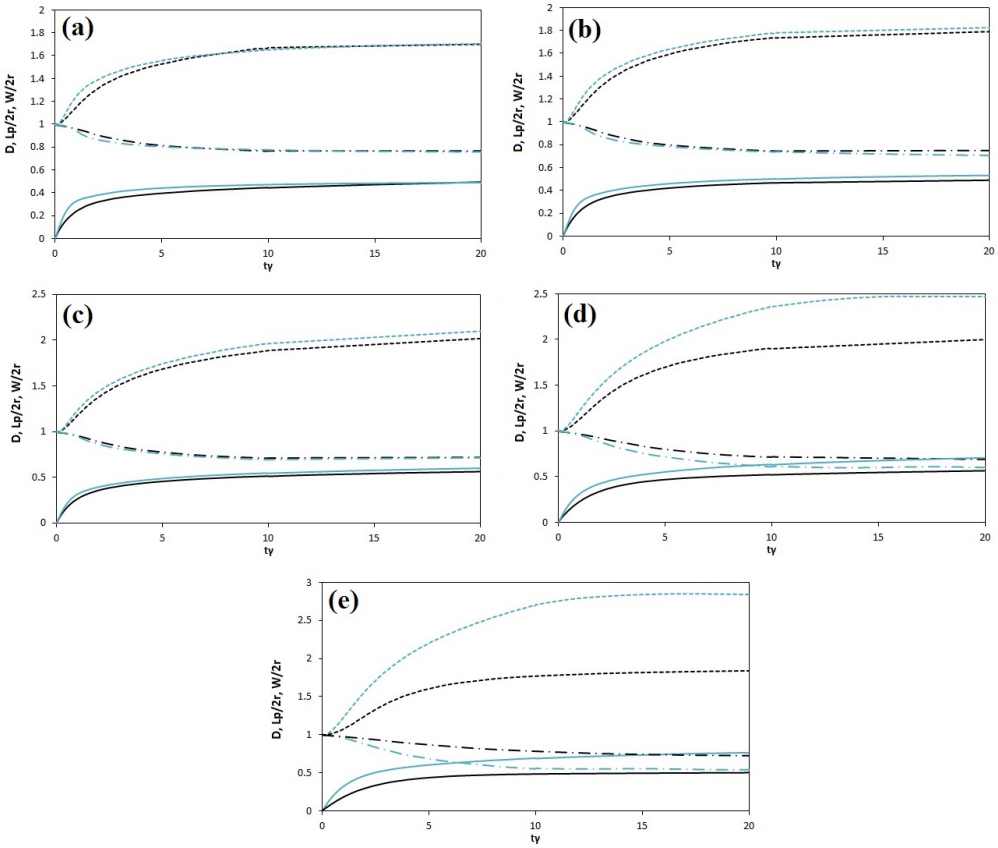

FIGURE 3.24: D (solid lines), $L_p/2r$ (dash lines) and $W/2r$ (dash dot lines) parameters Vs. t$\dot{\gamma}$ for subcritical cases of table 3.6. Black color lines are related to the results of λ_h and green color lines are related to the results of λ_l. $2r/S_z$= (a): 0.25, (b): 0.38, (c): 0.50, (d): 0.71 and (e): 0.83.

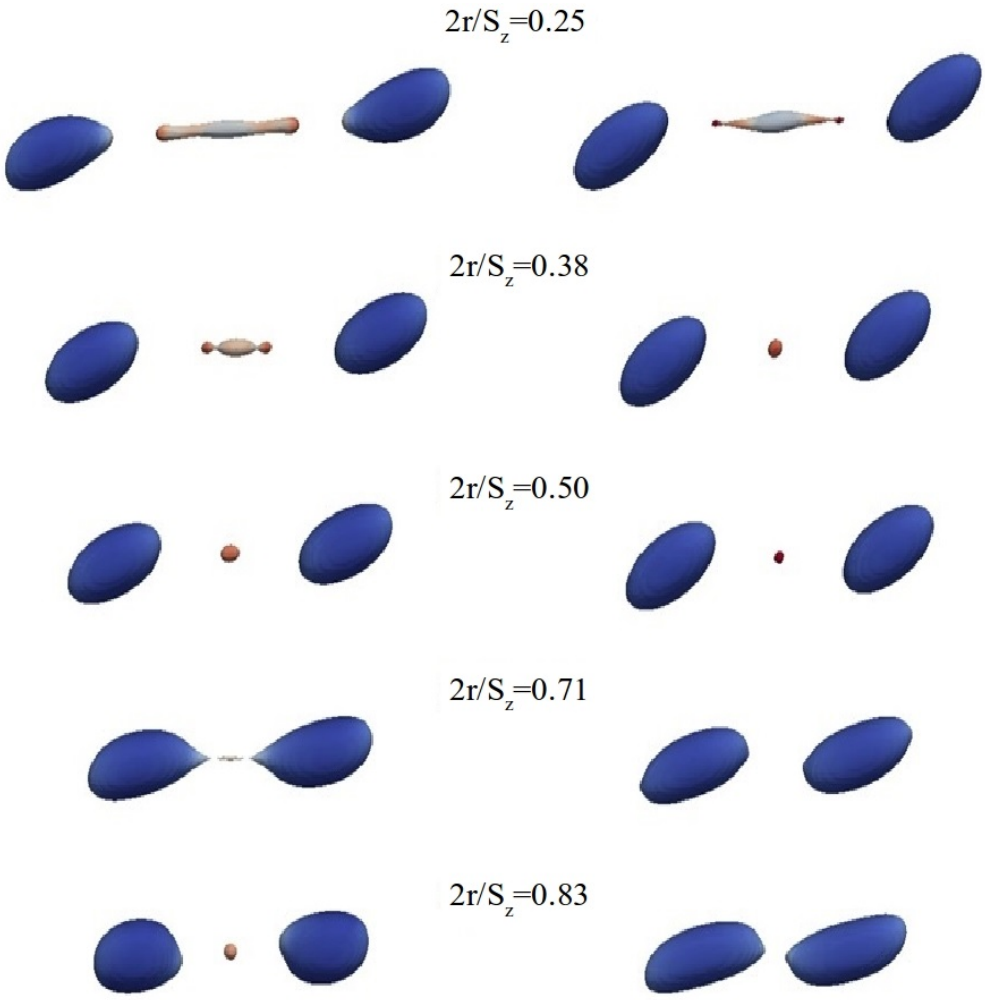

FIGURE 3.25: breakup of the droplet into daughter, satellite, and sub-satellite droplets for supercritical cases of table 3.6. The color contours are pressure on the droplet surface. The left column is related to droplet breakups of supercritical cases of the higher steady-state region. Right column is related to droplet breakups of supercritical cases of lower steady-state region.

TABLE 3.6: subcritical (sub) and supercritical (super) values of viscosity ratios for different walls confinement ratios along with the final values of D, θ, $L_p/2r$ and $W/2r$ for subcritical cases. l and h in λ stand for low and high as in each confinement ratio there are two values of λ_{cr}, one smaller than the other.

$2r/S_z$		λ_{sub}	λ_{super}	D	θ	$L_p/2r$	$W/2r$
0.25	λ_l	0.2	0.3	0.48	25.32	1.70	0.75
	λ_h	2.55	2.5	0.49	17.25	1.70	0.76
0.38	λ_l	0.35	0.4	0.53	21.64	1.82	0.74
	λ_h	2.2	2.0	0.49	17.52	1.79	0.75
0.50	λ_l	0.65	0.7	0.6	16.67	2.1	0.715
	λ_h	2.0	1.95	0.56	14.45	2.02	0.72
0.71	λ_l	1.4	1.5	0.7	11.16	2.47	0.6
	λ_h	5	4.5	0.56	11.03	2.0	0.69
0.83	λ_l	1.75	2.0	0.76	8.52	2.84	0.54
	λ_h	14	13	0.54	8.28	1.95	0.67

3.6.4). We realized that increasing the confinement ratio for subcritical cases increases the droplet deformation parameter (fig. 3.15) and for highly confined cases, induces retractions and expansions in the droplet which causes fluctuations in the deformation (fig. 3.18). We also noticed that by varying the viscosity ratio, the flow pattern inside of the droplet changes, as increasing the viscosity ratio from 0.28 to 1.2 decreased the number of internal vortices of the droplet from two to one, and also decreased the vorticity magnitude (fig. 3.20).

Gace [148] systematically studied the droplet breakup in simple shear flow as a function of viscosity ratio. These data are now known as Grace curve which is presented in figure 3.21 (left). In this figure, the values of λs which are above the fitted line prompt the breakup, while values of λ under it results in steady-state deformation of the droplet without breakup. According to this figure, for a constant capillary number bigger than the critical value, there are two critical viscosity ratios, one smaller than the other. For smaller critical viscosity ratio, increasing the λ will lead to breakup while for bigger critical viscosity ratios, decreasing the λ will lead to breakup. Simulations without the presence of confinement effect of walls, performed so far in this chapter, are in agreement with Grace curve. Our simulations in creeping flow condition presented in figure 3.10 ($\lambda = 1$, Ca=0.05, 0.1, 0.2, 0.3 and 0.4) as well as simulations

presented in figure 3.19 (Ca=0.2 and λ=0.28, 1.2 and 1.9), which all ended in steady-state deformation of the droplet, are in lower part of Grace curve (steady-state region) and simulation of figure 3.13 ($\lambda = 1$ and Ca=0.42), ended in breakup of the droplet, locates in the upper part of Grace curve (breakup region).

Despite the important information provided in this graph, the walls confinement effect is not taken into account. Figure 3.21 (right) illustrates the findings of Janssen et al. [140] on the effect of walls confinement ratio on critical capillary number. Despite the important information provided in this graph, the effect of different viscosity ratios is not taken into account. Although combined with the Grace curve, these two graphs provide essential information regarding the critical capillary number in different viscosity and walls confinement ratios; there is a need to specify the effect of viscosity ratio on the critical walls confinement ratio.

In this section, we study the effect of viscosity ratio on walls critical confinement ratio in droplet deformation and breakup for a constant capillary number of 0.3 and Reynolds number of 1.0. We perform a batch of simulations, where the walls confinement ratio and viscosity ratio of the droplet to the matrix are changed systematically. For each confinement ratio, we look for two values of critical viscosity ratios, one smaller than the other. Considering the conclusion of the Grace curve, for the lower critical viscosity ratio (λ_{cr}^{l}), decreasing the λ value will lead to steady-state deformation, and increasing the λ value will lead to the breakup of the droplet. Although for the higher critical viscosity ratio (λ_{cr}^{h}), we expect opposite behavior, as ascending from λ value is supposed to lead to steady-state deformation and descending from it is supposed to lead to breakup of the droplet.

In order to find the λ_{cr}^{l} and λ_{cr}^{h} as a function of $2r/S_z$, for each chosen value of walls confinement ratio, we were starting the simulation with arbitrary λs, searching for values where result in breakup of the droplet. We then gradually descend (ascent) from this value until simulation winds up in steady-state, with no breakup, to find λ_{cr}^{l} (λ_{cr}^{h}). This process was done for walls confinement ratios of $2r/S_z$=0.25, 0.38, 0.5, 0.71 and 0.83. A domain length of $S_x = 16r$ is used to guarantee that the droplet is not going to collide with its own image through periodic boundaries, and also to ensure an acceptable uniform velocity profile at the location of periodic boundaries. For each critical viscosity ratio found, there is one subcritical λ (λ_{sub}, leading to steady-state

deformation) and one supercritical λ (λ_{super}, leading to breakup). For the simulations performed, these values are extracted and presented in table 3.6 as well as steady-state values of D, θ, $L_p/2r$ and $W/2r$ for subcritical cases.

Figure 3.22 illustrates the data provided in table 3.6. In this figure, it is noticeable that two steady-state regions exist, one corresponding to λ values smaller than λ_{cr}^{l} (hereinafter refereed to as *lower steady-state* region) and another corresponding to λ values bigger than λ_{cr}^{h} (hereinafter refereed to as *higher steady-state* region). All the simulations in these two areas resulted in steady-state deformation of the droplet. In the area between these two regions, there is a breakup zone in which simulations in this area, resulted in the breakup of the droplet.

As mentioned before and as can be seen in the Grace curve (fig. 3.21), in creeping flow conditions without the effect of walls confinement, for λ values higher than 4, simulation always results in steady-state deformation. Although in our study, simulations with λ values as high as λ=13 ended-up in breakup. We believe this is associated with effect of walls confinement, even though slightly higher Reynolds number in our cases is affecting as well.

According to figure 3.22, in the *lower steady-state* region, by increasing the confinement ratio, the critical viscosity ratio monotonically increases. However, for the *higher steady-state* region, starting from $2r/S_z$=0.25, increasing the confinement ratio up to $2r/S_z \approx 0.45$, decreases the λ_{cr}^{h}, and after that, rapidly increases the λ_{cr}^{h}. The results of figure 3.22 combined with the Grace curve and the findings of Janssen et al. [140] provides important information on the role of viscosity ratio vs. critical walls confinement ratio, critical capillary number vs. viscosity ratio and critical capillary number vs. confinement ratio, respectively. These information are interesting and could be used to gain an understanding of the critical Grace number in different confinement ratios.

In order to gain a better understanding of the introduced graph, the steady-state shape of the droplet, streamlines of the flow inside of the droplet and the color contour of the vorticity magnitude all in x-z at $y = S_y/2$ plane for subcritical cases in different confinement ratios are presented in figure 3.23. In this figure, the left column corresponds to the subcritical cases of the *higher steady-state* region and right column corresponds to subcritical cases of the *lower steady-state* region. It is plain to see that

by increasing the confinement ratio, the droplet leans more towards the flow direction. This can be seen quantitatively in the data provided in table 3.6 in which for example in cases with $2r/S_z$=0.25, the value of inclination angle for subcritical cases in *lower and higher steady-state* regions are 25.32°and 17.25°, respectively. These values are bigger than the equivalent values in confinement ratio of $2r/S_z$=0.71 which are 11.16°and 11.03°. In all the cases in both *lower and higher steady-state* regions, by increasing the confinement ratio, the droplet stretches more in the flow direction and as a result, the width of the droplet decreases (see for example parameters $L_p/2r$ and $W/2r$ presented in table 3.6).

According to figure 3.23, and also information provided in table 3.6, in each confinement ratio, the value of inclination angle for subcritical cases in *lower steady-state* region is higher than the same parameter in *higher steady-state* region. In another word, in each confinement ratio, in subcritical cases, for viscosity ratios in the *lower steady-state* region, the droplet leans more towards the flow direction compared with the viscosity ratios in the *higher steady-state* region. Also in each confinement ratio, the $L_p/2r$ parameter which describes how much the droplet is stretched in the flow direction, for subcritical cases in the *lower steady-state* region is higher than subcritical cases in the *higher steady-state* region.

According to figure 3.23, for five cases, there are two vortices inside of the droplet, and for the rest, there are only one. The cases with two vortices inside of the droplet are ($2r/S_z$,λ)=(0.25, 0.2) and all the cases with $2r/S_z$=0.71 and 0.83. We suppose that for the case of ($2r/S_z$,λ)=(0.25, 0.2), this ratio (λ) is small enough to allow the existence of two vortices inside of the drop. For cases with $2r/S_z$=0.71 and 0.83, the existence of two vortices inside of the droplet could be linked to the effect of higher confinement ratios and the suppressing effect of the walls. In this figure, for cases in the *lower steady-state* region (right column of images), the vorticity magnitude is higher compared to the relative case in the *higher steady-state* region (left column of images). This could be associated with lower viscosity ratio of the cases of right column compared with the relative cases in the left column.

For cases introduced in figure 3.23, time-dependent changes of $L_p/2r$, $W/2r$ and D parameters are presented in figure 3.24. It is clear to see that simulations in these cases have reached steady-state over time. In this figure, for each confinement ratio, the

results of simulations with two viscosities of λ_l and λ_h are similar to each other, except for cases (d) and (e). In the case (d), the $L_p/2r$ parameter of the droplet in subcritical case of the *lower steady-state* region is approximately 23% more than its equivalent case in subcritical case of the *higher steady-state* region. In case (e) this difference in the $L_p/2r$ parameter between *lower and higher steady-state* regions increases to 45%. This difference which can be seen in figure 3.23 as well, could be associated with the bigger difference in λ values in subcritical cases compared with the other cases. For example, for subcritical cases in the domain with $2r/S_z$=0.71, the difference between λ^l_{sub} and λ^h_{sub} is 3.6, while this value for cases in domain with $2r/S_z$=0.50 is only 1.35.

Figure 3.25 illustrates the droplet breakup outcomes for supercritical cases mentioned in table 3.6 for different confinement ratios. According to this figure, figure 3.23 and information provided in table 3.6, eventhough for subcritical cases, by increasing the confinement ratio, droplet stretches more towards the flow direction, for the relative supercritical cases, by increasing the confinement ratio, the droplet stretches less before breaking-up. In another word, for smaller confinement ratios ($2r/S_z$=0.25, 0.38) the breakup mechanism is elongative end-pinching while increasing the confinement ratio changes this mechanism to mid-point-pinching.

3.7 Conclusions

A finite-volume conservative level-set based method was utilized to numerically simulate three-dimensional droplet deformation and breakup subjected to shear flow. A semi-implicit discretization approach was applied on momentum equation, enabling us to employ larger time-steps in low Reynolds number simulations. The results of Taylor deformation parameter and the inclination angle of the droplet for subcritical cases of creeping flow regime were extracted and compared with available experimental, numerical and analytical data. The ability of the method on capturing the breakup of the droplet was examined by simulating the supercritical case of creeping flow regime. The effect of walls confinement on droplet deformation in subcritical and near-critical regions was extracted and compared with available experimental and analytical data. The observed fluctuations in deformation of the droplet for the near-critical highly confined case were in agreement with the experimental data. The effect of viscosity ratio

on droplet deformation in subcritical cases was studied and the results were compared with available experimental and analytical data. In all the cases, a very good agreement was seen between the results extracted in the current study and the data available on literature. To further study the deformation and breakup of the droplet in shear flow, the effect of viscosity ratio on walls critical confinement ratio was studied. We found out that for each confinement ratio, there are two critical viscosity ratios. These two viscosity ratios create two steady-state regions and one breakup region between them. We further analyzed these regions by studying the droplet deformation and breakup parameters in these zones.

The insights gained from the research in this chapter on the effect of viscosity ratio on walls critical confinement ratio provide a clear roadmap to steady-state and breakup regions of droplets in shear. This information is valuable in more effective design of future droplet-based microfluidic devices, reactive dispersions, emulsification process, morphology development of blends and Lab-on-a-Chip systems for individual purposes with methods discussed in this chapter, namely, by adjusting the viscosity or confinement ratios of the existing shear flow to the appropriate values to control the droplet volume. For example, the provided information on the existence and relation of two steady-state and one breakup regions can be used to quantify emulsions stability by analyzing the droplet size spectrum in the emulsion.

Acknowledgments

This work has been financially supported by the *Ministerio de Economía y Competitividad, Secretaría de Estado de Investigación, Desarrollo e Innovación*, Spain (ENE2015-70672-P). I acknowledge the financial support of an FI research scholarship by the *Agència de Gestió d'Ajuts Universitaris i de Recerca (AGAUR) of Generalitat de Catalunya* (2016 FI_B 01059). I thankfully acknowledge the computer resources at Altamira and the technical support provided by Instituto de Física de Cantabria - Universidad de Cantabria (RES-FI-2018-3-0045).

Chapter 4

A numerical approach for non-Newtonian two-phase flows using a conservative level-set method

Abstract. A finite-volume based conservative level-set method is presented to numerically solve the non-Newtonian multiphase flow problems. One set of governing equations is written for the whole domain, and different phases are treated with variable material and rheological properties. Main challenging areas of numerical simulation of multiphase non-Newtonian fluids, including tracking of the interface, mass conservation of the phases, small timestep problems encountered by non-Newtonian fluids, numerical instabilities regarding the high Weissenberg Number Problem (HWNP), instabilities encouraged by low solvent to polymer viscosity ratio in viscoelastic fluids and instabilities encountered by surface tensions are addressed and proper numerical treatments are provided in the proposed method. The numerical method is validated for different types of non-Newtonian fluids, e.g. shear-thinning, shear-thickening and viscoelastic fluids using structured and unstructured meshes. The proposed numerical solver is capable of readily adopting different constitutive models for viscoelastic fluids to different stabilization approaches. The constitutive equation is solved fully coupled with the flow equations. The method is validated for non-Newtonian single-phase flows against the analytical solution of start-up Poiseuille flow and the numerical solutions of well-known lid-driven Cavity problem. For multiphase flows, impact of a viscoelastic droplet problem, non-Newtonian droplet passing through a contraction-expansion, and Newtonian/non-Newtonian drop deformation suspended in Newtonian/non-Newtonian matrix imposed to shear flow are solved, and the results are compared with the related analytical, numerical and experimental data.

4.1 Introduction

A Newtonian fluid is a fluid in which the viscous stresses emerging from its flow, are linearly proportional to the local rate of change of its deformation over time. Non-Newtonian fluid, on the other hand, does not obey this rule, and in most of the cases, its viscosity is dependent on shear-rate itself or its history. Most of the fluids found in either nature or industry are non-Newtonian, e.g. blood, proteins, slurries, polymers, suspensions, emulsions, chemical reactants etc. [7]. These types of fluids usually show many exceptional characteristics, for example, shear-thinning, shear-thickening,

viscoelasticity, etc. Non-Newtonian fluids have extensive applications in a variety of fields, e.g. biochemical, food, pharmaceuticals and petrochemical industries [150].

The most common type of time-independent non-Newtonian fluids are shear-thinning (or pseudoplastic), in which their apparent viscosity decreases with increasing shear rate. The shear-thickening fluids, on the other hand, are known as fluids in which their apparent viscosity increases with the shear-rate. Because of the specific characteristics, of shear-thinning and shear-thickening fluids (STF), they are used widely in different engineering applications, e.g. energy absorbers, vibration controllers, safety protectors, pharmaceutical and food industries [151–153]

Viscoelastic fluids, however, exhibit both viscous and elastic characteristics under typical flow conditions, as encountered for instance in polymer and food processing industries. While viscous liquids strain uniformly when a stress is applied, elastic solids strain instantaneously. Consequently, viscoelastic fluids exhibit time-dependent strain, i.e. when a stress is applied, their strain approaches its equilibrium value on a time-scale which is a characteristic of the fluid [150, 154].

In many of the mentioned applications, there exists a moving interface, separating two immiscible non-Newtonian fluids. For instance, the bubble behaviour in non-Newtonian fluids has vast number of applications in diverse fields, e.g., decompression sickness, volcanic eruption, glass manufacture, metallurgy, wastewater treatment, handling and processing of fermentation broths, polymer devolatilization, bubble columns, mechanical stirrers with multiphase flows, composites processing, plastic foam processing, multiphase reactors, etc. For example in different multiphase reactors of gas-liquid, fluidized bed, trickle bed, and slurry reactors used in many biochemical applications, fluids may exhibit non-Newtonian behavior [8]. A direct consequence of this behaviour is a significant change in the characteristics of the process [150, 155]. Thus, the development of accurate numerical tools for the simulation of non-Newtonian multiphase flows is vital from both fundamental and practical points of view. Different approaches are used in literature in order to develop numerical tools to solve non-Newtonian multiphase flow problems.

In the context of Marker-And-Cell (MAC) method, Tomé et al. [156] used a MAC-finite difference (FD) approach, employing a projection method to study the non-Newtonian droplet impact problem. Oishi et al. [157] used this method to study the

jet-buckling problem of viscoelastic fluids. Tome and McKee [158] proved the ability of their updated MAC method on capturing physical instabilities regarding the buckling of planar jets.

In the context of front-tracking interface capturing method, Mukherjee and Sarkar [135] used this method to study the deformation of a viscoelastic droplet in a Newtonian matrix under shear flow. Ferreira and Trierweiler [159] used this method to solve the motion of deformable bubbles in non-Newtonian fluids. They have used various Generalized Newtonian Fluid (GNF), and viscoelastic models to study the rule of matrix rheology on droplet rising problem. Aggarwal and Sarkar [160] used this approach to study the deformation of a Newtonian/viscoelastic droplet suspended in a viscoelastic matrix applied to shear flow. They elaborately studied the elastic and viscous stresses at the interface, polymer orientation, and the elastic and viscous forces in the solution domain to investigate their effect on droplet deformation.

In the context of Smoothed Particle Hydrodynamics (SPH) method, Fang et al. [161] and Jiang et al. [162] and Rafiee, Manzari, and Hosseini [163] used this technique to study the impacting problem of a viscoelastic droplet on a surface and also the buckling problem of a viscoelastic jet. Zainali et al. [164] presented an incompressible SPH method with an improved interface treatment procedure enabling them to model multiphase flow problems with the density and viscosity ratios up to 1000 and 100 respectively.

In the context of lattice Boltzmann method (LBM), Wagner, Giraud, and Scott [165] developed a new LBM to solve two-phase flow of viscoelastic liquid mixtures. They used this new approach to simulate a bubble rising in a viscoelastic fluid and were able to reproduce the experimentally observed cusp shape at the trailing end of the bubble. Frank et al. [166] presented a multiscale approach to describe the dynamics of a chain of bubbles rising in non-Newtonian fluids using the particle image velocimetry (PIV) and the LBM simulations. Wang, Liu, and Zhang [167] presented a multiple-relaxation-time colour-gradient lattice Boltzmann model and used it to solve the deformation and breakup of a confined droplet in shear flow with power-law rheology. It was demonstrated that their model could accurately solve power-law fluids with a broad range of indices. Gupta and Sbragaglia [168] used a numerical approach based on a combination of LBM and FD schemes to study the break-up of Newtonian/viscoelastic

droplets in a viscoelastic/Newtonian matrix imposed to confined shear flow. Sun et al. [169] used a LBM to study the non-Newtonian flow effects on the internal mixing subsequent to coalescence of initially stationary droplets.

In the context of volume of fluid (VOF) method, Lunkad, Buwa, and Nigam [170] used this approach to study the viscoelastic droplet impact problem over horizontal and inclined surfaces. Favero et al. [171] used this method embedded in OpenFoam package to study internal viscoelastic multiphase flow problems. Bonito, Picasso, and Laso [172] used a projection method to study the die-swell problem. Sun et al. [173] used this method to study the minimum in-line coalescence height of bubbles generated from a submerged nozzle in Carboxymethyl cellulose sodium (CMC) non-Newtonian aqueous solution. Torkkeli [174] used this approach to solve the dynamics of multiple horizontal bubbles rising from different orifice arrangements in a shear-thinning matrix employing a power-law GNF model. Moraga et al. [175] investigated the dam break problems of non-Newtonian fluids with applications in the sudden collapse of mine tailings, snow avalanches, debris and lava flows, and casting solidification by adopting a Carreau-Yasuda model [176]. Premlata et al. [177] used this model to study the dynamics of an air bubble rising in a non-Newtonian shear-thinning/shear-thickening matrix. Focke and Bothe [94] adopted an extended VOF method to investigate the binary droplet collisions at high Weber numbers. Abishek, King, and Narayanaswamy [178] used the VOF method imbedded in OpenFOAM package to study the dynamics of a Taylor bubble in the steady and pulsatile co-current flow of Newtonian and shear-thinning liquids in a vertical tube. Araújo, Miranda, and Campos [179] employed this method to investigate the Taylor bubbles rising through flowing non-Newtonian inelastic fluids.

In the context of Level-set method (LSM), Yu, Sakai, and Sethian [180] used a LSM based finite difference algorithm to solve viscoelastic ink ejection problem coupled with an equivalent circuit model to calculate the inflow pressure. Tezduyar et al. [181] used a Convected LSM to study the viscoelastic fluid buckling problem. Prieto [182] presented a particle LSM implemented using the Finite Element Method (FEM) and semi-Lagrangian schemes to perform stochastic, micro-macro simulations of droplets rising in non-Newtonian fluids. Pillapakkam et al. [183] used a finite-element solver based on the LSM to perform direct numerical simulations (DNS) of

the transient and steady-state motion of bubbles rising in a viscoelastic matrix. Their report depicted a more clear image on volume jump discontinuity phenomena in viscoelastic matrices.

Despite all the advances in the numerical simulation of non-Newtonian multiphase flows, this area is still a challenging topic regarding the difficulties related to the tracking of the interfaces, mass conservation of the phases, numerical instabilities regarding the high Weissenberg number problem (HWNP), instabilities encouraged by low solvent to polymer viscosity ratio in viscoelastic fluids and instabilities encountered by surface tensions. Therefore, the development of numerical methods capable of dealing with the aforementioned challenges in numerical simulations of multiphase non-Newtonian fluids is very demanding. Although previous efforts have been performed in the framework of front tracking, SPH, LBM, VOF, and standard LS methods, there are no previous works using the conservative level-set method [24, 184]. Therefore, objectives of this work are twofold: first to introduce a novel methodology to accurately solve multiphase flow problems in which the droplet and/or matrix represent non-Newtonian behaviour using the CLS method, integrated with numerical tools tackling aforementioned challenges, and second to use the implemented framework to study the influence of non-Newtonian rheology in droplet deformation. The present approach is numerically stable for High Weissenberg numbers and low solvent to polymer viscosity ratios. In the present CLS method, interface normals are computed using a least-squares method on a wide and symmetric nodes-stencil around the vertexes of the current cell [24]. These normals are then used for an accurate computation of surface tension, without additional reconstruction of the distance function, as in geometrical volume-of-fluid/level-set methods [25] or fast-marching methods. Moreover, most of the computational operations are local, which permit an efficient implementation on parallel platforms [30]. The CLS method has been designed for general unstructured meshes [24]. Indeed, the grid can be adapted to any domain, enabling for an efficient mesh distribution in regions where interface resolution has to be maximized, which is difficult by using structured grids. Furthermore, TVD flux-limiter schemes [24] are used to discretize convective terms, avoiding numerical oscillations around discontinuities, whereas the numerical diffusion is minimized. Finally, the present finite-volume formulation is attractive due to the satisfaction of the integral forms of the conservation

laws over the entire domain.

The rest of the chapter is organized as follows: mathematical formulations are presented in section 4.2, numerical discretization of governing equations are described in section 4.3. Special considered treatments for the main challenges of small time-step of the simulation encountered by non-Newtonian fluids, high Weissenberg number problem (HWNP), singularities of non-viscoelastic regions and low viscosity ratio problem (LVRP) are provided in sections 4.3.1, 4.3.2, 4.4.1 and 4.4.2, respectively. Numerical experiments and discussion are reported in section 4.7 and at the end, conclusion remarks are discussed in section 4.8.

4.2 Mathematical formulation

Navier-Stokes equations are used to describe the conservation of mass and momentum of two incompressible immiscible fluids on a spacial domain Ω with boundary $\partial\Omega$ as following [1, 24]:

$$\frac{\partial}{\partial t}(\rho\mathbf{v}) + \nabla\cdot(\rho\mathbf{v}\mathbf{v}) = -\nabla p + \nabla\cdot\tau + \rho\mathbf{g} + \sigma\kappa\mathbf{n}\delta_\Gamma \text{ in } \Omega \tag{4.1}$$

$$\nabla\cdot\mathbf{v} = 0 \text{ in } \Omega \tag{4.2}$$

where ρ is density of the fluid, $\mathbf{v}$ is the velocity field, $\mathbf{p}$ is the pressure field, $\mathbf{g}$ is the gravitational acceleration, τ is the stress response to the deformation of the fluid, δ_Γ is the Dirac delta function concentrated at the interface (Γ), $\mathbf{n}$ is the unit normal vector outward to interface, κ is the interface curvature and σ is the interface tension coefficient. In this formulation, the stress response τ is decomposed with the solvent-polymer stress splitting technique into a purely viscous term of τ_s corresponding to the instantaneous response of the solvent, and τ_p corresponding to the polymeric contribution of stress response:

$$\tau = \tau_s + \tau_p \tag{4.3}$$

where the solvent part, τ_s, is defined as below:

$$\tau_s = \mu_s(\dot{\gamma})\left(\nabla\mathbf{v} + (\nabla\mathbf{v})^T\right) \tag{4.4}$$

In this formulation, $\mu_s(\dot{\gamma})$ is the apparent viscosity of the fluids described in the context of generalized Newtonian fluid (**GNF**) models, with $\dot{\gamma}$ as shear-rate tensor of the fluid defined as:

$$\dot{\gamma} = \nabla \mathbf{v} + (\nabla \mathbf{v})^T \tag{4.5}$$

In this chapter, power-law **GNF** model is used to describe the relation of apparent viscosity of μ_s with shear-rate tensor of $\dot{\gamma}$ as below:

$$\mu_s(\dot{\gamma}) = K|\dot{\gamma}|^{m-1} \tag{4.6}$$

where $|\dot{\gamma}|$ is magnitude of the shear-rate tensor outlined as $|\dot{\gamma}| = \sqrt{(\dot{\gamma} : \dot{\gamma})/2}$, K is the consistency constant and **m** is the power-law index. The power-law **GNF** model is able to describe *shear-thinning* (pseudo-plastic) behaviour for $m < 1$, *shear-thickening* (Dilatant) behaviour for $m > 1$ and Newtonian behaviour for $m = 1$.

The polymeric stress tensor of equation 4.3 is written as:

$$\tau_p = \frac{\mu_p}{\lambda_1} f_s(c) \tag{4.7}$$

where λ_1 is the relaxation time of the viscoelastic fluid, μ_p is the polymeric viscosity, $f_s(c)$ is a strain function depending on the constitutive model and expressed in terms of the conformation tensor, **c**. This tensor is an internal tensorial variable representing the macromolecular configuration of the polymeric chains. Independent of the kinetic theory, conformation tensor by definition is *symmetric positive definite* and is equal to the identity matrix $\boldsymbol{I}$ when the polymer chain is at the equilibrium. The basic mechanism for stress build-up and relaxation is governed by a differential equation of the conformation tensor and a relaxation function of $f_r(c)$ that depends on the constitutive model as follows:

$$\frac{Dc}{Dt} = \nabla \mathbf{v}^T \cdot c + c \cdot \nabla \mathbf{v} - \frac{1}{\lambda_1} f_r(c) \tag{4.8}$$

Constitutive model	$f_s(c) = f_r(c)$
Oldroyd-B	$c - I$
FENE-P	$\frac{L^2-3}{L^2-tr(c)}c - I$
FENE-CR	$\frac{c-I}{1-tr(c)/L^2}$

TABLE 4.1: Strain and relaxation functions of three widely used viscoelastic constitutive models.

where Dc/Dt is the material derivative defined as:

$$\frac{Dc}{Dt} = \frac{\partial c}{\partial t} + \mathbf{v} \cdot \nabla c \tag{4.9}$$

The implementation of any constitutive equations is straight forward. The $f_s(c)$ and $f_r(c)$ functions of three widely used constitutive equations are defined in table 4.1. In this table, L is the ratio of the length of a fully extended polymer dumbbell to its equilibrium length, and $tr(c)$ is the first invarient of the conformation tensor $\boldsymbol{c}$. The summation of μ_s and μ_p of the fluid is defined as total viscosity and denoted as $\mu_0 = \mu_s + \mu_p$. The ratio of μ_s to μ_0 is defined as viscosity ratio of viscoelastic fluid also known as retardation ratio and denoted as, $\beta = \mu_s/\mu_0 \leq 1$.

The density, solvent and polymeric viscosities (μ_s and μ_p), and relaxation time are defined as scalar-fields inside the whole domain as follows:

$$\zeta = \zeta_1 H + \zeta_2 (1 - H) \tag{4.10}$$

where $\zeta \in \{\rho, \mu_s, \mu_p, \lambda_1\}$ and H is the Heaviside step function which takes the value one in dispersed phase and zero elsewhere.

In this research, conservative level-set (CLS) method [82], as introduced by Balcazar et al. [24] in the context of Newtonian fluids is used to track the interface. Instead of the signed distance function, d(x,t), used to represent the interface in the classical LS method, conservative LS method employs a regularized indicator function ϕ as below:

$$\phi(x,t) = \frac{1}{2}\left(tanh\left(\frac{d(x,t)}{2\varepsilon}\right) + 1\right) \tag{4.11}$$

where ε is the parameter that sets the thickness of the interface. ϕ varies from 0 in one

fluid to 1 in other fluid. With this formulation, interface is defined by $\Gamma = \{x|\phi(x,t) = 0.5\}$.

The level-set function is advected by velocity vector field, $\mathbf{v}$, provided from solution of Navier-Stokes equations. Since the velocity field is solenoidal ($\nabla \cdot \mathbf{v} = 0$), the interface transport equation can be written in conservative form [24, 82]:

$$\frac{\partial \phi}{\partial t} + \nabla \cdot \phi \mathbf{v} = 0 \tag{4.12}$$

Since sharp changes exist in level set function at the interface, Superbee flux limiter scheme is used in discretization of the convective term in order to minimize numerical diffusion and to avoid numerical instabilities at the interface. To keep the profile and thickness of the interface constant, an additional re-initialization equation [1, 88] is used:

$$\frac{\partial \phi}{\partial \tau} + \nabla \cdot \phi \left(1 - \phi\right) \mathbf{n}_{\tau=0} = \nabla \cdot \varepsilon \nabla \phi \tag{4.13}$$

which is advanced in pseudo-time τ. This equation consists of a compressive flux: $\phi(1-\phi)\mathbf{n}_{\tau=0}$ and a diffusion term: $\nabla.\varepsilon\nabla\phi$. The first one keeps the level-set function compressed onto the interface along the normal vector $\mathbf{n}$, and the second one keeps the profile in prescribed characteristic thickness of ε. This parameter is defined based on the mesh resolution as [24]:

$$\varepsilon_p = C_\varepsilon h^{1-\alpha} \tag{4.14}$$

where $h = (V_P)^{1/3}$ is the grid's characteristic length with V_P as the cell's volume. In all the simulations of this chapter, C_ε is constant and equal to 0.5. parameter α, however, varies in order to change the thickness of the interface and can take values between [0,0.1], to overcome the possible numerical instabilities. Normal vector $\mathbf{n}$ on the interface and curvature κ of the interface, are obtained using [24]:

$$\mathbf{n} = \frac{\nabla \phi}{||\nabla \phi||} \tag{4.15}$$

$$\kappa(\phi) = -\nabla \cdot \mathbf{n} \tag{4.16}$$

The continuous surface force model (CSF) [83] is used for surface tension computation which converts the term $\sigma\kappa\mathbf{n}\delta_\Gamma$ in Eq. 4.1 to a volume force term as follows [24]:

$$\sigma\kappa\mathbf{n}\delta_\Gamma = \sigma\kappa(\phi)\nabla\phi \tag{4.17}$$

where $\nabla\phi$ is computed using least-square method based on vertex node stencils. By applying this approach, the explicit tracking of the interface is not necessary.

4.3 Numerical method

Finite-volume (FV) approach is used for the spatial discretization of transport equations on a collocated grid [24], so all the computed variables are stored at centroids of the cells, including viscoelastic constitutive equations introduced in this work. A central difference (CD) scheme is used to discretize the compressive term of re-initialization equation (4.13) and diffusive fluxes at the faces. A distance-weighted linear interpolation is used to calculate the face values of physical properties and interface normals. The gradients are computed at the cell centroids using the least-squares method. A total-variation Diminishing (TVD) Superbee flux limiter is used to discretize the convective term as implemented in [24], in order to improve the numerical stability of the solver [1]. At discretized level, physical properties are regularized in the context of the CLS method. Therefore a linear average is used for density, viscosities (μ_s and μ_p) and relaxation time as $\zeta = \zeta_1\phi + \zeta_2(1-\phi)$, where $\zeta \in \{\rho, \mu_s, \mu_p, \lambda_1\}$. A classical fractional step projection method as described by [84] is used to solve the velocity-pressure coupling. In the rest of this section, the main challenges and difficulties of numerical simulations of non-Newtonian multiphase flow problems are addressed and the most prominent solution for each problem is being suggested and implemented into the solution procedure. Although none of these approaches completely solves the problem, they push the stability limits of numerical simulations of non-Newtonian flows to a higher limit.

4.3.1 Small time-step of the simulation

The allowable time step of the simulation is calculated by taking into account the CFL conditions on convective and diffusive terms and also by explicit treatment of surface tension. For this reason, in each cell the values of allowable times step are calculated as:

$$\Delta t_{conv} \equiv \alpha \times \left(\frac{h}{\|V_P\|} \right) \tag{4.18}$$

$$\Delta t_{visc} \equiv \alpha \times min \left(\frac{h^2 \rho(\phi)}{\mu_p(\phi)}, \frac{h^2 \rho(\phi)}{\mu_s(\phi, \dot{\gamma})} \right) \tag{4.19}$$

$$\Delta t_{cap} \equiv \alpha \times \left(h^{3/2} (\frac{\rho_1 + \rho_2}{4\pi\sigma})^{1/2} \right) \tag{4.20}$$

where α is CFL coefficient. The final global value of time step is the minimum of Δt_{conv}, Δt_{visc} and Δt_{cap} in the whole domain. The difficulty of the small time-step problem arises specially in the solution of non-Newtonian shear-thinning/shear-thickening fluids, where the varying value of viscosity can increase dramatically, leading to a very small timestep resulting in huge computational costs. To circumvent this issue, diffusion term could be treated implicitly. So we suggest a second-order implicit Crank-Nicolson scheme to be used to discretize the solvent part, τ_s of the stress term τ of equation 4.1 where the $\mu_s(\dot{\gamma})$ can take unexpectedly high values. A second-order Adams–Bashforth scheme is used on convective, gravity, surface tension and the polymeric part, τ_p, of the stress term τ as below:

$$\frac{\rho \mathbf{v}^* - \rho^n \mathbf{v}^n}{\Delta t} = \frac{3}{2}(R_h^v)^n - \frac{1}{2}(R_h^v)^{n-1} + \frac{1}{2}\left(\mathbf{D}_{hs}(\mathbf{v}^*) + \mathbf{D}_{hs}(\mathbf{v}^n)\right) - \nabla_h p^n \tag{4.21}$$

where $R_h^v = -\mathbf{C}_h(\rho\mathbf{v}) + \rho\mathbf{g} + \sigma\kappa\nabla_h(\phi) + \mathbf{D}_{hp}(\mathbf{v})$, $\mathbf{D}_{hp}(\mathbf{v}) = \nabla_h \cdot \tau_p$ and $\mathbf{D}_{hs}(\mathbf{v}) = \nabla_h \cdot \tau_s$ with $\mathbf{C}_h(\rho\mathbf{v}) = \nabla_h \cdot (\rho\mathbf{v}\mathbf{v})$ as the convective operator. In this equation, ∇_h represent the gradient operator.

A term of pressure gradient of previous time step is added to the discretized form of equation 4.1. Pressure-velocity coupling is solved by using a fractional-step projection method [84, 185], as follows:

- A correction to the predicted velocity applies as:

$$\frac{\rho \mathbf{v}^{n+1} - \rho \mathbf{v}^{*}}{\Delta t} = -\nabla_h \pi^{n+1} \tag{4.22}$$

- Poisson equation reads as follows and is solved using a preconditioned conjugated gradient method.:

$$\nabla_h \cdot \left(\frac{1}{\rho} \nabla_h (\pi^{n+1}) \right) = \frac{1}{\Delta t} \nabla_h \cdot (\mathbf{v}^{*}) \tag{4.23}$$

- The velocity $\mathbf{v}^{n+1}$ is corrected and pressure is update as:

$$\mathbf{v}^{n+1} = \mathbf{v}^{*} - \frac{\Delta t}{\rho} \nabla_h (\pi^{n+1}) \tag{4.24}$$

$$\mathbf{p}^{n+1} = \mathbf{p}^{n} + \pi^{n+1} \tag{4.25}$$

4.3.2 High Weissenberg Number Problem (HWNP)

Stiff hyperbolic nature of the constitutive equations make them prone to the numerical instabilities in numerical solution process which can lead to a blowup of the numerical values. It arises when the Weissenberg number (or equivalently the Deborah number) of the problem reaches a critical value. Weissenberg number is defined as the ratio of elastic forces to the viscous forces of the problem. It can be variously defined, but it is usually given by the relation of the value of λ_1 of the fluid and a specific characteristic time of the problem. HWNP is being linked to loss of positive definiteness of the conformation tensor [186]. This critical value varies in different problems and depends on the nature of the flow, spacial discretization and numerical algorithm. According to Fattal and Kupferman [187] and Hulsen, Heel, and Brule [188] and Lee et al. [189], the loss of positive-definiteness of the conformation tensor is the trigger to HWNP. Moreover, according to Renardy [190], solution of viscoelastic fluids tend to have stress boundary layers with large variation in stress gradients and exponential stress profiles near geometrical singularities. According to Fattal and Kupferman [191] and Hulsen, Fattal, and Kupferman [192], under resolution of these spatial stress profiles can cause numerical instabilities as well.

Therefore, several stabilization techniques have been developed to ensure the positive-definiteness of the conformation tensor. The most prominent stabilization approaches used in the context of finite-volume method are *the positive definiteness preserving scheme* (PDPS) of Stewart et al. [193] *the square-root conformation representation* (SRCR) of Balci et al. [194] and *the log-conformation tensor representation* (LCR) of Fattal and Kupferman [187, 191]. Chen et al. [186] Provided a detailed analysis on comparison of these approaches for finite-volume simulation of viscoelastic single-phase flows regarding their implementation complexity, stability, accuracy, efficiency and applicability to complex problems.

The log-conformation representation method of Fattal and Kupferman [187, 191] is among the most robust stabilization approaches for this problem. This method uses a matrix-logarithm change of variable of conformation tensor. In addition to positive-definiteness preserving characteristic of this method, since it linearizes the exponential stress profiles, it improves the resolution of large stress gradients. In this study we use this method to deal with the HWNP. Since we believe that literature lacks a comprehensive description of derivation of this method for the constitutive model of form of equation 4.8, we represent a detailed description of its derivation in section 4.4. Using this method, and considering the conformation tensor equation with the form of equation 4.8, implementing the log-conformation representation formulation for different viscoelastic constitutive equations is straight-forward. It is merely required to specify the strain and relaxation functions of the considered constitutive equation, the rest of the solution procedure will be identical.

For regular problems with Weissenberg numbers smaller than the critical values, in order to save-up on computational costs, the standard formulation (SF) of equation 4.8 with a first order backward Euler discretization approach could be used as below:

$$c^n = c^{n-1} + \Delta t \left[-\mathbf{v} \cdot \nabla c + \nabla \mathbf{v}^T \cdot c + c \cdot \nabla \mathbf{v} - \frac{1}{\lambda_1} f_r(c) \right]^{n-1} \tag{4.26}$$

In this case, the eigendecomposition of the conformation tensor **c** will not be required and hence computational costs will be decreased while maintaining the numerical stability of the simulations.

4.4 Derivation of formulation of Log-conformation representation method

We can consider the formulation for the eigendecomposition of the positive-definite tensor of $\mathbf{c}$ in three-dimensional space as $\mathbf{c} = \mathbf{R}\boldsymbol{\Lambda}\mathbf{R}^T$ with $\mathbf{R}$ as the orthogonal matrix containing the eigenvectors of $\mathbf{c}$ and $\boldsymbol{\Lambda}$ as a diagonal matrix containing the corresponding eigenvalues. By substituting the $\mathbf{c} = \mathbf{R}\boldsymbol{\Lambda}\mathbf{R}^T$ in equation 4.8 and defining $L := \nabla\mathbf{v}$, we will have:

$$\frac{DR}{Dt}\boldsymbol{\Lambda}R^T + R\frac{D\boldsymbol{\Lambda}}{Dt}R^T + R\boldsymbol{\Lambda}\frac{DR^T}{Dt} = R\boldsymbol{\Lambda}R^T L + L^T R\boldsymbol{\Lambda}R^T - \frac{1}{\lambda_1}f_r(R\boldsymbol{\Lambda}R^T) \tag{4.27}$$

Multiplying R^T and R into this equation from left and right, respectively, will result in:

$$\begin{aligned} R^T\left[\frac{DR}{Dt}\boldsymbol{\Lambda}R^T + R\frac{D\boldsymbol{\Lambda}}{Dt}R^T + R\boldsymbol{\Lambda}\frac{DR^T}{Dt}\right]R \quad &= \\ R^T\left[R\boldsymbol{\Lambda}R^T L + L^T R\boldsymbol{\Lambda}R^T - \frac{1}{\lambda_1}f_r(R\boldsymbol{\Lambda}R^T)\right]R \end{aligned} \tag{4.28}$$

Defining the skew-symmetric matrix of $\tilde{\Omega} := R^T\frac{DR}{Dt}$ and matrix of $\tilde{L} := R^T LR$ and substituting them in 4.28, will result in:

$$\tilde{\boldsymbol{\Omega}}\boldsymbol{\Lambda} + \boldsymbol{\Lambda}\tilde{\boldsymbol{\Omega}}^T + \frac{D\boldsymbol{\Lambda}}{Dt} = \boldsymbol{\Lambda}\tilde{L} + \tilde{L}^T\boldsymbol{\Lambda} - \frac{1}{\lambda_1}R^T f_r(R\boldsymbol{\Lambda}R^T)R \tag{4.29}$$

In this equation, the first two terms in the left hand side ($\tilde{\boldsymbol{\Omega}}\boldsymbol{\Lambda} + \boldsymbol{\Lambda}\tilde{\boldsymbol{\Omega}}^T$) are skew-symmetric and while $\frac{D\boldsymbol{\Lambda}}{Dt}$ is a diagonal matrix. As a result, the off-diagonal elements of the resultant matrix of right hand side of equation 4.29 will be equal to $\tilde{\boldsymbol{\Omega}}\boldsymbol{\Lambda} + \boldsymbol{\Lambda}\tilde{\boldsymbol{\Omega}}^T$ and diagonal elements of it will be equal to $\frac{D\boldsymbol{\Lambda}}{Dt}$. From this notion, the values of $\tilde{\boldsymbol{\Omega}}$ and $\frac{D\boldsymbol{\Lambda}}{Dt}$ will be obtained as:

$$\left(\frac{D\boldsymbol{\Lambda}}{Dt}\right)_{ii} = 2\Lambda_{ii}\tilde{L}_{ii} - \frac{1}{\lambda_1}\left(R^T f_r(R\boldsymbol{\Lambda}R^T)R\right)_{ii}, \quad \text{for i} \in \{1,2,3\} \tag{4.30}$$

$$\tilde{\Omega}_{ij} = \frac{\Lambda_{ii}\tilde{L}_{ij} + \tilde{L}_{ji}\Lambda_{jj} - \frac{1}{\lambda_1}\left(R^T f_r(R\boldsymbol{\Lambda}R^T)R\right)_{ij}}{\Lambda_{jj} - \Lambda_{ii}}, \qquad \text{for i} \neq \text{j} \tag{4.31}$$

As mentioned before, the log-conformation representation method uses a change of variable in the constitutive model in term of the matrix-logarithm of the conformation tensor as below:

$$\mathbf{\Psi} = \mathrm{Ln}\,\mathbf{c} = R\,\mathrm{Ln}\mathbf{\Lambda}\,R^T \tag{4.32}$$

Keeping in mind the definition of $\tilde{\Omega} := R^T \frac{DR}{Dt}$, and applying the material derivative operator to left and right hand sides of above equation, we will have:

$$\frac{D\mathbf{\Psi}}{Dt} = R\left[\left(\tilde{\mathbf{\Omega}}\,\mathrm{Ln}\mathbf{\Lambda} + \mathrm{Ln}\mathbf{\Lambda}\,\tilde{\mathbf{\Omega}}^T\right) + \frac{D\mathbf{\Lambda}}{Dt}\mathbf{\Lambda}^{-1}\right]R^T \tag{4.33}$$

Since $\frac{D\Lambda}{Dt}\mathbf{\Lambda}^{-1}$ is a diagonal matrix, and $(\tilde{\mathbf{\Omega}}\,\mathrm{Ln}\mathbf{\Lambda} + \mathrm{Ln}\mathbf{\Lambda}\,\tilde{\mathbf{\Omega}}^T)$ is a skew-symmetric matrix, with the help of equations 4.30 and 4.31, their values could be extracted as:

$$\left(\frac{D\mathbf{\Lambda}}{Dt}\mathbf{\Lambda}^{-1}\right)_{ii} = 2\tilde{L}_{ii} - \frac{1}{\lambda_1\Lambda_{ii}}\left(R^T f_r(R\mathbf{\Lambda}R^T)R\right)_{ii}, \text{for i } \in \{1,2,3\} \tag{4.34}$$

$$\begin{aligned}\left(\tilde{\mathbf{\Omega}}\,\mathrm{Ln}\mathbf{\Lambda} + \mathrm{Ln}\mathbf{\Lambda}\,\tilde{\mathbf{\Omega}}^T\right)_{ij} = \\ \tilde{\Omega}_{ij}\left(\mathrm{Ln}\Lambda_{jj} - \mathrm{Ln}\Lambda_{ii}\right) = \\ \left[\frac{\Lambda_{ii}\tilde{L}_{ij} + \tilde{L}_{ji}\Lambda_{jj} - \frac{1}{\lambda_1}\left(R^T f_r(R\mathbf{\Lambda}R^T)R\right)_{ij}}{\Lambda_{jj} - \Lambda_{ii}}\right]\left(\mathrm{Ln}\Lambda_{jj} - \mathrm{Ln}\Lambda_{ii}\right), \text{for i} \neq \text{j}\end{aligned} \tag{4.35}$$

For the sake of clarity, we define some extra variables as below:

$$\begin{aligned}\tilde{G} &= R^T f_r(R\mathbf{\Lambda}R^T)R & G &= R\tilde{G}R^T \\ \tilde{L} &= R^T L R & L &= \nabla\mathbf{v} \\ \tilde{B} &= \text{Diagonal matrix of}(\tilde{L}) & B &= R\tilde{B}R^T\end{aligned}$$

Using these variables, and definitions of equations 4.34 and 4.34, and taking into account that $\Lambda^{-1} = R^T e^{-\Psi} R$, the equation 4.33 could be written as:

$$\frac{D\mathbf{\Psi}}{Dt} = \mathbf{\Omega\Psi} - \mathbf{\Psi\Omega} + 2B - \frac{1}{\lambda_1} Ge^{-\mathbf{\Psi}} \tag{4.36}$$

This tensorial equation is discretized in time using a first order Euler scheme as:

$$\mathbf{\Psi}^n = \mathbf{\Psi}^{n-1} + \Delta t \left[-\mathbf{v}\cdot\nabla\mathbf{\Psi} + \mathbf{\Omega\Psi} - \mathbf{\Psi\Omega} + 2B - \frac{1}{\lambda_1} Ge^{-\mathbf{\Psi}} \right]^{n-1} \tag{4.37}$$

By having the new values of $\mathbf{\Psi}$, the new value of conformation tensor $\mathbf{c}$ can be recovered by matrix-exponential operator of $\mathbf{\Psi}$ as:

$$c = e^{\mathbf{\Psi}} \tag{4.38}$$

It is important to note that matrix-logarithm and matrix-exponential operators used in this section are tensor operators where the logarithm and the exponents are applied to the eigenvalues of the tensor.

4.4.1 Singularities of non-Viscoelastic regions

In the problems with viscoelastic/Newtonian interface, one-field formulation represented in section 4.2 leads to singularities where the value of relaxation time λ_1 is equal to zero in the Newtonian fluid causing numerical solution process to diverge. One solution to this problem would be to use the semi-analytical method (SAM) proposed by Sarkar and Schowalter [195]. Unlike the LCR approach, this method does not require any eigendecomposition and as a result imposes lower computation cost, however it does not circumvent the HWNP. In this method, the constitutive equation 4.8 is re-written as:

$$\lambda_1 \frac{\partial c}{Dt} + c = \Xi(t) \tag{4.39}$$

where Ξ is:

$$\Xi = c - f_r(c) - \lambda_1 \left(\mathbf{v}\cdot\nabla c - \nabla\mathbf{v}^T \cdot c - c\cdot\nabla\mathbf{v} \right) \tag{4.40}$$

Assuming a constant Ξ during the timestep of Δt, equation 4.39 could be integrated in time from $t = n-1$ till $t = n$, resulting in:

$$c^n = c^{n-1} e^{-\Delta t/\lambda_1} + \Xi^{n-1}\left(1 - e^{-\Delta t/\lambda_1}\right) \tag{4.41}$$

This formulation is consistent everywhere, including non-viscoelastic fluid regions with zero relaxation time ($\lambda_1 = 0$). The disadvantage of non-circumventing the HWNP prevents this method to be used thoroughly.

Another solution for this problem would be to utilize a cut-off value in the solution process. In this method, in each iteration, cells with $\lambda_1 > \varepsilon$ are being identified, and being updated to a list. The constitutive equation 4.8, independent of the formulation (Standard formulation or LCR) is being solved only in cells of this list.

Since SAM method does not circumvent the HWNP, and since the cut-off approach can be integrated with LCR formulation, in this study we use the cut-off approach in order to deal with the singularities of non-viscoelastic regions in one-field formulation of governing equations. To make sure of the accuracy of the results of this method, we perform two-dimensional simulations of deformation of a droplet in a simple-shear flow with both SAM and cut-off approaches. The results are extracted and compared with reference data of Chinyoka et al. [196] for different combinations of viscoelastic/Newtonian droplet in a viscoelastic/Newtonian matrix. These results along with the simulation details are presented in 4.5. According to these data, the results of cut-off approach is in complete agreement with the results of SAM and reference data of Chinyoka et al. [196]. Hence, in this study, the proposed cut-off approach with the value of $\varepsilon = 0.005$ is being used. The results have shown to be independent of the value of ε, as long as $\varepsilon \leq 0.005$.

4.4.2 Low viscosity ratio problem (LVRP)

A stability problem occurs when viscosity ratio β is relatively small. According to Amoreira and Oliveira [197], this problem causes the instabilities in numerical iterative methods to occur at lower Weissenberg numbers and impose an unbearable small timestep to the simulation. Comparing different formulations of viscoelastic fluids, Amoreira and Oliveira [197] proposed an approach named *Explicit diffusion (EDIF)*,

lately known as *both-sides diffusion* (BSD) approach. Chen et al. [186] mentioned that for single-phase lid-driven cavity test case, for a small viscosity ratio of $\beta = 0.0014$, the HWNP occurs at a small Weissenberg number of 0.1, and even with different stabilization approaches of PDPS, LCR and SRCR, this problem lingers. However, Chen et al. [186] mentioned that BSD approach can lift the HWNP to almost the same critical Weissenberg numbers as possible for large viscosity ratios. As a result they believe this method (BSD) can be used along with other stabilization approaches to cope with Low viscosity ratio instability problem. In this approach the constitutive equation is not reformulated, but additional diffusion term is added and subtracted from momentum equation, one treated implicitly and the other evaluated explicitly. The implicitly treated additional diffusive term contributes to the *ellipticity* of the problem and improves the stability of the solution in cases of LVRP.

In order to analyze this problem, and since it originates in the momentum equation and not the constitutive model, we have studied the performance of different discretizations of momentum equation on providing a stable solution in the context of fractional-step projection method for a LVRP of a two-dimensional lid-driven cavity test case. Five different discretizations of Forward Euler (**FE**), Backward Euler (**BE**), 2nd order Adams-Bashforth (**AB**), both side diffusion (**BSD**), and Semi-Implicit form as eq. 4.21 for predictor step of momentum equation are tested. The details of this study are provided in 4.6. According to this test, the Semi-Implicit discretization of predictor step of momentum equation with the form of eq. 4.21 outperforms other methods, including BSD, and is the only method capable of solving a challenging test case of flow inside of a lid-driven cavity with viscosity ratio as low as $\beta = 0.0014$ and Weissenberg number equal to 0.75. As a result, we propose the Semi-Implicit discretization of predictor step of momentum equation with the form of eq. 4.21 in order to overcome the difficulties arising by low viscosity ratios (LVRP).

4.4.3 Spatial discretization of constitutive equation

The spatial discretization of the constitutive equation in an arbitrary cell P as shown in figure 4.1, in the case of either Log-conformation representation (LCR), semi-analytical method (SAM) or standard formulation (SF) of constitutive equation could be written using the integral form of transport equation taking into account the incompressibility

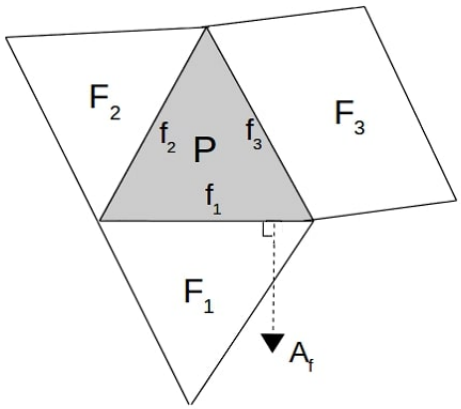

FIGURE 4.1: Control volume used to discretize equation 4.42.

Formulation	$\mathbf{\Upsilon}$	$S(\mathbf{\Upsilon})$
SF & SAM	c_{ij}	$\partial_k v_i c_{kj} + c_{ik}\partial_k v_j - \frac{1}{\lambda_1} f_r(c_{ij})$
LCR	Ψ_{ij}	$\Omega_{ik}\Psi_{kj} - \Psi_{ik}\Omega_{kj} + 2B_{ij} - \frac{1}{\lambda_1} G_{ik}(e^{-\Psi})_{kj}$

TABLE 4.2: Summary of the terms used in equation 4.42. In Cartesian tensor notation $i, j \in \{x, y, z\}$, k is dummy index $\in \{x, y, z\}$ and $\partial_k \in \{\partial/\partial x, \partial/\partial y, \partial/\partial z\}$. Tensors $\mathbf{\Psi}$, $\mathbf{\Omega}$, $\mathbf{B}$, and $\mathbf{G}$ are defined in section 4.4.

constraint of equation 4.2 as below:

$$\int_{V_p} \frac{\partial \mathbf{\Upsilon}}{\partial t} dV = \oint_{A_p} (-\mathbf{\Upsilon}\mathbf{v}) \cdot d\mathbf{A} + \int_{V_p} \mathbf{S}(\Upsilon) dV \tag{4.42}$$

where V_p is the volume of cell P and A_p is the relevant surface which separates two adjacent cells of P and F ($F_i \in \{F_1, F_2, ..., F_n\}$ are neighbour cells of cell P). A_p has the local area vector of d$\mathbf{A}$. Terms of $\mathbf{\Upsilon}$ and $S(\mathbf{\Upsilon})$ related to LCR, SAM and SF are presented in table 4.2 . In this formulation, value of $\mathbf{\Upsilon}$ at the cell (face) is assumed to be constant with the value localized at the cell (face) centroids with approximation of $\mathbf{\Upsilon}_P = \frac{1}{V_p} \int_{V_p} \mathbf{\Upsilon} dV$ ($\mathbf{\Upsilon}_f = \frac{1}{A_p} \int_{A_p} \mathbf{\Upsilon} dA$).

4.4.4 Solution process

The solution procedure of the proposed method would be as follows. Firstly the physical properties, interface geometric properties and velocity field are initialized. Then,

for the time $t = n+1$, the following steps are done consecutively.

1. Allowable time step is calculated using the equations 4.18 and 4.20. To decrease the computational costs, the maximum value of α which leads to a stable simulation is used. Unless otherwise mentions, this value is 0.1.

2. The advection equation (4.12) is integrated in time with a 3-step third order accurate TVD Runge-Kutta scheme [85].

3. The re-initialization equation (4.13) is integrated in pseudo time (τ) using a third order accurate TVD Runge-Kutta scheme. The time τ is used to lead the solution into a stationary state. Since an explicit scheme is used, the time step is restricted by the viscous term of equation 4.13 as follows [82, 198]:

$$\Delta\tau = C_\tau min\left(\frac{h^2}{\varepsilon_P}\right) \tag{4.43}$$

   One iteration is used to solve the discretized form of equation 4.13. The value of C_τ in this formula serving as a CFL-like coefficient for this equation, can take values between [0.01,0.05].

4. Physical properties in the domain (density, viscosites and relaxation time) and geometrical properties at the interface (curvature and interface normal) are updated from the level-set field.

5. If applied, the list of viscoelastic regions is being updated, based on the cut-off approach described in section 4.4.1 .

6. The constitutive equation is integrated in time as described in equation 4.37 for log-conformation representation approach or equation 4.26 for standard formulation approach, and the value of polymeric stress tensor at time $t = n$ are calculated.

7. The velocity and pressure fields are calculated using a fractional-step method described in section 4.3.1 and equations 4.21 through 4.25.

8. In order to fulfill the incompressible constraint, Eq. 4.2, and to avoid pressure-velocity decoupling on collocated meshes [86, 146], a cell-face velocity is used to advect the momentum and CLS function, as introduced in [29, 198].

The steps 1 to 8 are repeated to reach the desired time.

The reader is referred to [24] for further technical details on the CLS method on collocated unstructured grids. The numerical methods are implemented in an in-house parallel c++/MPI code called TermoFluids [47]. Validations and verification of the numerical methods in the context of Conservative level-set method used in this work have been reported in [1, 2, 24, 26, 28, 88, 89].

4.5 Singularities of non-Viscoelastic regions: A droplet in shear test case

A two-dimensional test case of a viscoelastic/Newtonian droplet suspended in a Newtonian/viscoelastic matrix, all imposed to a simple shear flow is being solved using two different approaches of SAM and cut-off as described in section 4.4.1. This test case is being solved to make sure of the accuracy of applying a cut-off parameter to the relaxation time at the interface of viscoelastic/Newtonian interfaces for dealing with singularities of constitutive equation in Newtonian regions. The simulations of this section are similar to the cases of section 4.7.5. The results extracted with both SAM and cut-off approaches are compared with the benchmark results of Chinyoka et al. [196]. Computations have been performed using both structured and unstructured meshes with the edge size of h. All the simulations details are the same as described in section 4.7.5, except that here a 2D domain is used in discretization. In all these simulations the value of β is equal to 0.5 meaning equal shares of polymeric and solvent parts in viscoelastic fluid.

We perform four cases of dNmN, dVmN, dNmV, dVmV, in which **d** and **m** stand for droplet and matrix, and **N** and **V** stand for Newtonian and Viscoelastic, respectively. With this explanation, for example the phrase dVmN stands for a viscoelastic droplet suspended in Newtonian matrix.

TABLE 4.3: Taylor deformation parameter (D) and inclination angle of the droplet (θ) for cases with different rheological properties solved with two approaches of (a) SAM and (b) cut-off, compared with the reference (ref) results of Chinyoka et al. [196].

Case	D_a	θ_a	D_b	θ_b	D_{ref}	θ_{ref}
dNmN	0.76	14.1	0.76	14.0	0.77	14.8
dVmN	0.71	15.2	0.71	15.3	0.72	15.7
dNmV	0.60	13.5	0.60	13.6	0.60	14.7
dVmV	0.55	14.4	0.55	14.5	0.55	15.8

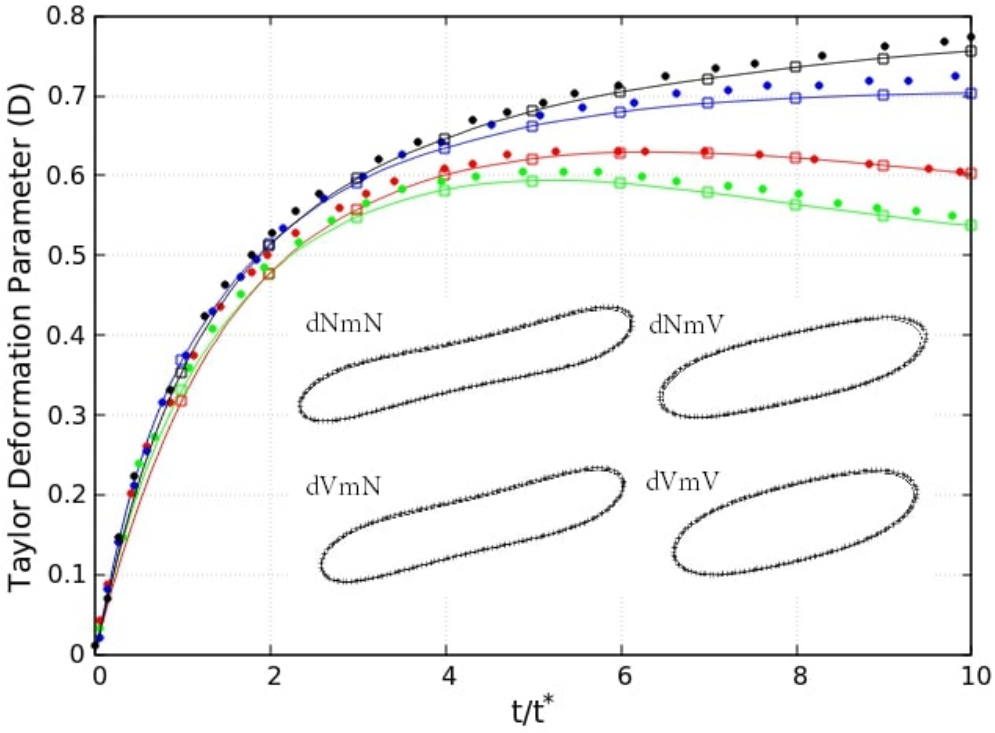

FIGURE 4.2: Taylor deformation parameter (D) vs. time for cases with different rheologies properties all with Capillary number of 0.6, Reynolds number of 0.3, Deborah number of 0.4 and retardation ratio of 0.5. The colors black, blue, green, and red present the results for cases of dNmN, dVmN, dVmV and dNmV, respectively. The line results are related to the solution of the problem with cut-off approach, the square symbols are related to the solution of the problem with the SAM approach, and the circle symbols are related to the reference results of Chinyoka et al. [196]. The droplet shapes at steady-state are provided as well. In theses figures bold lines are reference figures of Chinyoka et al. [196] and points are results extracted in current study solved using cut-off approach.

TABLE 4.4: Different discretizations of predictor step of momentum equation used to study the LVRP.

method	discretization
Forward Euler	$\frac{\rho\mathbf{v}^*-\rho^n\mathbf{v}^n}{\Delta t} = \mathbf{C}_h(\rho\mathbf{v}^n)+\mathbf{D}_{hs}(\mathbf{v}^n)+\mathbf{D}_{hp}^n(\mathbf{v}^{n-1})$
Backward Euler	$\frac{\rho\mathbf{v}^*-\rho^n\mathbf{v}^n}{\Delta t} = \mathbf{C}_h(\rho\mathbf{v}^*)+\mathbf{D}_{hs}(\mathbf{v}^*)+\mathbf{D}_{hp}^*(\mathbf{v}^n)$
2nd order Adams-Bashforth	$\frac{\rho v^*-\rho^n v^n}{\Delta t} = \frac{3}{2}\left(\mathbf{C}_h(\rho\mathbf{v}^n)+\mathbf{D}_{hs}(\mathbf{v}^n)+\mathbf{D}_{hp}^n(\mathbf{v}^{n-1})\right)$- $\frac{1}{2}\left(\mathbf{C}_h(\rho\mathbf{v}^{n-1})+\mathbf{D}_{hs}(\mathbf{v}^{n-1})+\mathbf{D}_{hp}^{n-1}(\mathbf{v}^{n-2})\right)$
BSD	$\frac{\rho\mathbf{v}^*-\rho^n\mathbf{v}^n}{\Delta t} = \mathbf{C}_h(\rho\mathbf{v}^*)+\mathbf{D}_{hs}(\mathbf{v}^*)+\mathbf{D}_{hp}(\mathbf{v}^n)+\mathbf{D}_{hk}(\mathbf{v}^*)-\mathbf{D}_{hk}(\mathbf{v}^n)$
Semi-Implicit form as eq. 4.21	$\frac{\rho\mathbf{v}^*-\rho^n\mathbf{v}^n}{\Delta t} = \frac{3}{2}(R_h^v)^n-\frac{1}{2}(R_h^v)^{n-1}+\frac{1}{2}\left(\mathbf{D}_{hs}(\mathbf{v}^*)+\mathbf{D}_{hs}(\mathbf{v}^n)\right)-\nabla_h p^n$

In all of these cases, Capillary number of 0.6, Reynolds number of 0.3 and Deborah number of 0.4 are used. The simulations were run until t=10$\dot{\gamma}$. Figure 4.2 presents the time variation of Taylor deformation parameter for solutions done in the current study using different approaches of SAM and cut-off, compared with the finite-difference/volume-of-fluid results of [196]. The steady-state droplet shape for the case solved in the current study using cut-off approach compared with the reference shapes of [196] are provided in this figure as well. The quantitative values of these cases are provided in table 4.3. According to these data, the cut-off approach provides results almost identical to the SAM approach. Both approaches are having good agreement with the reference data of [196].

4.6 The ability of different approaches in solving LVRP

The selected test case is a two-dimensional lid-driven cavity problem, with geometrical characteristics and boundary conditions identical to the viscoelastic test case solved in section 4.7.1. The Reynolds number is equal to 100, the value of viscosity ratio is $\beta = 0.0014$ and Weissenberg number is equal to 0.75.

Different discretizations of predictor step of momentum equation in the context of fractional-step projection method are being tested which are presented in table 4.4. In this table, in the BSD discretization method, the term $\mathbf{D}_{hk}(\mathbf{v})$ is equal to $\nabla_h.(\mu_k/\mu_s\tau_s)$ with μ_k recommended to be equal to μ_p.

The mentioned test case of two-dimensional lid-driven cavity with the predictor step of momentum equation being discretized according to the methods of table 4.4

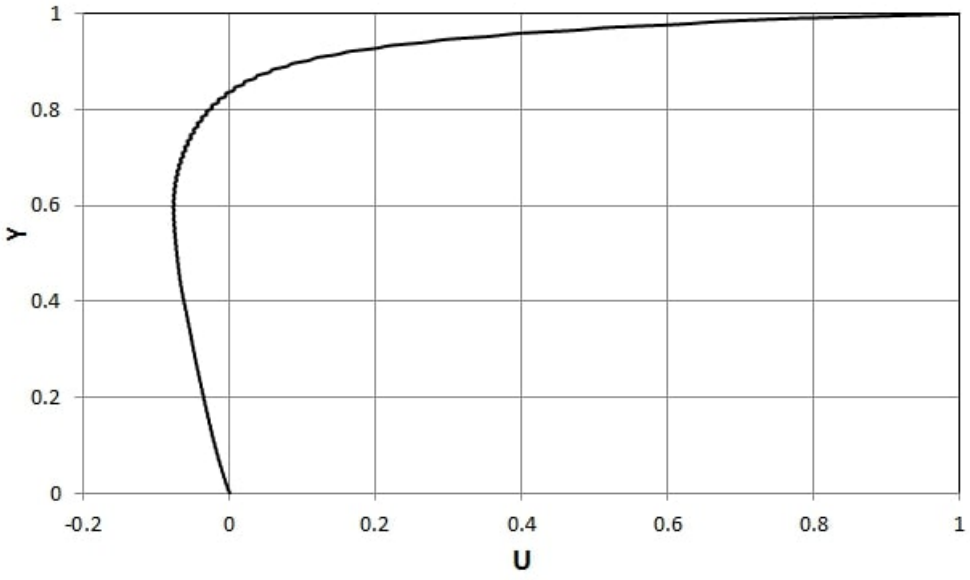

FIGURE 4.3: U(Y) graph in the vertical centerlines of lid-driven cavity test case, with Re=100, for a viscoelastic fluid with viscosity ratio of $\beta = 0.0014$ and Weissenberg number equal to 0.75. For this test case, the predictor step of momentum equation is discretized using the Semi-Implicit form as eq. 4.21

.

was solved for a long enough time of $t' = 10$ with $t' = t(U/D)$. A uniform structured square mesh with the edge size of $h = L/100$ was used in all the cases. Among all these methods tested, only the last method (Semi-Implicit form as eq. 4.21) was able to provide a stable solution for the aforementioned problem. The solution of methods of **Forward Euler** and **2nd order Adams-Bashforth** had an unbearably small timestep (around 5 orders of magnitude smaller than the other methods). With this small timestep, the solution process took a very long time to advance, however, for both of these methods the solution diverged for $t' \approx 1.2$. **Backward Euler** method didn't suffer from the significantly small timesteps as the two previous methods, however it failed to provide a solution and diverged at $t' \approx 3$. **BSD** method could benefit from timesteps as big as $dt' = 10^{-3}$. However this method also ended-up in diverging the solution process at $t' \approx 4.2$. Semi-Implicit form as eq. 4.21 was able to provide a stable solution using a constant timestep of $dt' = 10^{-3}$. The solution was successfully finished by the time $t' = 10$. Figure 4.3 illustrates the $U(Y)$ graph in the vertical centerlines of the geometry at time $t' = 10$ for this solution.

4.7 Numerical experiments and discussion

4.7.1 Lid-Driven Cavity

In this section, the results regarding the flow in classical two-dimensional lid-driven cavity test case will be presented. The lid-driven cavity problem has long been used as a validation case for new codes or new solution methods. This problem is of particular interest for testing for several reasons. There are many data available extracted from different experimental studies and numerical methods. The laminar solution of the flow is steady. Also, the geometry of problem is simple and two-dimensional, boundary conditions are simple and easy to implement. Numerical tests of this section are carried out on a benchmark problem studied in Carmona et al. [199], for GNFs and two different benchmark results of Chen et al. [186] and Yapici, Karasozen, and Uludag [200] for viscoelastic fluids. The test case is a 2-D lid-driven cavity with aspect ratio of 1, characteristic length of L and characteristic velocity of $U = 1$. The top boundary of the cavity is moving with a velocity of u(x,t) while no-slip boundary

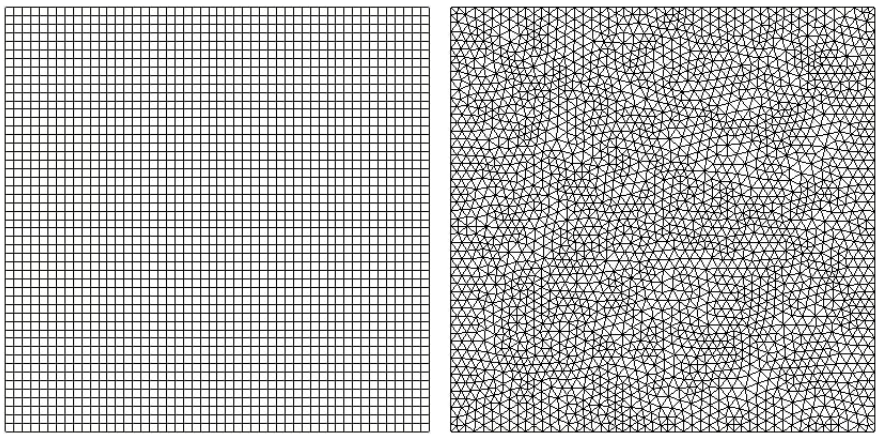

FIGURE 4.4: Structured and Unstructured mesh configurations used in simulation of lid-driven cavity test case.

condition is applied on other walls. Two different mesh types of structured and unstructured with a grid size of $h = L/100$ are used to discretize the solution domain as illustrated in figure 4.4. The simulations are done long enough to make sure that convergence to the steady-state has been reached. Three different sets of simulations are done for rheologies of viscoelastic, shear-thinning and shear-thickening fluids:

- For the case with viscoelastic fluid, Oldroyd-B constitutive equation is used. Three different formulations of Standard formulation, Log-Conformation Representation and semi analytical approaches of constitutive equation are used to verify the accuracy of the solver for this problem. Non-dimensional parameters of Reynolds number and Weissenberg number are defined as $Re = \rho UL/\mu_0$ and $Wi = \lambda_1 U/L$, respectively. In order to eliminate the singularities at the corners, the top wall moves with the space and time-dependent velocity profile as below:

$$u(x,t) = 8[1 + tanh(8t-4)]x^2(1-x^2) \tag{4.44}$$

  The lid velocity gradually increases until it reaches its maximum magnitude at the center of the lid. In order to gain more confidence on the accuracy of the viscoelastic solver, two cases are selected and solved with different parameters of Re, Wi, and β in both structured and unstructured domains as:

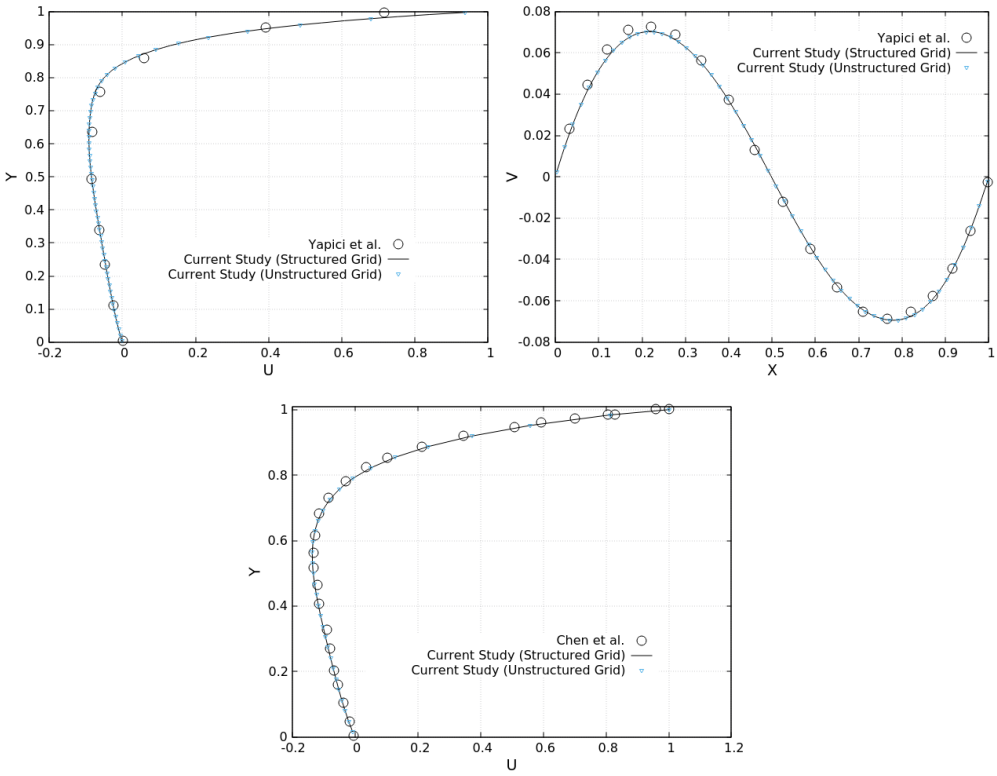

FIGURE 4.5: Top: U(Y) and V(X) graphs in the vertical and horizontal centerlines, respectively, for the lid-driven cavity problem, Case A compared with results of Yapici, Karasozen, and Uludag [200].
Bottom: U(Y) graph in the vertical centerline of the lid-driven cavity problem, Case B compared with the results of Chen et al. [186].

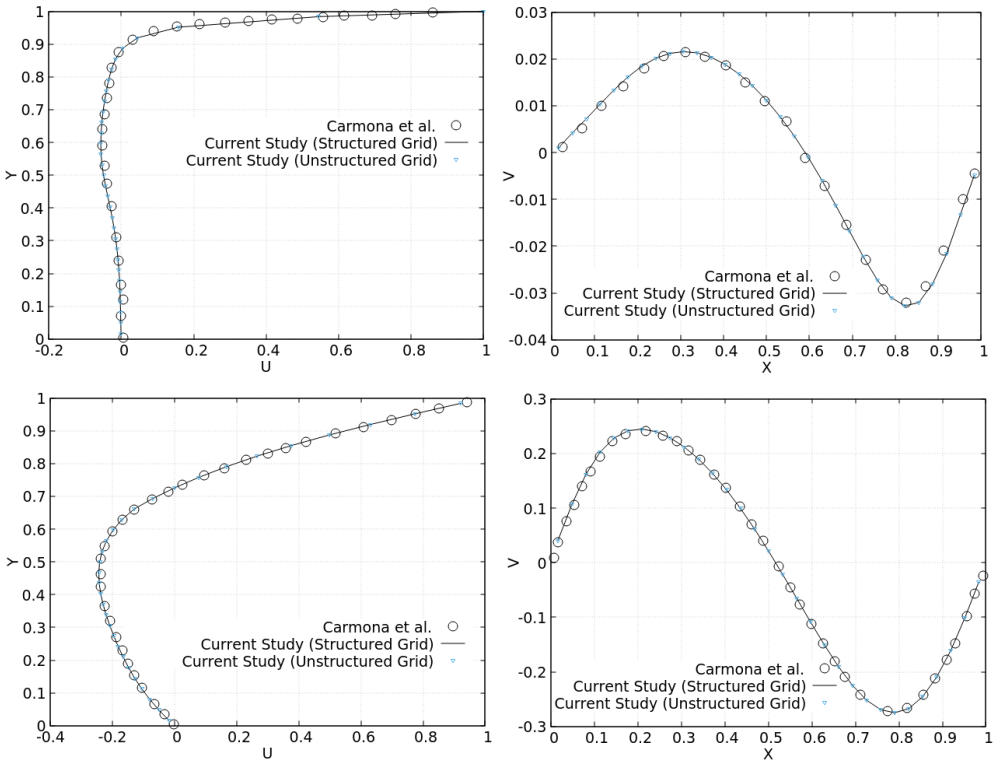

FIGURE 4.6: U(Y) and V(X) graphs in the vertical and horizontal centerlines, respectively, for the lid-driven cavity problem with shear-thinning and shear-thickening fluids. First row corresponds to Case C (n=0.25) and second row corresponds to Case D (n=1.75). These graphs are compared with the results of Carmona et al. [199]

Case A: Re=100, Wi=0.7 and β=0.3

Case B: Re=0.10, Wi=0.5 and β=0.5

The results are obtained for these cases in domains with structured and unstructured grids and are compared with two different benchmarks of Chen et al. [186] and Yapici, Karasozen, and Uludag [200], for cases A and B, respectively. Figure 4.5 top, represents the U(Y) and V(X) graphs in the vertical and horizontal centerlines of the domain, respectively. Figure 4.5 bottom, however, represents U(Y) graph in the vertical centerline of the domain. The results of this figure correspond to the solution of viscoelastic fluid employing the Standard Formulation approach. The results of solution of these cases using LCR and SAM approaches are identical to the presented results. Hence, in order to avoid redundancy, these results are not added.

- In order to validate the ability of solver in capturing the physics of shear-thinning and shear-thickening fluids, simulations of generalized newtonian fluid represented with power-law model with two indices of n=0.25 (as shear-thinning fluid) and n=1.75 (as shear-thickening fluid) are performed:

Case C: Re=100, n=0.25

Case D: Re=100, n=1.75

Top wall is moving with a constant velocity of u(x,t)=1. Reynolds number is defined as $Re = \rho UL/K$ Figure 4.6 represents the U(Y) and V(X) graphs in the vertical and horizontal centerlines of the domain extracted from solution in structured and unstructured grids, compared with results of Carmona et al. [199].

In all the cases presented in this section, a very good agreement is seen between the results extracted in this study, and the extracted data from literature.

4.7.2 Two-dimensional Poiseuille flow

In two dimensional Poiseuille flow test case, the flow between two infinite plates is driven by an external pressure gradient ($S = dP/dx$). Periodic boundary condition is applied in the flow direction (x), and no-slip boundary condition on the walls. This

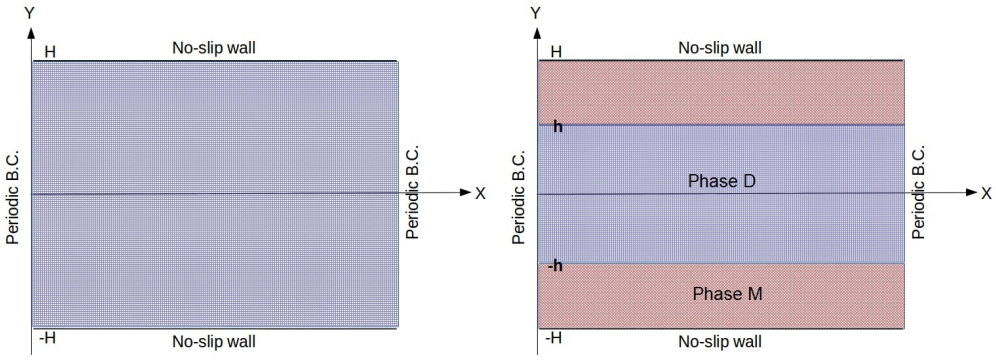

FIGURE 4.7: The schematic plot of the 2D domain of Poiseuille flow test case. Left: single-phase viscoelastic fluid problem, right: two-phase shear-thinning/shear-thickening fluids problem.

problem is solved for different rheologies of viscoelastic, shear-thinning and shear-thickening fluids and the results are compared with the exact solution extracted from analytical approaches.

- For viscoelastic fluid test case, the exact solution of the transient velocity and viscoelastic stress for Oldroyd-B constitutive model exist and are presented in [201]. The geometry of the channel is presented in figure 4.7 left. Lengths are non-dimensionalized using the domain's height ($y^* = y/H$), velocity using characteristic velocity of $u_0 = \frac{-SH^2}{8\nu_0}$ ($u^* = u/u_0$) in which ν_0 is the total kinematic viscosity, time using $t_0 = H^2/\nu_0$ ($t^* = t/t_0$) and stress tensor using $\tau_0 = \eta u_0/H$ ($\tau^* = \tau/\tau_0$). In which variables denoted with * are dimensionless. The exact solution of the flow for this case would be as:

$$u^*(t^*,y^*) = 4y^*(1-y^*) - 32\sum_{n=1}^{\infty}\frac{sin(Ny^*)}{N^3}G_N(El,t^*) \tag{4.45}$$

where

$$G_N(El,t^*) = \begin{cases} 0.5(a_N exp(P_N t^*) + b_N exp(Q_N t)), & \beta_N^2 \geq 0 \\ exp(-\alpha_N^* t^*)(cos(\beta_N^* t^*) + \frac{S_N}{\beta_N} sin(\beta_N^* t^*)), & \beta_N^2 < 0 \end{cases} \tag{4.46}$$

In this formulation, the parameters are presented in table 4.5.

TABLE 4.5: Related parameters of equation 4.46

Symbol	Equation
N	$(2n-1)\pi$
S_N	$1-17N^2El/9$
α_N	$1+N^2El/9$
β_N^2	$\alpha_N^2-4N^2El$
α_N^*	$\alpha_N/(2El)$
β_N^*	$\beta_N/(2El)$
α_N	$1+S_N/\beta_N$
b_N	$1-S_N/\beta_N$
P_N	$-\alpha_N^*+\beta_N^*$
Q_N	$-\alpha_N^*-\beta_N^*$

Using the given velocity profile, the viscoelastic stress tensor could be solved as:

$$\begin{aligned}\tau_{xx} &= 2Wi(1-\beta)(\frac{\partial u^*}{\partial y^*})^2\\ \tau_{xy} &= (1-\beta)(\frac{\partial u^*}{\partial y^*})\\ \tau_{yy} &= 0\end{aligned}$$

The initial condition is zero velocity and stress tensor in the whole domain. The numerical simulation is done in a domain with both structured and unstructured grid with the mesh size of h=H/100 until $t^*=10$. The results showed to be independent of the grid type, and were identical for structured and unstructured grids. Dimensionless numbers of Reynolds number and Weissenberg number are defined as $Re=\rho u_0 H/\nu_0$ and $Wi=\lambda_1 u_0/H$, respectively. The steady-state results of cross section velocity $u_x(y)$, along with the transient velocity at centerline and transient normal viscoelastic stress on fixed wall for a case with $\beta=0.1$, Re=1 and Wi=1 are presented in figure 4.8. These results are compared with the results of exact solution where perfect agreement is seen.

- For shear-thinning, and shear-thickening rheologies, power-law GNF model is

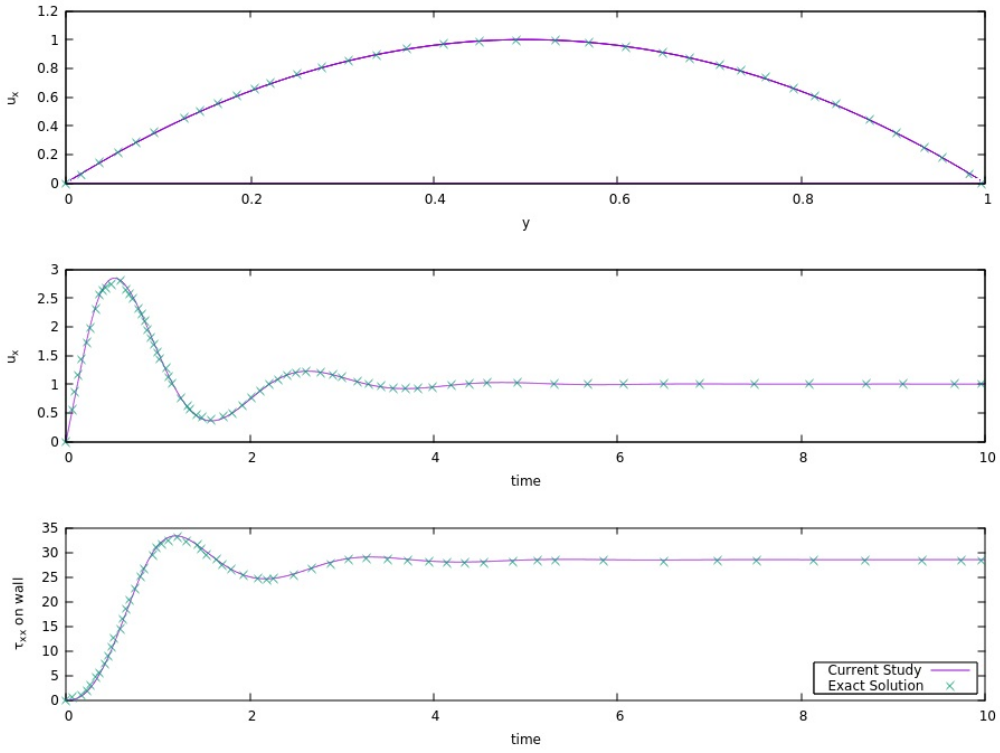

FIGURE 4.8: Numerical simulation of two-dimensional Poiseuille Oldroyd-B viscoelastic fluid flow compared with the analytical solution.

used to simulate the two-phase flow problem inside of a channel with aforementioned properties. Figure 4.8 right illustrates the schematic plot of the domain used for this problem with two phases called D and M. Extraction of analytical solution of this problem for power-law fluid is straight forward. The X-direction velocity profile (U) as a function of Y could be written as below:

$$U(Y) = \begin{cases} A(D)\left(h^{\frac{1+n_D}{n_D}} - |y|^{\frac{1+n_D}{n_D}}\right) + A(M)\left(H^{\frac{1+n_M}{n_M}} - h^{\frac{1+n_M}{n_M}}\right), & |y| \leq h. \\ A(M)\left(H^{\frac{1+n_M}{n_M}} - |y|^{\frac{1+n_M}{n_M}}\right), & \text{Elsewhere} \end{cases} \tag{4.47}$$

where $A(i)$ is defined as:

$$A(i) = \frac{n_i}{1+n_i}\left(-\frac{\partial P}{\partial x}.\frac{1}{K_i}\right)^{(1/n_i)} \tag{4.48}$$

In our simulations, the domain has a length of L=5H, and h=H/2 while a mesh with grid size of H/80 is used to discretize the domain. A constant pressure gradient of $\frac{\partial P}{\partial x} = 0.075$ and a surface tension coefficient of 24.5 is being applied in all the cases. Simulations with different rheological properties have been performed for a long enough time. The details of rheological properties of these cases are tabulated in table 4.6. For each case, the first norm of error of numerical simulation is calculates using: $L_1 = \sum_i |e_i|$, where e_i is the point-wise error of each cell compared with its analytical solution. The value of L_1 for all of these cases are presented in table 4.6. As can be seen in this table, the value of the L_1 for all the cases is in the order of $\approx O(10^{-3})$, which is considered as good agreement.

4.7.3 Impacting droplet problem

In this section, using the numerical method proposed, the falling of a two-dimensional viscoelastic droplet under gravitational force with the acceleration of g is being solved. The droplet with an initial diameter of d_0 is placed at the height of $H = 2d_0$ above a stationary plate. The computational domain has a length of $5.6d_0$ and a height of

Case	n_D	n_M	K_D/K_M	L_1
1	1	1	1	8.23×10^{-4}
2	0.5	1	1	9.72×10^{-4}
3	0.5	1	0.5	3.25×10^{-3}
4	0.5	1	2	1.89×10^{-2}
5	1.5	1	1	9.25×10^{-4}
6	1.5	1	0.5	2.64×10^{-3}
7	1.5	1	2	4.27×10^{-3}
8	1	0.5	1	2.91×10^{-3}
9	1	0.5	0.5	4.26×10^{-3}
10	1	0.5	2	1.68×10^{-2}
11	1	1.5	1	2.49×10^{-3}
12	1	1.5	0.5	1.37×10^{-2}
13	1	1.5	2	1.84×10^{-2}

TABLE 4.6: Characteristics of cases solved for shear-thinning/shear-thickening rheological properties, along with the relative error of the numerical results, compared with analytical solution.

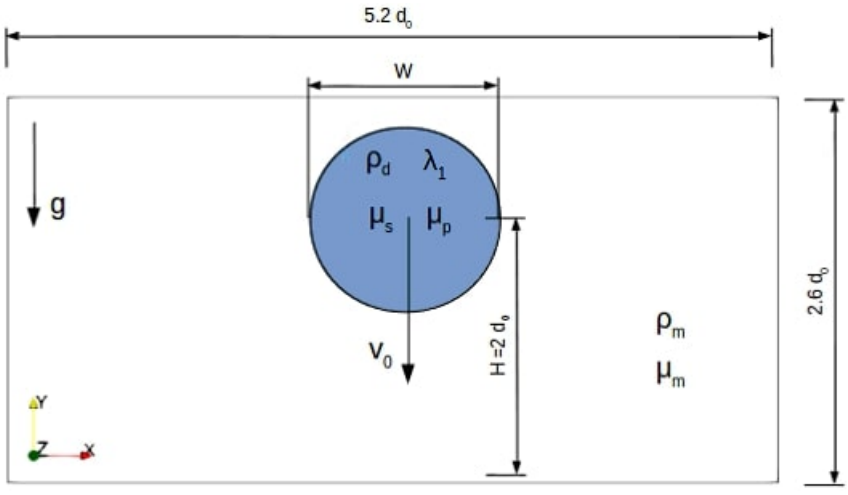

FIGURE 4.9: Initial computational setup of the impacting droplet problem.

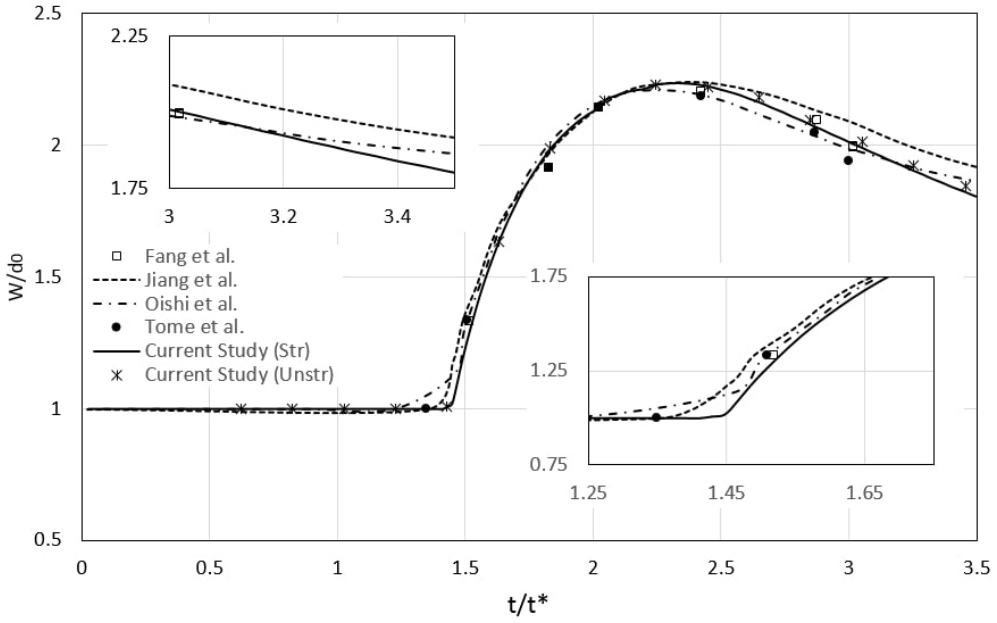

FIGURE 4.10: Time evolution of non-dimensional width of an Oldroyd-B droplet impacting on a surface for simulations with two different grid types of structured (Str) and unstructured (Unstr). The results of current study are compared with the (SPH) results of Fang et al. [161] and Jiang et al. [162] and MAC results of Tomé et al. [156] and Oishi et al. [157]

$2.6d_0$. Two different grid types of structured and unstructured are used to discretize the solution domain. Figure 4.9 illustrates the initial setup of the problem. At time $t/t^* = 0.0$, the droplet falls towards the wall with an initial velocity of V_0 (with $t^* = d_0/V_0$). Oldroyd-B constitutive equation is used to model the viscoelastic behaviour of the droplet with a retardation ratio of $\beta = 0.1$, while the effect of surface tension is neglected. Three sets of non-dimensional parameters of Reynolds (Re), Deborah (De) and Froude (Fr) numbers are used as below:

$$Re = \frac{\rho_d d_0 V_0}{\mu_{0d}} = 5 \quad De = \frac{\lambda_1 V_0}{d_0} = 1 \quad Fr = \frac{V_0}{\sqrt{g d_0}} = 2.26 \tag{4.49}$$

No-slip boundary condition is applied on the bottom wall while the free-slip boundary condition is applied on all the other walls. In order to minimize the effect of the matrix gas, a density and viscosity ratio of $\rho_d/\rho_m = \mu_{0d}/\mu_m = 1000$ is used. Figure 4.10 shows the time evolution of the non-dimensional width of the droplet (W/d_0)

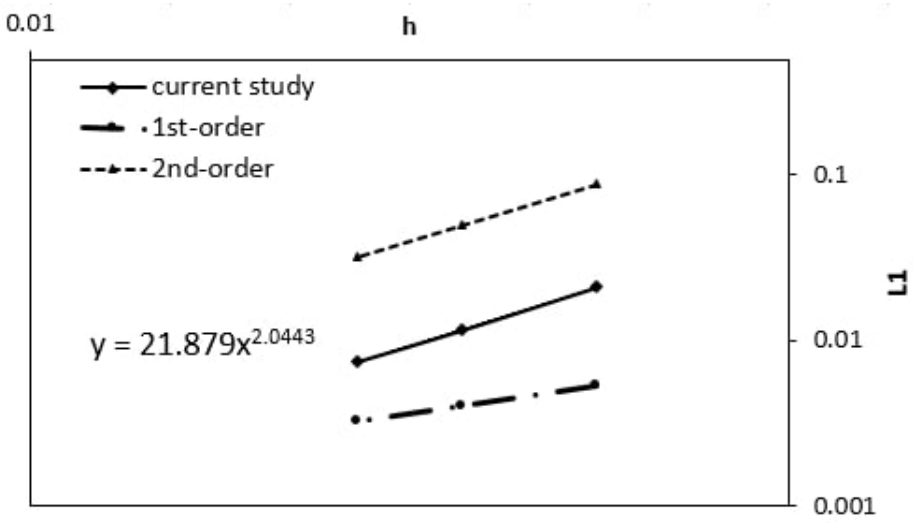

FIGURE 4.11: First norm of the error in calculation of width of the droplet (W) during the solution process of the impacting droplet problem inside of the domains with structured grids with sizes of $h = d_0/30, d_0/40$ and $d_0/50$ compared with the reference values of solution in a domain with the grid size of $h = d/60$.

for the solution done in this study in domains with structured and unstructured grids in comparison with results of different approaches available in literature, e.g. (SPH) method of Fang et al. [161] and Jiang et al. [162] and MAC method of Tomé et al. [156] and Oishi et al. [157]. Good agreement is seen for simulations both in structured and unstructured grids in comparison to the aforementioned results available in the literature.

A grid convergence study is performed for this case. Simulations of the reported case in a domain with structured grids with four different grid sizes of $h = d_0/30$, $d_0/40$, $d_0/50$ and $h = d_0/60$ are done. For each case, the numerical simulation is performed until $t/t^* = 3.5$. The variation of the width of the droplet (W) for the solution with the finest grid ($h = d_0/60$) is selected as the reference, where the results of other simulations are compared with it, to calculate the error associated to the droplet width (W) at each timestep. The accumulated value of these errors are measured as the first norm of the error using $L_1 = \sum_i |e_i|$, where e_i is the difference between droplet width (W) of the simulation and its corresponding value in reference solution at i-th iteration. Figure 4.11 presents the values of L_1 as a function of the grid size. As can be

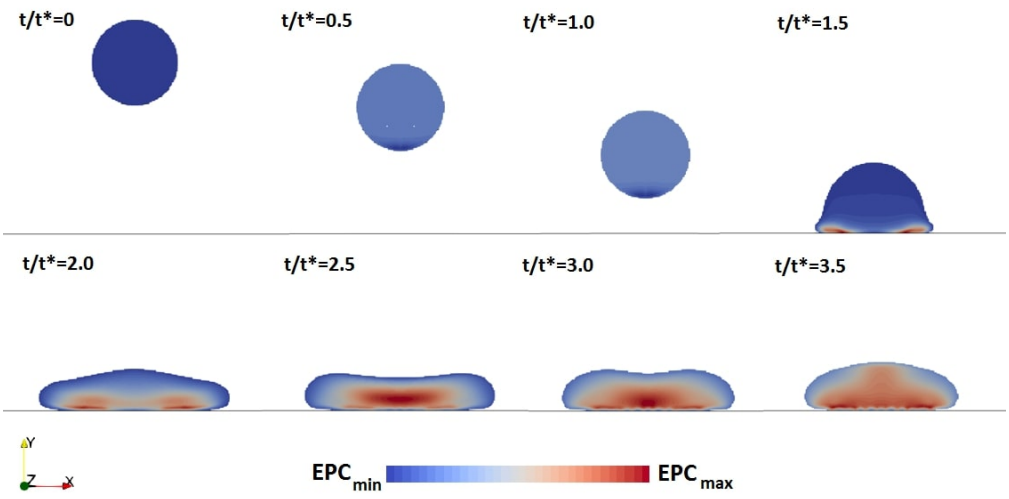

FIGURE 4.12: Snapshots of the impact of a viscoelastic droplet over a surface. The color contours present the elongation of the polymer chains (EPC) in the droplet.

seen, the solution process illustrates an order of convergence of 2.04 in space.

Trace of the conformation tensor indicates the elongation of the polymer chains (EPC). Figure 4.12 illustrates the snapshots of the droplet evolution, with the contours of elongation of the polymer chains. As can be seen, upon the impact of the droplet, the length of the polymeric chains increases in the triple points of the contact and spreads in spatial areas around this region. As the droplet evolves toward equilibrium, the length of the polymeric chains expands in the droplet core.

4.7.4 Sudden contraction/expansion

In this section, numerical simulation of a viscoelastic droplet suspended in Newtonian matrix, passing through a contraction/expansion geometry is done and the results are compared against available experimental images. Figure 4.13 illustrates the schematic representation of the domain's dimensions and mesh configuration. All the lengths are non-dimensionalized by the inlet's half width, H_{in}. Two types of meshes of structured cubic cells and unstructured triangular-prism cells with the edge size of $h = H_{in}/36$ are used to discretize the domain. To approximate the experimental dimensions, the contraction and expansion edges are bevelled with a side length of $0.1H_{in}$.

TABLE 4.7: Non-dimensional parameters defining the sudden contraction/expansion test case

Re	We	De	ρ_d/ρ_m	μ_{0d}/μ_{0m}	β
0.825	6.22×10^{-2}	0.598	1.17	31	0.586

The width of the domain in Z direction is $W = 0.33H_{in}$. A flow with uniform velocity of (U,V,W)=($\overline{U}$,0,0) enters the domain through the inlet and exits the domain through the outlet boundary conditions. Non-wetting boundary condition for level-set function, no-slip boundary condition for velocity components and Neumann boundary condition for pressure and extra-stress tensor are applied on the walls. A droplet with initial diameter of $d_0 = 0.864H_{in}$ is places in a quiescent Newtonian matrix. The Oldroyd-B constitutive equation is used to model the viscoelastic behavior of the droplet. Non-dimensional group of variables as below are used in addition to density ratio (ρ_d/ρ_m), total viscosity ratio (μ_{0d}/μ_{0m}) and retardation ratio (β) to physically define the problem:

$$Re = \frac{\rho_m \overline{U} H_{in}}{\mu_m} \quad We = \frac{\rho_m \overline{U}^2 H_{in}}{\sigma} \quad De = \frac{\lambda_1 \overline{U}}{H_{in}} \tag{4.50}$$

Time is non-dimensionalized as t/t^* with $t^* = (H_{in}/\overline{U})$. Table 4.7, presents the selected characteristics of the problem based on the introduced non-dimensional group of variables. The droplet is being imposed to a geometrical contraction, is forced to change its shape in order to pass through the narrow channel, and retrieves its more stable spherical shape after passing through the expansion. The simulation continues until $t/t^* = 2.14$. Figure 4.14 presents the results of the numerical simulation of the current study in structured grid compared with the experimental results of [202] for the same time instances. Please note, since the results obtained by structured grid were identical to the results of unstructured grid, in order to avoid redundancy, only the results obtained with one of them is being shown. In this figure, non-dimensional times of the simulations are provided at the bottom of the image. Note that the reference time of $t/t^* = 0.0$ is when the leading tip of the droplet enters the contraction zone. According to this figure, very good agreement is seen between the results of current study, and experimental results of Harvie, Cooper-White, and Davidson [202], which

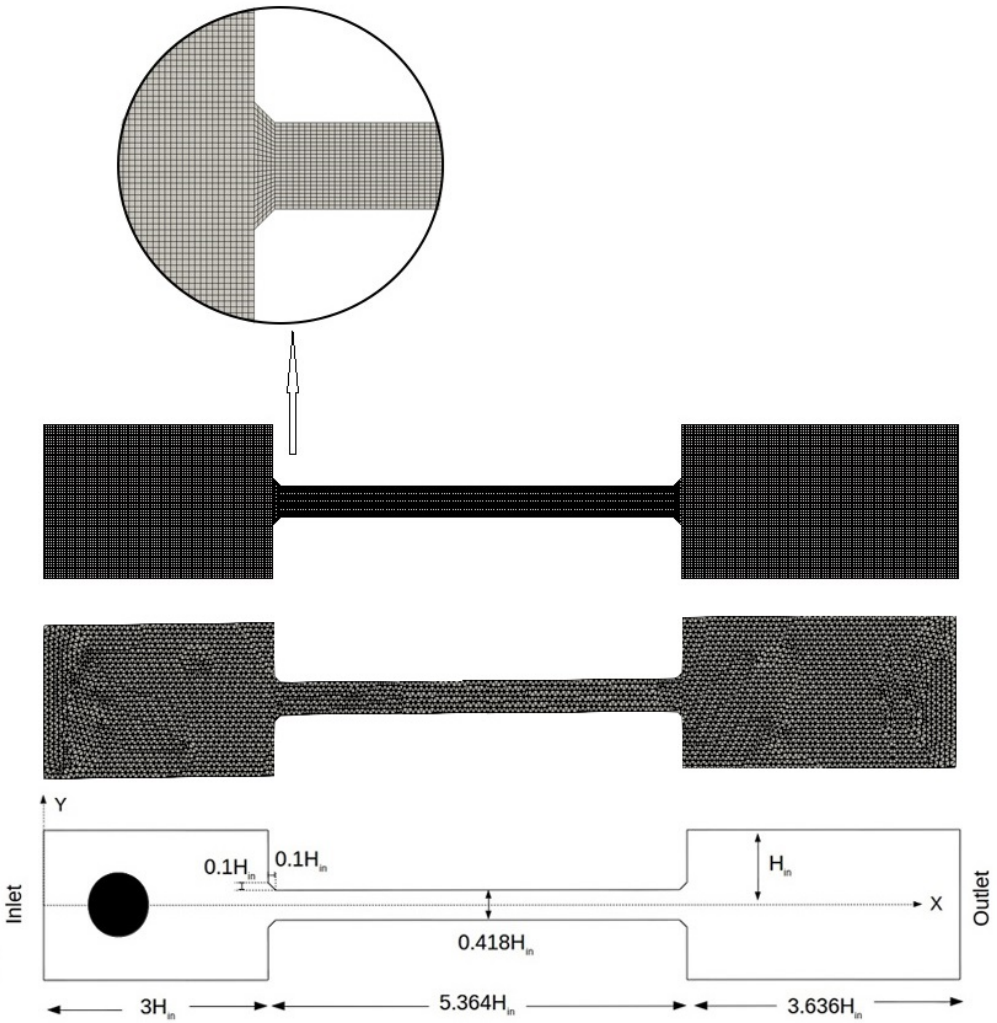

FIGURE 4.13: schematic representation of domain's dimensions and mesh configuration of sudden contraction/expansion test case with two different mesh types of structured and unstructured grids.

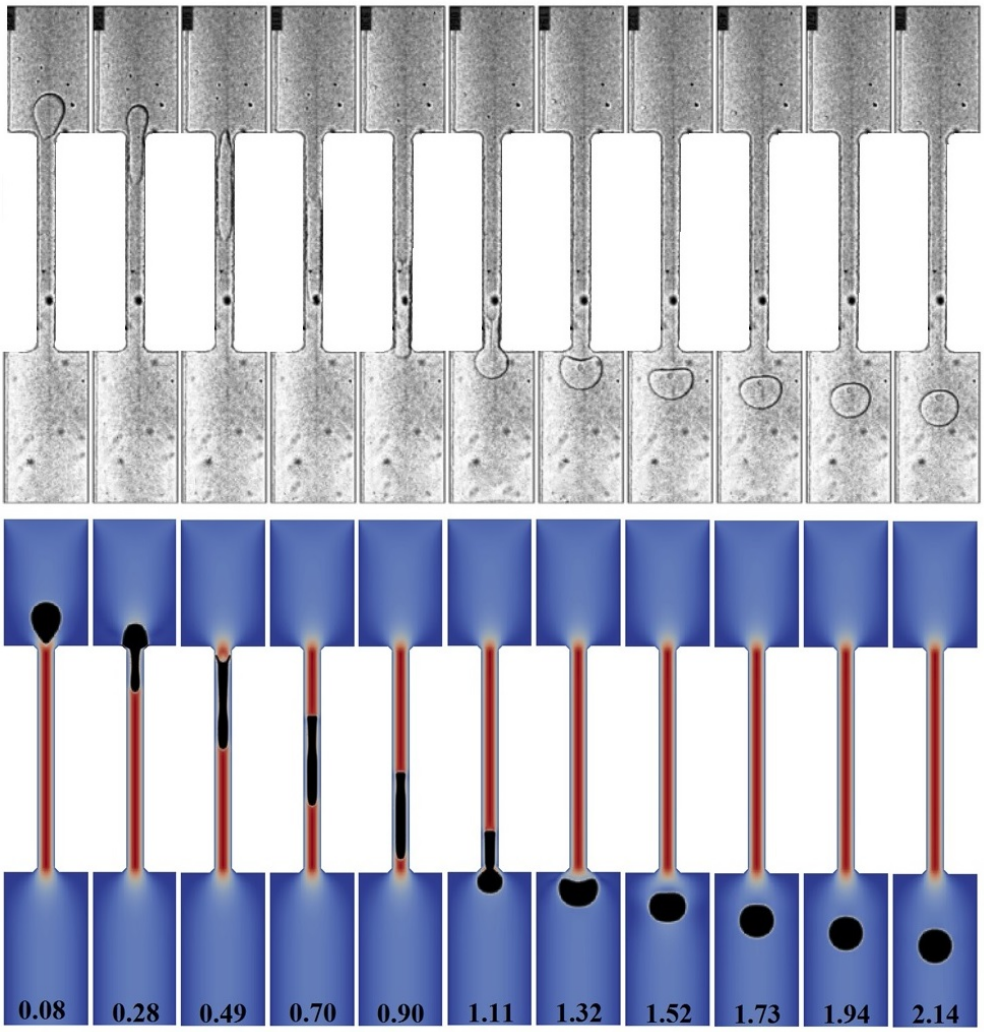

FIGURE 4.14: Sudden contraction/expansion of a viscoelastic droplet in a Newtonian matrix. Top: experiment results of [202], Bottom: results of current study, extracted at the same time instances of experimental images.

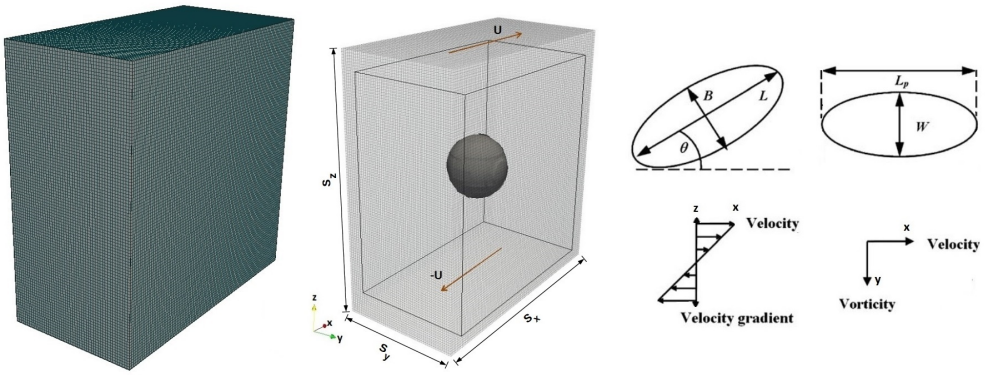

FIGURE 4.15: Left: Mesh configuration, structured cubic cells. Middle: computational setup, Right: Schematic presentation of a deformed droplet along with related geometrical measurements in velocity-velocity gradient, and velocity-vorticity planes.

validates the ability of the proposed method on capturing the physics of this problem.

4.7.5 Simple Shear flow

A circular Newtonian droplet with diameter d is suspended in a viscoelastic matrix in a domain with span $S_x = 5d$, $S_y = 5d$ and $S_z = 2.5d$ in x,y and z directions, respectively. Figure 4.15 illustrates the mesh configuration and computational setup. The opposite x-direction velocities of $+U$ and $-U$ are imposed at the top and bottom walls inducing a shear rate of $\dot{\gamma} = 2U/S_z$ in the domain. A periodic boundary condition is applied in the flow direction (x) and Neumann boundary condition in y direction. Computations have been performed using a Cartesian mesh of cubic cells with the edge size of h=d/30. This mesh was generated by a constant step extrusion of the two-dimensional y-z grid along the x-axis with the step size of h. A grid convergence analysis is provided at the end of this section for the most challenging cases. At the beginning of the simulation, a linear velocity field is applied inside of the domain varying from $-U$ at the bottom wall to $+U$ at the top wall.

For Newtonian droplet and matrix, the system can be physically defined by four parameters of Reynolds number (Re), Capillary number (Ca), total viscosity ratio (μ_{0d}/μ_{0m}) and walls confinement ratio ($2r/S_z$). For an arbitrary value of shear rate

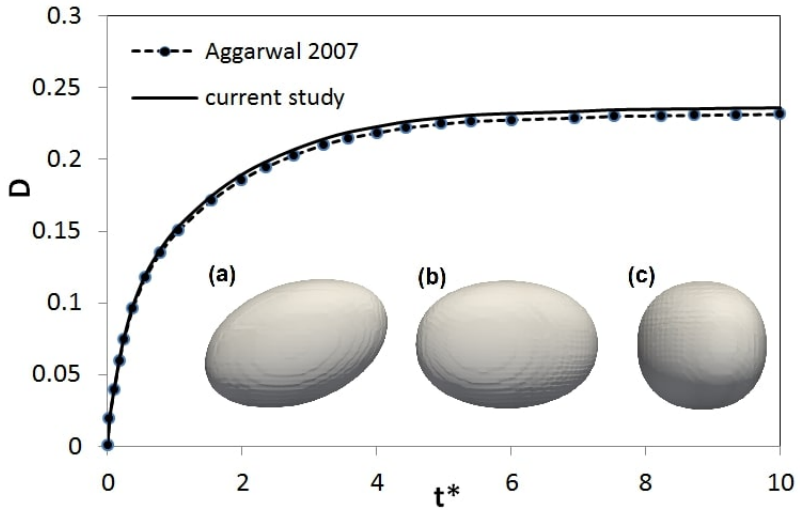

FIGURE 4.16: Taylor deformation parameter (D) vs. time ($t' = t\dot{\gamma}$) for a Newtonian droplet suspended in viscoelastic matrix imposed to a shear with Re=0.1, Ca=0.2 and De=1.5 compared with results of Aggarwal and Sarkar [160]. Subfigures of (a), (b) and (c) present the droplet shape at $t' = 10$ in (X-Y), (X-Z) and (Y-X) planes, respectively.

($\dot{\gamma}$), the velocity at the top and bottom walls are calculated as $U = \dot{\gamma} S_z/2$. Then viscosity is calculated using the Reynolds number as below:

$$Re = \frac{\rho_m \dot{\gamma} r^2}{\mu_{0m}} \tag{4.51}$$

where r is the droplet's radius. The Capillary number is a dimensionless parameter defining the relative effect of the shear stress versus surface tension across the interface, given by:

$$Ca = \frac{\dot{\gamma}\mu_{0m} r}{\sigma} \tag{4.52}$$

For a given value of Ca and Re numbers, and the calculated value of μ_{0m}, the related value of σ is determined.

In the case where the droplet evolves to a steady shape, different parameters have been used to measure the deformation attained by the droplet. The first one is the Taylor deformation parameter defined as $D = (L-B)/(L+B)$, where L and B are

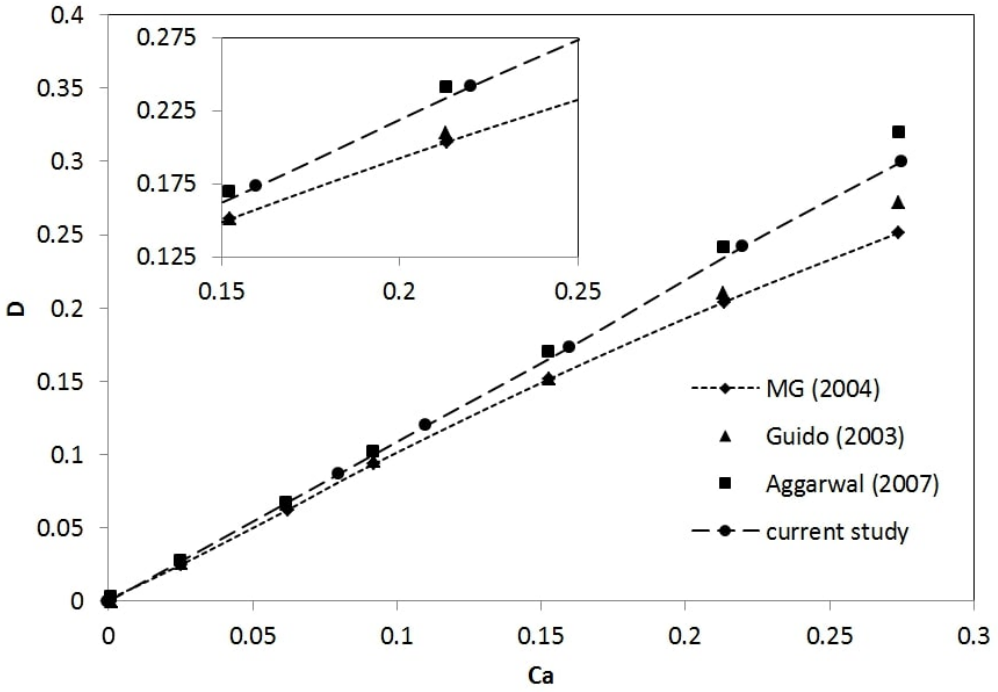

FIGURE 4.17: Steady-state Taylor deformation parameter (D) for simulations of a Newtonian droplet in viscoelastic matrix with different values of Capillary numbers, all with elasticity parameter of p=De/Ca=0.6. Results of current study are compared with the results of three different approaches, experimental data of Guido, Simeone, and Greco [203], analytical predictions of Maffettone and Greco [204] and numerical results of Aggarwal and Sarkar [160].

length and breadth of the drop, as shown in figure 4.15. Another parameter is the angle θ of orientation of the droplet with respect to the axis of shear strain. In addition to these parameters, L_p and W, as projected length and width of the droplet are used in literature and depicted in figure 4.15.

For viscoelastic rheological characteristics of the matrix, Oldroyd-B constitutive equation is solved. The initial condition of conformation tensor is Identity tensor in the whole domain leading to zero stress initial condition. Non-dimensional parameter of Deborah number ($De = \lambda_1 \dot{\gamma}$) and retardation ratio are used in addition to the four previously defined parameters of Re, Ca, total viscosity ratio and walls confinement ratio to fully define the system. In all the simulations, a low Reynolds number of 0.1, retardation ratio of $\beta = 0.5$, and droplet to matrix total viscosity ratio of 1 is being

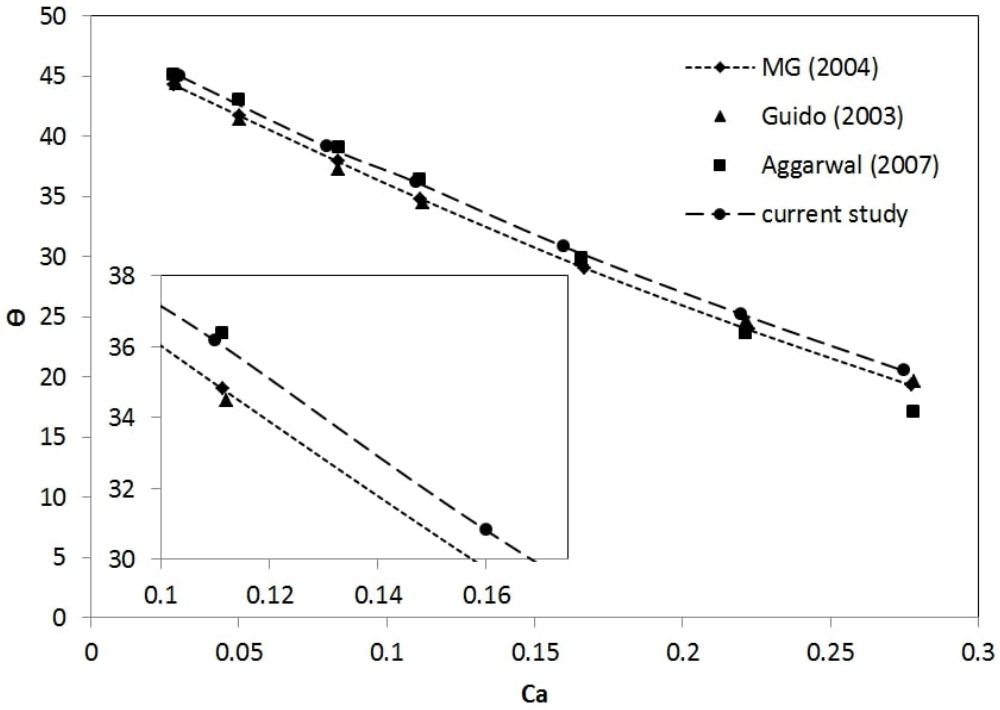

FIGURE 4.18: Droplet inclination angle (θ) parameter for simulations of a Newtonian droplet in viscoelastic matrix with different values of Capillary numbers, all with elasticity parameter of p=De/Ca=0.6. Results of current study are compared with the results of three different approaches, experimental data of Guido, Simeone, and Greco [203], analytical predictions of Maffettone and Greco [204] and numerical results of Aggarwal and Sarkar [160].

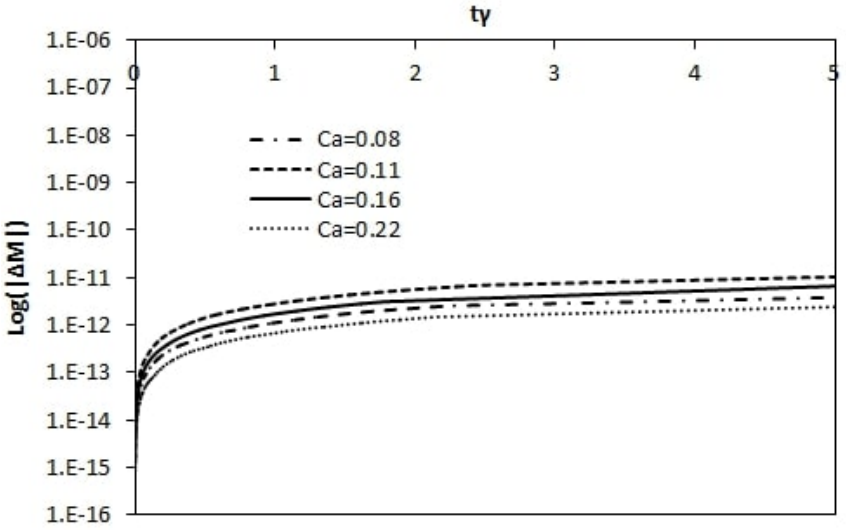

FIGURE 4.19: The evolution in the mass conservation error of the droplet for cases of Newtonian droplet suspended in viscoelastic matrix imposed to shear with four different Capillary numbers of 0.08, 0.11, 0.16 and 0.22, and Deborah numbers of $De = 0.6 \times Ca$. The value of ΔM for the droplet is $(M_t - M_0)/M_0$, where M_0 is droplet's initial mass and M_t is the mass at time t.

applied.

The accuracy of the proposed method on capturing the transient solution of this problem is studied by performing a simulation with Capillary number of 0.2 and Deborah number of 1.5. Figure 4.16 shows the time variation of Taylor deformation parameter (D) for this case compared with the results of finite-difference/front-tracking method of Aggarwal and Sarkar [160]. Good agreement is seen between these results.

In order to study the accuracy of the method on solving this problem for a wider range of Deborah numbers, simulations with different Capillary numbers but all with a constant elasticity parameter of P=De/Ca=0.6 are done for a long enough time to reach steady-state. For each case, Taylor deformation parameter (D), and droplet inclination angle of θ are extracted. Figures 4.17 and 4.18 illustrates these results compared with results of different methods, i.e. experimental data of Guido, Simeone, and Greco [203], analytical predictions of Maffettone and Greco [204] and numerical results of Aggarwal and Sarkar [160]. Good agreement is seen between the results of current study, and the results of numerical study of Aggarwal and Sarkar [160] in all the cases.

There is also a good agreement between the results of current study, and the experimental data of Guido, Simeone, and Greco [203] and also analytical predictions of Maffettone and Greco [204] for smaller Capillary numbers. For higher Capillary numbers in these two figures, however, the disparity of the numerical results compared with experimental data and analytical predictions grows. This disparity could be associated to the inability of the Oldroyd-B constitutive equation used in this study to correctly represents the experimental fluid used by Guido, Simeone, and Greco [203]. Figure 4.19 represents the evolution of mass conservation error of the droplet for different cases solved in this section. It could be seen that for all these cases, the mass conservation error of the droplet, ΔM, (calculated as $\Delta M = (M_t - M_0)/M_0$, with M_0 as droplet's initial mass and M_t as the mass at time t) has converged to a very small value in the order of $O(10^{-11})$.

In order to study the ability of the method in solving more challenging cases, the LCR method, integrated with cut-off approach is used to solve three high Deborah number shear deformation problems of:

(a) Newtonian droplet suspended in viscoelastic matrix with Deborah number of 5.0.

(b) Viscoelastic droplet with Deborah number of 7.5 suspended in a Newtonian matrix.

(c) Viscoelastic droplet with Deborah number of 7.5 suspended in a viscoelastic matrix with Deborah number of 5.0.

In all these cases, the $Re = 1.0$, $Ca = 2.0$, $\beta = 0.5$ and $\mu_{d0}/\mu_{m0} = 1.0$ are applied. Simulation of case (b) was converged to steady-state within the limit of $t/t^* = 10$. Cases (a) and (c), however, required more time to reach steady-state. Figure 4.20 presents the Taylor deformation (D), L_P and W parameters as introduced in figure 4.15, as a function of time. There is an overshoot in the value of Taylor deformation parameter of case (b).The overshoots in sub-critical deformation of Newtonian droplets suspended in Newtonian matrix happens only in highly confined domains. Thus the overshoot in the value of D witnessed in figure 4.20, corresponds to the non-Newtonian highly viscoelastic nature of the droplet.

Case (a) on the other hand, exhibits a more uniform deformation, carried on with a retraction in deformation of the droplet at times around $t/t^* = 14$. Similar to case (b),

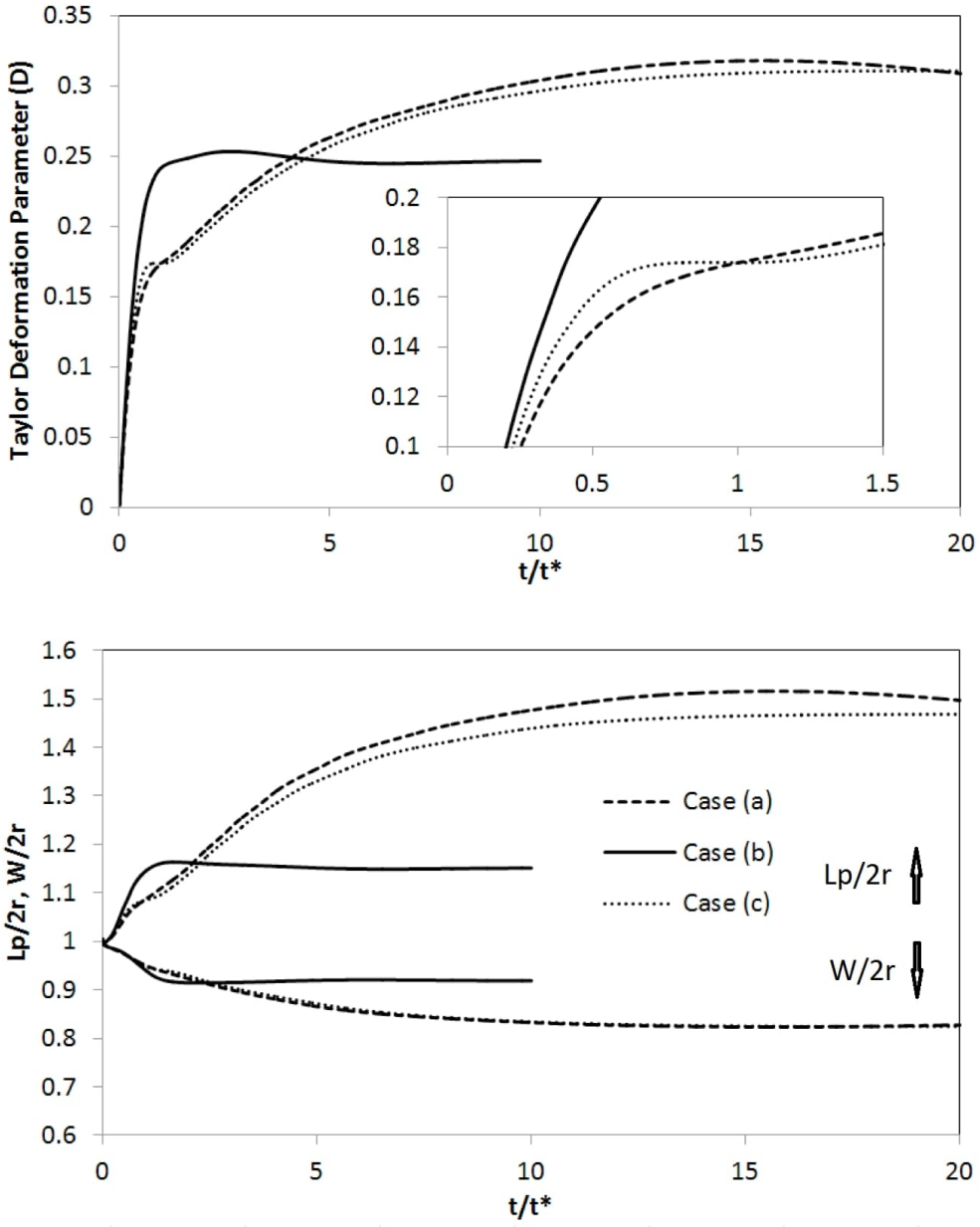

FIGURE 4.20: Startup variation of Top: Taylor Deformation Parameter (D) and Bottom: $L_p/2r$ and W/2r parameters Vs. t/t^* for cases (a), (b) and (c) of droplet deformation in shear flow.

in case (c), at times around $t/t^* = 1$ there is an overshoot in deformation of the droplet. By observing the existence of overshoot in deformation of the droplets, in cases (b) and (c) and its absence in case (a), one can conclude that the highly viscoelastic nature of the droplet can cause the droplet to retract after an initially larger deformation, and undertake overshoots in its deformation. On the other hand, by observing a more uniform deformation of the droplet in cases (a) and (c), one can conclude that the viscoelastic nature of the matrix results in a more smooth deformation of the droplet over time.

Figure 4.21 illustrates the droplets shape along with the flow streamlines with vorticity magnitude and pressure contours for the cases (a), (b) and (c) at the end of the solution process. According to this figure, The viscoelastic matrix causes that the Newtonian droplet to loose its elliptical shape. Droplet inclination angle of case (b) is notably higher than the other two cases, which is in agreement with its lower Taylor deformation parameter. In the solution process of all of these cases, no numerical difficulties were witnessed.

A grid convergence analysis is performed for the case (c), viscoelastic droplet with Deborah number of 7.5 suspended in a viscoelastic matrix with Deborah number of 5.0. Four different grid sizes of h=d/25, d/30, d/35 and d/40 are selected to discretize the aforementioned domain. For each case, the numerical simulation was done until $t/t^* = 20$. The variation of Taylor deformation parameter (D) of the solution with the finest grid (h=d/40) is selected as the reference data and the results of other simulations are compared with it. For each case, the error related to the Taylor deformation parameter (D) at each timestep is calculated. Accumulated value of these errors are calculated as the first norm of the error using $L_1 = \sum_i |e_i|$, where e_i is the difference between Taylor deformation parameter of the simulation and its corresponding value in reference solution at i-th iteration. Figure 4.22 presents the values of L_1 as a function of the grid size. As can be seen, the solution process illustrates an order of convergence of 1.88 in space.

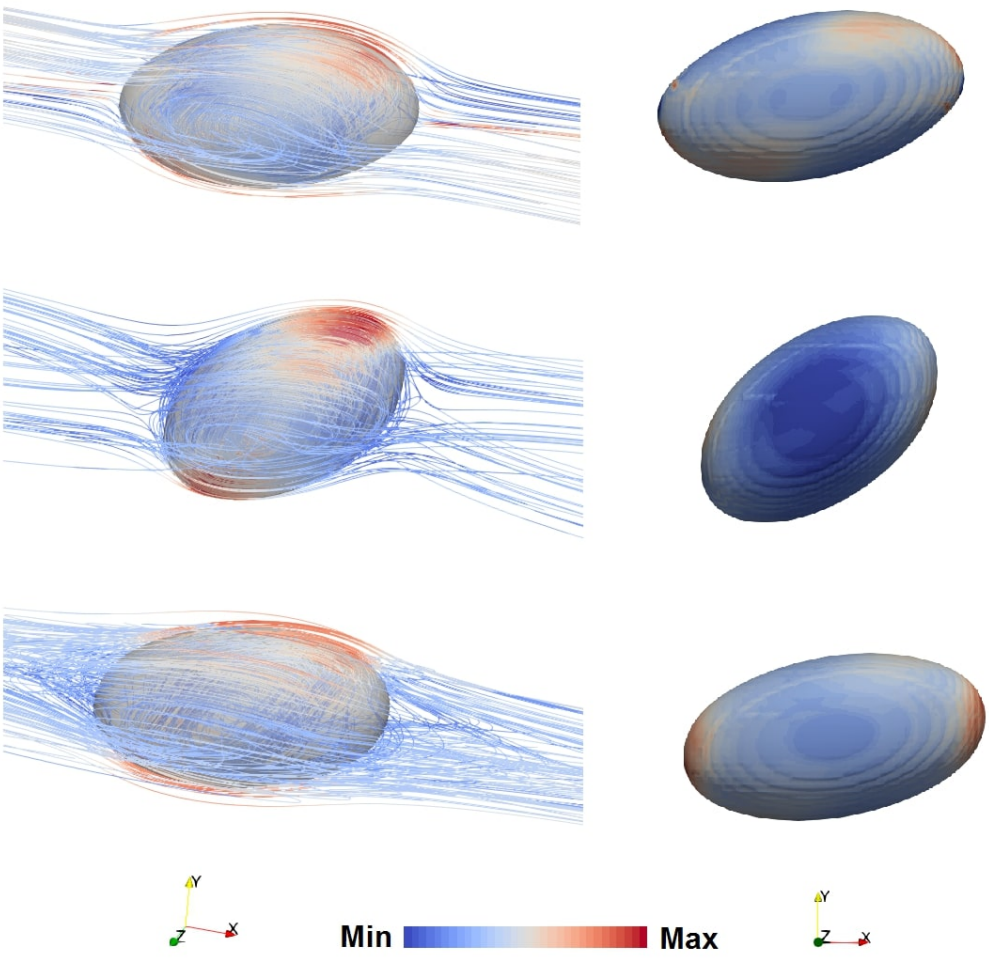

FIGURE 4.21: Left: droplets shape along with the flow streamlines with vorticity magnitude contours, Right: droplets shape along with pressure contours. Images correspond to the cases, Top: case (a) extracted at t/t^*=20, Middle: case (b) extracted at t/t^*=10, and Bottom: case (c) extracted at t/t^*=20.

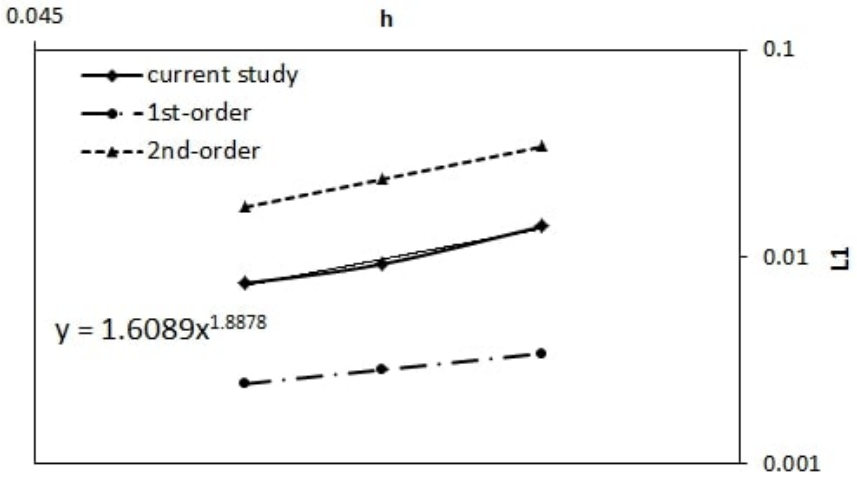

FIGURE 4.22: First norm of the error in calculation of Taylor deformation parameter (D) during the solution process of the case (c) inside of the domains with grid sizes of $h = d/25, d/30$ and $d/35$ compared with the reference values of solution in a domain with grid size of $h = d/40$.

4.8 Conclusions

A finite-volume conservative level-set based method was introduced in order to solve non-Newtonian multiphase flow problems. The main challenges in this area including tracking of interfaces, mass conservation of the phases, small timestep problems encountered by non-Newtonian fluids, numerical instabilities regarding the high Weissenberg number problem (HWNP), instabilities encouraged by low solvent to polymer viscosity ratio in viscoelastic fluids (LVRP) and instabilities encountered by surface tensions were addressed and proper numerical treatments were provided in the proposed method. For small timestep problem, specially in shear-thinning and shear-thickening fluids where the unexpected increase in kinematic viscosity can dramatically decrease the timestep of the simulation, our proposed discretization method successfully eliminated the timestep restrictions encountered by viscosity. The proposed cut-off approach was investigated for different viscoelastic combinations of droplet/matrix. Using this approach enables us to substitute the SAM method with LCR formulation, resulting in elimination of HWNP for multiphase fluids. The proposed discretization of predictor step of momentum equation eliminated the LVRP for

a challenging case with $\beta = 0.0014$. The conservative formulation of the level-set function preserves the mass of the droplet during the whole simulation.

Different test cases with different rheological properties were solved in order to validate the accuracy of the method. The fluid of a Poiseuille flow was solved for rheologies of shear-thinning, shear-thickening and viscoelastic fluids and the results were compared with analytical exact solutions. For viscoelastic droplet, a test case of impacting droplet problem was selected and the results were compared with the available data in literature. A three-dimensional sudden contraction/expansion test case was solved and the results were compared with the experimental figures. For viscoelastic matrix, a three-dimensional shear deformation problem was solved for a wide range of Deborah parameters. The extracted results were compared with analytical, experimental and numerical predictions. In all these cases, good agreement was seen between the results extracted in the current study, and the benchmark data available in the literature. In addition to validation cases, three challenging high Weissenberg number test cases were solved and the results were discussed.

Acknowledgments

This work has been financially supported by the *Ministerio de Economía y Competitividad, Secretaría de Estado de Investigación, Desarrollo e Innovación*, Spain (ENE2015-70672-P). I acknowledges the financial support of an FI research scholarship by the *Agència de Gestió d'Ajuts Universitaris i de Recerca (AGAUR) of Generalitat de Catalunya* (2016 FI_B 01059). I thankfully acknowledge the computer resources at Altamira and the technical support provided by Instituto de Física de Cantabria - Universidad de Cantabria (RES-FI-2018-3-0045).

Chapter 5

Conclusions and further work

5.1 Concluding remarks

In this thesis, two multiphase problems which are being frequently encountered in industrial applications were studied, i.e. deformation and breakup of a droplet in shear flow and collision of the droplets. The main challenges in each of these problems were discussed in details, while the proper numerical solutions for these challenges were proposed. Besides, a set of numerical tools were developed to solve non-Newtonian multiphase flow problems for fluids with rheologies of shear-thinning, shear-thickening and viscoelastic. The focus of this work has been on the simulation of interfacial flows, where a distinguishable interface exists between the phases. The numerical methods have been implemented in an in-house C++ code called TermoFluids [47].

In chapter 2, a conservative level-set method was used to perform DNS of head-on, and off-center binary droplets collision in the main collision regimes. A novel lamella stabilization approach was introduced to numerically resolves the lamella film, independent of its formation direction. The use of this approach results in a considerable reduction of computational cost while maintaining a good accuracy. Also, a new gas-film stabilization approach was proposed to prevent adding mass into the droplet which was used to extract the gas-film rupture time in collisions with retarded coalescence. For all the simulations of this chapter, the snapshots of the evolution of the collision process were compared with available experimental data where good agreement was seen. Very comprehensive energy analysis was done to provide more insight into the collision process.

In chapter 3, a finite-volume conservative level-set based method was utilized to numerically simulate three-dimensional droplet deformation and breakup subjected to shear flow. A semi-implicit discretization approach was applied to the momentum equation, enabling us to employ larger time-steps in low Reynolds number simulations. Similar to the previous chapter, utmost efforts were devoted to the accuracy of the results. Thus we highly validated and verified our numerical method against experimental data available in the literature. We have selected validation test cases that concern the physical behaviours appearing in deformation and breakup of the droplet, including break-up of the droplet into satellite and sub-satellite droplets, deformation of the droplet under walls confinement effect, deformation of the droplet in different

viscosity ratios, etc. Afterwards, we elaborately studied the mutual effect of viscosity ratio and confinement of the walls on droplet deformation and breakup. Our results illustrate the existence of two steady-state regions separated by one breakup region for droplet under different confinements and viscosity ratios. This information is valuable in more effective design of future droplet-based microfluidic devices, reactive dispersions, emulsification process, morphology development of blends and Lab-on-a-Chip systems for individual purposes with methods discussed in this paper, namely, by adjusting the viscosity or confinement ratios of the existing shear flow to the appropriate values to control the droplet volume.

In chapter 4, we introduced a novel numerical methodology to accurately solve the interfacial flow problems where one or more phases represents non-Newtonian behaviour. We discussed the challenges in this field that are added to the previous challenges in numerical simulation of multiphase flows. Complexity in numerical simulation of non-Newtonian multiphase flows does not arise only from the interface tracking of different fluids or the mass conservation of the phases but also from the physics that governs the system, e.g. instabilities caused by relaxation characteristics of viscoelastic fluids, the high Weissenberg number problem (HWNP), instabilities encouraged by the low solvent to polymer viscosity ratio in viscoelastic fluids and instabilities encountered by surface tensions. We suggested the most prominent solution for each of these challenges and highly validated and verified our numerical method against experimental, analytical and numerical data available in the literature. Our proposed approach has proven to be numerically stable for solutions with high Weissenberg number, and low solvent to polymer viscosity ratio.

5.2 Further work

Regarding the droplets collision study presented in chapter 2, one may notice that in a wide range of applications of this field, the droplets may illustrate non-Newtonian behaviour. E.g. gelled hypergolic propellants (GHP), which are promising fuels for next-generation missile and rocket engines are known to have non-Newtonian rheologies, which are much less understood compared with collision roadmap of Newtonian fluids. In this regard, a detailed study on the collision outcome of non-Newtonian

droplets with different rheologies of shear-thinning, shear-thickening and viscoelastic would be of high interest.

Regarding the droplet deformation and breakup in shear flow presented in chapter 3, we have illustrated the existence of two steady-state regions separated by one breakup region for droplet under different confinements and viscosity ratios, all for a constant capillary number of 0.3. However, it will be of high interest to investigate the effect of different capillary numbers on the steady-state and breakup regions illustrated in this chapter. Besides, the effect of shear flow on the coalescence of adjacent droplets is not fully understood.

A large number of complex engineering applications and physical phenomena require the analysis of the free surface flows, e.g. in casting, coating, motion and breakup of waves, as well as their interaction with solid boundaries, etc. In many of these free-surface applications, the fluids exhibit non-Newtonian rheologies. Thus, it will be of high interest to study the applicability of the proposed numerical approach for the solution of non-Newtonian multiphase flows in chapter 4 on free surface problems.

Slug flow is a frequently found multiphase flow pattern when a system of a gas bubble suspended in a matrix fluid concurrently flow in a pipe. For example in side-stream (airlift) membrane bioreactors (MBR), the vertical tubular membranes are located outside of the bioreactor, the sludge is pumped from the bioreactor to the membrane modules, and the air is added at the base of the membranes to gain a two-phase slug flow of appropriate regime. Taylor bubbles are the primary units of this pattern. Taylor bubbles are characterised by their width which almost fills the cross-section of the tube and by their length which is usually above 2 or 3 tube diameters long. They are separated from the tube wall by a thin matrix film which expands when it reaches the rear end of the bubble. This expansion leads to the formation of a wake. Compared to the related topic in Newtonian fluids, state of the art about the characteristics of Taylor bubbles rising in non-Newtonian matrices is still in an early stage. Although this two-phase flow pattern is frequently found in different practical applications, i.e. oil and gas transportation in wells, processing of polymers, wastewater treatment, geothermal applications, polymer devolatilisation, air-lift reactors, phase-change cooling systems, emboli in bloodstreams, reverse osmosis systems, etc. Therefore, there is a need for extending the slug flow research towards non-Newtonian liquids.

Appendix A

List of publications

International Journals

A. Amani, N. Balcázar, E. Gutiérrez, A. Oliva. *Numerical study of binary droplets collision in the main collision regimes.* Chemical Engineering Journal, 1385-8947, 2019, https://doi.org/10.1016/j.cej.2019.03.188

A. Amani, N. Balcázar, J. Castro, A. Oliva. *Numerical study of droplet deformation in a shear flow using a conservative level-set method.* Chemical Engineering Science, 207 (2019), 153-171, https://doi.org/10.1016/j.ces.2019.06.014

Papers in Preparation

A. Amani, N. Balcázar, A. Naseri, A. Oliva. *A numerical approach for non-Newtonian two-phase flows using a conservative level-set method.* Under review for publication in Chemical Engineering Journal.

Conference Proceedings

A. Amani, N. Balcázar, A. Naseri, A. Oliva. *A Study on Binary Collision of*

GNF Droplets Using a Conservative Level-Set Method. In proceeding of 7th European Conference on Computational Fluid Dynamics (ECFD 7), June 2018, Glasgow.

A. Amani, N. Balcázar, E. Gutiérrez, A. Oliva. *DNS of un-equal size droplets collision using a moving-mesh/level-set method.* ERCOFTAC WORKSHOP DIRECT AND LARGE EDDY SIMULATION 12 (DLES 12), June 2019, Madrid.

Supercomputing projects

RES-FI-2018-3-0045: DNS of binary droplet collision in Newtonian and non-Newtonian fluids. 750kh at Altamira, from 2018-11-01 to 2019-03-01

Bibliography

[1] Ahmad Amani et al. “Numerical study of binary droplets collision in the main collision regimes”. In: *Chemical Engineering Journal* (2019). DOI: https://doi.org/10.1016/j.cej.2019.03.188.

[2] Ahmad Amani et al. “A Study on Binary Collision of GNF Droplets Using a Conservative Level-Set Method”. In: *6th European Conference on Computational Mechanics (ECCM 6)- 7th European Conference on Computational Fluid Dynamics (ECFD 7)*. Glasgow, UK, 2018.

[3] Ahmad Amani et al. “DNS of un-equal size droplets collision using a moving-mesh/level-set method”. In: *ERCOFTAC workshop direct and large eddy simulation 12 (DLES 12)*. Madrid, Spain, 2019.

[4] Ahmad Amani et al. “Numerical study of droplet deformation in shear flow using a conservative level-set method”. In: *Chemical Engineering Science* (2019). DOI: https://doi.org/10.1016/j.ces.2019.06.014.

[5] † T. G. Mason* and and J. Bibette‡. “Shear Rupturing of Droplets in Complex Fluids”. In: *Langmuir* 13.17 (1997), pp. 4600–4613. DOI: 10.1021/la9700580.

[6] J Gounley et al. “Influence of surface viscosity on droplets in shear flow”. In: *J. Fluid Mech* 791 (2016), pp. 464–494. DOI: 10.1017/jfm.2016.39.

[7] R P Chhabra and J F Richardson. “Non-Newtonian flow in the process industries : fundamentals and engineering applications”. In: (1999), pp. xiii, 436.

[8] Lorenzo Tassi. “Chapter 5 - Kinematic viscosity and viscous flow in binary mixtures containing ethane-1,2-diol”. In: *Advances in Engineering Fluid Mechanics: Multiphase Reactor and Polymerization System Hydrodynamics*. Ed. by Nicholas P Cheremisinoff. Burlington: Gulf Professional Publishing, 1996,

pp. 79–104. DOI: https://doi.org/10.1016/B978-088415497-6/50007-3.

[9] Andrey Itkin. "Basics of the Finite Difference Method". In: *Pricing Derivatives Under Lévy Models : Modern Finite-Difference and Pseudo-Differential Operators Approach*. New York, NY: Springer New York, 2017, pp. 3–19. DOI: 10.1007/978-1-4939-6792-6{_}1.

[10] "Fundamentals of Finite Element Method". In: *Meshless Methods in Solid Mechanics*. New York, NY: Springer New York, 2006, pp. 31–54. DOI: 10.1007/0-387-33368-1{_}3.

[11] Bastian E Rapp. "Chapter 31 - Finite Volume Method". In: *Microfluidics: Modelling, Mechanics and Mathematics*. Ed. by Bastian E Rapp. Micro and Nano Technologies. Oxford: Elsevier, 2017, pp. 633–654. DOI: https://doi.org/10.1016/B978-1-4557-3141-1.50031-9.

[12] N G Deen, M Sint Annaland van, and J A M Kuipers. "Multi-scale modeling of dispersed gas-liquid two-phase flow". In: *Chemical Engineering Science* 59.8-9 (2004), pp. 1853–1861. DOI: 10.1016/j.ces.2004.01.038.

[13] Yang Ge and Liang-Shih Fan. "3-D Direct Numerical Simulation of Gas–Liquid and Gas–Liquid–Solid Flow Systems Using the Level-Set and Immersed-Boundary Methods". In: *Computational Fluid Dynamics*. Ed. by Guy B Marin. Vol. 31. Advances in Chemical Engineering. Academic Press, 2006, pp. 1–63. DOI: https://doi.org/10.1016/S0065-2377(06)31001-0.

[14] S Morales-Ruiz et al. "Numerical resolution of the liquid–vapour two-phase flow by means of the two-fluid model and a pressure based method". In: *International Journal of Multiphase Flow* 43 (2012), pp. 118–130. DOI: https://doi.org/10.1016/j.ijmultiphaseflow.2012.03.004.

[15] B G M van Wachem and A E Almstedt. "Methods for multiphase computational fluid dynamics". In: *Chemical Engineering Journal* 96.1 (2003), pp. 81–98. DOI: https://doi.org/10.1016/j.cej.2003.08.025.

[16] Salih Ozen Unverdi and Grétar Tryggvason. "A front-tracking method for viscous, incompressible, multi-fluid flows". In: *Journal of Computational Physics* 100.1 (1992), pp. 25–37. DOI: https://doi.org/10.1016/0021-9991(92)90307-K.

[17] G. Tryggvason et al. "A Front-Tracking Method for the Computations of Multiphase Flow". In: *Journal of Computational Physics* 169.2 (2001), pp. 708–759. DOI: 10.1006/jcph.2001.6726.

[18] Ruben Scardovelli and Stéphane Zaleski. "Direct numerical simulation of free-surface and interfacial flow". In: *Annual Review of Fluid Mechanics* 31.1 (1999), pp. 567–603. DOI: 10.1146/annurev.fluid.31.1.567.

[19] M Sussman and E Fatemi. "An Efficient, Interface-Preserving Level Set Redistancing Algorithm and Its Application to Interfacial Incompressible Fluid Flow". In: *SIAM Journal on Scientific Computing* 20.4 (1999), pp. 1165–1191. DOI: 10.1137/S1064827596298245.

[20] N G Deen, M van Sint Annaland, and J A M Kuipers. "Direct numerical simulation of complex multi-fluid flows using a combined front tracking and immersed boundary method". In: *Chemical engineering science* 64.9 (2009), pp. 2186–2201. DOI: 10.1016/j.ces.2009.01.029.

[21] F Dabbagh et al. "On the evolution of flow topology in turbulent Rayleigh-Bénard convection". In: *Physics of Fluids* 28.11 (2016), p. 115105. DOI: 10.1063/1.4967495.

[22] F X TRIAS et al. "Direct numerical simulations of two- and three-dimensional turbulent natural convection flows in a differentially heated cavity of aspect ratio 4". In: *Journal of Fluid Mechanics* 586 (2007), 259–293. DOI: 10.1017/S0022112007006908.

[23] J Ventosa-Molina et al. "Large Eddy Simulation of aTurbulent Diffusion Flame: Some Aspects of Subgrid Modelling Consistency". In: *Flow, Turbulence and Combustion* 99.1 (July 2017), pp. 209–238. DOI: 10.1007/s10494-017-9813-2.

[24] Nestor Balcazar et al. “A finite-volume/level-set method for simulating two-phase flows on unstructured grids”. In: *International Journal of Multiphase Flow* 64 (2014), pp. 55–72. DOI: 10.1016/j.ijmultiphaseflow.2014.04.008.

[25] Néstor Balcázar et al. “A coupled volume-of-fluid/level-set method for simulation of two-phase flows on unstructured meshes”. In: *Computers & Fluids* 124 (2016), pp. 12–29. DOI: 10.1016/j.compfluid.2015.10.005.

[26] Néstor Balcázar et al. “Level-set simulations of buoyancy-driven motion of single and multiple bubbles”. In: *International Journal of Heat and Fluid Flow* 56 (2015), pp. 91–107. DOI: http://dx.doi.org/10.1016/j.ijheatfluidflow.2015.07.004.

[27] Néstor Balcázar et al. “A multiple marker level-set method for simulation of deformable fluid particles”. In: *International Journal of Multiphase Flow* 74 (2015), pp. 125–142. DOI: 10.1016/j.ijmultiphaseflow.2015.04.009.

[28] E Gutiérrez et al. “Numerical approach to study bubbles and drops evolving through complex geometries by using a level set – Moving mesh – Immersed boundary method”. In: *Chemical Engineering Journal* 349.February (2018), pp. 662–682. DOI: 10.1016/j.cej.2018.05.110.

[29] Néstor Balcázar et al. “A level-set model for thermocapillary motion of deformable fluid particles”. In: *International Journal of Heat and Fluid Flow* 0 (2016), pp. 1–20. DOI: 10.1016/j.ijheatfluidflow.2016.09.015.

[30] Néstor Balcázar et al. “DNS of the wall effect on the motion of bubble swarms”. In: *Procedia Computer Science*. Vol. 108. 2017, pp. 2008–2017. DOI: 10.1016/j.procs.2017.05.076.

[31] Néstor Balcázar-Arciniega et al. “A level-set model for mass transfer in bubbly flows”. In: *International Journal of Heat and Mass Transfer* 138 (2019), pp. 335–356. DOI: 10.1016/j.ijheatmasstransfer.2019.04.008.

[32] Oscar Antepara et al. “Numerical study of rising bubbles with path instability using conservative level-set and adaptive mesh refinement”. In: *Computers and Fluids* (2019). DOI: 10.1016/j.compfluid.2019.04.013.

[33] Eugenio Schillaci et al. “A numerical study of liquid atomization regimes by means of conservative level-set simulations”. In: *Computers and Fluids* (2019). DOI: 10.1016/j.compfluid.2018.10.017.

[34] E Gutiérrez et al. “Numerical study of Taylor bubbles rising in a stagnant liquid using a level-set/moving-mesh method”. In: *Chemical Engineering Science* 164.Supplement C (2017), pp. 158–177. DOI: https://doi.org/10.1016/j.ces.2017.02.018.

[35] Eugenio Schillaci et al. “A low-dissipation convection scheme for the stable discretization of turbulent interfacial flow”. In: *Computers and Fluids* (2017). DOI: 10.1016/j.compfluid.2017.05.009.

[36] Eugenio Schillaci et al. “A level-set aided single-phase model for the numerical simulation of free-surface flow on unstructured meshes”. In: *Computers and Fluids* 140 (2016), pp. 1339–1351. DOI: 10.1016/j.compfluid.2016.09.014.

[37] N. Balcázar et al. “DNS of thermocapillary migration of deformable droplets In: Salvetti M., Armenio V., Fröhlich J., Geurts B., Kuerten H. (eds)”. In: *Direct and Large-Eddy Simulation XI. ERCOFTAC Series*. 25th ed. Springer, 2019. DOI: 10.1007/978-3-030-04915-7{_}28.

[38] O.; Castro J.; Oliva A. Balcázar N.; Lehmkuhl. “DNS of the rising motion of a swarm of bubbles in a confined vertical channel”. In: *ERCOFTAC Symposium on Direct and Large-Eddy Simulations, DLES10*. Limassol, Cyprus.

[39] Néstor Balcázar et al. “DNS of falling droplets in a vertical channel”. In: *International Journal of Computational Methods and Experimental Measurements* (2018). DOI: 10.2495/CMEM-V6-N2-398-410.

[40] Eugenio Schillaci et al. “Numerical study of an impulse wave generated by a sliding mass”. In: *International Journal of Computational Methods and Experimental Measurements* (2018). DOI: 10.2495/CMEM-V6-N1-98-109.

[41] Enrique Gutiérrez et al. “On the solution of the problem of a drop falling against a plane by using a level set – Moving mesh – Immersed boundary

method". In: *International Journal of Computational Methods and Experimental Measurements* (2018). DOI: 10.2495/CMEM-V6-N1-208-219.

[42] A.; Rigola J. Balcázar N.; Oliva. "A level-set method for thermal motion of bubbles and droplets." In: *7th European Thermal-Sciences Conference (Eurotherm2016). Journal of Physics: Conference Series 745*. 2016. DOI: 10.1088/1742-6596/745/3/032113.

[43] Nestor Balcazar. "Numerical simulation of Multiphase Flows: Level-Set Techniques". PhD thesis. Universitat Politecnica de Catalunya – BarcelonaTech (UPC), 2014, p. 218.

[44] F Favre et al. "Numerical simulations of conjugate convection combined with surface thermal radiation using an Immersed-Boundary Method". In: *Journal of Physics: Conference Series* 745 (Sept. 2016), p. 32017. DOI: 10.1088/1742-6596/745/3/032017.

[45] F X Trias, A Gorobets, and A Oliva. "A simple approach to discretize the viscous term with spatially varying (eddy-)viscosity". In: *Journal of Computational Physics* 253 (2013), pp. 405–417. DOI: https://doi.org/10.1016/j.jcp.2013.07.021.

[46] R Borrell et al. "Optimising the Termofluids CFD code for petascale simulations". In: *International Journal of Computational Fluid Dynamics* 30.6 (2016), pp. 425–430. DOI: 10.1080/10618562.2016.1221503.

[47] *Termo Fluids S.L.* \url{http://www.termofluids.com/}.

[48] Milorad P. Dudukovic, Faical Larachi, and Patrick L. Mills. "Multiphase reactors - revisited". In: *Chemical Engineering Science* 54.13-14 (1999), pp. 1975–1995. DOI: 10.1016/S0009-2509(98)00367-4.

[49] Zaillang Hu and R C Srivastava. "Evolution of Raindrop Size Distribution by Coalescence, Breakup, and Evaporation: Theory and Observations". In: *Journal of the Atmospheric Sciences* 52.10 (1995), pp. 1761–1783. DOI: 10.1175/1520-0469(1995)052<1761:EORSDB>2.0.CO;2.

[50] N. Ashgriz and J. Y. Poo. "Coalescence and separation in binary collisions of liquid drops". In: *Journal of Fluid Mechanics* 221 (1990), pp. 183–204. DOI: 10.1017/S0022112090003536.

[51] J. Qian and C. K. Law. "Regimes of coalescence and separation in droplet collision". In: *Journal of Fluid Mechanics* 331 (1997), pp. 59–80. DOI: 10.1017/S0022112096003722.

[52] Carole Planchette, Elise Lorenceau, and Günter Brenn. "Binary collisions of immiscible liquid drops for liquid encapsulation". In: *Fluid Dynamics and Materials Processing* 7.3 (2011), pp. 279–302. DOI: 10.3970/fdmp.2011.007.279.

[53] P. R. Brazier-Smith, S. G. Jennings, and J. Latham. "The Interaction of Falling Water Drops: Coalescence". In: *Proceedings of the Royal Society A: Mathematical, Physical and Engineering Sciences* 326.1566 (1972), pp. 393–408. DOI: 10.1098/rspa.1972.0016.

[54] G Brenn and A Frohn. "Collision and coalescence of droplets of various liquids". In: *Journal of Aerosol Science* 20.8 (1989), pp. 1027–1030. DOI: https://doi.org/10.1016/0021-8502(89)90753-2.

[55] Y. J. Jiang, A. Umemura, and C. K. Law. "An experimental investigation on the collision behaviour of hydrocarbon droplets". In: *Journal of Fluid Mechanics* 234 (1992), pp. 171–190. DOI: 10.1017/S0022112092000740.

[56] K D Willis and M E Orme. "Experiments on the dynamics of droplet collisions in a vacuum". In: *Experiments in Fluids* 29.4 (Oct. 2000), pp. 347–358. DOI: 10.1007/s003489900092.

[57] Kuo Long Pan, Chung K. Law, and Biao Zhou. "Experimental and mechanistic description of merging and bouncing in head-on binary droplet collision". In: *Journal of Applied Physics* 103.6 (2008). DOI: 10.1063/1.2841055.

[58] Chenglong Tang, Peng Zhang, and Chung K. Law. "Bouncing, coalescence, and separation in head-on collision of unequal-size droplets". In: *Physics of Fluids* 24.2 (2012). DOI: 10.1063/1.3679165.

[59] Kuo Long Pan, Ping Chung Chou, and Yu Jen Tseng. "Binary droplet collision at high Weber number". In: *Physical Review E - Statistical, Nonlinear, and Soft Matter Physics* 80.3 (2009), pp. 1–8. DOI: 10.1103/PhysRevE.80.036301.

[60] C. Planchette et al. "Colliding drops as coalescing and fragmenting liquid springs". In: *Journal of Fluid Mechanics* 814 (2017), pp. 277–300. DOI: 10.1017/jfm.2016.852.

[61] K. L. Pan et al. "Controlling droplet bouncing and coalescence with surfactant". In: *Journal of Fluid Mechanics* 799 (2016), pp. 603–636. DOI: 10.1017/jfm.2016.381.

[62] J. P. Estrade et al. "Experimental investigation of dynamic binary collision of ethanol droplets - a model for droplet coalescence and bouncing". In: *International Journal of Heat and Fluid Flow* 20.5 (1999), pp. 486–491. DOI: 10.1016/S0142-727X(99)00036-3.

[63] Thierry L. Georjon Reitz and Rolf D. "A drop-shattering collision model for multidimensional spray computations". In: *Atomization and Sprays* 9.1044-5110 (1999), pp. 231–254.

[64] Donald L Gopinath Arvind Koch. "Collision and rebound of small droplets in an incompressible continuum gas". In: *Journal of Fluid Mechanics* 454 (2002), 145–201. DOI: 10.1017/S0022112001006966.

[65] Gloria A Bach, Donald L Koch, and Arvind Gopinath. "Coalescence and bouncing of small aerosol droplets". In: *Journal of Fluid Mechanics* 518 (2004), 157–185. DOI: 10.1017/S0022112004000928.

[66] Peng Zhang and Chung K. Law. "An analysis of head-on droplet collision with large deformation in gaseous medium". In: *Physics of Fluids* 23.4 (2011). DOI: 10.1063/1.3580754.

[67] Jie Li. "Macroscopic model for head-on binary droplet collisions in a gaseous medium". In: *Physical Review Letters* 117.21 (2016), pp. 1–5. DOI: 10.1103/PhysRevLett.117.214502.

[68] N. Nikolopoulos and G. Bergeles. "The effect of gas and liquid properties and droplet size ratio on the central collision between two unequal-size droplets in the reflexive regime". In: *International Journal of Heat and Mass Transfer* 54.1-3 (2011), pp. 678–691. DOI: 10.1016/j.ijheatmasstransfer.2010.09.002.

[69] N. Nikolopoulos, A. Theodorakakos, and G. Bergeles. "Off-centre binary collision of droplets: A numerical investigation". In: *International Journal of Heat and Mass Transfer* 52.19-20 (2009), pp. 4160–4174. DOI: 10.1016/j.ijheatmasstransfer.2009.04.011.

[70] Xiaodong Chen et al. "Energy and Mass Transfer during Binary Droplet Collision". In: *49th AIAA Aerospace Sciences Meeting including the New Horizons Forum and Aerospace Exposition*. Aerospace Sciences Meetings. American Institute of Aeronautics and Astronautics, Jan. 2011. DOI: doi:10.2514/6.2011-771.

[71] Yu Pan and Kazuhiko Suga. "Numerical simulation of binary liquid droplet collision". In: *Physics of Fluids* 17.8 (2005), pp. 1–14. DOI: 10.1063/1.2009527.

[72] Sébastien Tanguy and Alain Berlemont. "Application of a level set method for simulation of droplet collisions". In: *International Journal of Multiphase Flow* 31 (2005), pp. 1015–1035. DOI: 10.1016/j.ijmultiphaseflow.2005.05.010.

[73] Marcel Kwakkel, Wim Paul Breugem, and Bendiks Jan Boersma. "Extension of a CLSVOF method for droplet-laden flows with a coalescence/breakup model". In: *Journal of Computational Physics* 253 (2013), pp. 166–188. DOI: 10.1016/j.jcp.2013.07.005.

[74] M R Nobari, Y.-J Jan, and G Tryggvason. "Head-on Collisions of Drops - A Numerical Investigation". In: *Physics of Fluids* 8.1 (1996), pp. 29–42.

[75] Zhenyu Zhang and Peng Zhanga. "Kinetic energy recovery and interface hysteresis of bouncing droplets after inelastic head-on collision". In: *Physics of Fluids* 29.10 (2017). DOI: 10.1063/1.5000547.

[76] Ali Mazloomi Moqaddam, Shyam S. Chikatamarla, and Ilya V. Karlin. "Simulation of binary droplet collisions with the entropic lattice Boltzmann method". In: *Physics of Fluids* 28.2 (2016). DOI: 10.1063/1.4942017.

[77] Kannan N. Premnath and John Abraham. "Simulations of binary drop collisions with a multiple-relaxation-time lattice-Boltzmann model". In: *Physics of Fluids* 17.12 (2005), pp. 1–21. DOI: 10.1063/1.2148987.

[78] Pablo M. Dupuy et al. "Modelling of high pressure binary droplet collisions". In: *Computers and Mathematics with Applications* 61.12 (2011), pp. 3564–3576. DOI: 10.1016/j.camwa.2010.05.044.

[79] Lina Baroudi, Masahiro Kawaji, and Taehun Lee. "Effects of initial conditions on the simulation of inertial coalescence of two drops". In: *Computers and Mathematics with Applications* 67.2 (2014), pp. 282–289. DOI: 10.1016/j.camwa.2013.05.002.

[80] Kai Sun, Ming Jia, and Tianyou Wang. "Numerical investigation on the head-on collision between unequal-sized droplets with multiple-relaxation-time lattice Boltzmann model". In: *International Journal of Heat and Mass Transfer* 70 (2014), pp. 629–640. DOI: 10.1016/j.ijheatmasstransfer.2013.11.055.

[81] A M Mazloomi, S S Chikatamarla, and I V Karlin. "Entropic Lattice Boltzmann Method for Multiphase Flows". In: *Physical Review Letters* 114.17 (2015), p. 174502. DOI: 10.1103/PhysRevLett.114.174502.

[82] Elin Olsson and Gunilla Kreiss. "A conservative level set method for two phase flow". In: *Journal of Computational Physics* 210.1 (2005), pp. 225–246. DOI: http://dx.doi.org/10.1016/j.jcp.2005.04.007.

[83] J U Brackbill, D B Kothe, and C Zemach. "A continuum method for modeling surface tension". In: *Journal of Computational Physics* 100.2 (1992), pp. 335–354. DOI: http://dx.doi.org/10.1016/0021-9991(92)90240-Y.

[84] Alexandre Joel Chorin. "Numerical solution of the Navier-Stokes equations". In: *Mathematics of Computation* 22.104 (1968), pp. 745–745. DOI: 10.1090/S0025-5718-1968-0242392-2.

[85] Sigal Gottlieb and Chi-Wang Shu. "Total variation diminishing Runge-Kutta schemes". In: *Mathematics of computation of the American Mathematical Society* 67.221 (1998), pp. 73–85.

[86] C M Rhie and W L Chow. "Numerical study of the turbulent flow past an airfoil with trailing edge separation". In: *AIAA journal* 21.11 (1983), pp. 1525–1532.

[87] Néstor Balcázar et al. "A level-set model for thermocapillary motion of deformable fluid particles". In: *International Journal of Heat and Fluid Flow* 62.Part B (2016), pp. 324–343. DOI: https://doi.org/10.1016/j.ijheatfluidflow.2016.09.015.

[88] Néstor Balcázar et al. "A multiple marker level-set method for simulation of deformable fluid particles". In: *International Journal of Multiphase Flow* 74 (2015), pp. 125–142. DOI: http://dx.doi.org/10.1016/j.ijmultiphaseflow.2015.04.009.

[89] Néstor Balcázar et al. "A coupled volume-of-fluid/level-set method for simulation of two-phase flows on unstructured meshes". In: *Computers and Fluids* 124 (2016), pp. 12–29.

[90] Néstor Balcázar et al. "DNS of the wall effect on the motion of bubble swarms". In: *Procedia Computer Science* 108.Supplement C (2017), pp. 2008–2017. DOI: https://doi.org/10.1016/j.procs.2017.05.076.

[91] Lachlan R Mason, Geoffrey W Stevens, and Dalton J E Harvie. "Multi-scale volume of fluid modelling of droplet coalescence". In: *The 9th International Conference on CFD in the Minerals and Process Industries* December (2012), pp. 1–6.

[92] X. Jiang and A. J. James. "Numerical simulation of the head-on collision of two equal-sized drops with van der Waals forces". In: *Journal of Engineering Mathematics* 59.1 (2007), pp. 99–121. DOI: 10.1007/s10665-006-9091-9.

[93] K Willis and M Orme. "Binary droplet collisions in a vacuum environment: an experimental investigation of the role of viscosity". In: *Experiments in Fluids* 34.1 (Jan. 2003), pp. 28–41. DOI: 10.1007/s00348-002-0526-4.

[94] C Focke and D Bothe. “Direct numerical simulation of binary off-center collisions of shear thinning droplets at high Weber numbers”. In: *Physics of Fluids* 24.7 (2012). DOI: 10.1063/1.4737582.

[95] M. Liu and D. Bothe. “Numerical study of head-on droplet collisions at high Weber numbers”. In: *Journal of Fluid Mechanics* 789 (2016), pp. 785–805. DOI: 10.1017/jfm.2015.725.

[96] P. H. Gaskell and A. K C Lau. “Curvature-compensated convective transport: SMART, A new boundedness preserving transport algorithm”. In: *International Journal for Numerical Methods in Fluids* 8.6 (1988), pp. 617–641. DOI: 10.1002/fld.1650080602.

[97] P. K. Sweby. “High Resolution Schemes Using Flux Limiters for Hyperbolic Conservation Laws”. In: *SIAM Journal on Numerical Analysis* 21.5 (1984), pp. 995–1011. DOI: 10.1137/0721062.

[98] F. Mashayek and N. Ashgriz. “Nonlinear oscillations of drops with internal circulation”. In: *Physics of Fluids* 10.5 (1998), pp. 1071–1082. DOI: 10.1063/1.869632.

[99] C. Tufano, G. W M Peters, and H. E H Meijer. “Confined flow of polymer blends”. In: *Langmuir* (2008). DOI: 10.1021/la7036636.

[100] H A Stone, A D Stroock, and A Ajdari. “Engineering flows in small devices: Microfluidics toward a lab-on-a-chip”. In: *Annual Review of Fluid Mechanics* (2004).

[101] A E Komrakova et al. “Lattice Boltzmann simulations of drop deformation and breakup in shear flow”. In: *International Journal of Multiphase Flow* 59 (2014), pp. 24–43. DOI: http://dx.doi.org/10.1016/j.ijmultiphaseflow.2013.10.009.

[102] Ali Abou-Hassan, Olivier Sandre, and Valérie Cabuil. *Microfluidics in inorganic chemistry*. 2010. DOI: 10.1002/anie.200904285.

[103] Liang Li et al. “A plug-based microfluidic system for dispensing lipidic cubic phase (LCP) material validated by crystallizing membrane proteins in lipidic mesophases”. In: *Microfluidics and Nanofluidics* (2010). DOI: 10.1007/s10404-009-0512-8.

[104] A. C. Rowat et al. “Tracking lineages of single cells in lines using a microfluidic device”. In: *Proceedings of the National Academy of Sciences* (2009). DOI: 10.1073/pnas.0903163106.

[105] Ashleigh B. Theberge et al. *Microdroplets in microfluidics: An evolving platform for discoveries in chemistry and biology*. 2010. DOI: 10.1002/anie.200906653.

[106] Saurabh Vyawahare, Andrew D. Griffiths, and Christoph A. Merten. *Miniaturization and parallelization of biological and chemical assays in microfluidic devices*. 2010. DOI: 10.1016/j.chembiol.2010.09.007.

[107] Ralf Seemann et al. “Droplet based microfluidics”. In: *Reports on Progress in Physics* 75.1 (2012). DOI: 10.1088/0034-4885/75/1/016601.

[108] M R Kennedy, C Pozrikidis, and R Skalak. “Motion and deformation of liquid drops, and the rheology of dilute emulsions in simple shear flow”. In: *Computers and Fluids* 23.2 (1994), pp. 251–278. DOI: http://dx.doi.org/10.1016/0045-7930(94)90040-X.

[109] G I Taylor. “The Viscosity of a Fluid Containing Small Drops of Another Fluid”. In: *Proceedings of the Royal Society of London A: Mathematical, Physical and Engineering Sciences* 138.834 (1932), pp. 41–48. DOI: 10.1098/rspa.1932.0169.

[110] G I Taylor. “The Formation of Emulsions in Definable Fields of Flow”. In: *Proceedings of the Royal Society of London A: Mathematical, Physical and Engineering Sciences* 146.858 (1934), pp. 501–523. DOI: 10.1098/rspa.1934.0169.

[111] J M Rallison. “The Deformation of Small Viscous Drops and Bubbles in Shear Flows”. In: *Annual Review of Fluid Mechanics* 16.1 (1984), pp. 45–66. DOI: 10.1146/annurev.fl.16.010184.000401.

[112] H A Stone. "Dynamics of Drop Deformation and Breakup in Viscous Fluids". In: *Annual Review of Fluid Mechanics* 26.1 (1994), pp. 65–102. DOI: 10.1146/annurev.fl.26.010194.000433.

[113] V Cristini and Y Renardy. "Scalings for droplet sizes in shear-driven breakup: non-microfluidic ways to monodisperse emulsions". In: *Fluid Dyn. Mater. Process* 2.2 (2006), pp. 77–94.

[114] Charles Raphael Marks. "Drop breakup and deformation in sudden onset strong flows". In: (1998).

[115] B J Bentley and L G Leal. "An experimental investigation of drop deformation and breakup in steady, two-dimensional linear flows". In: *Journal of Fluid Mechanics* 167 (1986), pp. 241–283. DOI: 10.1017/S0022112086002811.

[116] Anja Vananroye, Peter Van Puyvelde, and Paula Moldenaers. "Structure development in confined polymer blends: steady-state shear flow and relaxation". In: *Langmuir* 22.5 (2006), pp. 2273–2280.

[117] Vincenzo Sibillo et al. "Drop deformation in microconfined shear flow". In: *Physical Review Letters* 97.5 (2006). DOI: 10.1103/PhysRevLett.97.054502.

[118] M Shapira and S Haber. "Low reynolds number motion of a droplet between two parallel plates". In: *International Journal of Multiphase Flow* 14.4 (1988), pp. 483–506. DOI: http://dx.doi.org/10.1016/0301-9322(88)90024-9.

[119] M Shapira and S Haber. "Low Reynolds number motion of a droplet in shear flow including wall effects". In: *International Journal of Multiphase Flow* 16.2 (1990), pp. 305–321. DOI: http://dx.doi.org/10.1016/0301-9322(90)90061-M.

[120] Tobias Roths et al. "Dynamics and rheology of the morphology of immiscible polymer blends – on modeling and simulation". In: *Rheologica Acta* 41.3 (), pp. 211–222.

[121] R G M van der Sman and S van der Graaf. "Emulsion droplet deformation and breakup with Lattice Boltzmann model". In: *Computer Physics Communications* 178.7 (2008), pp. 492–504. DOI: http://dx.doi.org/10.1016/j.cpc.2007.11.009.

[122] S Richardson. "Two-dimensional bubbles in slow viscous flows". In: *Journal of Fluid Mechanics* 33.03 (1968), pp. 475–493. DOI: 10.1017/S0022112068001461.

[123] E M Toose, B J Geurts, and J G M Kuerten. "A boundary integral method for two-dimensional (non)-Newtonian drops in slow viscous flow". In: *Journal of Non-Newtonian Fluid Mechanics* 60.2–3 (1995), pp. 129–154. DOI: http://dx.doi.org/10.1016/0377-0257(95)01386-3.

[124] Mario Minale. "A phenomenological model for wall effects on the deformation of an ellipsoidal drop in viscous flow". In: *Rheologica Acta*. Vol. 47. 5-6. 2008, pp. 667–675. DOI: 10.1007/s00397-007-0237-0.

[125] S Kwak and C Pozrikidis. "Adaptive Triangulation of Evolving, Closed, or Open Surfaces by the Advancing-Front Method". In: *Journal of Computational Physics* 145.1 (1998), pp. 61–88. DOI: http://dx.doi.org/10.1006/jcph.1998.6030.

[126] P J A Janssen and P D Anderson. "Boundary-integral method for drop deformation between parallel plates". In: *Physics of Fluids* 19.4 (2007). DOI: http://dx.doi.org/10.1063/1.2715621.

[127] C Pozrikidis. *Boundary Integral and Singularity Methods for Linearized Viscous Flow (Cambridge Texts in Applied Mathematics)*. Cambridge University Press, Feb. 1992.

[128] Haowen Xi and Comer Duncan. "Lattice Boltzmann simulations of three dimensional single droplet deformation and breakup under simple shear flow". In: *Phys. Rev. E* 59.3 (Mar. 1999), pp. 3022–3026. DOI: 10.1103/PhysRevE.59.3022.

[129] Xiaowen Shan and Hudong Chen. "Lattice Boltzmann model for simulating flows with multiple phases and components". In: *Phys. Rev. E* 47.3 (Mar. 1993), pp. 1815–1819. DOI: 10.1103/PhysRevE.47.1815.

[130] Jie Li, Yuriko Y Renardy, and Michael Renardy. "Numerical simulation of breakup of a viscous drop in simple shear flow through a volume-of-fluid method". In: *Physics of Fluids* 12.2 (2000).

[131] Yuriko Y Renardy and Vittorio Cristini. "Effect of inertia on drop breakup under shear". In: *Physics of Fluids* 13.1 (2001).

[132] Y Renardy, V Cristini, and J Li. "Drop fragment distributions under shear with inertia". In: *International Journal of Multiphase Flow* 28.7 (2002), pp. 1125–1147. DOI: http://dx.doi.org/10.1016/S0301-9322(02)00022-8.

[133] Damir B Khismatullin, Yuriko Renardy, and Vittorio Cristini. "Inertia-induced breakup of highly viscous drops subjected to simple shear". In: *Physics of Fluids* 15.5 (2003).

[134] Kristof Verhulst et al. "Influence of viscoelasticity on drop deformation and orientation in shear flow Part 1. Stationary states". In: *J. Non-Newtonian Fluid Mech* 156 (2009), pp. 29–43. DOI: 10.1016/j.jnnfm.2008.06.007.

[135] Swarnajay Mukherjee and Kausik Sarkar. "Effects of viscoelasticity on the retraction of a sheared drop". In: *Journal of Non-Newtonian Fluid Mechanics* 165.7-8 (2010), pp. 340–349. DOI: 10.1016/j.jnnfm.2010.01.008.

[136] Adam S. Hsu and L. Gary Leal. "Deformation of a viscoelastic drop in planar extensional flows of a Newtonian fluid". In: *Journal of Non-Newtonian Fluid Mechanics* 160.2-3 (Aug. 2009), pp. 176–180. DOI: 10.1016/j.jnnfm.2009.03.004.

[137] Nikolaos Ioannou et al. "Droplet Dynamics of Newtonian and Inelastic Non-Newtonian Fluids in Connement". In: *Micromachines* 8.2 (2017), p. 57. DOI: 10.3390/mi8020057.

[138] Néstor Balcázar et al. "Level-set simulations of buoyancy-driven motion of single and multiple bubbles". In: *International Journal of Heat and Fluid Flow* 56 (2015), pp. 91–107. DOI: 10.1016/j.ijheatfluidflow.2015.07.004.

[139] Anja Vananroye, Peter Van Puyvelde, and Paula Moldenaers. "Effect of confinement on droplet breakup in sheared emulsions". In: *Langmuir* 22.9 (2006), pp. 3972–3974. DOI: 10.1021/la060442+.

[140] P. J. a. Janssen et al. “Generalized behavior of the breakup of viscous drops in confinements”. In: *Journal of Rheology* 54.5 (2010), p. 1047. DOI: 10.1122/1.3473924.

[141] Niels G. Deen and J. A.M. Kuipers. “Direct numerical simulation of wall-to liquid heat transfer in dispersed gas-liquid two-phase flow using a volume of fluid approach”. In: *Chemical Engineering Science* (2013). DOI: 10.1016/j.ces.2013.08.025.

[142] S.V. Patankar. *Numerical Heat Transfer and Fluid Flow*. 1980.

[143] Andrea Prosperetti. “Navier-Stokes Numerical Algorithms for Free-Surface Flow Computations: An Overview”. In: *Drop-Surface Interactions*. Ed. by Martin Rein. Vienna: Springer Vienna, 2002, pp. 237–257.

[144] S. Armfield and R. Street. “An analysis and comparison of the time accuracy of fractional-step methods for the Navier-Stokes equations on staggered grids”. In: *International Journal for Numerical Methods in Fluids* 38.3 (Jan. 2002), pp. 255–282. DOI: 10.1002/fld.217.

[145] J. Kim and P. Moin. “Application of a fractional-step method to incompressible Navier-Stokes equations”. In: *Journal of Computational Physics* 59.2 (1985), pp. 308–323. DOI: 10.1016/0021-9991(85)90148-2.

[146] Frédéric N Felten and Thomas S Lund. “Kinetic energy conservation issues associated with the collocated mesh scheme for incompressible flow”. In: *Journal of Computational Physics* 215.2 (2006), pp. 465–484. DOI: http://dx.doi.org/10.1016/j.jcp.2005.11.009.

[147] R. G. Cox. “The deformation of a drop in a general time-dependent fluid flow”. In: *Journal of Fluid Mechanics* (1969). DOI: 10.1017/S0022112069000759.

[148] Gace. “Dispersion phenomena in high viscosity immiscible fluid systems and application of static mixers as dispersion devices in such systems”. In: *Chemical Engineering Communications* (1982), pp. 37–41. DOI: 10.1080/00986449408936233.

[149] Anja Vananroye et al. “Effect of confinement and viscosity ratio on the dynamics of single droplets during transient shear flow”. In: *Journal of Rheology* 52.6 (2008), pp. 1459–1475. DOI: 10.1122/1.2978956.

[150] R Byron Bird et al. *Dynamics of Polymeric Liquids, Kinetic Theory (Dynamics of Polymer Liquids Vol. 2) (Volume 2)*. Volume 2. Wiley-Interscience, June 1987.

[151] P N B Reis et al. "Impact response of Kevlar composites with filled epoxy matrix". In: *Composite Structures* 94.12 (2012), pp. 3520–3528. DOI: https://doi.org/10.1016/j.compstruct.2012.05.025.

[152] Abhijit Majumdar, Bhupendra Singh Butola, and Ankita Srivastava. "Development of soft composite materials with improved impact resistance using Kevlar fabric and nano-silica based shear thickening fluid". In: *Materials & Design (1980-2015)* 54 (2014), pp. 295–300. DOI: https://doi.org/10.1016/j.matdes.2013.07.086.

[153] Oren E Petel et al. "A comparison of the ballistic performance of shear thickening fluids based on particle strength and volume fraction". In: *International Journal of Impact Engineering* 85 (2015), pp. 83–96. DOI: https://doi.org/10.1016/j.ijimpeng.2015.06.004.

[154] Fridtjov Irgens. *Rheology and non-newtonian fluids*. Vol. 9783319010. 2013, pp. 1–190. DOI: 10.1007/978-3-319-01053-3.

[155] Ajay Bansal, R. K. Wanchoo, and S. K. Sharma. "Two-phase pressure drop in a trickle bed reactor involving newtonian/ non-newtonian liquid phase". In: *Chemical Engineering Communications* 195.9 (2008), pp. 1085–1106. DOI: 10.1080/00986440801907268.

[156] M. F. Tomé et al. "A finite difference technique for simulating unsteady viscoelastic free surface flows". In: *Journal of Non-Newtonian Fluid Mechanics* 106.2-3 (2002), pp. 61–106. DOI: 10.1016/S0377-0257(02)00064-2.

[157] C M Oishi et al. "Numerical simulation of drop impact and jet buckling problems using the eXtended Pom-Pom model". In: *Journal of Non-Newtonian Fluid Mechanics* 169-170.1 (2012), pp. 91–103. DOI: 10.1016/j.jnnfm.2011.12.001.

[158] Murilo F. Tome and Sean McKee. "Numerical simulation of viscous flow: Buckling of planar jets". In: *International Journal for Numerical Methods in Fluids* 29.6 (1999), pp. 705–718. DOI: 10.1002/(SICI)1097-0363(19990330)29:6<705::AID-FLD809>3.0.CO;2-C.

[159] Luciane S. Ferreira and Jorge O. Trierweiler. "Modeling and simulation of the polymeric nanocapsule formation process". In: *IFAC Proceedings Volumes (IFAC-PapersOnline)* 7.PART 1 (2009), pp. 405–410. DOI: 10.1002/aic.

[160] Nishith Aggarwal and Kausik Sarkar. "Effects of matrix viscoelasticity on viscous and viscoelastic drop deformation in a shear flow". In: *Journal of Fluid Mechanics* 601 (2008), pp. 63–84. DOI: 10.1017/S0022112008000451.

[161] Jiannong Fang et al. "A numerical study of the SPH method for simulating transient viscoelastic free surface flows". In: *Journal of Non-Newtonian Fluid Mechanics* 139.1-2 (2006), pp. 68–84. DOI: 10.1016/j.jnnfm.2006.07.004.

[162] Tao Jiang et al. "The SPH method for simulating a viscoelastic drop impact and spreading on an inclined plate". In: *Computational Mechanics* 45.6 (2010), pp. 573–583. DOI: 10.1007/s00466-010-0471-7.

[163] A Rafiee, M T Manzari, and M Hosseini. "An incompressible SPH method for simulation of unsteady viscoelastic free-surface flows". In: *International Journal of Non-Linear Mechanics* 42.10 (2007), pp. 1210–1223. DOI: 10.1016/j.ijnonlinmec.2007.09.006.

[164] A. Zainali et al. "Numerical investigation of Newtonian and non-Newtonian multiphase flows using ISPH method". In: *Computer Methods in Applied Mechanics and Engineering* 254 (2013), pp. 99–113. DOI: 10.1016/j.cma.2012.10.005.

[165] A J Wagner, L Giraud, and C E Scott. "Simulation of a cusped bubble rising in a viscoelastic fluid with a new numerical method". In: *Computer Physics Communications* 129.1 (2000), pp. 227–232. DOI: 10.1016/S0010-4655(00)00109-0.

[166] Xavier Frank et al. “A Multiscale Approach for Modeling Bubbles Rising in Non-Newtonian Fluids”. In: *Ind. Eng. Chem. Res* 51 (2012), pp. 2084–2093. DOI: 10.1021/ie2006577.

[167] Ningning Wang, Haihu Liu, and Chuhua Zhang. “Deformation and breakup of a confined droplet in shear flows with power-law rheology”. In: *Journal of Rheology* 61.4 (2017), pp. 741–758. DOI: 10.1122/1.4984757.

[168] Anupam Gupta and Mauro Sbragaglia. “Deformation and break-up of Viscoelastic Droplets Using Lattice Boltzmann Models”. In: *Procedia IUTAM*. Vol. 15. 15. 2015, pp. 215–227. DOI: 10.1016/j.piutam.2015.04.030.

[169] Kai Sun et al. “Non-Newtonian flow effects on the coalescence and mixing of initially stationary droplets of shear-thinning fluids”. In: *Physical Review E - Statistical, Nonlinear, and Soft Matter Physics* 91.2 (2015), pp. 1–10. DOI: 10.1103/PhysRevE.91.023009.

[170] Siddhartha F. Lunkad, Vivek V. Buwa, and K. D.P. Nigam. “Numerical simulations of drop impact and spreading on horizontal and inclined surfaces”. In: *Chemical Engineering Science* 62.24 (2007), pp. 7214–7224. DOI: 10.1016/j.ces.2007.07.036.

[171] J L Favero et al. “Viscoelastic fluid analysis in internal and in free surface flows using the software OpenFOAM”. In: *Computers and Chemical Engineering* 34 (2010), pp. 1984–1993. DOI: 10.1016/j.compchemeng.2010.07.010.

[172] Andrea Bonito, Marco Picasso, and Manuel Laso. “Numerical simulation of 3D viscoelastic flows with free surfaces POOPING”. In: *Journal of Computational Physics* 215.2 (2006), pp. 691–716. DOI: 10.1016/j.jcp.2005.11.013.

[173] Wanpeng Sun et al. “The minimum in-line coalescence height of bubbles in non-Newtonian fluid”. In: *International Journal of Multiphase Flow* 92 (2017), pp. 161–170. DOI: 10.1016/j.ijmultiphaseflow.2017.03.011.

[174] Altti Torkkeli. “Droplet microfluidics on a planar surface”. In: *VTT Publications* 61.504 (2003), pp. 3–194. DOI: 10.1002/aic. arXiv: 0201037v1 [physics].

[175] Nelson O Moraga et al. "VOF/FVM prediction and experimental validation for shear-thinning fluid column collapse". In: *Computers and Mathematics with Applications* 69 (2015), pp. 89–100. DOI: 10.1016/j.camwa.2014.11.018.

[176] B P Leonard. "The ULTIMATE conservative difference scheme applied to unsteady one-dimensional advection". In: *Computer Methods in Applied Mechanics and Engineering* 88.1 (1991), pp. 17–74. DOI: https://doi.org/10.1016/0045-7825(91)90232-U.

[177] A R Premlata et al. "Dynamics of an air bubble rising in a non-Newtonian liquid in the axisymmetric regime". In: *Journal of Non-Newtonian Fluid Mechanics* 239 (2017), pp. 53–61. DOI: 10.1016/j.jnnfm.2016.12.003.

[178] S. Abishek, A. J.C. King, and R. Narayanaswamy. "Dynamics of a Taylor bubble in steady and pulsatile co-current flow of Newtonian and shear-thinning liquids in a vertical tube". In: *International Journal of Multiphase Flow* 74 (2015), pp. 148–164. DOI: 10.1016/j.ijmultiphaseflow.2015.04.014.

[179] J. D.P. Araújo, J. M. Miranda, and J. B.L.M. Campos. "Taylor bubbles rising through flowing non-Newtonian inelastic fluids". In: *Journal of Non-Newtonian Fluid Mechanics* 245 (2017), pp. 49–66. DOI: 10.1016/j.jnnfm.2017.04.009.

[180] Jiun Der Yu, Shinri Sakai, and J A Sethian. "Two-phase viscoelastic jetting". In: *Journal of Computational Physics* 220.2 (2007), pp. 568–585. DOI: 10.1016/j.jcp.2006.05.020.

[181] Tayfun E Tezduyar et al. "Convected level set method for the numerical simulation of fluid buckling". In: *International Journal for Numerical Methods in Fluids* October 2007 (2008), pp. 601–629. DOI: 10.1002/fld.

[182] J L Prieto. "Stochastic particle level set simulations of buoyancy-driven droplets in non-Newtonian fluids". In: *Journal of Non-Newtonian Fluid Mechanics* 226 (2015), pp. 16–31. DOI: 10.1016/j.jnnfm.2015.10.002.

[183] Shriram B. Pillapakkam et al. "Transient and steady state of a rising bubble in a viscoelastic fluid". In: *Journal of Fluid Mechanics* 589 (2007), pp. 215–252. DOI: 10.1017/S0022112007007628.

[184] Elin Olsson and Gunilla Kreiss. "A conservative level set method for two phase flow". In: *Journal of Computational Physics* 210.1 (2005), pp. 225–246. DOI: 10.1016/j.jcp.2005.04.007.

[185] Ann S. Almgren et al. "A Conservative Adaptive Projection Method for the Variable Density Incompressible Navier-Stokes Equations". In: *Journal of Computational Physics* 142.1 (1998), pp. 1–46. DOI: 10.1006/jcph.1998.5890.

[186] X. Chen et al. "A comparison of stabilisation approaches for finite-volume simulation of viscoelastic fluid flow". In: *International Journal of Computational Fluid Dynamics* 27.6-7 (2013), pp. 229–250. DOI: 10.1080/10618562.2013.829916.

[187] Raanan Fattal and Raz Kupferman. "Constitutive laws for the matrix-logarithm of the conformation tensor". In: *Journal of Non-Newtonian Fluid Mechanics* 123.2-3 (2004), pp. 281–285. DOI: 10.1016/j.jnnfm.2004.08.008.

[188] M A Hulsen, A P G van Heel, and B.H.A.A van den Brule. "Simulation of viscoelastic flows using Brownian configuration fields". In: *Journal of Non-Newtonian Fluid Mechanics* 70.1 (1997), pp. 79–101. DOI: https://doi.org/10.1016/S0377-0257(96)01503-0.

[189] Jaewook Lee et al. "Practical comparison of differential viscoelastic constitutive equations in finite element analysis of planar 4:1 contraction flow". In: *Rheologica Acta* 44.2 (Dec. 2004), pp. 188–197. DOI: 10.1007/s00397-004-0399-y.

[190] Michael Renardy. "Current issues in non-Newtonian flows: A mathematical perspective". In: *Journal of Non-Newtonian Fluid Mechanics* 90.2-3 (2000), pp. 243–259. DOI: 10.1016/S0377-0257(99)00081-6.

[191] Raanan Fattal and Raz Kupferman. "Time-dependent simulation of viscoelastic flows at high Weissenberg number using the log-conformation representation". In: *Journal of Non-Newtonian Fluid Mechanics* 126.1 (2005), pp. 23–37. DOI: https://doi.org/10.1016/j.jnnfm.2004.12.003.

[192] Martien A Hulsen, Raanan Fattal, and Raz Kupferman. "Flow of viscoelastic fluids past a cylinder at high Weissenberg number: Stabilized simulations using matrix logarithms". In: *Journal of Non-Newtonian Fluid Mechanics* 127.1 (2005), pp. 27–39. DOI: https://doi.org/10.1016/j.jnnfm.2005.01.002.

[193] P. A. Stewart et al. "An improved sharp interface method for viscoelastic and viscous two-phase flows". In: *Journal of Scientific Computing* 35.1 (2008), pp. 43–61. DOI: 10.1007/s10915-007-9173-5.

[194] Nusret Balci et al. "Symmetric factorization of the conformation tensor in viscoelastic fluid models". In: *Journal of Non-Newtonian Fluid Mechanics* 166.11 (2011), pp. 546–553. DOI: 10.1016/j.jnnfm.2011.02.008.

[195] Kausik Sarkar and William R. Schowalter. "Deformation of a two-dimensional viscoelastic drop at non-zero Reynolds number in time-periodic extensional flows". In: *Journal of Non-Newtonian Fluid Mechanics* 95.2-3 (2000), pp. 315–342. DOI: 10.1016/S0377-0257(00)00156-7.

[196] T. Chinyoka et al. "Two-dimensional study of drop deformation under simple shear for Oldroyd-B liquids". In: *Journal of Non-Newtonian Fluid Mechanics* 130.1 (2005), pp. 45–56. DOI: 10.1016/j.jnnfm.2005.07.005.

[197] L. J. Amoreira and P. J. Oliveira. "Comparison of different formulations for the numerical calculation of unsteady incompressible viscoelastic fluid flow". In: *Advances in Applied Mathematics and Mechanics* 2.4 (2010), pp. 483–502. DOI: 10.4208/aamm.10-m1010.

[198] Néstor Balcázar et al. "A finite-volume/level-set method for simulating two-phase flows on unstructured grids". In: *International Journal of Multiphase Flow* 64 (2014), pp. 55–72. DOI: http://dx.doi.org/10.1016/j.ijmultiphaseflow.2014.04.008.

[199] A. Carmona et al. "Numerical analysis of the transpose diffusive term for viscoplastic-type non-newtonian fluid flows using a collocated variable arrangement". In: *Numerical Heat Transfer, Part B: Fundamentals* 67.5 (2015), pp. 410–436. DOI: 10.1080/10407790.2014.964575.

[200] Kerim Yapici, Bulent Karasozen, and Yusuf Uludag. "Journal of Non-Newtonian Fluid Mechanics Finite volume simulation of viscoelastic laminar flow in a lid-driven cavity". In: 164 (2009), pp. 51–65. DOI: 10.1016/j.jnnfm.2009.08.004.

[201] E. O. Carew, P. Townsend, and M. F. Webster. "Taylor-Galerkin algorithms for viscoelastic flow: Application to a model problem". In: *Numerical Methods for Partial Differential Equations* 10.2 (Mar. 1994), pp. 171–190. DOI: 10.1002/num.1690100204.

[202] D. J E Harvie, J. J. Cooper-White, and M. R. Davidson. "Deformation of a viscoelastic droplet passing through a microfluidic contraction". In: *Journal of Non-Newtonian Fluid Mechanics* 155.1-2 (2008), pp. 67–79. DOI: 10.1016/j.jnnfm.2008.05.002.

[203] S. Guido, M. Simeone, and F. Greco. "Deformation of a Newtonian drop in a viscoelastic matrix under steady shear flow Experimental validation of slow flow theory". In: *Journal of Non-Newtonian Fluid Mechanics* 114.1 (2003), pp. 65–82. DOI: 10.1016/S0377-0257(03)00118-6.

[204] Pier Luca Maffettone and Francesco Greco. "Ellipsoidal drop model for single drop dynamics with non-Newtonian fluids". In: *Journal of Rheology* 48.1 (2004), pp. 83–100. DOI: 10.1122/1.1626675.